Faculty of Science
Department of Physics
Earth and Life Institute

Royal Meteorological Inst.
of Belgium
Climate Dynamics Department

Dynamics of Atmospheric Multi-Scale Systems: A Low-Order Model Perspective

Doctoral Dissertation presented by

Oisín Hamilton

in partial fulfillment of the requirements for the degree of
Doctor in Sciences of the Université catholique de Louvain

Thesis committee:

Prof. Michel Crucifix (Supervisor)	UC Louvain, Belgium
Dr. Jonathan Demaeyer	Royal Meteorological Institute of Belgium
Prof. Dr. Ulrike Feudel	Carl von Ossietzky University of Oldenburg, Germany
Prof. Valerio Lucarini	University of Leicester, UK
Prof. François Massonnet (Secretary)	UC Louvain, Belgium
Dr. Stéphane Vannitsem (Supervisor)	Royal Meteorological Institute of Belgium
Prof. Qiuzhen Yin (President)	UC Louvain, Belgium

Louvain-la-Neuve
September 2025

If you march your Winter Journeys you will have your reward,
so long as all you want is a penguin's egg. -*Cherry-Garrard*

Acknowledgments

This thesis would not have been possible without the help from many people. Here I would like to acknowledge the assistance I have received. This support has taken many forms, from guidance in work and how to navigate the world of academia. I also want to acknowledge the crucial support that I have received from friends and family, outside of work.

My supervisors Stéphane Vannitsem and Michel Crucifix have been instrumental to this thesis. Stéphane, thank you for your constant support and expertise in the topic. I have always greatly appreciated how you balance giving the time and room for discovery and investigating new directions in research, yet were always available when I was struggling. Thank you Michel for always providing a critical eye and targeted feedback. I have always appreciated your drive to link my relatively theoretical work with the bigger picture, and the high standard of work that you expect from your students. A huge thanks to Michel for also helping secure the funds for the final year of my doctorate. Jonathan Demaeyer has played a vital role in helping me over the last four years, and many parts of this thesis would not have been possible without his assistance. In addition to the invaluable help with science and coding aspects, thank you Jonathan for teaching me about the parts of science that are behind the scenes, and how they work.

This project included two research visits, and I would like to thank the two professors, Mark Holland and Henk Dijkstra, who took me under their expert guidance during this time. I found these visits invaluable for my research. Perhaps equally importantly to the scientific results, I also learnt valuable lessons about juggling research projects and focusing on new directions of research outside my usual areas of expertise, and I would like to thank the professors for also helping guide me through these crucial skills as researchers.

Thank you to all the members of my jury; Ulrike Feudel, Valerio Lucarini, and François Massonnet. I am extremely grateful to you all for taking so much time out of your busy schedule to read the original version of this thesis and provide

comments and critiques. They have led to, I hope, a vastly improved work. Your attention to detail and engagement with my work have been a privilege to receive. Thank you also to the president of my jury, Qiuzhen Yin for the professional and enjoyable manner in which the defences were run.

I have been fortunate to work as part of a network of PhD students as part of the CritialEarth project. I thank all the other 14 students for teaching me a huge amount from discussions with all of ye, getting to ask stupid questions, and learn about the wider field over a drink in some amazing places. A special thank to the groups in Exeter and Utrecht for making me feel so welcome during my time there.

I have been fortunate enough to have a fantastic bunch of colleges around me, both at UC Louvain and at RMIB, who have been fantastic help. It has been brilliant to be surrounded by people doing a wide range of topics on climate science as well as those doing more day to day meteorology. I would like to especially thank Anupama K. Xavier for being always being around to discuss work and life.

Thank you to all my friends for visits, chats, and escapes from work. I have been so lucky to live with an amazing group of people that have taught me so much about how to be a considerate and respectful human and made my years in Brussels some of my fondest. Luca, the only colocataire who managed to put up with me for the entire four years, thank you for all the food and impromptu camping trips.

My family have been a massive support. I want to thank my wider family for always being interested in my work, regardless of how poorly I described it. Thank you to my siblings, Sorcha and Cian, for visiting me in Brussels, and to keep me pushing myself to find what brings me meaning. My parents, Phillida and Tedd, thank you for your constant encouragement to try living in new places and to keep learning. I hope this thesis provides some physical proof that your seven years of home schooling must have been alright, and that I was right when I said, at the age of 10, that you don't need to know your times tables to be able to do maths. All other thanks are reserved for my partner Éabha. Without your love and care this thesis would be a poorer piece of work - and I would be a less complete person.

This project has received funding from the European Union's Horizon 2020 research and innovation programme under the Marie Sklodowska-Curie grant agreement No.956170. In addition, funding has been provided through the "Fédération Wallonie-Bruxelles" with the instrument "Fonds Spéciaux de Recherche".

Résumé

L'atmosphère aux latitudes moyennes présente une variabilité basse fréquence (LFV en anglais), mobilisant des des échelles de temps beaucoup plus longues que l'horizon habituel de prévision de deux semaines. Cette LFV provient de couplages, ou interactions, entre l'atmosphère et d'autres composantes du système climatique, ainsi que de la variabilité interne au sein de l'atmosphère. L'objectif général de cette thèse est d'étudier la LFV pour améliorer notre compréhension de la façon dont une telle variabilité prend naissance, et évaluer dans quelle mesure elle pourrait être impactée par le changement climatique. Cette thèse aborde ces questions en utilisant des modèles d'ordre réduit, qui visent à simplifier la dynamique fondamentale du comportement atmosphérique couplé. Les domaines spécifiques suivants sont abordés.

Le blocage atmosphérique est ici considéré comme un régime persistant dont le comportement est lié aux structures sous-jacentes de l'espace des phases. Nous avons utilisé les orbites périodiques instables (UPO en anglais) pour comprendre l'origine de la répartition observée des solutions d'un modèle couplant l'équilibre énergétique de la surface et la dynamique de l'atmosphère. Nous avons montré que l'initiation et la disparition des blocages peuvent être liés aux transitions entre des familles d'orbites. Dans cette étude, nous avons également élargi la méthode de masquage (shadowing en anglais) des trajectoires avec des orbites périodiques instable, en examinant le nombre cumulatif de fois qu'une UPO "recouvre" la solution du modèle sur une période de temps fixée. Ce concept a été utilisé pour identifier les différents cycles de vie de chaque groupe dans l'espace des phases en créant des ensembles correspondants d'UPO.

L'analyse ci-dessus a également été étendue pour comprendre comment le changement climatique pourrait impacter la LFV aux latitudes moyennes. Ceci a été fait en utilisant le même modèle, mais avec des valeurs de paramètres dépendantes de l'espace, ainsi qu'en altérant la résolution du modèle. Les résultats confirment la littérature qui montre que le changement climatique induit des réponses opposées au sein de l'atmosphère en fonction des modifications effectuées. Cela crée une incertitude sur la façon dont l'atmosphère pourrait répondre au changement climatique. Nous montrons également que les modèles spectraux d'ordre réduit peuvent présenter différentes dynamiques, selon la résolution, ou, ce qui est équivalent, le nombre de modes d'onde inclus. Pour surmonter cette limitation, nous avons testé des modèles de résolution intermédiaire.

Les régimes climatiques ont également été explorés dans le contexte d'un système océan-atmosphère d'ordre réduit. En incorporant un schéma complet de rayonnement non linéaire, plutôt que sa version linéarisée, il a été montré que plusieurs états climatiques peuvent émerger, avec des températures globales moyennes distinctes et coexistent pour les mêmes valeurs de paramètres. En plus de différentes structures d'écoulement et de variabilité basse fréquence distinctes, ce travail a montré que les attracteurs chaotiques présentent des niveaux de prévisibilité et de dimensionnalité très différents.

Finalement, comme les modèles classiques d'ordre réduit se concentrent seulement sur les grandes échelles de l'écoulement, nous avons analysé l'impact sur les transferts d'énergie, de l'inclusion d'un grand nombre d'échelles spatiales. Un modèle simplifié pour étudier les transferts d'énergie turbulente (un modèle en "coquilles") a été développé pour étudier comment l'énergie est transférée entre les échelles de l'atmosphère. Le but de ceci est de clarifier quelles sont les échelles et les interactions de triades nécessaires pour modéliser une atmosphère quasigéostrophique à deux couches. Ce travail a montré que des modèles extrêmement simplifiés peuvent capturer la même cascade turbulente que prédite par la théorie. Ceci fournit un cadre naturel et élégant pour étudier les propriétés des transferts d'énergie dans les modèles spectraux quasigéostrophiques à deux couches que nous avons utilisé tout au long de cette thèse.

En résumé, dans cette thèse, nous avons construit un nombre de modèles d'ordre réduit permettant d'analyser certaines propriétés de la dynamique de l'atmosphère, révélant la richesse et la diversité des comportements dynamiques présents. Les découvertes de cette thèse fournissent de nouvelles pistes d'études de l'émergence of la variabilité basse-fréquence des modèles climatiques plus sophistiqué, ainsi que la façon dont différentes composantes du système climatique interagissent entre elles.

Abstract

The weather in the midlatitudes displays low frequency variability (LFV), or long term repetitions, over time spans much longer than the usual two week forecasting horizon. This LFV originates from couplings, or interactions, between the atmosphere and other components of the climate system, as well as internal variability within the atmosphere. The overall aim of this thesis is to study LFV to increase our understanding of how such variability originates, and how it could be impacted by the changing climate. This thesis goes about answering these questions using reduced order models, which aim to distil the core dynamics of the coupled atmosphere behaviour. The following specific areas are addressed.

Atmospheric blocking is studied from a regime perspective, where persistent weather patterns are linked with specific structures in state space. We used unstable periodic orbits (UPOs) to understand the observed clustering behaviour of the model. We found that the onsets and decay of blockings can be linked with transitions between clusters of orbits. In this study we also extended a method of approximating trajectories with orbits, known as shadowing, by looking at the cumulative number of times a UPO shadows a model trajectory over a fixed time period. This concept was used to identify different life cycles of each cluster in state space by creating corresponding sets of UPOs.

The above analysis was used to also investigate how climate change could impact LFV in the midlatitudes. This was done using the same model, but with non-constant parameter values across the domain, as well as altering the model resolution. The results align with the literature, to show that climate change has opposing responses in the atmosphere, leading to uncertainties in how the atmosphere could respond to climate change. We also confirm that reduced order spectral models can present different dynamics, depending on the resolution, or number of wave modes included. To overcome this limitation this study developed and tested models of intermediate resolution.

Climate regimes have also been explored in the context of a reduced order ocean-atmosphere system. By incorporating the full nonlinear longwave radiation scheme, rather than the previous linearised version, it was found that multiple climate states, with distinct average global temperatures, coexist for the same parameter values. In addition to different flow structures and low frequency variability patterns in the atmosphere, this work showed that the distinct chaotic attractors present different levels of predictability and dimensionality.

Finally, as classical reduced-order models only focus on the large scales of the flow, we investigated the impact, on the energy transfers, of including a large number of spatial scales. A simplified model to study turbulent energy transfers (a shell model) was developed to study how energy is transferred between scales in the atmosphere. The aim of this is to investigate the scales and wave triad interactions that are required to model a two layer quasigeostrophic atmosphere. This work demonstrated that extremely simplified models can capture the same turbulent cascade as predicted by theory. This provides a framework to study the accuracy of energy transfers in the spectral two layer quasigeostrophic model, that we used throughout this thesis.

In short, in this thesis, we built a number of reduced order models to investigate the dynamics of the atmosphere, revealing the richness and diversity of the dynamical behaviours present. The findings of this thesis could guide future studies, using more accurate climate models, on the emergence of LFV, and investigations into how different components of the climate system interact.

Contents

Contents **ix**

List of abbreviations **xi**

1 Introduction **1**
1.1 The Weather of the Midlatitudes 1
1.2 Equations for Modelling the Midlatitude Circulation 4
1.3 The Quasi-Geostrophic Approximation 14
1.4 Idealised Climate Models 22
1.5 Chaos 27
1.6 Unstable Periodic Orbits 33
1.7 Thesis Outline and Objectives 38

2 Quasi Geostrophic Spectral Models **41**
2.1 Spectral Models 41
2.2 Quasi-Geostrophic Spectral (qgs) Model 44
2.3 Atmosphere Model 44
2.4 Land-Atmosphere Coupled Model 45
2.5 Ocean-Atmosphere Model 49
2.6 Symbolic qgs 57

3 Using Unstable Periodic Orbits to Understand Blocking Behaviour in a Low Order Land-Atmosphere Model **59**
3.1 Introduction 60
3.2 Methods 63
3.3 Results 66
3.4 Conclusions 82

4 Climate Change Forcings in a Reduced Order Coupled Atmosphere Model **85**
4.1 Introduction 85
4.2 Methodology 88
4.3 Results 91
4.4 Conclusions 106

5 Multistability in a Coupled Ocean–Atmosphere Reduced-Order Model: Nonlinear Temperature Equations 109
5.1 Introduction . . . 110
5.2 Model . . . 113
5.3 Results . . . 115
5.4 Discussion . . . 130

6 A Shell Model of Geostrophic Turbulence 133
6.1 Introduction . . . 133
6.2 Two Dimensional Turbulence . . . 136
6.3 Model Development . . . 140
6.4 Results . . . 149
6.5 Discussion and Conclusions . . . 155

7 Conclusions 159
7.1 Specific Conclusions . . . 159
7.2 General Conclusions . . . 163
7.3 Perspectives . . . 164

A Appendix to the Introduction 167
A.1 Conservation Form of the PV QG equation . . . 167
A.2 Rossby Waves in the Barotropic Model . . . 168
A.3 Baroclinic Instability in Two Layer Model . . . 169
A.4 Lyapunov Vectors . . . 175
A.5 Tensor Correction Method for Finding UPOs . . . 183

B Appendix to Chapter 3 187
B.1 Model Climatology . . . 187
B.2 Origin of Blocking Clusters - Continued . . . 187
B.3 UPO shadowing - RHS figures . . . 187

C Appendix to Chapter 4 191
C.1 Projection of Parameters on Basis Modes . . . 191
C.2 Jet Stream . . . 192

D Appendix to Chapter 5 195
D.1 Video Links . . . 195
D.2 High Resolution Model Attractors . . . 195

E Appendix to Chapter 6 197
E.1 Deriving Nonlinear Interaction Coefficients . . . 197
E.2 Deriving Barotropic Energy Transfer Expressions . . . 198

F List of Publications Related to the Thesis 201

References 203

List of abbreviations

AA	Arctic Amplification
BLV	Backwards Lyapunov Vectors
CLV	Covariant Lyapunov Vectors
CS	Cumulative Shadowing
DE	Dynamic Equilibria
EBM	Energy Balance Model
FLV	Forward Lyapunov Vectors
GPH	Geopotential Height
LFV	Low Frequency Variability
LLE	Largest Lyapunov Exponents
LM	Linear Model
MAOOAM	Modular Arbitrary-Order Ocean-Atmosphere Model
NAO	North Atlantic Oscillation
NSE	Navier-Stokes Equations
NWP	Numerical Weather Prediction
ODE	Ordinary Differential Equations
PDE	Partial Differential Equations
QG	Quasi-Geostrophic
qgs	quasi-geostrophic spectral (model)
T4	Non-Linear (quartic temperature terms)
TE	Tropical Expansion
UPO	Unstable Periodic Orbit

1

Introduction

1.1 The Weather of the Midlatitudes

The day to day weather in the midlatitudes, the area bounded between the Tropic of Cancer/Capricorn and the Arctic/Antarctic circles, is governed by large eddies, called synoptic scale systems [Holton, 2004]. These eddies consist of relatively high or low pressure systems that typically bring settled and unsettled weather, respectively. They are usually over three thousand kilometres in diameter, and they tend to move from west to east due to the jet stream, which is a fast moving band of air located at an altitude of approximately 10km [Stendel et al., 2021]. In North Western Europe the flow of the jet brings, on average, warm moist air from the Atlantic, leading to a relatively mild and moist climate. Figure 1.1 shows the location of the midlatitudes.

The eddies in the midlatitudes are generated by instabilities that form in the jet stream. This is called baroclinic instability [Barry and Chorley, 2003], and is caused by the difference in the amount of solar heating that the equatorial region receives, compared with the polar regions. In other words, a temperature gradient exists between the equator and the poles, and this drives the eddies. This temperature gradient is larger in winter and weaker in summer, due to where the sun is hitting the planet. This leads to an increase in baroclinic instability in the winter, which leads to more powerful eddies [Charney, 1947]. Examples of this are Storm Éowyn that hit Ireland and Britain in early 2025, leading to wind speed records being broken, as well as a strong high pressure systems that brought sustained cold temperatures over the winter of 2017-2018 (Storm Emma, a.k.a “the beast from the east") [Met-Office, 2025; Moore et al., 2018].

Eddies can remain over one location for extended periods of time. An example of this is called atmospheric blocking, where high pressure systems remain relatively stationary over one geographical location, and the usual westerly (zonal) flow is diverted [Tibaldi and Molteni, 2018]. This leads to heat waves in summer, or cold snaps in winter. An example of atmospheric blocking, that occurred during April 2025, is shown in Figure 1.2. The variation in possible weather events, that are seen in the midlatitudes, is referred to as Low

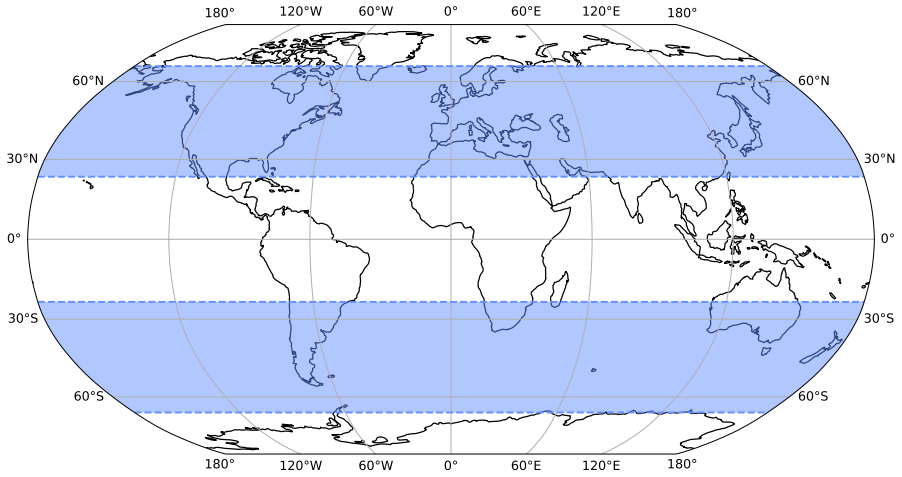
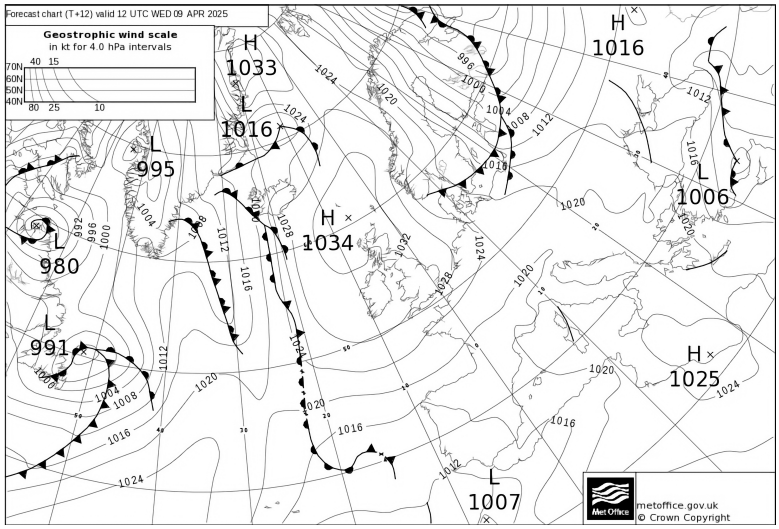


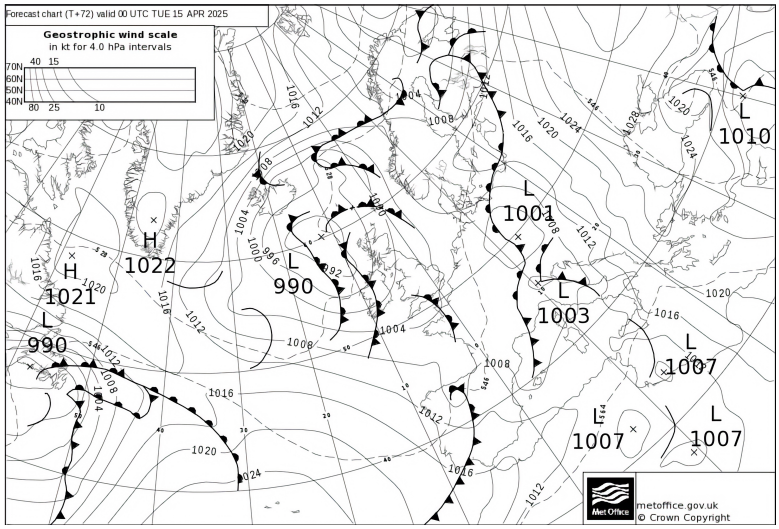
Figure 1.1: Area of the midlatitudes, bounded between the Arctic Circle and the Tropic of Cancer in the Northern Hemisphere, and the Tropic of Capricorn and the Antarctic Circle in the Southern Hemisphere. Image created by Oisín Hamilton, using library of Elson et al. [2024].

Frequency Variability (LFV). This covers a large category of possible weather events that can occur over time spans of weeks to months, longer than the life cycle of an individual eddy [Holton, 2004]. This can include blocking events that disrupt the regular movements of eddies which last a week or so, all the way up to interannual variability that can oscillate over the course of years, such as the El Niño-Southern Oscillation [Ghil and Lucarini, 2020].

Climate change is altering the global radiation balance, resulting in the atmosphere capturing increased amount of solar radiation. As stated earlier, the weather events of the midlatitudes are driven by a temperature gradients, so a change to the global distribution of heating will impact the weather and possible variability in the midlatitudes [Vallis et al., 2015]. Currently, heat waves in Europe are responsible for tens of thousands of deaths per year [Bhatnagar, 2024]. As climate change increases the average temperature of the planet, extreme heat events are expected to increase the number of mortalities in the future [Ballester et al., 2023]. In Western Europe it has been found that climate models are underestimating the temperature and frequencies of extreme temperature events due to changes in the atmospheric circulation [Vautard et al., 2023]. The concern is that the current state of the art models do not accurately capture all of the circulation responses to external forcings, or that they systematically underestimate the strengths of possible eddies. In addition, there is a growing concern that tipping elements in the climate system could alter the climate abruptly and irreversibly [Armstrong McKay et al., 2022]. These tipping elements could have a major impact on atmospheric circulation. For example, the jet



(a) An example of atmospheric blocking, where a high pressure is situated over Scotland, deflecting low pressure systems over Greenland.



(b) A typical North Atlantic low pressure system, bringing unsettled weather to Ireland.

Figure 1.2: Examples of synoptic systems, or eddies, over Europe and the North Atlantic.

© British Crown copyright 2025, the Met Office

stream over Western Europe could be impacted greatly by the weakening of the Atlantic Meridional Ocean Circulation [Van Westen et al., 2024].

Our current understanding of how LFV in the atmosphere forms is still not complete. Numerical Weather Prediction (NWP), or weather forecasting, struggles with accurately forecasting certain aspects of this variability. For example, when atmospheric blocking events will occur or decay [Davini and D'Andrea, 2020]. Conversely, this inherent variability offers an opportunity to extend the usual limit of weather forecasting (approximately two weeks), by understanding the mechanisms behind the repeating patterns [Hannachi et al., 2017]. However, this first requires understanding the dynamical behaviour in the atmosphere that leads to this variability.

1.2 Equations for Modelling the Midlatitude Circulation

The atmosphere contains a huge range of spatial scales and these different scales can be governed by different processes [Holton, 2004]. On the global scale ($\sim 10,000\text{km}$) the general circulation of the atmosphere is driven by large thermal heating, which drives the features such as the Hadley cell and the trade winds. This circulation changes over time spans of seasons to years. Baroclinic instability forces the atmosphere at scales larger than $1,000\text{km}$ and creates synoptic scale systems, which last on the order of days to weeks. Convection and moisture create fronts and thunderstorms at the $10 - 100\text{km}$ scale and these can change in a matter of hours. This continues down to viscosity and small scale turbulence, which occurs on scales of less than one meter. A sketch of the primary scales in the atmosphere is shown in Figure 1.3.

Important atmospheric processes and energy flows occur across at least eight orders of magnitude and a range of time periods from minutes to decades, and for this reason the weather cannot be studied using purely observational and experimental techniques [Edwards, 2011]. Instead, mathematical models, which are based on our understanding of physics that simulate the underlying mechanics, are a necessary part of understanding how the atmosphere behaves. Describing the behaviour of the atmosphere requires consideration of Newton's laws of motion, fluid dynamics, mass conservation, and thermodynamics [Edwards, 2011]. However, due to the large number of scales involved, as well as the large number of components that interact with the atmosphere, modelling all of these processes at once, to an equal degree of accuracy, is not feasible. It is therefore necessary to make simplifications, depending on the scale of interest, to reduce the number of considerations that we must analyse.

1.2.1 Deriving Equations to Model the Atmosphere

At the turn of the twentieth century, Vilhelm Bjerknes derived the primitive equations [Bjerknes, 2009; Lynch, 2008], the equations that describe the large scale flow of the atmosphere and oceans as a set of partial differential equations. Such equations do not have a closed form solution, meaning that they must be solved numerically. At the time, the machinery to numerically solve such equations did not exist, and it was not until the 1910s-1920s

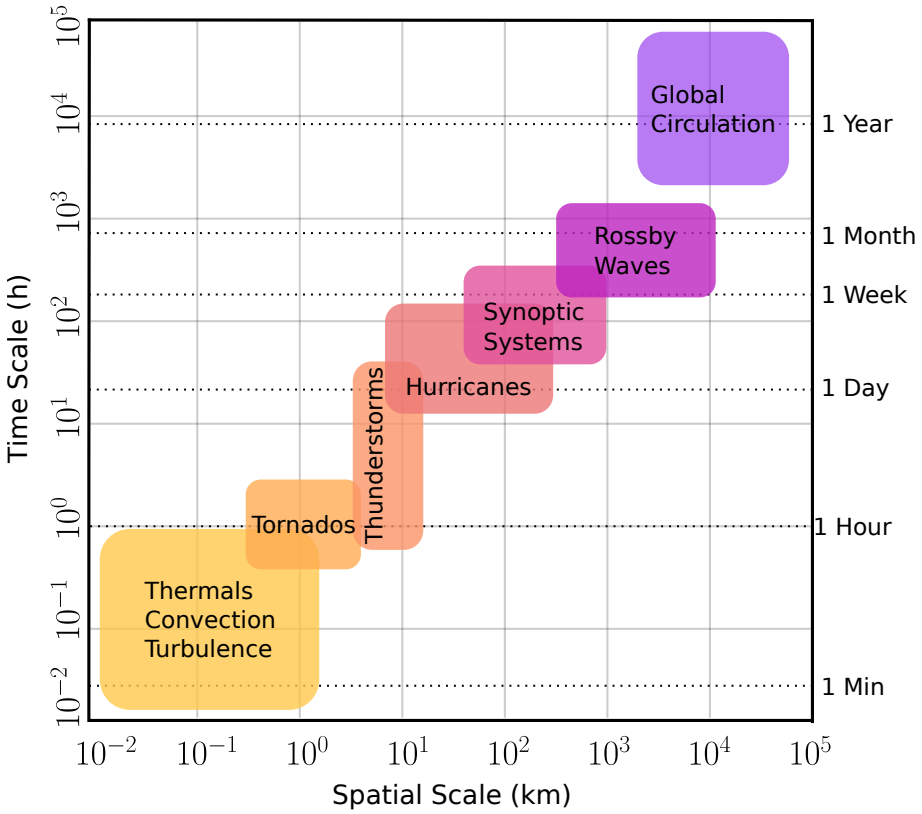


Figure 1.3: Approximate spatial and temporal scales of different atmospheric phenomenon. Image created by Oisín Hamilton, with scales taken from Holton [2004]; Barry and Chorley [2003].

that Richardson [1922] created a framework for numerically solving the equations. This required simplifying the equations, as well as developing numerical methods [Lynch, 2008].

In the period after the Second World War, the invention of electronic computers allowed Richardson's framework to be used to attempt weather forecasting in a reasonable length of time[1]. This work required filtering out sound and gravity waves from the equations, which are not important for larger scale forecasts [Charney, 1947]. The resulting equations are known as the quasi-geostrophic equations, which we will introduce in the next section. Using these simplified equations, the first numerical weather forecast was produced that could reasonably accurately predict large scale features in the mid-troposphere [Charney

[1] Richardson had previously attempted a forecast in the 1910s, numerically integrating the equations by hand. It took him two years to integrate the equations forwards in time by six hours [Lynch, 2014]. While his framework was based on solid foundations, his results were woefully inaccurate due to how initial conditions were used in the process.

et al., 1950]. Since these early days of Numerical Weather Prediction, mathematical and computational advancements have allowed the primitive equations to be directly integrated into the forecasting process and are used in all major climate and weather models [Edwards, 2011].

As correctly identified by Abbe and Bjerknes, at the turn of the 20th century, the flow of the atmosphere is governed by three fundamental physical conservation principles: the conservation of mass, momentum, and energy [Holton, 2004; Lynch, 2014]. The primitive equations, which describe the flow and energy state of the atmosphere, can be derived from these three conservations. In this section we will introduce these three category of equations. Our summary is based from the textbooks of Holton [2004] and Katsafados et al. [2022].

Mass Continuity

The mass continuity equation describes how the fluid flows into and out of a volume in space, and how the fluid density changes. By requiring that the mass of fluid in a unit volume is constant, the equation is given by

$$\frac{\partial \rho}{\partial t} + \nabla \cdot (\rho \mathbf{u}) = \frac{\mathrm{D}\rho}{\mathrm{D}t} + \rho \nabla \cdot \mathbf{u} = 0 \tag{1.1}$$

where ρ is the density. The material derivative is given by

$$\frac{\mathrm{D}}{\mathrm{D}t} = \frac{\partial}{\partial t} + u\frac{\partial}{\partial x} + v\frac{\partial}{\partial y} + w\frac{\partial}{\partial z}$$

for some flow $\mathbf{u} = u\hat{\imath} + v\hat{\jmath} + w\hat{k}$

Momentum Equation

The momentum equation governs the velocity of a fluid, as it responds to forces on it. This can be derived using Newton's second law in a rotating reference frame, resulting in the Euler equations. They consist of three equations, one for each direction in 3-dimensional space, and can be expressed as

$$\frac{\mathrm{D}\mathbf{u}}{\mathrm{D}t} = -\frac{\nabla p}{\rho} - 2\boldsymbol{\Omega} \times \mathbf{u} + F \tag{1.2}$$

where $\boldsymbol{\Omega}$ is the angular velocity of the Earth, p is the pressure, and F incorporates forces on the fluid, such as gravity and friction. For purely horizontal flow, the Coriolis force term can be written as $f\hat{k} \times \mathbf{u}$, where $f \equiv 2\boldsymbol{\Omega} \sin\phi$, where ϕ is the latitude.

Thermodynamic Equation

Lastly, the thermodynamic energy equation describes the conservation of energy of the fluid. This equation is derived from the first law of thermodynamics, where the change in

the internal energy of the system is equal to the difference between the heat added to the system, and the work done by the system. This can be written as

$$c_v \frac{\mathrm{D}T}{\mathrm{D}t} + p\frac{\mathrm{D}\alpha}{\mathrm{D}t} = J \tag{1.3}$$

where c_v is the specific heat for a constant volume, $\alpha \equiv \rho^{-1}$ and J is the rate of heating per unit mass due to radiation, conduction, and latent heat release.

Equation of State

The mass continuity, momentum equations, and the thermodynamic equation provide five equations, but they have six unknowns. The unknowns are the three velocity variables, the density, pressure, and temperature. To understand how the thermodynamic variables relate to one another we use an equation of state. As we will see, for large scale flows the ideal gas law, $p\alpha = RT$, provides an accurate link between pressure and temperature.

1.2.2 Simplifications to the Primitive Equations

As shown by Charney [1947], the primitive equations can be simplified in ways that allow large scale systems to be tracked reasonably accurately, while reducing the complexity of the equations. This allows the equations to be integrated with fewer computational resources. In addition, due to the reduction of scales, and nonlinear interactions, such simplifications also allow us to gain a better understanding of the key physical processes by reducing the complexity of the governing equations [Maher et al., 2019]. In this section we will introduce the assumptions that we will use to later derive the quasi-geostrophic equations, which are tailored for the midlatitude synoptic scale systems, which are the focus of this thesis.

Scale Analysis

To understand the key scales and prominent terms in the equations, we can use a scale analysis of the governing equations. From Table 1.1 we can immediately see some key features of synoptic systems. First, the ratio of the height of the atmosphere to the horizontal length of the average system is about two orders of magnitude. Vertical velocities are approximately three orders of magnitude smaller than horizontal velocities. This can be made more precise by investigating the terms of the horizontal momentum equations ($\mathbf{u} = u\hat{\imath} + v\hat{\jmath}$) (Equation 1.2)

Term	**I**		**II**			**III**		**IV**		**V**
Equation	$\frac{\partial \mathbf{u}}{\partial t}$	$+$	$\mathbf{u}\cdot\nabla\mathbf{u}$	$=$	$-$	$\frac{\nabla p}{\rho}$	$-$	$f\times\mathbf{u}$	$+$	F_H
Scale	$\frac{U}{T}$		$\frac{U^2}{L}$			$\frac{P}{\rho L}$		fU		F_H
Size (ms^{-2})	10^{-4}		10^{-4}			10^{-3}		10^{-3}		10^{-12}

(1.4)

Feature	Scale	Description
Horizontal wind (U)	10m s^{-1}	Approximate average wind speeds in the midlatitudes (36km h^{-1}, 20kn)
Vertical wind (W)	0.01m s^{-1}	Approximate average vertical wind speeds (36m h^{-1})
Length Scale (L)	10^6m	Approximate size of eddies in the midlatitudes (1000km)
Time Scale (T)	10^5s	$L/U \sim 1$ day
Rotation Speed (f)	10^{-4}s^{-1}	Rotation speed at 45° latitude ($f \equiv 2\boldsymbol{\Omega}\sin\phi$)
Atmosphere Depth	10^4m	The effective height of the atmosphere (10km)
Radius of Earth	$6.37 \times 10^6\text{m}$	$a \approx 6370\text{km}$ at 45° latitude
β-parameter	$10^{-11}\text{m}^{-1}\,\text{s}^{-1}$	$\beta = (2\boldsymbol{\Omega}\cos\phi_0)/a$ for $\phi_0 = 45^\circ$ latitude

Table 1.1: Key scales of midlatitude synoptic scale systems [Holton, 2004; Vallis, 2017]

For the horizontal flow, the force F_H is the internal drag of the atmosphere, and the boundary layer, and has the scale of $\nu U/H^2$, where ν is the viscosity, and H is the layer thickness.

Similarly, the scales of the vertical momentum equation can be found to be

Term	**I**		**II**		**III**		**IV**		**V**
Equation	$\frac{\mathrm{D}w}{\mathrm{D}t}$	$=$ $-$	$\frac{1}{\rho}\frac{\partial p}{\partial z}$	$-$	$f \times \mathbf{u}$	$-$	g	$+$	F_V
Scale	$\frac{UW}{L}$		$\frac{P}{\rho H}$		fU		g		F_V
Size (ms^{-2})	10^{-7}		10		10^{-3}		10		10^{-15}

(1.5)

In the vertical direction, the force on the fluid has a scale $\nu W/H^2$, but also includes the force of gravity, with scale g. We will now analyse the terms in these equations to derive the dominant scales, for midlatitude synoptic systems.

Geostrophic Approximation

From the horizontal momentum equations, Equation 1.4, we can see that the magnitude of terms **III** and **IV** are approximately equal, and dominate the equations. This leads to the geostrophic approximate or geostrophic balance. The geostrophic balance provides an approximation for the pressure and horizontal flow of the atmosphere for large scale midlatitude systems. the geostrophic balance is given by

$$f\hat{k} \times \mathbf{u} \approx -\frac{1}{\rho}\nabla p$$

where $\hat{k}$ is a vertical basis vector and f is the Coriolis parameter. Here, we are only looking at horizontal flow, and thus only take the horizontal gradient of the pressure p.

Geostrophic flow is parallel to lines of constant pressure (isobars). If the atmosphere was exactly geostrophic, the wind would flow parallel to isobars, clockwise around the high pressure systems, and anti-clockwise around the lows, in the Northern Hemisphere. An example of synoptic systems and the isobars are shown in Figure 1.2. Large scale flows in the atmosphere are approximately geostrophic (within about 10% in the midlatitudes). This can be seen in the middle panel of Figure 1.4, where the flow is close to parallel with the geopotential height.

The ratio between the advective term and the rotational term is U/fL, which is called the Rossby number, is a measure of how much the flow is impacted by the rotation. The accuracy of the geostrophic approximation can be measured using the Rossby number. The smaller the Rossby number, the better the approximation of the geostrophic balance. In the midlatitudes, using the scalings shown in Table 1.1, the Rossby number is approximately

$$Ro = U/fL \approx 10\mathsf{m\,s}^{-1}/(10^{-4}\mathsf{s}^{-1}\ \ 10^{6}\mathsf{m}) = 0.1$$

Hydrostatic Balance

When we look at the scales in the vertical momentum equation, Equation 1.5, we find that the dominant terms are the force of gravity (Term **IV**), and the pressure term (Term **II**), by multiple orders of magnitude. This means that the flow is in hydrostatic equilibrium, or that the pressure of a parcel of air can be accurately calculated by the weight of air above it. In the vertical direction the pressure term will scale as $P_0/(\rho H)$, where P_0 is the reference pressure (at the ground, or about $1000\mathrm{hPa}$) and H is the depth of of the atmospheric layer[1].

$$\frac{\mathrm{d}p}{\mathrm{d}z} = -\rho g \tag{1.6}$$

The hydrostatic balance can be more systematically shown using a perturbation analysis of the pressure and density around a reference height, but the result is that for synoptic

[1] $H \sim 10\mathrm{km}$, this is an order of magnitude less than the usually recognised hight of the atmosphere but here we are referring to the depth of the layer where synoptic scales eddies exist.

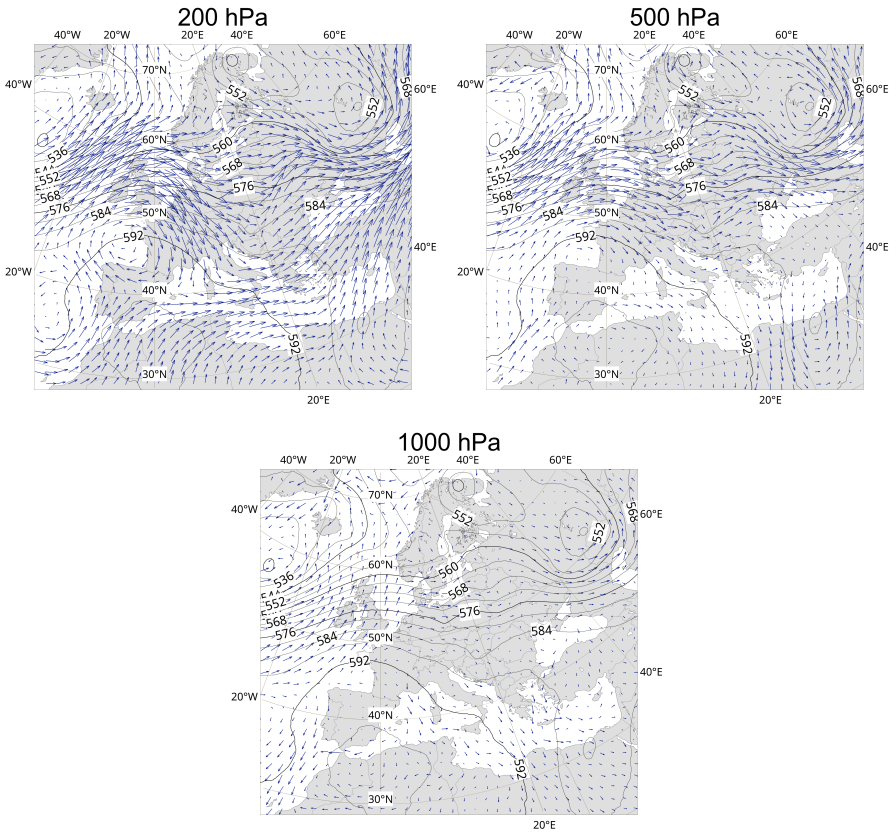


Figure 1.4: Wind velocity at three different elevations for the same time, and 500hPa geopotential height, in decametres. The pressure in the title correspond approximately to elevations of 12km, 5.5km, and 0km for pressures of 200, 500 and 1000hPa respectively. At 500hPa the wind is in approximate geostrophic balance, where the wind approximately follows the isobars, or the height contours shown. The real atmosphere is clearly very baroclinic, shown by the clear differences in the flow at different altitudes. The arrow lengths are scaled, with the longest arrows showing a velocity of $30\,\mathrm{m\,s^{-1}}$

© European Centre for Medium-Range Weather Forecasts (ECMWF), Source: www.ecmwf.int Licence: CC-BY-4.0

scale motions, the vertical accelerations are negligible. This means that the vertical velocity cannot be calculated from the vertical momentum equation, and must be calculated indirectly.

Pressure Coordinates

Using the hydrostatic balance, and assuming that the air is incompressible, it is possible to simplify the primitive equations, by converting from height to pressure coordinates. We begin by expressing the horizontal momentum ($\mathbf{u} = u\hat{\imath} + v\hat{\jmath}$) equation (Equation 1.2) in pressure coordinates, using the geopotential Φ. First, we convert the horizontal momentum ($\mathbf{u} = u\hat{\imath} + v\hat{\jmath}$) equation (Equation 1.2) from vertical to pressure coordinates. This requires deriving the conversion, using the chain rule

$$\left(\frac{\partial p}{\partial x}\right)_z = -\left(\frac{\partial p}{\partial z}\right)_x \left(\frac{\partial z}{\partial x}\right)_p$$

where the negative sign appears due to pressure increasing as height decreases. The subscripts here give the variables that remain constant when taking the derivative. We then introduce the geopotential, which is defined as the work required to raise a unit mass to height z

$$\Phi = \int_0^z g\mathrm{d}z \Rightarrow \mathrm{d}\Phi = g\mathrm{d}z$$

Using the hydrostatic balance (Equation 1.6), and the geopotential, we can express the pressure gradient term as

$$-\frac{1}{\rho}\left(\frac{\partial p}{\partial x}\right)_z = -g\left(\frac{\partial z}{\partial x}\right)_p = -\left(\frac{\partial \Phi}{\partial x}\right)_p$$

and the same can be done in the y direction. This, finally, allows us to make the substitution

$$\frac{1}{\rho}(\nabla p)_z = (\nabla \Phi)_p$$

This gives us the (unforced) horizontal momentum equation

$$\frac{\mathrm{D}\mathbf{u}}{\mathrm{D}t} + f\vec{k} \times \mathbf{u} = -\nabla_p \Phi \tag{1.7}$$

Where the material derivative is now given as

$$\begin{aligned}\frac{\mathrm{D}}{\mathrm{D}t} &:= \frac{\partial}{\partial t} + \frac{\mathrm{D}x}{\mathrm{D}t}\frac{\partial}{\partial x} + \frac{\mathrm{D}y}{\mathrm{D}t}\frac{\partial}{\partial y} + \frac{\mathrm{D}p}{\mathrm{D}t}\frac{\partial}{\partial p} \\ &= \frac{\partial}{\partial t} + u\frac{\partial}{\partial x} + v\frac{\partial}{\partial y} + \omega\frac{\partial}{\partial p}\end{aligned}$$

Here $\omega := \frac{\mathrm{D}p}{\mathrm{D}t}$ is the pressure coordinate equivalent of the vertical velocity $w = \frac{\mathrm{D}z}{\mathrm{D}t}$, also known as the omega vertical velocity equation. As seen in Table 1.1 the vertical velocity is about three orders of magnitude smaller than the horizontal velocity. Due to precision in

measuring the wind flows, usually the vertical motion is determined from other fields rather than being measured directly. This is also a consequence of using the hydrostatic balance. As we have seen, in the vertical momentum equation, the forces of gravity and pressure are orders of magnitude larger than the other terms, which removes the possibility of directly tracking the vertical flow.

We can also convert the continuity equation (Equation 1.1) to pressure coordinates, by considering a Lagrangian control volume $\delta V = \delta x \delta y \delta z$ and by using the hydrostatic balance $\delta p = -\rho g \, \delta z$. We can express the volume in terms of pressure $\delta V = \delta x \delta y \delta p / (\rho g)$, with a mass of $\rho \delta V$. We insist that the mass in the volume does not change, this means that

$$\frac{\mathrm{D}}{\mathrm{D}t} \rho \, \delta V = 0$$
$$\frac{\mathrm{D}}{\mathrm{D}t} (\delta x \delta y \delta p) = 0$$

where g is assumed constant. This is just the Lagrangian conservation of volume in an incompressible fluid, and therefore $\nabla \cdot \mathbf{u} = 0$, or in pressure coordinates

$$\nabla_p \cdot \mathbf{u} + \frac{\partial \omega}{\partial p} = 0 \tag{1.8}$$

this means that the continuity equation is independent of density and time. This is a large simplification over the previous form of the equation.

Ideal Gas

As discussed above, we require an equation of state to provide a relation between pressure, temperature, and density, to reduce the number of unknowns. For midlatitude flows, the ideal gas law provides a reasonable approximation, due to the moderate temperatures, pressures, and densities of synoptic scale systems. This is modelled as $p\alpha = RT$, where $\alpha = \rho^{-1}$, and thus removes the need to track the density. Here, T is the temperature of the gas, and R is the ideal gas constant ($R \approx 8.314 \mathsf{m}^2\mathsf{s}^{-2}\mathsf{kgK}^{-1}\mathsf{mol}^{-1}$). This assumption, however, can neglect important contributions, such as water vapour.

To use this assumption to simplify the thermodynamic equation, we begin by taking the material derivative of the ideal gas law

$$p \frac{\mathrm{D}\alpha}{\mathrm{D}t} + \alpha \frac{\mathrm{D}p}{\mathrm{D}t} = R \frac{\mathrm{D}T}{\mathrm{D}t} \tag{1.9}$$

We then substitute Equation 1.9 into the thermodynamic equation (Equation 1.3), and use $c_p = c_v + R$ to obtain

$$\frac{\mathrm{D}T}{\mathrm{D}t} - \frac{\alpha}{c_p} \frac{\mathrm{D}p}{\mathrm{D}t} = \frac{J}{c_p} \tag{1.10}$$

where $c_p \approx 1004 \mathsf{J\,kg^{-1}\,K^{-1}}$ is the specific heat at a constant pressure. We now write this in pressure coordinates using the omega vertical velocity equation and the material derivative in pressure coordinates

$$\left(\frac{\partial T}{\partial t} + u \frac{\partial T}{\partial x} + v \frac{\partial T}{\partial y} + \omega \frac{\partial T}{\partial p} \right) - \frac{\alpha}{c_p} \omega = \frac{J}{c_p} \tag{1.11}$$

which can be simplified to

$$\left(\frac{\partial T}{\partial t} + u\frac{\partial T}{\partial x} + v\frac{\partial T}{\partial y}\right) - S_p\omega = \frac{J}{c_p} \tag{1.12}$$

where

$$S_p := \frac{\alpha}{c_p} - \frac{\partial T}{\partial p} = \frac{RT}{c_p p} - \frac{\partial T}{\partial p}$$

Finally, we introduce potential temperature θ

$$\theta = T\left(\frac{p_s}{p}\right)^{R/c_p}$$

This is known as the Poission's equation, which relates temperature with pressure to define the potential temperature. The potential temperature is the temperature that a fluid would be at if moved adiabatically to the reference pressure (usually set to 1000hPa). This allows us to define the static stability in pressure coordinates

$$S_p := \frac{RT}{c_p\, p} - \frac{\partial T}{\partial p} = -\frac{T}{\theta}\frac{\partial \theta}{\partial p} = -T\frac{\partial \ln\theta}{\partial p}$$

Static stability of the atmosphere refers to the atmosphere's tendency to resist or enhance vertical motion of air parcels. In a stable atmosphere, as we will focus on in this section, a small vertical perturbation of an air parcel will cause the air to become cooler/warmer than the surrounding air, as it rises/drops. This creates a buoyancy force that restores the parcel of air back to its original position.

β-plane

Another assumption that we make is that we are modelling the flow in the midlatitudes, where the Coriolis parameter changes approximately linearly with latitude. This allows us to use a (midlatitude) beta (β) plane approximation, defined as $f = 2\mathbf{\Omega}\sin\phi \approx f_0 + \frac{\mathrm{d}f}{\mathrm{d}y}y = f_0 + \beta y$, where $\beta = (2\mathbf{\Omega}\cos\phi_0)/a$ and a is the radius of the Earth, y is the difference in latitude compared to the reference latitude. This is exactly a two term Taylor series around the reference latitude ϕ_0 [Holton, 2004].

The β-plane approximation retains a differential rotation speed, depending on the latitude, or the y coordinate. This is not the case when using an f-plane approximation (a first order approximation $f_0 = 2\mathbf{\Omega}\sin\phi_0$). By including a variable rotation rate, we retain important atmospheric dynamics, such as Rossby waves in our model. At the same time, the β-plane approximation is linear, and does not add nonlinear terms to the model, which would increase the complexity. However, the linear approximation to the rotation rate of the Earth only holds in the midlatitudes.

1.2.3 Tailoring the Equations for the Midlatitudes

We have introduced some key assumptions that can be made, to reduce the complexity of the primitive equations. This was done by analysing the equations with respect to the

primary atmospheric scales of the midlatitudes. We found that there are key balances in the governing equations that we can use to make these simplifications. Primarily, the geostrophic balance in the horizontal momentum equations and the hydrostatic balance in the vertical.

However, as we alluded to, the real atmosphere is in close, but not perfect geostrophic balance [Holton, 2004]. This regime, where the flow is nearly but not exactly geostrophic, is described by the quasi-geostrophic approximation. In the next section we will formalise the approximations introduced in this section, and develop a set of equations for quasi-geostrophic flow. We will derive the simplest models capable of capturing the essential dynamics of midlatitude synoptic systems: baroclinic instability and Rossby wave propagation.

1.3 The Quasi-Geostrophic Approximation

As outlined in the introduction, the atmospheric behaviour in the midlatitudes is dominated by synoptic systems. The formation of these systems is driven by baroclinic instability, which then form eddies whose structure and propagation are governed by Rossby wave dynamics [Holton, 2004]. Focusing on these two features alone is obviously a simplification of the real atmosphere, which is impacted by numerous other factors, such as orography and temperature anomalies. However, as we will see, simplified models of the atmosphere, which focus primarily on incorporating these key instabilities, can accurately model the large scale midlatitude circulation [Charney and Phillips, 1953].

In this section, to derive a model that incorporates Rossby waves and baroclinic instability, we take the following approach. We begin by using the simplified version of the primitive equations, that we discussed in the previous section, to derive the quasi-geostrophic vorticity equation. Using this we derive a single layer barotropic model and show how this model preserves Rossby waves. We then step up to a two layer model, due to the inability of the single layer model to produce baroclinic instability. We then use this model to display some properties of baroclinic instability and derive features of synoptic scale systems.

1.3.1 Deriving QG Vorticity Equation

While the geostrophic approximation is accurate at large planetary scales, the flow at synoptic scales shows some deviation from this balance, as shown in Figure 1.4. In addition, the atmosphere is baroclinic, seen in the differing flows at the different altitudes. The fastest winds are found in jets, that form between the troposphere and stratosphere (approximately 200hPa). Synoptic systems tend to form in the locations of these jets, and are then pushed by the jet along what are called storm tracks, which are modulated by Rossby waves.

To study large scale atmospheric flows in the midlatitudes there are some assumptions that we can make to reduce the complexity of the primitive equations [Vallis, 2017; Holton, 2004], as outlined in the previous section. First, we assume a near, but not perfect,

geostrophic balance. To do this we separate the three-dimensional flow in the atmosphere $\mathbf{u} = (u, v, w)$ into a geostrophic and an ageostrophic component, where $\mathbf{u} = \mathbf{u}_\mathrm{g} + \mathbf{u}_\mathrm{a}$.

The geostrophic component, $\mathbf{u}_\mathrm{g}$, follows isobars exactly, meaning that the pressure gradient and the Coriolis force balance perfectly. In the real world the atmosphere does not perfectly follow isobars, so we allow the flow to differ from this balance by a small amount, called the ageostrophic component, where $|\mathbf{u}_\mathrm{a}| \ll |\mathbf{u}_\mathrm{g}|$. This assumption removes the fast moving and small wavelength waves (such as gravity waves) from the primitive equations. We express the geostrophic wind as $\mathbf{u}_\mathrm{g} = f_0^{-1}\vec{k} \times \nabla\Phi$, where Φ is the geopotential, and f_0 is the Coriolis parameter at a reference latitude ϕ_0. We also use the β-plane approximation, as outlined in the previous section.

The acceleration $\frac{\mathrm{D}\mathbf{u}}{\mathrm{D}t}$ of the flow is equal to the difference between the Coriolis ($f\vec{k} \times \mathbf{\Phi}$) and the pressure gradient ($\nabla\Phi$) forces, as shown in the momentum equation (Equation 1.2), when additional external forces are omitted ($F = 0$). This is dependant on the ageostrophic magnitude, as the geostrophic term balances the two forces exactly. We take the two forces and substitute in the assumptions we outlined above

$$\begin{aligned} f\vec{k} \times \mathbf{u} + \nabla\Phi &= (f_0 + \beta y)\vec{k} \times (\mathbf{u}_\mathrm{g} + \mathbf{u}_\mathrm{a}) - f_0\vec{k} \times \mathbf{u}_\mathrm{g} \\ &= \beta y\vec{k} \times \mathbf{u}_\mathrm{g} + f_0\vec{k} \times \mathbf{u}_\mathrm{a} + \beta y\vec{k} \times \mathbf{u}_\mathrm{a} \\ &\approx \beta y\vec{k} \times \mathbf{u}_\mathrm{g} + f_0\vec{k} \times \mathbf{u}_\mathrm{a} \end{aligned}$$

where the last step is using the assumption that $|\mathbf{u}_\mathrm{a}| \ll |\mathbf{u}_\mathrm{g}|$. Here $\vec{k}$ is the unit basis vector in the vertical direction. Together this results in a simplified horizontal momentum equation

$$\frac{\mathrm{D}_\mathrm{g}\mathbf{u}_\mathrm{g}}{\mathrm{D}t} + \beta y\vec{k} \times \mathbf{u}_\mathrm{g} + f_0\vec{k} \times \mathbf{u}_\mathrm{a} = 0 \tag{1.13}$$

Another assumption that can be made is to assume that any vertical movements in the flow is small. At large scales in the atmosphere this is a reasonable assumption to make (see Table 1.1). We, therefore, consider the (geostrophic) vorticity as $\zeta_\mathrm{g} = \vec{k} \cdot \nabla \times \mathbf{u}_\mathrm{g}$. The vorticity can be thought of as the amount the flow is spinning, hence it is defined as the curl of the flow.

Expanding out the definition for vorticity, and substituting the definition of the geostrophic wind, we get $\zeta_\mathrm{g} = f_0^{-1}\nabla^2\Phi$. Taking Equation 1.13 and expressing it as u and v flow components, we get

$$\begin{aligned} \frac{\partial u_\mathrm{g}}{\partial t} + \mathbf{u}_\mathrm{g} \cdot \nabla u_\mathrm{g} - f_0 v_\mathrm{a} - \beta y v_\mathrm{g} = 0 \\ \frac{\partial v_\mathrm{g}}{\partial t} + \mathbf{u}_\mathrm{g} \cdot \nabla v_\mathrm{g} + f_0 u_\mathrm{a} + \beta y u_\mathrm{g} = 0 \end{aligned}$$

taking the derivative of the second with respect to x, and then subtracting the derivative of the first equation with respect to y, and noting that $\nabla \cdot \mathbf{u}_\mathrm{g} = 0$, we can now write this as a single equation using vorticity

$$\frac{\partial \zeta_\mathrm{g}}{\partial t} + \mathbf{u}_\mathrm{g} \cdot \nabla\zeta_\mathrm{g} = -f_0\left(\frac{\partial u_\mathrm{a}}{\partial x} + \frac{\partial v_\mathrm{a}}{\partial y}\right) - \beta v_\mathrm{g} \tag{1.14}$$

Finally, we can take the mass continuity equation, Equation 1.1 but written in pressure coordinates, which relates horizontal motion with the change in pressure and the vertical motion

$$\nabla \cdot \mathbf{u} + \frac{\partial \omega}{\partial p} = \frac{\partial u_{\mathrm{a}}}{\partial x} + \frac{\partial v_{\mathrm{a}}}{\partial y} + \frac{\partial \omega}{\partial p} = 0 \tag{1.15}$$

This only contains ageostrophic components as the geostrophic wind is non divergent. We use this to replace the divergence of the ageostrophic flow in the vorticity equation above

$$\begin{aligned} \frac{\partial \zeta_{\mathrm{g}}}{\partial t} &= -\mathbf{u}_{\mathrm{g}} \cdot \nabla \zeta_{\mathrm{g}} - \beta \mathbf{u}_{\mathrm{g}} + f_0 \frac{\partial \omega}{\partial p} \\ &= -\mathbf{u}_{\mathrm{g}} \cdot \nabla (\zeta_{\mathrm{g}} + f) + f_0 \frac{\partial \omega}{\partial p} \end{aligned} \tag{1.16}$$

This equation describes how the rate of change of geostrophic vorticity is determined by the advection of the absolute vorticity by the geostrophic wind, and the change in the column height.

We will see later, that writing this equation in a conservation form will allow us to investigate wave properties of the model. The steps to convert the quasigeostropic vorticity equation to a conserved form are shown in Appendix A.1. This results in the quasigeostropic potential vorticity equation

$$\left(\frac{\partial}{\partial t} + \mathbf{u}_{\mathrm{g}} \cdot \nabla \right) q = \frac{\mathrm{D}q}{\mathrm{D}t} = 0 \tag{1.17}$$

where

$$q = \frac{1}{f_0} \zeta + f + \frac{\partial}{\partial p} \left(\frac{f_0}{\sigma} \frac{\partial \Phi}{\partial p} \right)$$

where Φ is the geopotential and σ is the static stability of the atmosphere. The potential vorticity term q is made up of (from left to right) relative vorticity, planetary vorticity, and the vertical stretching term which governs the vorticity that results from stretching columns of the flow. This equation states that as flow moves, the different types of vorticity may change, but their sum must remain constant. This equation was first derived by Charney, through scale analysis of the primitive equations [Charney, 1948].

Potential vorticity, more precisely, is the absolute circulation of an air parcel that is enclosed by two surfaces. It is a conserved quantity in an idealised atmosphere (assuming no friction, incompressibility, and no moisture). This conservation is analogous to the conservation of angular momentum, for the atmosphere. The conservation property was first introduced by Rossby and then in the general form by Ertel in the 1940s [Schubert et al., 2004]. It has since become an important quantity in modern meteorology, as the flow fields can be calculated from this one term, called the invertibility principle [Hoskins et al., 1985].

1.3.2 Quasigeostrophic Thermodynamic Equation

We now look at simplifications that can be made to the thermodynamic equation (Equation 1.12). This section is a summary of sections in Chapters 3 and 6 of Holton [2004].

The horizontal advection $\mathbf{u}$ can be approximated using only the geostrophic component, as the ageostrophic component is small. Despite the fact that vertical velocities are small, on synoptic scales the static stability is usually large enough so that the heating or cooling due to vertical motion is approximately the same magnitude as the horizontal temperature advection. In other words, the stable nature of the midlatitude atmosphere results in relatively large changes in temperature for only small changes in height, or pressure.

To show this, we can approximate the vertical and horizontal temperature exchanges, using Equation 1.12 and the synoptic scale values given in Table 1.1. To do this we use the ideal gas law, assuming density is constant $\alpha\Delta p = R\Delta T$. From Equation 1.4 we see that $|\alpha\nabla p| \sim P/(\rho L) \sim 10^{-3}\mathsf{ms}^{-2}$. This provides us with an approximation for $|\alpha\Delta p| \sim 10^{3}\mathsf{m}^{2}\mathsf{s}^{-2}$. The specific value of the ideal gas constant for dry air is $R \approx 287\mathsf{m}^{2}\mathsf{s}^{-2}\mathsf{K}^{-1}$. Altogether, this provides an order of magnitude for a change in temperature of $|\Delta T| \sim 10\mathsf{K}$.

Using this scaling analysis we can find the approximate magnitude of the horizontal and vertical transfers of heat energy. Using Equation 1.12 we see that the horizontal temperature advection is modelled using

$$|\mathbf{u}\cdot\nabla T| \sim U\frac{\Delta T}{L} \sim 10^{-4}\mathsf{K}\,\mathsf{s}^{-1}$$

likewise, the vertical temperature term gives

$$|S_p\omega| \sim S_pW \sim 10^{-4}\mathsf{K}\,\mathsf{s}^{-1}$$

where $S_p \approx 5\times10^{-4}\mathsf{K}\,\mathsf{Pa}^{-1}$, which can be calculated using the definition of S_p, the lapse rate $\gamma \approx -6\times10^{-3}\mathsf{K}\,\mathsf{m}^{-1}$, and the hydrostatic balance. This shows that both of these terms have the same order of magnitude, and that in the case of temperature change, the vertical velocity term cannot be neglected.

We can now split the temperature into a base temperature, which only depends on pressure, and a perturbation term $T(t,x,y,p) = T_0(p) + \delta T(t,x,y,p)$. As $|\mathrm{d}T_0/\mathrm{d}p| \gg |\partial\Delta T/\partial p|$ we can write the thermodynamic equation (Equation 1.12) as

$$\left(\frac{\partial}{\partial t} + \mathbf{u}_\mathrm{g}\cdot\nabla\right)T - \frac{\sigma p}{R}\omega = \frac{J}{c_p} \tag{1.18}$$

where

$$\sigma := \frac{RT}{p}\frac{\mathrm{d}\ln\theta_0}{\mathrm{d}p}$$

where θ_0 is the potential temperature that corresponds to the base temperature T_0.

1.3.3 Barotropic Model

Looking again at the key scaling terms of synoptic scale systems in Table 1.1, we see that the height scale is about three orders of magnitude less than the length scale. For this reason, it is natural to wonder if we could model the entire atmosphere as a single 2-dimensional layer. If we assume this, we then say $\mathbf{u} = u\vec{i} + v\vec{j}$ where $w = 0$. Then the only non-zero component of the relative vorticity is $\zeta = (\frac{\partial v}{\partial x} - \frac{\partial u}{\partial y})$, or $\vec{k}\cdot(\nabla\times\mathbf{u})$. This means

that in 2D flow, the vorticity is perpendicular to the velocity, and there is no stretching or tilting of the vorticity, assuming a constant depth. Substituting these into Equation 1.17 we get

$$\frac{\mathrm{D}(\zeta + f)}{\mathrm{D}t} = \frac{\partial \zeta}{\partial t} + \mathbf{u} \cdot \nabla(\zeta + f) = 0 \tag{1.19}$$

where f is the Coriolis parameter. This is called the barotropic vorticity equation, and it states that the absolute vorticity is conserved within each fluid parcel as it is advected.

For synoptic scale flows in the mid troposphere, this equation provides reasonable accuracy, over short time scales, of the 500hPa field. In fact, the first successful numerical weather forecasts in the 1950s were conducted using this equation [Charney et al., 1950][1]

The barotropic vorticity equation can capture one of the most important features of the midlatitude circulation: Rossby waves [Holton, 2004]. Barotropic Rossby waves are waves that form in an inviscid barotropic fluid of constant depth that result from the variation of the Coriolis parameter with latitude. They are important for the formation of blocking events and transferring heat from the equator to the poles [Woollings et al., 2008; Pelly and Hoskins, 2003]. Figure 1.5 shows a snapshot of the 500hPa level of the atmosphere, and Rossby waves are visible in the flow.

Barotropic Rossby waves form due to the change in the planetary vorticity, or Coriolis parameter, changes with latitude. Due to the conservation of absolute vorticity, given in Equation 1.19, the relative vorticity of the flow must decrease as the planetary vorticity increases. This leads to a reduction in the relative vorticity of the flow at higher latitudes, and similarly an increase at lower latitudes. This process is sketched in Figure 1.6, and described more formally in Appendix A.2.

While the single layer version of the model does produce the large scale baro-tropic dynamics, it has some severe limitations. Primarily the temperature is not related to pressure, meaning that the flow in that atmosphere is the same regardless of pressure, or altitude [Holton, 2004]. As we can see in Figure 1.4, this is clearly not the case in the real atmosphere. In addition, the barotropic model model cannot capture the baroclinic instability that we discussed in the first section, due to the lack of horizontal shear. As we will see, while the atmosphere is a thin layer relative to the length scale, vertical shears in the atmosphere are what lead to the growth of synoptic scale systems. It is this missing ingredient that we will focus on in the next section.

1.3.4 Incorporating Baroclinicity

We have seen that it is possible to oversimplify. By converting the equations to only a 2D flow, we have lost some important features, namely, baroclinicity. In this section we will

[1] This forecast consisted of a single layer barotropic (the flow depends only on pressure) run of 24 hours, which itself took 24 hours meaning the virtual weather could only just keep pace with the real world. Their initial results were surprisingly accurate, given the entire atmosphere was being simplified to a single layer [Lynch, 2008; Golding et al., 2004].

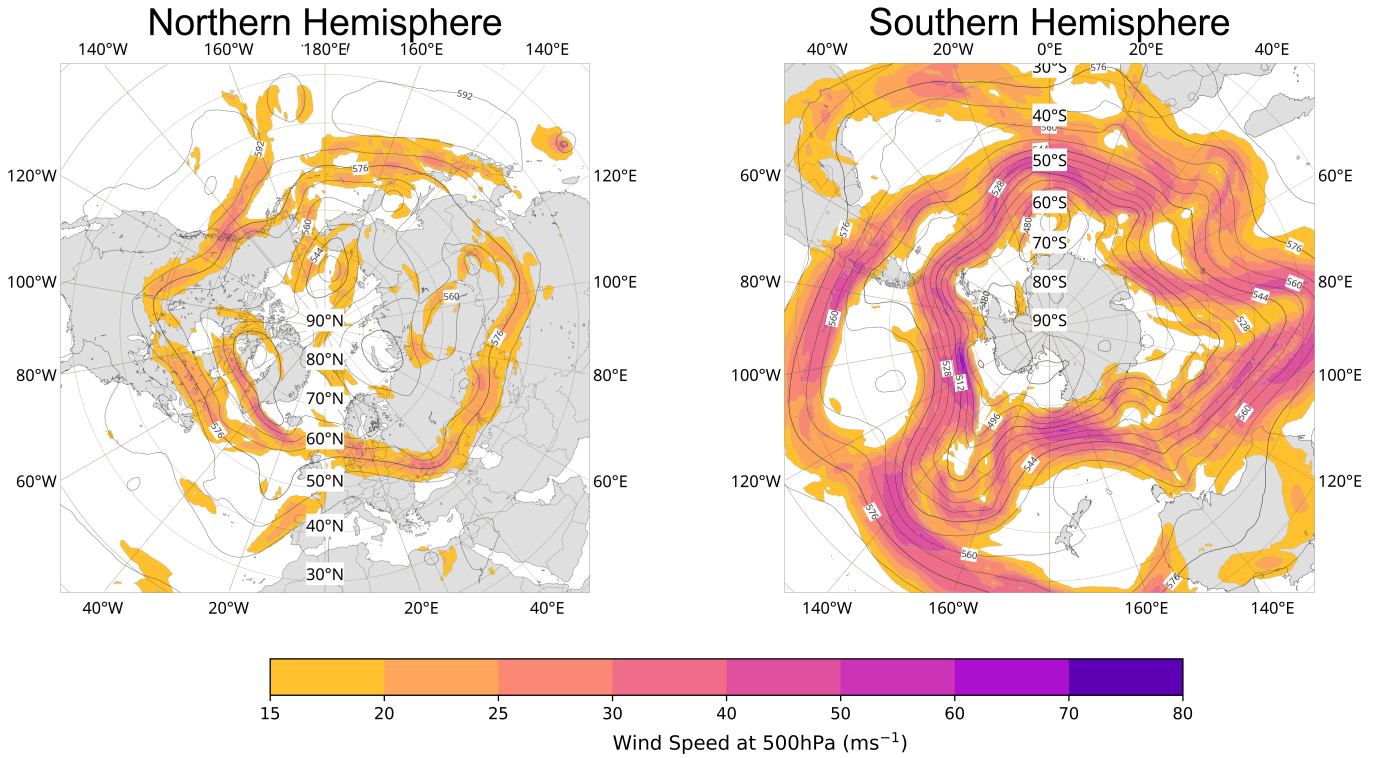


Figure 1.5: Rossby waves in the atmosphere, for both hemispheres. Contours show the 500hPa geopotential height in decametres, and the shading shows the wind speed in meters per second. The darker shading shows the location of the jet stream. The Rossby waves can be seen in the wave structure in the jet and the geopotential height. The flow is significantly faster in the southern hemisphere as it is the Southern Hemisphere winter, which means there is a larger temperature gradient between the equator and the pole. In addition, the orography in the Northern Hemisphere also contributes to reducing the flow speed. Both hemispheres shown at 0000h on the 11th of August, 2025.

© European Centre for Medium-Range Weather Forecasts (ECMWF), Source: www.ecmwf.int Licence: CC-BY-4.0.

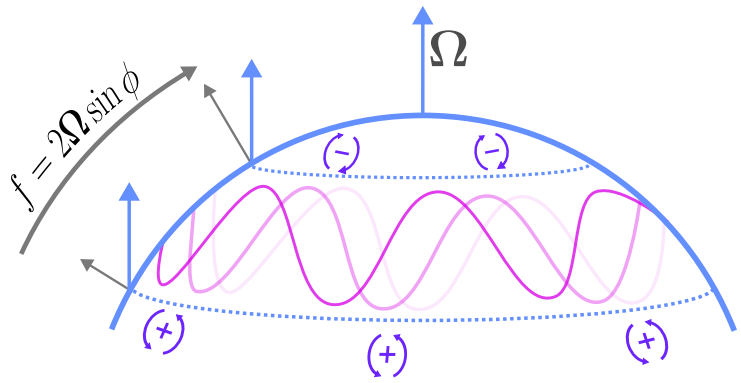


Figure 1.6: Sketch of the mechanism behind Rossby waves in a barotropic atmosphere. As the latitude increases, the vorticity due to the Coriolis parameter $f = 2\Omega \sin\phi$ increases. From the barotropic vorticity equation, Equation 1.19, absolute vorticity $\zeta + f$ is conserved, which requires ζ to decrease. This means that as latitude increases, the relative vorticity of the fluid decreases, causing a clockwise turn in the flow. The opposite happens at lower latitude, causing the fluid to gain positive relative vorticity. This sketch also gives some intuition for the westward propagation of the waves, relative to the westerly flow, due to the to advection by the induced velocity. Darker pink waves show the propagation of the wave to the west over time. Image created by Oisín Hamilton, influenced by Holton [2004].

take one step back, and derive a slightly more complex model in order to retain baroclinic processes, which are critical to producing baroclinic instability in the atmosphere.

The most simple model that incorporates baroclinicity, or a vertical shear, requires at least two horizontal layers at different heights. To derive a two later model we begin by setting two layers at 750hPa and 250hPa, or at altitudes of approximately 2.3km and 10km respectively. The quasi-geostrophic vorticity equation can now be written as

$$\frac{\partial}{\partial t}\nabla^2\psi_i = -\mathbf{u}_g \cdot \nabla(\nabla^2\psi_i) - \beta\frac{\partial\psi_i}{\partial x} + f_0\frac{\partial\omega_i}{\partial p}, \qquad i = \{1, 3\}$$

We now define the streamfunction on the two separate layers, ψ_3 on the bottom layer (750hPa) and ψ_1 at the top layer (250hPa). This produces a discrete vertical resolution, so we need to approximate the omega vertical velocity term, which we do using a first order approximation of the derivative

$$\frac{\partial\omega_1}{\partial p} = \frac{\omega - \omega_{\text{top}}}{\Delta p} = \frac{\omega}{\Delta p}, \qquad \frac{\partial\omega_3}{\partial p} = \frac{\omega_{\text{bottom}} - \omega}{\Delta p} = -\frac{\omega}{\Delta p}$$

where ω is the vertical wind at the intermediate virtual layer (500hPa) and we assume that at the top and bottom layers the vertical wind speed is negligible and set them to zero. Here Δp is the difference in pressure between the top and bottom layers (500hPa). This results

in a set of equations that describes the two layer quasigeostrophic flow

$$\frac{\partial}{\partial t}\nabla^2\psi_1 = -\mathbf{u}_1\cdot\nabla(\nabla^2\psi_1) - \beta\frac{\partial\psi_1}{\partial x} + f_0\frac{\omega}{\Delta p}$$
$$\frac{\partial}{\partial t}\nabla^2\psi_3 = -\mathbf{u}_3\cdot\nabla(\nabla^2\psi_3) - \beta\frac{\partial\psi_3}{\partial x} - f_0\frac{\omega}{\Delta p}$$

As we did for the barotropic model, we write the flow velocity in terms of the streamfunction and we use the Jacobian to denote the advection ($J(f,g) = \partial_x f\partial_y g - \partial_y f\partial_x g$)

$$\begin{aligned}\frac{\partial}{\partial t}\nabla^2\psi_1 + J(\psi_1,\nabla^2\psi_1) &= -\beta\frac{\partial\psi_1}{\partial x} + f_0\frac{\omega}{\Delta p}\\ \frac{\partial}{\partial t}\nabla^2\psi_3 + J(\psi_3,\nabla^2\psi_3) &= -\beta\frac{\partial\psi_3}{\partial x} - f_0\frac{\omega}{\Delta p}\end{aligned} \tag{1.20}$$

This is the two layer quasigeostrophic model, and is the atmosphere model that we use in this thesis. As mentioned, this model is the most simple model of the atmosphere that incorporates baroclinic instability, and is therefore the most simple model that can reproduce behaviours similar to the synoptic scale eddies that are seen in the midlatitudes. We now will discuss baroclinic instability in more detail, focusing on how it forms and the impact that it has on synoptic eddies.

Baroclinic Instability

We now have the theory to more concretely describe baroclinic instability, the instability that leads to the weather systems that we see in the midlatitudes. Here we provide an informal intuition for the mechanism behind baroclinic instability, and how it arises. A more formal analysis is contained in Appendix A.3. This section is a summary of Vallis [2017] chapter 6, and Holton [2004] chapter 8.

Using a linearisation of the model, similar to the approach taken for finding Rossby waves in the barotropic model (Appendix A.2), we can search for wave solutions of the two layer model. It can be shown (see Appendix A.3) that the phase speed of a wave solution has the form

$$c_p = \frac{\omega}{k} = U_Z - \frac{\beta(k^2+\lambda^2)}{k^2(k^2+2\lambda^2)} \pm \frac{\sqrt{\delta}}{k}$$

where

$$\delta = \frac{\beta^2\lambda^4}{k^2(k^2+2\lambda^2)^2} + \frac{k^2U_T^2(k^2-2\lambda^2)}{k^2+2\lambda^2}$$

where U_T is the thermal, or shear wind, between the two levels. k is the wavenumber, and $\lambda^2 = f_0^2/(\sigma\Delta p^2)$, which governs the scale at which buoyancy forces become as important as rotational effects.

If $\delta < 0$ then the phase speed has an imaginary component, which results in an exponential term in the phase speed. This leads to baroclinic instability, or an exponentially growing wave. We can use this condition on δ to find a lower bound on the wavenumber for

baroclinic instability to exist (see derivation of Equation A.16)

$$\sqrt{\beta/(2U_T)} \lesssim k$$

and when we substitute the approximate values from the real midlatitude atmosphere, as given in Table 1.1. We can find that the minimum thermal wind required for instability is $U_T \approx 2.5\mathrm{m\,s}^{-1}$, which is equivalent to a shear of $5\mathrm{m\,s}^{-1}$. Such shears are commonly observed in the real atmosphere. Using these values we can obtain a lower bound for the wavelength, of approximately $3000\mathrm{km} < L$. This provides us with a lower limit on the size of synoptic scale systems, which approximately matches eddies in the real midlatitudes.

In this section we have presented how the two layer model is capable of generating synoptic scale systems through baroclinic instability, and how these systems are propagated by Rossby waves. In the next section we will now begin to look at how cycles of lengths longer than individual systems can be incorporated into this model.

1.3.5 Low Frequency Variability

As mentioned at the beginning of this chapter, weather systems in the midlatitudes can, at times, act on time scales longer than the individual transient eddies [Holton, 2004]. These oscillations in the climate can last from weeks to years, which is much longer than the common life span of synoptic systems. Such large scale fluctuations are referred to as Low Frequency Variability (LFV) and are characterised by persistent anomalies in the atmospheric flow patterns [Ghil and Robertson, 2002].

This variability in the atmosphere is caused by the atmosphere interacting with other components of the climate system such as orography and the oceans. These climate components couple to the atmosphere through transfers in energy in the form of momentum and heat exchanges. In addition, variability is present in the atmosphere naturally, called internal variability. LFV has been observed in different parts of the atmosphere, and it is thought that differing regions of the atmosphere have their own key contributors to the atmospheric variability [Nauw and Dijkstra, 2001].

To better understand key drivers of LFV in the atmosphere we need to derive a model of the atmosphere which takes such couplings into account. In particular, there is a rich history of using low order, or idealised models, to study the underlying couplings and internal variabilities in the climate system that produce LFV [Vannitsem et al., 2015; Pierini, 2011; Itoh and Kimoto, 1996; Vautard and Legras, 1988; Reinhold and Pierrehumbert, 1982]. Building such a coupled model will be the focus of the next section.

1.4 Idealised Climate Models

We now turn to talk about the climate more generally, rather than only focussing on the atmosphere. The climate system is made up of many interacting components - namely the atmosphere, oceans, the land or cryosphere, and the biosphere to name some of the key

components. Each of these display complex spatio-temporal variability, and each component interact with one another, often with non-linear relationships [Dijkstra, 2013]. These interactions are referred to as couplings, and models that combine multiple different model processes as coupled models. Studying the climate, therefore, requires studying the behaviour of these features combined [Goosse, 2015]. Unlike with weather modelling, where the aim is to accurately forecast systems a couple of weeks into the future, climate studies the coupled system across many seasonal cycles. This is to gain an understanding of the statistical and dynamical behaviours of the climate on the long term, rather than the behaviour of an individual synoptic system.

Our current generation of Global Climate Models (GCMs) can capture large scale dynamics, usually to a high level of accuracy. However, these models have some drawbacks. First, they are still not perfect, and have biases. This means that they do not capture the statistics of the Earth's atmosphere perfectly, or smaller scale processes are only approximated [Goosse, 2015]. Second, they are computationally expensive to operate, meaning that it can take weeks or months to run these models to get outputs. Lastly, due to the number of different interacting components within these models, they can have over a billion degrees of freedom [Haarsma et al., 2016], making it difficult to identify key physical behaviours.

For this reason it is common in climate modelling to employ a hierarchy of models, each with different levels of complexity, for investigating particular behaviour [Randall et al., 2007]. As we work our way down the hierarchy to increasingly simple models, we remove complexity to focus on a particular type of behaviour, with the aim of increasing our understanding of said behaviour [Maher et al., 2019; Jeevanjee et al., 2017]. The trade off is that we usually sacrifice the accuracy at which we model other parts of the system, or the precision at which we model the processes. In the following sections we outline how the non-atmosphere components of the model that we used in this thesis is derived. Similar models have been used widely in the literature to study LFV [Vannitsem and De Cruz, 2014; Brunetti et al., 2019; Li et al., 2018; Kravtsov et al., 2006; Hogg et al., 2003]. For more information on the history on the use of idealised models in climate science, with a focus on modelling low frequency variability, we present a literature review in the introduction of Chapter 5.

1.4.1 Energy Balance Models

All weather on the planet is caused by solar heating. While a large number of complicated interactions occur from solar heating, the impacts on the global temperature can be approximated in only a couple of equations. To do this we use an energy balance model, which adds up all incoming radiation sources, and subtracts the outgoing radiation. Such models have been used since the 19th century to model the impact of solar cycles on the Earth's temperature [Edwards, 2011], and have been used for over 80 years to connect atmospheric levels of CO_2 with rising temperatures, or climate change [Callendar, 1938].

A simple energy balance model can be constructed as follows [Goosse, 2015; Barry and Chorley, 2003]. Shortwave energy, in the form of sunlight, hits the top of the atmosphere,

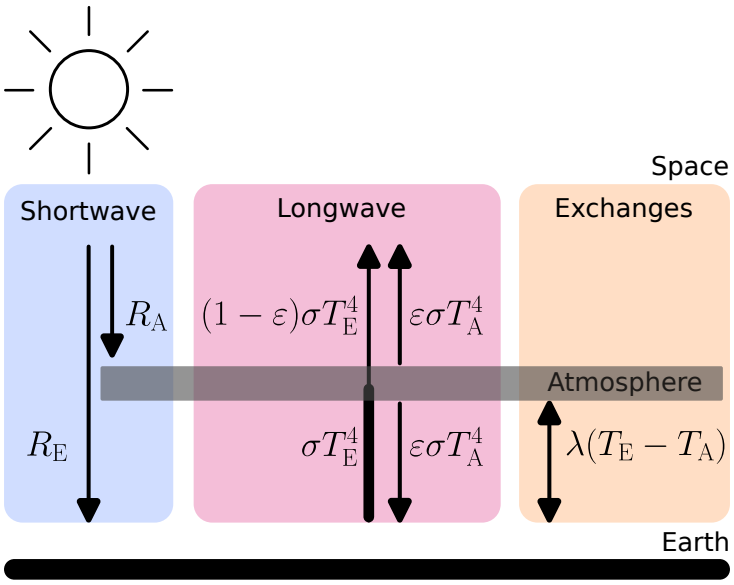


Figure 1.7: Sketch of the energy balance model, as described in Barsugli and Battisti [1998]. Image created by Oisín Hamilton, based of off [Demaeyer et al., 2022; Barsugli and Battisti, 1998]

with some of it being immediately reflected. The rest of the energy travels through the atmosphere. Most of the shortwave radiation that enters the atmosphere hits the surface as the atmosphere is relatively transparent to this form of radiation. The radiation is absorbed by the Earth and then emitted as longwave radiation. The atmosphere is not so transparent to longwave radiation, with clouds and moisture absorbing the longwave radiation. This causes the atmosphere to 'trap' some of this outgoing radiation, this is colloquially referred to as the greenhouse effect. As we are working over the midlatitudes, we neglect the impact of albedo, or refection of short wave radiation from the surface, and instead account for it directly in the incoming solar radiation [Barsugli and Battisti, 1998]. We will model the incoming radiation that is absorbed by the Earth as a constant R_{E}, and the shortwave radiation absorbed by the atmosphere as R_{A}.

For the Earth to remain at the same mean temperature, the same amount of energy must be emitted as is received from the sun. The heat radiated from each square meter of the Earth's surface can be modelled using the Stefan-Boltzmann law σT_{E}^4, where $\sigma = 5.67 \times 10^{-8}\mathrm{Wm}^{-2}\mathrm{K}^{-4}$ is the Stefan-Boltzmann constant, and T_E is the temperature of the Earth.

The atmosphere also captures some of this energy, both as the shortwave radiation as sunlight enters the atmosphere, and again as it leaves the Earth in the form of longwave radiation. The amount of energy captured in the atmosphere from the outgoing longwave radiation can be modelled using the emissivity ($\varepsilon \approx 0.76$), where the atmosphere captures

a proportion ε of the outgoing longwave radiation. The radiation emitted by the atmosphere is modelled as $2\varepsilon\sigma T_{\mathrm{E}}^4$. Here the factor of 2 comes from radiation emissions to the ground and the emissions to space. Lastly, the atmosphere and ground layers also transfer heat between each other through sensible, latent, and turbulent heat fluxes. The rate at which the transfer occurs is proportional to the difference in temperatures between the atmosphere and the Earth: $\lambda\Delta T$, where $\lambda \approx 10\mathrm{W\,m^{-2}\,K^{-1}}$. The resulting model is sketched in Figure 1.7, and we can express the energy balance as a coupled pair of Ordinary Differential Equations (ODEs)

$$\begin{aligned} \textbf{Atmosphere:} \quad \dot{T_A} &= R_{\mathrm{A}} + \varepsilon\sigma T_E^4 - 2\varepsilon\sigma T_A^4 + \lambda(T_E - T_A) \\ \textbf{Earth:} \quad \dot{T_E} &= R_{\mathrm{E}} - \sigma T_E^4 + \varepsilon\sigma T_A^4 + \lambda(T_A - T_E) \end{aligned} \tag{1.21}$$

For estimated parameter values mentioned in the text, the equilibria for this system $(\dot{T_A}, \dot{T_E}) = (0, 0)$, or the average temperature, is found to be $(T_A, T_E) \approx (18°\mathrm{C}, 31°\mathrm{C})$. This is higher than the mean planetary temperature, of approximately $15°\mathrm{C}$, but in this simplistic model we are excluding multiple important factors such as cloud albedo, which would further improve this estimate. In addition, we are only aiming to model the midlatitudes, which are of a higher average temperature compared with the global average.

1.4.2 Coupling Idealised Models

The atmospheric model that we derived in Section 1.3 does not make any mention of the ground or oceans, and treats the atmosphere in isolation. This is obviously a gross simplification of the Earth's climate system. One possible origin of low frequency variability in the atmosphere is forcing due to anomalies in sea surface temperature, which themselves arise from air–sea interaction [Holton, 2004]. Because of the large heat capacity of the oceans, the time scales that the ocean temperature fluctuates over can influence the atmosphere over months and years. Another potential source of low frequency variability in the atmosphere occurs due to deflections in the atmospheric flow from mountains, or orography [Charney and DeVore, 1979].

To study the impacts of couplings between the large scale atmospheric behaviour, and other components of the system, it is natural to create a coupled model, that incorporates not only the key physical behaviour of each subsystem, but also the key couplings between each subsystem. As mentioned already, solar insolation, and the resulting temperature gradients, drive the flow of the atmosphere in the midlatitudes. We can combine the atmospheric equations and an energy balance model through couplings in heat and momentum exchanges [De Cruz et al., 2016a].

This coupling of the quasigeostrophic equations (Equation 1.20) with an energy balance model (Equation 1.21) requires using the hydrostatic balance, which provides an expression for the vertical dependence of the pressure

$$\frac{\partial \Phi_i}{\partial p} = f_0 \frac{\partial}{\partial p}\psi_i = \frac{-1}{\rho} \qquad i = \{1, 3\}$$

In the two layer model, given in Equation 1.20, the derivative of the streamfunctions with respect to pressure simplifies to $(\psi_1 - \psi_3)/\Delta p$. We now use the ideal gas law $p = \rho R T_{\mathrm{A}}$ to remove ρ and introduce an expression between the (baroclinic) streamfunctions and the atmospheric temperature

$$f_0(\psi_1 - \psi_3) = R T_{\mathrm{A}} \frac{\Delta p}{p} = R \Delta T_{\mathrm{A}} \tag{1.22}$$

A mechanical coupling can also be introduced to the bottom layer of the model by adding an advection term, modelling the impact of the physical barrier on the flow. In addition, differing bottom layers impart a friction on the lower layer of the atmosphere, which can be modelled using a diffusion term. We will expand on how the couplings can be included in Chapter 2.

1.4.3 Numerically Integrating Idealised Models

As mentioned previously, even simple climate models, such as the one introduced in this section, do not have closed form solutions, and cannot be solved analytically. While analytical solutions may exist under highly restrictive assumptions, general solutions to these systems are not possible [Pedlosky, 1987]. In our case, the equations are not analytically solvable due to the presence of non-linear terms (advection terms, and longwave radiation scheme) and the coupling between systems with different time scales in the model.

This requires solving such models numerically, which involves approximating the derivatives in the equations, usually by discretising the equations in time which converts the differential equations into a discrete time system [Parker and Chua, 1989]. This thesis will primarily use a Galerkin expansion method to convert the system of partial differential equations into a system of ordinary differential equations, which can then be integrated using a finite difference scheme [Ehrendorfer, 2011]. We will discuss this process in more detail in Chapter 2.

Numerical methods have been employed since the beginning of numerical weather prediction to create weather forecasts [Richardson, 1922]. Numerical weather forecasting has required large advancements in such methods to accurately model the complex set of governing equations [Bauer et al., 2015]. However, it became apparent during the middle of the 20th century that the growth in initial errors, while integrating the governing equations, were not eliminated by advancements in numerical methods and computational resources [Lorenz, 1963a; Leith, 1971; Lorenz, 1969]. This behaviour was found to be an intrinsic property of the original system, rather than being introduced through the numerical estimation of the solutions. The property of systems, to display sensitivity to initial conditions, is called chaos. In this thesis all the models of the atmosphere and climate system that we will focus on exhibit chaotic behaviour. Understanding chaotic climate systems requires specialised analytical tools, which can characterise the structure and behaviour of solutions in state space. The next section will be dedicated to introducing these tools.

1.5 Chaos

Systems can be deterministic, meaning that we can in theory exactly track how a system evolves in time, but yet be chaotic. This means that the motion of the deterministic system appears stochastic or random [Cvitanović et al., 2020]. The meaning of the word chaos here is therefore quite different to the everyday use of the word. Chaotic systems, while they may appear to behave randomly, are in fact deterministic under the hood. Chaotic systems are sensitive to initial conditions, meaning that two states will diverge from one another exponentially fast as the system is evolved, even though the evolution of the system can exactly described. This is a problem for modelling such systems as little errors, introduced through numerical precision or from imperfect observations of the initial state, will explode. This is a huge problem in weather forecasting, for example, where numerical simulations, and the real weather, diverge quickly, leading to inaccurate forecasts.

As we have discussed before, the weather and climate systems can be described using a set of nonlinear dynamical equations. These equations are a chaotic system, meaning that when we use these equations to produce a weather forecast, any errors in the initial conditions provided to the model will grow exponentially. This is why numerical weather forecasting methods that integrate the primitive equations have a forecast horizon of approximately two weeks [Zhang et al., 2019]. Sensitivity to initial conditions means that we need to shift away from a typical approach in mathematics of trying to find exact solutions or exactly predict the path a trajectory will take, to instead describe the possible paths that a trajectory may take.

An interesting feature of chaos is that while trajectories diverge exponentially from one another, the distance they get from one another remain bounded. Then they eventually will be brought back together, or mixed. This means that the error between trajectories, at some point, will saturate. Weather and climate models are dissipative. This is because the energy received from the sun is transferred around the planet, which causes the circulation. At the same time there are also significant departures from the mean steady state climate, which is seen as variability in the weather [Paltridge, 1979]. This means that the state space has regions of contraction, or attracting directions. In dissipative systems chaos leads to the existence of a ‘strange attractor’ [Kuznetsov, 2012], which is an attracting set, or surface, that trajectories converge to, while still remaining sensitive to initial conditions [Eckmann and Ruelle, 1985].

1.5.1 An Example of a Chaotic System

The most famous example of a strange attractor is the Lorenz (63) system [Lorenz, 1963a], which is an idealised atmospheric model, made famous by the butterfly effect and the but-

terfly wing shape of the attractor (see Figure 1.10a). The system $\dot{\mathbf{x}} = f(x)$ is given by

$$\begin{aligned}\frac{\mathrm{d}x}{\mathrm{d}t} &= \sigma(y - x)\\ \frac{\mathrm{d}y}{\mathrm{d}t} &= x(\rho - z) - y\\ \frac{\mathrm{d}z}{\mathrm{d}t} &= xy - \beta z\end{aligned}$$

where x is is proportional to the rate of convection, y to the horizontal temperature variation, and z to the vertical temperature variation. The constants σ, ρ, and β are system parameters proportional to fluid dynamics constants. The classical values for the parameters are $(\sigma, \rho, \beta) = (28, 10, 8/3)$

We can show that this system is dissipative by finding the divergence of the system

$$\begin{aligned}\nabla \cdot f &= \frac{\partial f_1}{\partial x} + \frac{\partial f_2}{\partial y} + \frac{\partial f_3}{\partial z}\\ &= -(\sigma + 1 + \beta) < 0\end{aligned}$$

This means that overall, the state space of the system contracts. However, when we numerically integrate two trajectories that only differ by a small amount, they exponentially diverge from one another showing the system displays sensitivity to initial conditions, an example of this divergence is given in Figure 1.8a.

1.5.2 Introduction to Lyapunov Analysis

Through out this thesis we will study the behaviour of the resulting strange attractor of the climatic models that we derive. To do this we require the mathematical and numerical tools to describe features of the attractor. The following sections will introduce the core concepts of Lyapunov analysis, which covers the key properties and intuition behind Lyapunov exponents and vectors.

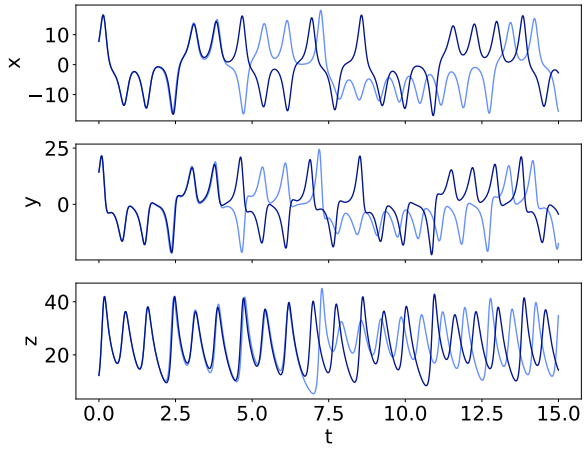
To make the statement "sensitivity to initial conditions" more precise, we look at the separation between two trajectories over time $\delta\boldsymbol{x}(t) = |\boldsymbol{x}_1(t) - \boldsymbol{x}_2(t)|$, where $\boldsymbol{x}_2(0) = \boldsymbol{x}_1(0) + \varepsilon$. As we expect these two trajectories to diverge exponentially fast, we model it as an exponential function

$$|\delta\boldsymbol{x}(t)| \approx e^{\lambda t}|\delta\boldsymbol{x}(0)|$$

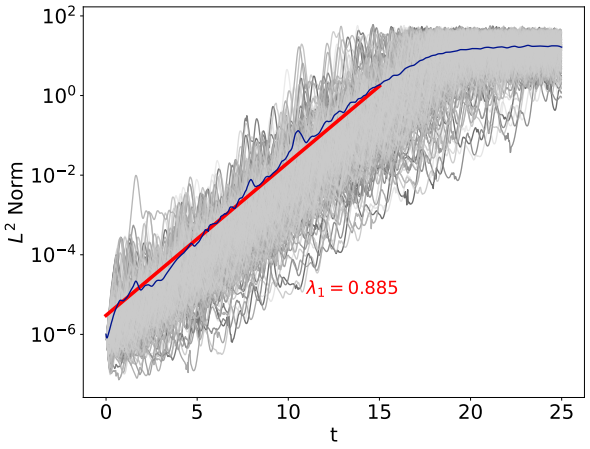
where λ is the mean rate of separation between trajectories, and is called the leading Lyapunov exponent. The leading, or largest, Lyapunov exponent measures the fastest rate of expansion, and can be estimated by

$$t_i\tilde{\lambda}_i \approx \ln\frac{|\delta\boldsymbol{x}(t_i)|}{|\delta\boldsymbol{x}(0)|}$$

for a finite time t_i. The time must be finite as eventually the error will saturate, as shown in Figure 1.8b for the Lorenz system. The saturation of the error thus requires rescaling the trajectories, so that the error is again of magnitude $\delta\boldsymbol{x}(0)$, and storing the value of $\tilde{\lambda}_i$.



(a) Two trajectories of the Lorenz system, with initial conditions $|\mathbf{x}_1(0) - \mathbf{x}_2(0)| = 10^{-6}$, are shown in different blues. After $t \approx 7$ the error grows so the two trajectories no longer show any resemblance to one another.



(b) The error growth of the Lorenz system is numerically estimated to be $\lambda_1 = 0.885$. Each grey line shows the difference between two trajectories $|\mathbf{x}_1(t) - \mathbf{x}_2(t)|$, where $\mathbf{x}_2(0) = \mathbf{x}_1(0) + \varepsilon$, $O(\varepsilon) = 1 \times 10^{-6}$. The average of the differences is shown in blue, and the red line shows the curve $e^{\lambda_1 t}$, where λ_1 was estimated using a Largest Lyapunov finding algorithm.

Figure 1.8: Error growth in trajectories of the Lorenz system.

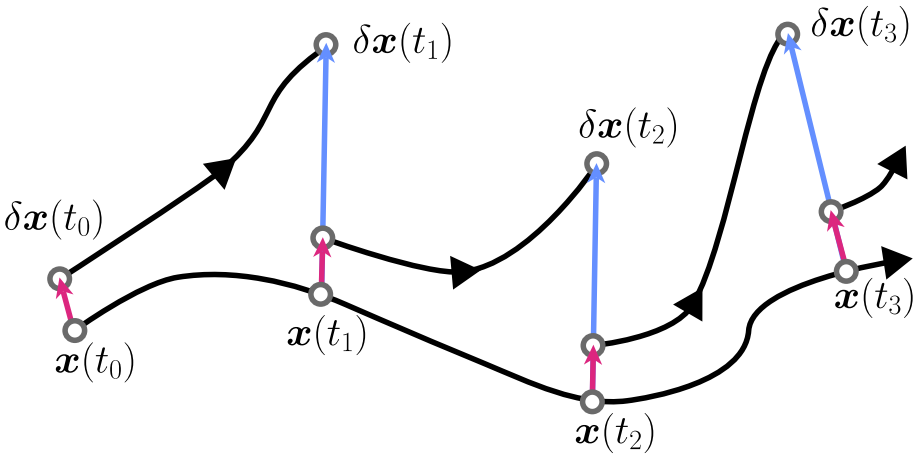


Figure 1.9: A trajectory, $\boldsymbol{x}(t)$, is shown. At time t_0 we perturb the trajectory by vector $\delta\boldsymbol{x}(t_0)$ (pink arrow on the left), where $||\delta\boldsymbol{x}(t_0)|| = \varepsilon$. At time step t_1, the two trajectories have diverged exponentially, and the error between the trajectories is $||\delta\boldsymbol{x}(t_1)||$ (blue arrow). We rescale $\delta\boldsymbol{x}(t_1)$ to have magnitude ε and start the process again.

The two two trajectories are then integrated forwards, and exponentially diverge again. The Largest Lyapunov Exponent is then defined as

$$\lambda_1 = \lim_{t\to\infty} \frac{1}{t} \sum_i t_i \tilde{\lambda}_i$$

where $t = \sum_i t_i$. This process is sketched in Figure 1.9.

However, as we have shown, the Lorenz system is dissipative, meaning that there is an overall contraction in state space. This means, that while there are certain directions in state space that expand, and lead to chaotic behaviour, other directions shrink, which leads trajectories to collapse onto a strange attractor. To understand the rates of expansion and contraction, and the number of expanding and contracting dimensions, it is possible to define additional Lyapunov exponents.

Beyond telling us whether a system displays chaotic behaviour, Lyapunov exponents have been studied widely in the context of meteorology as precise information on the rate of expansion of initial conditions has been vital in building efficient ensemble forecasting techniques. Understanding the directions and rate of the fastest growing perturbations allows forecasters to choose a low number of perturbations to test, as testing all possible perturbations is not feasible [Legras and Vautard, 1996; Molteni et al., 1994].

In addition Lyapunov exponents provide quantifiable data on important properties of chaotic systems, such as local entropy production and attractor dimension [Eckmann and

Ruelle, 1985]. These provide information about the number of degrees of freedom of the system and information flow in the system, providing a measure of how predictable the system is to model. Other important properties can be determined from the finite time Lyapunov exponents of the attractor, such as hyperbolicity and unstable dimensions variability [Nese, 1989; Kostelich et al., 1997]. These provide information about where the rates of contraction and expansion change on different parts of the attractor. The atmosphere and climate systems are characterised by strong violations in hyperbolicity [Lucarini and Gritsun, 2019].

We now track what happens to an initial perturbation $\delta\boldsymbol{x}(t)$ when integrated forward by the system $\dot{\boldsymbol{x}} = f(\boldsymbol{x}(t))$. For infinitesimal perturbations to a trajectory of the system, the tangent linear system describes the evolution of the perturbation

$$\delta\dot{\boldsymbol{x}}(t) = \mathbf{J}(\boldsymbol{x}, t)\delta\boldsymbol{x}(t)$$

where the Jacobian is defined as $\mathbf{J}(\boldsymbol{x}, t) = \frac{\partial f(\boldsymbol{x}(t))}{\partial \boldsymbol{x}(t)}$. The solution of this system can be described using the fundamental matrix $\mathbf{M} \in \mathrm{R}^{m\times m}$

$$\dot{\mathbf{M}} = \mathbf{J}(\boldsymbol{x}, t)\mathbf{M}$$

We define the tangent linear propagator (also known as the resolvent) as

$$\mathcal{F}(t_1, t_2) = \mathbf{M}(t_2)\mathbf{M}(t_1)^{-1}$$

this $m \times m$ matrix allows us to evolve solutions to the tangent linear problem at time t_1 to time t_2

$$\boldsymbol{v}(t_2) = \mathcal{F}(t_1, t_2)\boldsymbol{v}(t_1)$$

where $\boldsymbol{v}$ are solutions of the tangent linear problem, or are tangent vectors at time t_1 and t_2.

Now, when we propagate the solution forwards in time, using the above relation, we see that the growth of the Euclidean norm of tangent vectors is governed by the matrix $\mathcal{F}(t_1, t_2)^{\mathrm{T}}\mathcal{F}(t_1, t_2)$, as

$$||\boldsymbol{v}(t_2)|| = ||\mathcal{F}(t_1, t_2)\boldsymbol{v}(t_1)|| = \sqrt{\boldsymbol{v}(t_1)^{\mathrm{T}}\mathcal{F}(t_1, t_2)^{\mathrm{T}}\mathcal{F}(t_1, t_2)\boldsymbol{v}(t_1)} \tag{1.23}$$

to understand how $\mathcal{F}(t_1, t_2)^{\mathrm{T}}\mathcal{F}(t_1, t_2)$ grows or shrinks we will keep track of the eigenvectors ($\mathbf{f}_i^+(t_1, t_2)$) and the eigenvalues ($\sigma_i(t_1, t_2)^2$). Now, any matrix product $A^{\mathrm{T}}A$ will be positive semi-definite, meaning that it is symmetric and that all the eigenvalues are positive real numbers. We define the indexing to order the square root of the eigenvalues so that $\sigma_1 \geq \sigma_2 \geq \cdots \geq \sigma_m \geq 0$.

From the definition of the propagator we can see that it is always non singular and is given by $\mathcal{F}(t_1, t_2) = \mathcal{F}(t_2, t_1)^{-1}$, called the inverse propagator. The same analysis as above shows that the growth rate in backwards time is governed by $\mathcal{F}(t_1, t_2)^{-\mathrm{T}}\mathcal{F}(t_1, t_2)^{-1}$, and has eigenvectors ($\mathbf{f}_i^-(t_1, t_2)$) and eigenvalues $\sigma_i(t_1, t_2)^{-1}$. Using singular value decomposition of the resolvent $\mathcal{F}(t_1, t_2)V(t_1, t_2) = U(t_1, t_2)\Sigma(t_1, t_2)$ we write

$$\mathcal{F}(t_1, t_2)^{\mathrm{T}}\mathcal{F}(t_1, t_2)V(t_1, t_2) = \mathcal{F}(t_1, t_2)^{\mathrm{T}}U(t_1, t_2)\Sigma(t_1, t_2) = V(t_1, t_2)\Sigma(t_1, t_2)^2$$
$$\mathcal{F}(t_1, t_2)^{-\mathrm{T}}\mathcal{F}(t_1, t_2)^{-1}U(t_1, t_2) = \mathcal{F}(t_1, t_2)^{-\mathrm{T}}V(t_1, t_2)\Sigma(t_1, t_2)^{-1} = U(t_1, t_2)\Sigma(t_1, t_2)^{-2}$$

using the definition of eigenvalues and vectors we see that

$$\mathcal{F}(t_1,t_2)^{\mathrm{T}}\mathcal{F}(t_1,t_2)\mathbf{f}_i^+(t_1,t_2) = \mathbf{f}_i^+(t_1,t_2)\sigma_i(t_1,t_2)^2$$
$$\mathcal{F}(t_1,t_2)^{-\mathrm{T}}\mathcal{F}(t_1,t_2)^{-1}\mathbf{f}_i^-(t_1,t_2) = \mathbf{f}_i^-(t_1,t_2)\sigma_i(t_1,t_2)^{-2}$$

from the above we can see that the collection of the eigenvectors $\mathbf{f}_i^+$ form the basis of the right singular vectors, and the eigenvectors $\mathbf{f}_i^-$ the left singular vectors of $\mathcal{F}(t_1,t_2)$. Likewise, the values $\sigma_i(t_1,t_2)$ are the singular values. As they form the singular value decomposition for the propagator, the singular vectors are orthonormal. Therefore, the propagator stretches or contracts the state space, which can be tracked using the singular values and vectors.

Given a trajectory point at time t_1, the propagator $\mathcal{F}(t_1,t_2)$ transforms the singular vectors $\mathbf{f}_i^+(t_1,t_2)$ to $\mathbf{f}_i^-(t_1,t_2)$, which is associated with the trajectory point at time t_2, and is stretched by a factor $\sigma_i(t_1,t_2)$. Taking a unit ball around the trajectory point at t_1, this ball will be transformed into an ellipsoid at time t_2, with axis along the vectors $\mathbf{f}_i^-(t_1,t_2)$ and lengths $\sigma_i(t_1,t_2)$. The resulting volume of this ellipsoid will be

$$V(t_2) = V(t_1)\exp\left(-(t_2-t_1)\sum_i \ln\frac{\sigma_i(t_1,t_2)}{t_2-t_1}\right) \tag{1.24}$$

However, this only describes the stretching or contracting of state space for a time interval $[t_1,t_2]$. To extend this to obtain the limit of the stretching or contracting, over the entire state space, we need to introduce the Oseledec theorem.

1.5.3 Forward and Backward Lyapunov Vectors

The Oseledec multiplicative ergodic theorem [Oseledec, 1968] states that the limit of the stretching ratios and the the singular vectors exists for $t_2 \to \infty$. To find this limit, we introduce the far-future operator

$$\begin{aligned}\mathbf{W}^+(t) &= \lim_{t_2\to\infty}[\mathcal{F}(t,t_2)^{\mathrm{T}}\mathcal{F}(t,t_2)]^{\frac{1}{2(t_2-t_1)}} \\ &= \lim_{t_2\to\infty}[\mathbf{F}^+(t,t_2)\Sigma(t,t_2)^{\frac{1}{2(t_2-t_1)}}\mathbf{F}^+(t,t_2)^{\mathrm{T}}]\end{aligned}$$

where $\mathbf{F}^+(t,t_2) = [\mathbf{f}^+(t,t_2),\ldots,\mathbf{f}_m^+(t,t_2)]$ and $\Sigma(t,t_2)_{i,i} = \sigma_i(t,t_2)$, where $\Sigma(t,t_2)_{i,j} = 0$ for $i \neq j$. These are matrices constructed from the singular vectors and values. The eigenvectors of the far-future operator ($\boldsymbol{\varphi}_i^+(t)$) are the limits of the singular vectors [Reynolds and Errico, 1999] $\mathbf{f}_i^+(t,t_2)$ and are called Forward Lyapunov Vectors (FLV). These vectors are orthonormal and are dependant on t. The logarithm of the eigenvalues of the far-future operator are called Lyapunov exponents $\lambda_1 \leq \lambda_2 \leq \cdots \leq \lambda_m$, and they do not depend on time. Similarly, the Backwards Lyapunov Vectors (BLVs) $\boldsymbol{\varphi}_i^-(t)$ are the eigenvectors of the far-past operator, and are the limits of the singular vectors $\mathbf{f}_i^-(t_1,t)$ for $t_1 \to -\infty$. The logarithm of the eigenvalues of the far-past operator are equal to the previously defined Lyapunov exponents, but with the opposite sign.

The Lyapunov exponents can also be defined by modifying Equation 1.24 to give

$$\sum_{i=1} \lambda_i = \lim_{t_2 \to \infty} \left(\frac{1}{t_2 - t_1} \ln \frac{V(t_2)}{V(t_1)} \right)$$

We go into further details about the different types of Lyapunov vectors that we use as part of this thesis, in Appendix A.4. We also provide an overview of how these vectors, and Lyapunov exponents, are numerically calculated in Appendix A.4.4.

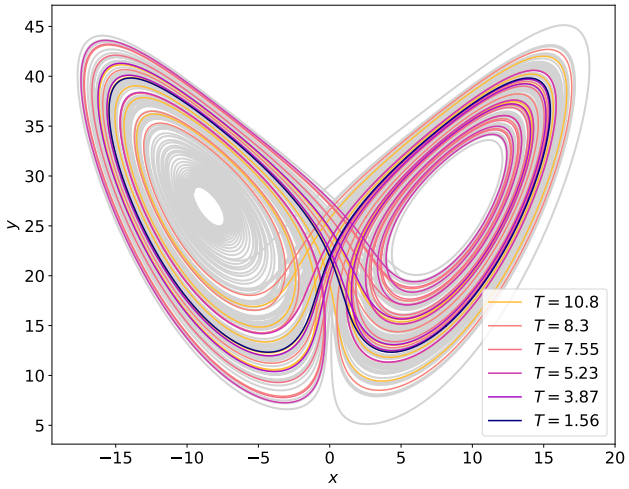
1.6 Unstable Periodic Orbits

There is, however, structure in chaos. Within chaotic systems there is an infinite set of periodic, or closed, orbits. These unstable periodic orbits (UPOs) are dense in the strange attractor, meaning that any trajectory will be approximated for some time by a nearby UPO, before being repelled by the orbit into the neighbourhood of another UPO [Cvitanović, 1988]. The use of these orbits to gain information about the chaotic system is called periodic orbit theory, and in Chapter 3 we will use this to understand the behaviour of the strange attractor of the coupled atmosphere model. Examples of strange attractors, and some interesting UPOs are shown in Figure 1.10. From a climate science perspective, orbits have been studied with the aim of identifying regions of state space where trajectories may remain for long periods, or where near oscillations occur [Ghil and Robertson, 2002]. The aim is to link such regions of state space with reoccurring behaviours, or low frequency variability, in the climate model [Plaut and Vautard, 1994].

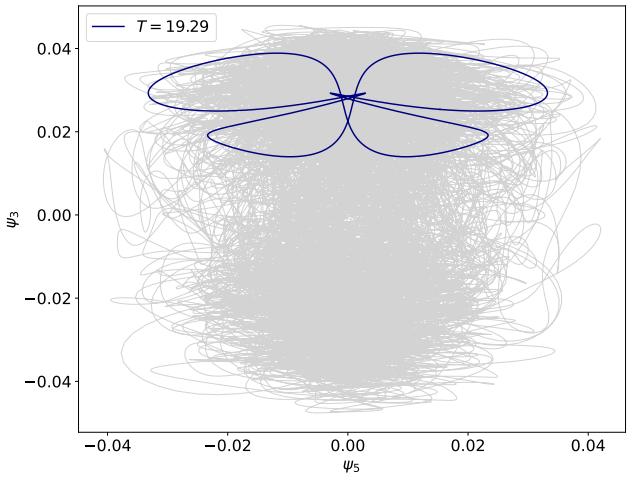
1.6.1 Properties of UPOs

First we introduce some terminology and notation used to describe UPOs. Given a system of ordinary differential equations $\dot{\mathbf{x}} = f(\mathbf{x})$, when given an initial condition $\mathbf{x}_0$, we can integrate this system forwards for a time t_i, to end at a new point in state space $S^{t_i}(\mathbf{x}_0)$. This integration tracks out a trajectory in state space $S^t(\mathbf{x}_0)$, for $0 \leq t \leq t_i$. If this trajectory forms a closed loop in state space, or after a time $t = T$ the $S^T(\mathbf{x}_0) = S^0(\mathbf{x}_0)$, we say that the closed loop is a periodic orbit, with period T, and denote this orbit as $\overline{S}^T_{\mathbf{x}_0}$. Periodic orbits are topological invariants, meaning they remain periodic in any representation of the dynamics [Cvitanović et al., 2020]. In addition, any change to the representation of the dynamics preserves the topological relations between periodic orbits, such as their inter-windedness, and thus such orbits can be sued to partially organise the state space. Of course, if $S^T(\mathbf{x}_0) = S^0(\mathbf{x}_0)$, then any multiple of this period nT will also be a closed loop. In the following we assume that we are looking at the minimal prime period, such that only one orbit along the closed trajectory occurs.

To understand the stability properties of this orbit we use Floquet theory. We begin by looking at what the Jacobian matrix does to an initial spherical neighbourhood, centred at $\mathbf{x}_0$ on the orbit $\overline{S}^T_{\mathbf{x}_0}$, when iterated forwards for a time T. The original sphere can be tracked using the linear system $\delta\mathbf{x}^t = J^t \delta\mathbf{x}^0$, which is continued up to time T. The resulting



(a) The Lorenz 63 attractor (in grey), with a selection of UPOs shown in colour. The Lorenz system was the first system to be studied for its sensitivity to initial conditions.



(b) A projection of the attractor of the coupled atmosphere model that we introduced. A single UPO of the attractor is displayed, to show that the Lorenz system is not the only climate model with an embedded butterfly.

Figure 1.10: The strange attractors and UPOs of two idealised climate models. The legends show the period of the UPOs.

Jacobian matrix J^T is called a Floquet matrix, and its eigenvalues $\Lambda_i^{(j)}$ are called Floquet multipliers, and the Floquet exponents are defined as

$$\lambda_i^{(j)} = \mu_i^{(j)} + i\omega_i^{(j)}$$

where the superscript specifies the index of the exponent, and the subscript is an index that specifies the UPO. The real part of the Floquet exponents provide the expanding or shrinking rates per unit time

$$\mu_i^{(j)} = \frac{1}{T} \ln |\Lambda_i^{(j)}|$$

it is common to order the multipliers by magnitude $|\Lambda_i^{(1)}| \geq |\Lambda_i^{(2)}| \geq \cdots \geq |\Lambda_i^{(m)}|$ which is equivalent to ordering by the real part of the exponent $\mu_i^{(1)} \geq \mu_i^{(2)} \geq \cdots \geq \mu_i^{(m)}$.

The expanding and shrinking directions can be split into the following three sets

$$\begin{aligned}
\text{expanding:} \quad \{\Lambda\}_e &= \left\{ \Lambda_i^{(j)} : \left| \Lambda_i^{(j)} \right| > 1 \right\} \\
\{\lambda\}_e &= \left\{ \lambda_p^{(j)} : \mu_p^{(j)} > 0 \right\} \\
\\
\text{marginal:} \quad \{\Lambda\}_m &= \left\{ \Lambda_i^{(j)} : \left| \Lambda_i^{(j)} \right| = 1 \right\} \\
\{\lambda\}_m &= \left\{ \lambda_i^{(j)} : \mu_i^{(j)} = 0 \right\} \\
\\
\text{shrinking:} \quad \{\Lambda\}_s &= \left\{ \Lambda_i^{(j)} : \left| \Lambda_i^{(j)} \right| < 1 \right\} \\
\{\lambda\}_s &= \left\{ \lambda_i^{(j)} : \mu_i^{(j)} < 0 \right\}
\end{aligned}$$

a periodic orbit is stable if $\{\Lambda\}_e = \{\Lambda\}_m = \emptyset$, or all Floquet multipliers have a magnitude less than one: $|\Lambda_i^{(j)}| < 1$. If $\{\Lambda\}_e \neq \emptyset$ then the orbit is unstable. Unstable orbits can either be saddles when $\{\Lambda\}_e \neq \emptyset$ and $\{\Lambda\}_s \neq \emptyset$, or are sources when $\{\Lambda\}_e \neq \emptyset$ and $\{\Lambda\}_s = \emptyset$.

Floquet multipliers are invariant to the flow, meaning that each orbit has a set of multipliers which define the entire orbit, regardless of initial condition on the orbit. Say we have an orbit $\overline{S}^T_{\mathbf{x}_i}$ with a Floquet matrix J^T. We calculate the jth eigenvalue and eigenvector of the Floquet matrix $J^T|_{\mathbf{x}_1}$, which is evaluated at some point on the orbit $\mathbf{x}_1 \in \overline{S}^T_{\mathbf{x}_i}$, namely $(\Lambda^{(j)}_{\mathbf{x}_1}, \mathbf{e}^{(j)}_{\mathbf{x}_1})$, then by definition we have

$$J^T|_{\mathbf{x}_1} \mathbf{e}^{(j)}_{\mathbf{x}_1} = \Lambda^{(j)}_{\mathbf{x}_1} \mathbf{e}^{(j)}_{\mathbf{x}_1} \tag{1.25}$$

if we now take another point on the orbit, $\mathbf{x}_2$, at a time t later, so that $S^t(\mathbf{x}_1) = \mathbf{x}_2$, and we evaluate the Jacobian at this new point ($J^T|_{\mathbf{x}_2}$) and take the eigenvalues and vectors as $(\Lambda^{(j)}_{\mathbf{x}_2}, \mathbf{e}^{(j)}_{\mathbf{x}_2})$. Using the fact that the Jacobian satisfies the semi-group property, we can write

$$J^T|_{\mathbf{x}_2} = J^{T+t}|_{\mathbf{x}_1} = J^T|_{\mathbf{x}_2} J^t|_{\mathbf{x}_1} = J^T|_{\mathbf{x}_1} J^t|_{\mathbf{x}_1}$$

using the above, and multiplying Equation 1.25 by $J^t|_{\mathbf{x}_1}$ we get

$$J^t|_{\mathbf{x}_1} \left(J^T|_{\mathbf{x}_1} \mathbf{e}^{(j)}_{\mathbf{x}_1} \right) = J^T|_{\mathbf{x}_2} \mathbf{e}^{(j)}_{\mathbf{x}_2} = \Lambda^{(j)}_{\mathbf{x}_1} \mathbf{e}^{(j)}_{\mathbf{x}_2}$$

where $\mathbf{e}_{\mathbf{x}_2}^{(j)} = J^t|_{\mathbf{x}_1}\mathbf{e}_{\mathbf{x}_1}^{(j)}$. Thus, the Floquet matrix evaluated at $\mathbf{x}_2$ has the same Floquet multiplier as the matrix evaluated at $\mathbf{x}_1$.

1.6.2 Newton-Raphson Method for Numerically Finding UPOs

Given a system of ordinary differential equations $\dot{\mathbf{x}} = f(\mathbf{x})$. We want to solve the equation: $S^T(\mathbf{x}_0) - \mathbf{x}_0 = 0$. This is a system of N equations, where we have $N+1$ unknowns; N-dimensional space unknowns in space, and the period T. Given an initial guess $(\mathbf{x}_0, T_0)$, which we discuss how to find in the following section, we define the i-th iteration of the variables $(\mathbf{x}_i, T_i)$. The algorithm aims to calculate corrections $(\Delta\mathbf{x}_i, \Delta T_i)$ to improve the initial guesses, in other words

$$\left\| S^{T_i+\Delta T_i}\left(\mathbf{x}_i + \Delta\mathbf{x}_i\right) - \left(\mathbf{x}_i + \Delta\mathbf{x}_i\right)\right\| < \left\| S^{T_i}\left(\mathbf{x}_i\right) - \mathbf{x}_i\right\|,$$

These correction terms are calculated by $x_{i+1} = \mathbf{x}_i + \Delta\mathbf{x}_i$ and $T_{i+1} = T_i + \Delta T_i$. Expanding the original problem using a Taylor series

$$\begin{aligned} &S[T_i + \Delta T_i](\mathbf{x}_i + \Delta\mathbf{x}_i) - (\mathbf{x}_i + \Delta\mathbf{x}_i) \\ &\qquad \approx S^{T_i}(\mathbf{x}_i) + \Delta\mathbf{x}_i \frac{\partial S^{T_i}(X)}{\partial X}\bigg|_{X=\mathbf{x}_i} + \Delta T_i \frac{\partial S^T(\mathbf{x}_i)}{\partial T}\bigg|_{T=T_i} - \left(\mathbf{x}_i - \Delta\mathbf{x}_i \frac{\partial X}{\partial X}\right) \\ &\qquad \approx S^{T_i}(\mathbf{x}_i) - \mathbf{x}_i + \Delta\mathbf{x}_i\left(\frac{\partial S^{T_i}(X)}{\partial X}\bigg|_{X=\mathbf{x}_i} - \mathrm{I}\right) + \Delta T_i \frac{\partial S^T(\mathbf{x}_i)}{\partial T}\bigg|_{T=T_i} \end{aligned} \tag{1.26}$$

where I is the identity matrix and $\frac{\partial S^{T_i}(X)}{\partial X}$ is the tangent linear operator. The term $\frac{\partial S^{T_i}}{\partial T}(\mathbf{x}_i)$ is the derivative of the solution of $\dot{\mathbf{x}} = f(\mathbf{x})$ w.r.t time, which is evaluated at the iteration. This is equivalent to $f(S^{T_i}(\mathbf{x}_i))$.

To reduce the number of degrees of freedom, the phase condition is added that requires the orbit and the correction vector to be orthogonal to one another

$$f(S^{T_i}(\mathbf{x}_i)) \cdot \Delta\mathbf{x}_i = 0$$

Together, this becomes a problem involving $N+1$ unknowns with $N+1$ equations and can be expressed as

$$\begin{bmatrix} \frac{\partial S^{T_i}(X)}{\partial X} - \mathrm{I} & f\left(S^{T_i}\left(\mathbf{x}_i\right)\right) \\ \left(f\left(\mathbf{x}_i\right)\right)^{\mathrm{T}} & 0 \end{bmatrix} \begin{bmatrix} \Delta\mathbf{x}_i \\ \Delta T_i \end{bmatrix} = \begin{bmatrix} \mathbf{x}_i - S^{T_i}\left(\mathbf{x}_i\right) \\ 0 \end{bmatrix} \tag{1.27}$$

This iteration is continued until the following two conditions are smaller than a specified magnitude

$$|S^{T_i}(\mathbf{x}_i) - \mathbf{x}_i| < \Delta_a$$
$$|(\Delta\mathbf{x}_i, \Delta T_i)| < \Delta$$

Once a correction step is calculated, a line search optimisation step is used to choose the largest step that should be taken in the direction $(\Delta \mathbf{x}_i, \Delta T_i)$ [Gritsun, 2008].

This method can fail when the matrix in Equation 1.27 is close to a singular matrix. This makes the linear system prone to large errors, and the algorithm will not converge. In Appendix A.5 we discuss a method to over come this using a second order tensor method.

1.6.3 Initial Conditions for Finding UPOs

The Newton-Raphson method can be very sensitive to initial conditions. This means that which UPO you end up on, or whether you end up on a UPO at all, is highly dependent on the initial conditions fed into the algorithm. The initial conditions refer to the starting location of the closed loop in state space, and the initial guess at the period of the closed loop. If the state space is of dimension n the initial condition is of dimension $n+1$. In this study we used the following four methods to guess initial conditions:

Random Initial Conditions

The initial conditions, the starting location in space and the period, were chosen randomly. We used a uniform distribution, where the bounds of the uniform distribution were set by finding the bounds of the attractor. Here we set the maximum period to be 225 days. This upper bound on the period was set as the probability of finding longer period UPOs is low.

Near Misses

We first ran a very long trajectory. We then passed a sliding window of length 225 days over this trajectory, and by calculating a norm between every point within this sliding window, we determined points ($\mathbf{x}_0$) where after some time t_i the trajectory passes sufficiently close to itself again: $\left\| S^{t_i}(\mathbf{x}_0) - \mathbf{x}_0 \right\| < \varepsilon$. This provided us with a guess of the period ($T_0 = t_i$) and the starting point in space $\mathbf{x}_0$.

Perturbed UPOs

Starting from a UPO we take a random point on the UPO and perturb the point and the period. We use this perturbed point as a new initial condition and feed this to the algorithm. This utilises the fact that UPOs should be dense in the attractor, so there should be another UPO living close to the given one. Usually this will result in the method producing the original UPO, so a filter needs to be used to ignore the result if it does not produce a new UPO.

UPO Continuation

UPOs could be found for certain parameter values more easily than others, in certain regions of the state space. This can occur when there is a change in to the stability landscape of the attractor for different parameter values, specifically when the attractor is not

hyperbolic or when there are UPOs present with different numbers of stable dimensions, or unstable dimensional variability [Pereira et al., 2007; Barreto et al., 1997; Lai et al., 1997].

This method takes advantage of this, by first finding a UPO at parameter values where it is easier to do so. Continuation software is then used to track the UPO back to the sought after parameter values. In our case, we used the work of Xavier et al. [2024] to understand for which parameter values the largest Lyapunov exponent was close to zero, suggesting that the flow is diverging more slowly at these values. We then used the Newton-Raphson method to find UPOs for these parameter values and tracked these branches back to the original values using AUTO. This method will fail when the branch does not extend to the desired parameters either due to a fold bifurcation, or the continuation software not being able to track the branch.

1.7 Thesis Outline and Objectives

In this thesis we analysed the regime dynamics of an idealised quasigeostrophic atmosphere, using 2-layer models of different resolutions and couplings, to study low frequency variability. We also studied the impact of climate change on the low frequency variability in these models. This was done by posing the following questions, each which makes up a chapter of this thesis.

Can periodic orbit theory be used to categorise transitions? Low order models of the atmosphere display low frequency variability, meaning that there can be repeating patterns in the behaviour of the atmosphere over long time spans. Such behaviour could be useful for providing longer range forecasts than traditional weather forecasts are capable of. In particular, we wanted to study the atmospheric blocking behaviour observed in low order atmosphere models. In such models there is a clear repeating behaviour seen over specific variables of the model. Previous studies have found that the onset and decay, or transitions in the state space appear to occur in the regions of specific structures in the chaotic attractor [Lucarini and Gritsun, 2019].

We wanted to investigate if a similar technique could be applied to studying low frequency variability in a coupled model framework. We chose a reduced order model for a variety of reasons. The blocking behaviour in the atmosphere has been well documented in a number of studies, but no clear description for the transitions between regimes of the attractor have been put forwards. In addition the underlying structure of the chaotic attractor, beyond the presence of multiple fixed points, has not been studied in detail. Lastly, these models provide the most simple description of the baroclinic behaviour in the atmosphere, thus providing the potential for a dynamical understanding of the resulting physical behaviour.

Unstable periodic orbits have been used before to categorise parts of the state space, and provide some level of predictability on the future path of trajectories. Here we wanted to identify whether these orbits can help us understand transitions between parts of the state space. This was studied in the context of variability in the ground temperature of a coupled model, and how this impacts blocking locations in the model. We found that the orbits

can identify regimes in the attractor, and that they can provide an indicator of transitions between these regimes (Chapter 3).

What does quasigeostrophic theory tell us about bifurcations in the model climate? There is still great uncertainty in the impact of climate change on the circulation in the midlatitudes. This is exacerbated by multiple changing processes in the atmosphere producing the opposite responses. This can lead to a small over all change in complex models, and thus overshadow the underlying individual responses. It is crucial to have a solid understanding of each of the potential processes that could be impacted by climate change so we can ensure global climate models are capturing each of these processes, and hopefully as a result the combined response, accurately.

To study complex behaviour, it is common to employ a hierarchy of models to investigate the key underlying behaviours from a particular change in forcings. For this reason in this chapter we employ a reduced order atmospheric model to investigate the impacts at the 'bottom rung' of the hierarchy.

However, studies in the past have highlighted that low order models are susceptible to inaccurate solutions due to overly harsh truncations in model resolution. For this reason, we also want to investigate the impact of model resolution on low order models. Specifically we want to do this by incorporating a continuous transition between model resolutions, where we can continuously add higher order nonlinear terms to investigate the impact of these on the model behaviour. This is in contrast to previous studies that have investigated only a binary 'on/off' inclusion of these modes.

Climate change will have many consequences on the midlatitude climate. To investigate the impacts of certain forcings we use an idealised climate model to conduct sensitivity tests on certain forcings. We also investigate the impact of model resolutions on the underlying low frequency variability by using both continuation software to transition between model resolutions, as well as investigating the resulting climatologies of the models (Chapter 4).

Is it possible to create multiple stable climatologies in a coupled atmosphere model by altering the radiation scheme? To model the weather and climate systems it is necessary to make certain assumptions to reduce the complexity of the system to allow us to model these in a feasible amount of time, with limited resources. There are almost always tradeoffs between accuracy and efficiency, however, when making these approximations. The resulting climate states in models are largely impacted by the radiation scheme used for transferring energy in the model, for example.

Previous studies have used reduced order coupled models to investigate the low frequency variability in the coupled atmosphere system. These models employ a simplified energy balance model to couple the atmosphere with another layer that introduces a time scale separation through heat capacities. In such models the radiation terms are modelled using the nonlinear Stefan-Boltzmann law. However, in the past, to reduce the complexity of the numerical integration, this nonlinear term has been linearised. Linearisations are often a necessary assumption to make when modelling non linear processes to simplify

the dynamics. However, linearising nonlinear processes can also remove the possibility for multistable solutions.

We wanted to study the possibility of multiple solutions existing in the coupled model. This was done by implementing the full Stefan-Boltzmann law, rather than the original linearisation, and we found that the model produces multiple stable climatologies. These climatologies result in distinct flow patterns and low frequency variability behaviour. We examined the influence of ocean-atmosphere coupling strength and atmospheric emissivity representing enhanced greenhouse effects on these regimes. While multistability is present, no tipping between attractors was found under constant solar forcing. (Chapter 5)

Are simplified turbulence models able to describe the turbulent energy transfers in a quasigeostrophic atmosphere? Turbulent energy exchanges in the atmosphere are important to model to understand how energy is transferred between scales as this can have a large impact on the resulting weather. At large scales, the atmosphere acts similar to that of a two dimensional flow. As a result, it also displays some behaviours that are found in two dimensional turbulence. The turbulence observed in the atmosphere is called geostrophic turbulence. This is seen primarily in an inverse energy flow, or cascades. However, observational data does not always match well with the theory of geostrophic turbulence.

In addition, in the other chapters of this thesis we have used different reduced order models to model features of the midlatitude large scale atmospheric flow. However, such models have been shown to be sensitive to the number of wavenumbers included in the spectral decomposition. One reason for this has been that these models do not accurately deal with energy flows between scales, due to atmospheric turbulence.

The behaviour of geostrophic turbulence is difficult to model due to the scales involved. To help understand these issues mentioned we built and investigated the properties of a simplified model of geostrophic turbulence. This model was based on the two layer quasigeostrophic model to provide a link with the previous chapters in this thesis, with the hope that such models could provide a useful tool for modelling energy transfers in future. We found that the shell model can capture the same energy flows and energy spectra that theory of two layer quasigeostrophic models predicts. The derived model also displays sensitivity to initial conditions. We end the chapter by discussing why two layer models potentially struggle with describing some features of atmospheric turbulence (Chapter 6).

2

Quasi Geostrophic Spectral Models

2.1 Spectral Models

Spectral methods, as opposed to a grid point or finite element methods, uniquely retain a finite-dimensional system of ordinary differential equations (ODEs) of the amplitudes of the decomposed model variables. These ODEs, which preserve important structural properties of the original partial differential equations, can be directly analysed using dynamical systems theory [Krishnamurti et al., 2006].

The method was first used in a meteorological context by Silberman [1954] for studying barotropic vorticity equation. Later Lorenz [1960] used a Fourier decomposition to reduce the same equation to a system of only three dynamical equations, to study important features of atmospheric dynamics. Other systems ODEs, derived from decompositions of physical processes, were also used to discover and understand chaotic systems [Saltzman, 1962; Lorenz, 1963a]. Since the 1970s, improvements in spectral techniques have made spectral methods competitive with, and accurate as, finite difference methods, and now spectral methods are used in many global numerical weather prediction models [Ehrendorfer, 2011; Krishnamurti et al., 2006]. Alongside high resolution spectral models, large scale atmospheric dynamics have been studied using reduced order spectral models (examples can be found in Vanderborght et al. [2024]; Vannitsem et al. [2015]; O'Brien and Branscome [1989]; Mak [1989]; Vautard and Legras [1988]; Reinhold and Pierrehumbert [1982]; Charney and DeVore [1979])

There are a number of benefits of spectral methods for modelling the atmosphere. Most importantly, spectral models are capable of capturing the wavelike structures that are visibly present at multiple scales of the atmosphere [Grenci and Nese, 2018]. Such structures can be lost when taking a gridded solution approach. Another benefit is that the boundary conditions are prescribed by the basis modes used, thus greatly simplifying the modelling process [Ellsaesser, 1966]. Of course, with any method, there are some drawbacks. In general, in spectral methods it can be more difficult to implement in the first place, and parametrisations can be more difficult to include. While simple boundary conditions are

more easily implemented using a spectral method, for regional models it can be difficult to find a set of modes which satisfy the required more complex boundary conditions. Lastly, due to the nature of the modes used, it can be difficult to model abrupt changes or shocks in the system that do not cleanly map to smooth functions, an example of this could be fronts in synoptic systems [Bourke, 1988].

2.1.1 Spectral Decomposition

As we will see, the coupled atmosphere model will consist of a collection of coupled partial differential equations (PDEs). To numerically solve the system we convert the PDEs to a set of ordinary differential equations (ODEs) by projecting them onto a set of basis functions, a method called a Galerkin method [Canuto et al., 2007; Krishnamurti et al., 2006]. To do this, we project all the model variables onto a set of Fourier modes defined as

$$\begin{aligned} F_P^A(x,y) &= \sqrt{2}\cos\left(P\frac{y}{L}\right) \\ F_{M,P}^K(x,y) &= 2\cos\left(Mn\frac{x}{L}\right)\sin\left(P\frac{y}{L}\right) \\ F_{H,P}^L(x,y) &= 2\sin\left(Hn\frac{x}{L}\right)\sin\left(P\frac{y}{L}\right) \end{aligned} \tag{2.1}$$

where M, H, P are integers. Here, the domain has been non-dimensionalised by dividing the coordinates by the characteristic length L. As a result, the model's domain is then defined over ($0 \leq x/L \leq 2\pi n$, $0 \leq y/L \leq \pi$), where n is the aspect ratio between the meridional and zonal extents, defined by $n = 2L_y/L_x$. We will discuss the scaling of the model further in Section 2.4.3. The basis basis functions have been chosen to ensure that there are periodic boundary conditions in the zonal direction and no-flux boundary conditions in the meridional direction $\frac{\partial}{\partial x}(\cdot) = 0$. This results in a periodic channel behaviour, or a cylinder, aiming to model the band around the midlatitudes.

Once the basis modes are selected, all of the model variables are projected onto the basis modes, using the expansion $\psi_{\mathrm{a}}(t,x,y) = \sum_i \psi_{\mathrm{a},\,i}(t)F_i(x,y)$. The modes have been selected to ensure that they are orthogonal with respect to the inner product

$$\frac{n}{2\pi^2}\int_0^{\pi}\int_0^{2\pi/n} F_i(x,y)F_j(x,y)\mathrm{d}x\,\mathrm{d}y = \delta_{ij} \tag{2.2}$$

To outline the method, we take the abstracted barotropic atmosphere equation as

$$\frac{\partial}{\partial t}(\nabla^2\psi_{\mathrm{a}}) + J(\psi_{\mathrm{a}}, \nabla^2\psi_{\mathrm{a}}) + \cdots = \ldots$$

we then project the model variables onto the set of basis functions to get

$$\frac{\partial}{\partial t}\left(\nabla^2\sum_i \psi_{\mathrm{a},\,i}F_i\right) + J\left(\sum_j \psi_{\mathrm{a},\,j}F_j,\ \nabla^2\sum_m \psi_{\mathrm{a},\,m}F_m\right) + \cdots = \ldots$$

we now have a set of equations for each basis mode F_i

$$\frac{\partial}{\partial t}\left(\psi_{\mathrm{a},\,i}\nabla^2F_i\right) + J\left(\psi_{\mathrm{a},\,j}F_j,\ \psi_{\mathrm{a},\,m}\nabla^2F_m\right) + \cdots = \ldots$$

to obtain a set of equations for how $\psi_{\mathrm{a},\,i}$ changes with time, we multiply the equations by F_i and then take the inner product $\langle F_i, F_j \rangle$

$$\frac{\partial \psi_{\mathrm{a},\,i}}{\partial t}\langle F_i, \nabla^2 F_i\rangle + \psi_{\mathrm{a},\,j}\psi_{\mathrm{a},\,m}\left\langle F_i,\ J\left(F_j,\ \nabla^2 F_m\right)\right\rangle + \cdots = \ldots$$

In this thesis we will work with severely truncated expansions, where the resulting model consists of approximately 100 degrees of freedom. Simplifying the atmosphere dynamics into such a low number of degrees of freedom, unsurprisingly, comes with some trade offs. This thesis will explore a number of such trade offs, and below we outline some of the most pressing issues with reduced order spectral methods.

2.1.2 Limitations

While the benefits of using spectral methods for solving PDEs are numerous, there are limitations compared with using other methods. Here, we will focus on some limitations of severely truncated spectral decompositions, which are not necessarily limitations of the method itself, but also due to the low number of degrees of freedom that we use.

Our aim is to reduce the dynamics of the coupled atmosphere system to its bare bones. To do this, following in the footsteps of people such as Lorenz and Charney [Lorenz, 1960], we try to reduce the system equations to the extract the key dynamics. In this work that consists of taking severe truncations in spectral space, where the equations are projected onto 10 or fewer modes. Of course a natural question to ask when doing this is, how low can we go? A particular concern when taking a low number of modes is that the resulting dynamics can be impacted by resonances that originate from improper removal of energy at particular scales [Cehelsky and Tung, 1987]. This occurs due to energy and enstrophy cascades that move energy from large to small scales, and if the smallest scale that exists in the model, due to a low number of modes being chosen, there can occur an inaccurate pooling of energy, due to insufficient removal [O'Brien and Branscome, 1989]. The result of this energy buildup is that the resulting dynamics can be altered greatly by slightly changing the number of modes, making it unclear whether the truncated model is accurately capturing the dynamics of the original system.

On the other hand, increasing the number of modes, using the spectral method, causes an exponential increase in the number of degrees of freedom. While increasing the number of modes leads to a convergence in the model behaviour [De Cruz et al., 2016a], the resulting large number of degrees of freedom make it difficult to then study the system using dynamical systems theory. There is, therefore, a trade-off that needs to be found between simplicity of the system and accuracy of the system dynamics. This cross over point is still not well understood in the context of reduced order spectral models.

In this chapter, we introduce the framework of models used in this thesis. We present the key steps used in deriving these model, by spectrally decomposing the partial differential equations into a set of ordinary differential equations. We then derive the coupled quasi-geostrophic models that are used later in the thesis.

2.2 Quasi-Geostrophic Spectral (qgs) Model

Reduced-order spectral quasi-geostrophic models of the atmosphere, with a sufficient number of modes, offer a good representation of the dry atmospheric dynamics [O'Brien and Branscome, 1989]. The qgs model [Demaeyer et al., 2020; Demaeyer and Hamilton, 2025] was built to help answer questions about the large scale dynamics of the atmosphere, especially when the atmosphere is coupled to layers with slower dynamics, a key ingredient for low frequency variability. In addition, the qgs framework was developed with ease for the user in mind, and to encourage the future use of such models for investigating large scale atmospheric behaviour. The qgs model framework is a collection of sub models that share the same quasi-geostrophic atmosphere. The framework was designed to allow the user to easily incorporate a bottom layer, and to alter the spectral resolution or basis modes used. The framework was developed in the Python programming language to facilitate its use in Jupyter notebooks and the multiple recent machine learning libraries that are available in Python.

In the remainder of this chapter we present, and outline the derivation, of the three primary models in the qgs model framework

- The atmosphere model (Section 2.3)
- The coupled land-atmosphere model (Section 2.4)
- The coupled ocean-atmosphere model or MAOOAM (Section 2.5)

2.3 Atmosphere Model

The atmosphere model used is the two-layer QG model, that we derived in Section 1.3.4, and shown in Equation 1.20. The model was first developed by Charney and Straus [1980] (as a baroclinic modification to the barotropic model of Charney and DeVore [1979]). Additional modes were added by Reinhold and Pierrehumbert [1982] to better simulate synoptic systems. More recently similar atmosphere models have been used to study postprocessing methods and response theory on understanding low frequency variability [Demaeyer and Vannitsem, 2020; Vanderborght et al., 2024].

Section 1.4.2 omitted certain coupling terms of the two layer model, in the interest of clarity, that we will now include to gain a more accurate model. In particular, the interaction between the two layers at the interface between them, was overlooked. A dissipative mechanism can be used to model the impact of a difference in flows between the upper and lower levels. If there is a difference in flows between the two layers, there exists a shear layer, similar to an Ekmann layer, where the velocities transition from one layer to another. This can be modelled by looking at the difference in vorticity at the interface of the two layers, or equivalently the vertical fluxes caused by the differences in horizontal momentum between the layers, as a result of Reynolds stress [Cavallini and Crisciani, 2013]. This results in the addition of the following terms in the two layer model

$$\pm k_d' \nabla^2 (\psi_{\mathrm{a}}^1 - \psi_{\mathrm{a}}^3)$$

where the sign of the term is dependant on which atmospheric layer it is added to. This term can be thought of as a frictional coupling term between the two layers. Similarly the drag on the bottom layer on the atmosphere is also modelled using a Laplacian, and can be thought of as a frictional force on the bottom layer. We discuss this in the following sections, as it is dependant on what bottom layer we are modelling. This results in the following partial differential equations for the atmosphere

$$\begin{aligned} \frac{\partial}{\partial t}\overbrace{\left(\nabla^2\psi_{\mathrm{a}}^1\right)}^{\text{vorticity}} + \overbrace{J\left(\psi_{\mathrm{a}}^1, \nabla^2\psi_{\mathrm{a}}^1\right)}^{\text{horizontal advection}} + \overbrace{\beta\frac{\partial\psi_{\mathrm{a}}^1}{\partial x}}^{\beta\text{-plane approx}} &= \overbrace{-k_d'\nabla^2\left(\psi_{\mathrm{a}}^1 - \psi_{\mathrm{a}}^3\right)}^{\text{friction}} + \overbrace{\frac{f_0}{\Delta p}\omega}^{\text{vertical stretch}} \\ \frac{\partial}{\partial t}\left(\nabla^2\psi_{\mathrm{a}}^3\right) + J\left(\psi_{\mathrm{a}}^3, \nabla^2\psi_{\mathrm{a}}^3\right) + \beta\frac{\partial\psi_{\mathrm{a}}^3}{\partial x} &= +k_d'\nabla^2\left(\psi_{\mathrm{a}}^1 - \psi_{\mathrm{a}}^3\right) - \frac{f_0}{\Delta p}\omega \end{aligned} \tag{2.3}$$

Instead of modelling the streamfunctions ψ_{a}^1 and ψ_{a}^3 we will model the mean and shear streamfunctions, which act as a barotropic and baroclinic streamfunction respectively, on an intermediate virtual layer

$$\psi_{\mathrm{a}} = \frac{\psi_{\mathrm{a}}^1 + \psi_{\mathrm{a}}^3}{2} \qquad \theta_{\mathrm{a}} = \frac{\psi_{\mathrm{a}}^1 - \psi_{\mathrm{a}}^3}{2} \tag{2.4}$$

By adding the two atmosphere layers, and by subtracting the bottom atmosphere layer from the top, we can derive a model that uses the barotropic and baroclinic streamfunctions

$$\begin{aligned} \frac{\partial}{\partial t}\left(\nabla^2\psi_{\mathrm{a}}\right) + \quad J\left(\psi_{\mathrm{a}}, \nabla^2\psi_{\mathrm{a}}\right) + J\left(\theta_{\mathrm{a}}, \nabla^2\theta_{\mathrm{a}}\right) + \quad \beta\frac{\partial\psi_{\mathrm{a}}}{\partial x} &= 0 \\ \frac{\partial}{\partial t}\left(\nabla^2\theta_{\mathrm{a}}\right) + \quad J\left(\psi_{\mathrm{a}}, \nabla^2\theta_{\mathrm{a}}\right) + J\left(\theta_{\mathrm{a}}, \nabla^2\psi_{\mathrm{a}}\right) + \quad \beta\frac{\partial\theta_{\mathrm{a}}}{\partial x} &= -2k_d'\nabla^2\theta_{\mathrm{a}} + \frac{f_0}{\Delta p}\omega \end{aligned} \tag{2.5}$$

2.4 Land-Atmosphere Coupled Model

The coupled land-atmosphere model, with temperature exchanges, was first implemented by Li et al. [2018]. It was influenced by the coupled ocean-atmosphere model [Vannitsem et al., 2015] (which we introduce in Section 2.5). It consists of a two layer quasi-geostrophic atmosphere that is coupled through friction and heat transfers with a stationary land layer that includes a simple orography. This model was originally developed to study the impact of a coupled model on multiple equilibria that were known to exist in the atmosphere section of this model [Reinhold and Pierrehumbert, 1982], that correspond to different atmospheric waves. This model has also been used to study the predicability of different types of atmospheric blocking [Xavier et al., 2024].

2.4.1 Atmosphere Component

The land component consists of the atmosphere model coupled through friction and temperature exchanges to a land bottom layer. This involves introducing the following friction

term to the bottom later of the atmosphere model that we show in Equation 2.3

$$-k_d\nabla^2\psi_{\mathrm{a}}^3$$

We also include orography to the model. This allows profile of the land layer to impact the flow in the atmosphere. This is done to simulate planetary Rossby waves, through the instability that arises as a result of the interaction between the zonal flow with the orography [Charney and DeVore, 1979]. Here, we use the same method as in Charney and Straus [1980] to include the impact of topography, by using an advection term to the lower atmospheric layer

$$J(\psi_{\mathrm{a}}^3, f_0 h/H_{\mathrm{a}})$$

where H_{a} is the characteristic depth of the fluid layer, h is the height of the orography, and f_0 is the Coriolis parameter.

Then we convert this model to use barotropic and baroclinic streamfunctions, as described in the previous section, to obtain the coupled land-atmosphere model

$$\begin{aligned}
\frac{\partial}{\partial t}\left(\nabla^2\psi_{\mathrm{a}}\right) + J\left(\psi_{\mathrm{a}}, \nabla^2\psi_{\mathrm{a}}\right) + J\left(\theta_{\mathrm{a}}, \nabla^2\theta_{\mathrm{a}}\right) + \frac{1}{2}J(\psi_{\mathrm{a}} - \theta_{\mathrm{a}}, f_0 h/H_{\mathrm{a}}) \\
= -\beta\frac{\partial\psi_{\mathrm{a}}}{\partial x} - \frac{k_d}{2}\nabla^2(\psi_{\mathrm{a}} - \theta_{\mathrm{a}}) \\
\frac{\partial}{\partial t}\left(\nabla^2\theta_{\mathrm{a}}\right) + J\left(\psi_{\mathrm{a}}, \nabla^2\theta_{\mathrm{a}}\right) + J\left(\theta_{\mathrm{a}}, \nabla^2\psi_{\mathrm{a}}\right) - \frac{1}{2}J(\psi_{\mathrm{a}} - \theta_{\mathrm{a}}, f_0 h/H_{\mathrm{a}}) \\
= -\beta\frac{\partial\theta_{\mathrm{a}}}{\partial x} + \frac{k_d}{2}\nabla^2(\psi_{\mathrm{a}} - \theta_{\mathrm{a}}) \\
- 2k_d'\nabla^2\theta_{\mathrm{a}} + \frac{f_0}{\Delta p}\omega
\end{aligned} \tag{2.6}$$

2.4.2 Temperature Equations

To model the temperature of the atmosphere and the land components, and how heat energy is transferred between the layers, we use an energy balance model (EBM), similar to that introduced in Section 1.4.1, and sketched in Figure 1.7. Here, we track two variables, the atmospheric temperature across space and time $T_{\mathrm{a}}(t, x, y)$, at a virtual intermediate layer at 500hPa, and the ground temperature $T_{\mathrm{g}}(t, x, y)$. However, we have not yet considered how the flow in the atmosphere moves heat within the atmosphere. Warm and cool spots are advected by the flow. This is modelled using the following advection term, multiplied by the heat capacity of the atmosphere γ_{a}

$$\gamma_{\mathrm{a}}\, J(\psi_{\mathrm{a}}, T_{\mathrm{a}})$$

In addition the vertical mixing of the atmosphere impacts the temperature. Defining the static stability of the atmosphere as $\sigma = -\frac{R}{p}\left(\frac{\partial T_{\mathrm{a}}}{\partial p} - \frac{RT_{\mathrm{a}}}{c_p\, p}\right)$, which we assume to be constant. This results in the change in temperature dependant on the vertical velocity ω

$$-\gamma_{\mathrm{a}}\,\sigma\omega\frac{p}{R}$$

Modifying Equation 1.21 accordingly, this results in the energy balance model for the coupled land-atmosphere model

$$\begin{aligned}\gamma_{\mathrm{a}}\left(\frac{\partial T_{\mathrm{a}}}{\partial t}+J\left(\psi_{\mathrm{a}},T_{\mathrm{a}}\right)-\sigma\omega\frac{p}{R}\right) &= -\lambda\left(T_{\mathrm{a}}-T_{\mathrm{g}}\right)+\varepsilon_{\mathrm{a}}\sigma_{\mathrm{B}}T_{\mathrm{g}}^{4}-2\epsilon_{\mathrm{a}}\sigma_{\mathrm{B}}T_{\mathrm{a}}^{4}+R_{\mathrm{a}}\\ \gamma_{\mathrm{g}}\frac{\partial T_{\mathrm{g}}}{\partial t} &= -\lambda\left(T_{\mathrm{g}}-T_{\mathrm{a}}\right)-\sigma_{\mathrm{B}}T_{\mathrm{g}}^{4}+\varepsilon_{\mathrm{a}}\sigma_{\mathrm{B}}T_{\mathrm{a}}^{4}+R_{\mathrm{g}}\end{aligned} \tag{2.7}$$

where p is the pressure, R is the ideal gas constant, λ is a parameter that controls the temperature exchange through sensible and turbulent heat transfers, ε_{a} is the emissivity of the atmosphere, σ_{B} is the Stefan-Boltzmann constant, and $R_{\mathrm{a}},\ R_{\mathrm{g}}$ is the incoming solar radiation in the atmosphere and the ground respectively. Here the heat capacity of the ground γ_{g} is larger than the heat capacity of the atmosphere, meaning that the ground temperature has a longer memory than that of the atmosphere, or that the ground temperature will change more slowly than that of the atmosphere. This leads to low frequency variability in the coupled system.

To simplify the non-linear terms, from the Stefan-Boltzmann law, in the EBM we introduce the linearisation $T_{\mathrm{a}}=T_{\mathrm{a},0}+\delta T_{\mathrm{a}}$ and $T_{\mathrm{g}}=T_{\mathrm{g},0}+\delta T_{\mathrm{g}}$. We fix the temperatures $T_{\mathrm{a},0}$ and $T_{\mathrm{g},0}$ to be constant, meaning the atmosphere and land temperatures now can be tracked by the temperature anomalies δT_{a} and δT_{g}. This necessitates taking the linearisation of the incoming short wave radiation as $R_{\mathrm{a}}=R_{\mathrm{a},0}+\delta R_{\mathrm{a}}$ and $R_{\mathrm{g}}=R_{\mathrm{g},0}+\delta R_{\mathrm{g}}$, and by taking only terms that are linear in δT_{a} and δ_{g}, we obtain a set of coupled PDEs for the temperature anomalies

$$\begin{aligned}\gamma_{\mathrm{a}}\left(\frac{\partial\delta T_{\mathrm{a}}}{\partial t}+J\left(\psi_{\mathrm{a}},\delta T_{\mathrm{a}}\right)-\sigma\omega\frac{p}{R}\right) &= -\lambda\left(\delta T_{\mathrm{a}}-\delta T_{\mathrm{g}}\right)+4\varepsilon_{\mathrm{a}}\sigma_{\mathrm{B}}T_{\mathrm{g},0}^{3}\delta T_{\mathrm{g}}\\ &\quad -8\epsilon_{\mathrm{a}}\sigma_{\mathrm{B}}T_{\mathrm{a},0}^{3}\delta T_{\mathrm{a}}+\delta R_{\mathrm{a}}\\ \gamma_{\mathrm{g}}\frac{\partial\delta T_{\mathrm{g}}}{\partial t} &= -\lambda\left(\delta T_{\mathrm{g}}-\delta T_{\mathrm{a}}\right)-4\sigma_{\mathrm{B}}T_{\mathrm{g},0}^{3}\delta T_{\mathrm{g}}\\ &\quad +4\varepsilon_{\mathrm{a}}\sigma_{\mathrm{B}}T_{\mathrm{a},0}^{3}\delta T_{\mathrm{a}}+\delta R_{\mathrm{g}}\end{aligned} \tag{2.8}$$

Using the ideal gas law and the hydrostatic relation at 500hPa we can express the temperature of the atmosphere in relation to the baroclinic streamfunctions, which we derived in Equation 1.22

$$\delta T_{\mathrm{a}}=2\frac{f_0}{R}\,\theta_{\mathrm{a}}$$

This model is forced using uneven solar insolation. This is done by using the basis function $F_1=\sqrt{2}\cos y$, which simulates the north-south temperature gradient, giving the solar forcing on the atmosphere as $\delta R_{\mathrm{a}}(x,y)=C_{\mathrm{a},1}F_1(x,y)$, and similarly for the the solar insolation on the bottom layer.

2.4.3 Numerically Solving the Model

We now use a Galerkin expansion, as outlined in Section 2.1.1, to convert the system of PDEs into ODEs. The model equations are first non-dimensionalised using the following

scaling

$$\begin{aligned} t &\to f_0^{-1}\,\tilde{t} \\ x &\to L_x\,\tilde{x} = 2\pi L/n\,\tilde{x} \\ y &\to L_y\,\tilde{y} = \pi L\,\tilde{y} \\ p &\to \Delta p\,\tilde{p} \\ T_\mathrm{a} &\to f_0^2 L^2/R\,\tilde{T}_\mathrm{a} \\ T_\mathrm{g} &\to f_0^2 L^2/R\,\tilde{T}_\mathrm{g} \\ \psi_\mathrm{a} &\to L^2 f_0\,\tilde{\psi}_\mathrm{a} \\ \theta_\mathrm{a} &\to L^2 f_0\,\tilde{\theta}_\mathrm{a} \end{aligned} \tag{2.9}$$

where n is the model domain aspect ratio $n = 2L_y/L_x$. This scaling means that the baroclinic streamfunctions and atmospheric temperature are related by $\tilde{T_\mathrm{a}} \equiv 2\tilde{\theta_\mathrm{a}}$.

We now use a Galerkin expansion, as described in Section 2.1.1, to convert the model PDEs into a set of ODEs. In addition, we eliminate the vertical velocities in the baroclinic atmosphere equations, and the atmospheric temperature equations. This leads to the following set of equations, for the land-atmosphere coupled model

$$\begin{aligned} \dot{\psi}_{\mathrm{a},i} = &-a_{i,i}^{-1} \sum_{j,m=1}^{n_\mathrm{a}} b_{i,j,m}\left(\psi_{\mathrm{a},j}\,\psi_{\mathrm{a},m} + \theta_{\mathrm{a},j}\,\theta_{\mathrm{a},m}\right) \\ &- \frac{a_{i,i}^{-1}}{2} \sum_{j,m=1}^{n_\mathrm{a}} g_{i,j,m}\,h_m\left(\psi_{\mathrm{a},j} - \theta_{\mathrm{a},j}\right) \\ &- \beta\,a_{i,i}^{-1} \sum_{j=1}^{n_\mathrm{a}} c_{i,j}\,\psi_{\mathrm{a},j} - \frac{k_d}{2}\left(\psi_{\mathrm{a},i} - \theta_{\mathrm{a},i}\right) \end{aligned}$$

$$\begin{aligned} \dot{\theta}_{\mathrm{a},i} = &\frac{\sigma/2}{a_{i,i}\,\sigma/2 - 1}\Bigg\{ - \sum_{j,m=1}^{n_\mathrm{a}} b_{i,j,m}\left(\psi_{\mathrm{a},j}\,\theta_{\mathrm{a},m} + \theta_{\mathrm{a},j}\,\psi_{\mathrm{a},m}\right) - \beta \sum_{j=1}^{n_\mathrm{a}} c_{i,j}\,\theta_{\mathrm{a},j} \\ &+ \frac{1}{2}\sum_{j,m=1}^{n_\mathrm{a}} g_{i,j,m}\,h_m\left(\psi_{\mathrm{a},j} - \theta_{\mathrm{a},j}\right) + \frac{k_d}{2}\,a_{i,i}\left(\psi_{\mathrm{a},i} - \theta_{\mathrm{a},i}\right) - 2\,k_d'\,a_{i,i}\,\theta_{\mathrm{a},i}\Bigg\} \\ &+ \frac{1}{a_{i,i}\,\sigma/2 - 1}\Bigg\{ \sum_{j,m=1}^{n_\mathrm{a}} g_{i,j,m}\,\psi_{\mathrm{a},j}\,\theta_{\mathrm{a},m} + \left(\lambda_\mathrm{a}' + S_{B,\mathrm{a}}\right)\theta_{\mathrm{a},i} \\ &\qquad - \left(\frac{\lambda_\mathrm{a}'}{2} + S_{B,\mathrm{g}}\right)\delta T_{\mathrm{g},i} - C_{\mathrm{a},i}'\Bigg\} \end{aligned} \tag{2.10}$$

$$\dot{\delta T}_{\mathrm{g},i} = -\left(\lambda_\mathrm{g}' + s_{B,\mathrm{g}}\right)\delta T_{\mathrm{g},i} + \left(2\,\lambda_\mathrm{g}' + s_{B,\mathrm{a}}\right)\theta_{\mathrm{a},i} + C_{\mathrm{g},i}'$$

where the non-dimensionalised parameters are

$$\begin{aligned}
\lambda'_{\mathrm{a}} &= \frac{\lambda}{\gamma_{\mathrm{a}} f_0} & \lambda'_{\mathrm{g}} &= \frac{\lambda}{\gamma_{\mathrm{g}} f_0} \\
S_{\mathrm{B,a}} &= 8\frac{\varepsilon_{\mathrm{a}}\sigma_{\mathrm{B}}}{\gamma_{\mathrm{a}} f_0} T_{\mathrm{a},0}^3 & S_{\mathrm{B,g}} &= 2\frac{\varepsilon_{\mathrm{a}}\sigma_{\mathrm{B}}}{\gamma_{\mathrm{a}} f_0} T_{\mathrm{g},0}^3 \\
s_{\mathrm{B,a}} &= 8\frac{\varepsilon_{\mathrm{a}}\sigma_{\mathrm{B}}}{\gamma_{\mathrm{g}} f_0} T_{\mathrm{a},0}^3 & s_{\mathrm{B,g}} &= 8\frac{\varepsilon_{\mathrm{a}}\sigma_{\mathrm{B}}}{\gamma_{\mathrm{g}} f_0} T_{\mathrm{g},0}^3 \\
C'_{\mathrm{a},i} &= \frac{R}{2\gamma_{\mathrm{a}} L^2 f_0^3} C_{\mathrm{a},i} & C'_{\mathrm{g},i} &= \frac{R}{\gamma_{\mathrm{g}} L^2 f_0^3} C_{\mathrm{g},i}
\end{aligned} \tag{2.11}$$

and the tensors, which define the inner products are

$$\begin{aligned}
a_{i,j} &= \frac{n}{2\pi^2}\int_0^{\pi}\int_0^{2\pi/n} F_i(x,y)\nabla^2 F_j(x,y)\mathrm{d}x\,\mathrm{d}y = -\delta_{ij}a_i^2 \\
g_{i,j,m} &= \frac{n}{2\pi^2}\int_0^{\pi}\int_0^{2\pi/n} F_i(x,y) J\left(F_j(x,y), F_m(x,y)\right)\mathrm{d}x\,\mathrm{d}y \\
b_{i,j,m} &= \frac{n}{2\pi^2}\int_0^{\pi}\int_0^{2\pi/n} F_i(x,y) J\left(F_j(x,y), \nabla^2 F_m(x,y)\right)\mathrm{d}x\,\mathrm{d}y \\
c_{i,j} &= \frac{n}{2\pi^2}\int_0^{\pi}\int_0^{2\pi/n} F_i(x,y)\frac{\partial}{\partial x} F_j(x,y)\mathrm{d}x\,\mathrm{d}y
\end{aligned} \tag{2.12}$$

2.5 Ocean-Atmosphere Model

The coupled ocean-atmosphere model, also known as the Modular Arbitrary Order Ocean Atmosphere Model (MAOOAM) [De Cruz et al., 2016a], consists of a two layer quasi-geostrophic atmosphere, coupled through momentum and heat exchange to a single layer quasi-geostrophic shallow water layer. The model was developed as a combination of the atmosphere model of Reinhold and Pierrehumbert [1982] (originally influenced by [Charney and Straus, 1980]) with the ocean model of Pierini [2011]. The atmospheric and ocean temperatures are modelled using the energy balance model derived in Barsugli and Battisti [1998]. The model was originally presented in Vannitsem et al. [2015], and later refined in De Cruz et al. [2016a]. It has been used to study a wide range of low frequency variability features of the coupled ocean-atmosphere system, as well as predictability and instability features of the coupled atmosphere [Hamilton et al., 2023; Alberti et al., 2021; Vannitsem et al., 2021; Demaeyer et al., 2021; Demaeyer and Vannitsem, 2018; De Cruz et al., 2018; Vannitsem and Ghil, 2017; Vannitsem, 2017].

2.5.1 Ocean Component

The ocean component consists of a barotropic shallow water layer, which sits above a deep ocean layer that is stationary. This is modelled by the reduced gravity quasi-geostrophic

vorticity equation given by

$$\frac{\partial}{\partial t}\overbrace{\left(\nabla^2\psi_{\rm o}\right)}^{\text{vorticity}}-\frac{\partial}{\partial t}\overbrace{\left(\frac{\psi_{\rm o}}{L_{\rm R}^2}\right)}^{\text{deformation}}+\overbrace{J\left(\psi_{\rm o},\nabla^2\psi_{\rm o}\right)}^{\text{horizontal advection}}+\overbrace{\beta\frac{\partial\psi_{\rm o}}{\partial x}}^{\beta\text{-plane approx}}=\overbrace{-r\nabla^2\psi_{\rm o}}^{\text{friction}} \tag{2.13}$$

where $L_{\rm R}=\sqrt{g'h}/f_0$ is the reduced gravity Rossby deformation radius, where g' is reduced gravity, which is used in the ocean due to the small difference in water density above and below a parcel.

To couple the ocean layer with the QG atmosphere, we include a frictional coupling term to the ocean model, in Equation 2.13. This term forces the ocean layer, depending on the flow in the lower layer of the atmosphere

$$+d\,\nabla^2(\psi_{\rm a}^3-\psi_{\rm o})$$

where $d=C/\rho_{\rm o}h$ is the ocean-atmosphere coupling, and $\rho_{\rm o}$ is the density of the ocean, h is the depth of the shallow water layer, and C is a tunable parameter.

Likewise, the lower layer of the atmosphere is coupled to the ocean. This introduces the frictional term to the lower atmospheric layer in Equation 2.3

$$-k_d\nabla^2(\psi_{\rm a}^3-\psi_{\rm o})$$

where k_d is a parameter which quantifies the friction between the atmosphere and the surface.

We include these term to the atmosphere model, and introduce the barotropic and baroclinic streamfunctions (Equation 2.4), and this results in the coupled ocean-atmosphere model

$$\begin{aligned}
\frac{\partial}{\partial t}\left(\nabla^2\psi_{\rm a}\right)+J\left(\psi_{\rm a},\nabla^2\psi_{\rm a}\right)+J\left(\theta_{\rm a},\nabla^2\theta_{\rm a}\right)+\beta\frac{\partial\psi_{\rm a}}{\partial x}&=-\frac{k_d}{2}\nabla^2\left(\psi_{\rm a}-\theta_{\rm a}-\psi_{\rm o}\right)\\
\frac{\partial}{\partial t}\left(\nabla^2\theta_{\rm a}\right)+J\left(\psi_{\rm a},\nabla^2\theta_{\rm a}\right)+J\left(\theta_{\rm a},\nabla^2\psi_{\rm a}\right)+\beta\frac{\partial\theta_{\rm a}}{\partial x}&=-2k_d'\nabla^2\theta_{\rm a}\\
&\quad+\frac{k_d}{2}\nabla^2\left(\psi_{\rm a}-\theta_{\rm a}-\psi_{\rm o}\right)+\frac{f_0}{\Delta p}\omega\\
\frac{\partial}{\partial t}\left(\nabla^2\psi_{\rm o}-\frac{\psi_{\rm o}}{L_{\rm R}^2}\right)+J\left(\psi_{\rm o},\nabla^2\psi_{\rm o}\right)+\beta\frac{\partial\psi_{\rm o}}{\partial x}&=-r\nabla^2\psi_{\rm o}\\
&\quad+d\,\nabla^2\left(\psi_{\rm a}-\theta_{\rm a}-\psi_{\rm o}\right)
\end{aligned} \tag{2.14}$$

2.5.2 Temperature Equations

The energy balance model is similar to that presented in Section 2.4.2, for the land atmosphere model. In this case, however, the ocean flow can also advect heat, requiring us to include an advection term in the ocean temperature equation ($\gamma_{\rm o}\ J(\psi_{\rm o},\nabla^2\psi_{\rm o})$). This

results in the following EBM for the coupled ocean-atmosphere system

$$\begin{aligned}\gamma_{\mathrm{a}}\left(\frac{\partial T_{\mathrm{a}}}{\partial t}+J\left(\psi_{\mathrm{a}},T_{\mathrm{a}}\right)-\sigma\omega\frac{p}{R}\right)&=-\lambda\left(T_{\mathrm{a}}-T_{\mathrm{o}}\right)+\varepsilon_{\mathrm{a}}\sigma_{\mathrm{B}}T_{\mathrm{o}}^{4}-\varepsilon_{\mathrm{a}}\sigma_{\mathrm{B}}T_{\mathrm{a}}^{4}+R_{\mathrm{a}}\\ \gamma_{\mathrm{o}}\left(\frac{\partial T_{\mathrm{o}}}{\partial t}+J\left(\psi_{\mathrm{o}},T_{\mathrm{o}}\right)\right)&=-\lambda\left(T_{\mathrm{o}}-T_{\mathrm{a}}\right)-\sigma_{\mathrm{B}}T_{\mathrm{o}}^{4}+\varepsilon_{\mathrm{a}}\sigma_{\mathrm{B}}T_{\mathrm{a}}^{4}+R_{\mathrm{o}}\end{aligned}\tag{2.15}$$

As in Section 2.4.2 we linearise the temperatures around a reference temperature $T_{\mathrm{a},0}$ and $T_{\mathrm{o},0}$, and anomalies $\delta T_{\mathrm{a},\,0}$ and $\delta T_{\mathrm{o},\,0}$, which results in the following PDEs which track the temperature anomalies in the system

$$\begin{aligned}\gamma_{\mathrm{a}}\left(\frac{\partial\delta T_{\mathrm{a}}}{\partial t}+J\left(\psi_{\mathrm{a}},\delta T_{\mathrm{a}}\right)-\sigma\omega\frac{p}{R}\right)&=-\lambda\left(\delta T_{\mathrm{a}}-\delta T_{\mathrm{o}}\right)+4\varepsilon_{\mathrm{a}}\sigma_{\mathrm{B}}T_{\mathrm{o},0}^{3}\delta T_{\mathrm{o}}\\ &\quad-8\varepsilon_{\mathrm{a}}\sigma_{\mathrm{B}}T_{\mathrm{a},0}^{3}\delta T_{\mathrm{a}}+\delta R_{\mathrm{a}}\\ \gamma_{\mathrm{o}}\left(\frac{\partial\delta T_{\mathrm{o}}}{\partial t}+J\left(\psi_{\mathrm{o}},\delta T_{\mathrm{o}}\right)\right)&=-\lambda\left(\delta T_{\mathrm{o}}-\delta T_{\mathrm{a}}\right)-4\sigma_{\mathrm{B}}T_{\mathrm{o},0}^{3}\delta T_{\mathrm{o}}\\ &\quad+4\varepsilon_{\mathrm{a}}\sigma_{\mathrm{B}}T_{\mathrm{a},0}^{3}+\delta T_{\mathrm{a}}\delta R_{\mathrm{o}}\end{aligned}$$

2.5.3 Numerically Solving the Model

We convert the four PDEs into a set of ODEs, using the same methodology that we presented in Section 2.4.3. One slight difference is that we want to model the ocean over a closed basin, to better simulate ocean basins such as the North Atlantic. This means that we need to introduce a different set of basis modes, compared to the atmosphere which is modelled with periodic boundary conditions to simulate a channel. More precisely, we want a set of basis modes which have no flux boundary conditions on both the zonal and meridional boundaries. Using the same domain as introduced in Section 2.1.1, the ocean basis modes used here are given by

$$\phi_{H_{\mathrm{o}},P_{\mathrm{o}}}(x,y)=2\sin\left(\frac{H_{\mathrm{o}}\,n}{2}x\right)\sin(P_{\mathrm{o}}y)\tag{2.16}$$

where H_{o} and P_{o} are integers. Again, these modes are orthogonal with respect to the inner product $\langle\phi_i,\phi_j\rangle=\delta_{ij}$.

By non-dimensionalising the system, doing a Galerkin expansion of the atmospheric variables over the modes F_i and the ocean modes over ϕ_i, and finally eliminating vertical velocities, we get the following set of equations for the ocean-atmosphere coupled model

$$\dot{\psi}_{\mathrm{a},i} = -a_{i,i}^{-1} \sum_{j,m=1}^{n_\mathrm{a}} b_{i,j,m} \left(\psi_{\mathrm{a},j}\, \psi_{\mathrm{a},m} + \theta_{\mathrm{a},j}\, \theta_{\mathrm{a},m}\right) - \beta\, a_{i,i}^{-1} \sum_{j=1}^{n_\mathrm{a}} c_{i,j}\, \psi_{\mathrm{a},j} - \frac{k_d}{2} \left(\psi_{\mathrm{a},i} - \theta_{\mathrm{a},i}\right) + \frac{k_d}{2}\, a_{i,i}^{-1} \sum_{j=1}^{n_\mathrm{o}} d_{i,j}\, \psi_{\mathrm{o},j}$$

$$\begin{aligned}\dot{\theta}_{\mathrm{a},i} = {} & \frac{\sigma/2}{a_{i,i}\,\sigma/2 - 1} \left\{ - \sum_{j,m=1}^{n_\mathrm{a}} b_{i,j,m} \left(\psi_{\mathrm{a},j}\, \theta_{\mathrm{a},m} + \theta_{\mathrm{a},j}\, \psi_{\mathrm{a},m}\right) - \beta \sum_{j=1}^{n_\mathrm{a}} c_{i,j}\, \theta_{\mathrm{a},j} \right. \\ & \left. + \frac{k_d}{2}\, a_{i,i} \left(\psi_{\mathrm{a},i} - \theta_{\mathrm{a},i}\right) - \frac{k_d}{2} \sum_{j=1}^{n_\mathrm{o}} d_{i,j}\, \psi_{\mathrm{o},j} - 2\, k_d'\, a_{i,i}\, \theta_{\mathrm{a},i} \right\} \\ & + \frac{1}{a_{i,i}\,\sigma/2 - 1} \left\{ \sum_{j,m=1}^{n_\mathrm{a}} g_{i,j,m}\, \psi_{\mathrm{a},j}\, \theta_{\mathrm{a},m} + \left(\lambda_\mathrm{a}' + S_{B,\mathrm{a}}\right)\, \theta_{\mathrm{a},i} \right. \\ & \left. - \left(\frac{\lambda_\mathrm{a}'}{2} + S_{B,\mathrm{o}}\right) \sum_{j=1}^{n_\mathrm{o}} s_{i,j}\, \delta T_{\mathrm{o},j} - C_{\mathrm{a},i}' \right\}\end{aligned} \tag{2.17}$$

$$\dot{\psi}_{\mathrm{o},i} = \frac{1}{(M_{i,i} + G)} \left\{ - \sum_{j,m=1}^{n_\mathrm{o}} C_{i,j,k}\, \psi_{\mathrm{o},j}\, \psi_{\mathrm{o},k} - \beta \sum_{j=1}^{n_\mathrm{o}} N_{i,j}\, \psi_{\mathrm{o},j} - (d + r) \sum_{j=1}^{n_\mathrm{o}} M_{i,j}\, \psi_{\mathrm{o},j} + d \sum_{j=1}^{n_\mathrm{a}} K_{i,j}\, \left(\psi_{\mathrm{a},j} - \theta_{\mathrm{a},j}\right) \right\}$$

$$\dot{\delta T}_{\mathrm{o},i} = - \sum_{j,m=1}^{n_\mathrm{o}} O_{i,j,m}\, \psi_{\mathrm{o},j}\, \delta T_{\mathrm{o},m} - \left(\lambda_\mathrm{o}' + s_{B,\mathrm{o}}\right)\, \delta T_{\mathrm{o},i} + \left(2\,\lambda_\mathrm{o}' + s_{B,\mathrm{a}}\right) \sum_{j=1}^{n_\mathrm{a}} W_{i,j}\, \theta_{\mathrm{a},j} + \sum_{j=1}^{n_\mathrm{a}} W_{i,j}\, C_{\mathrm{o},j}'$$

where the non-dimensionalised parameters are given in Equation 2.11, with $T_{\mathrm{o},0}$ replacing $T_{\mathrm{g},0}$. The tensors, which define the inner products, in addition to those presented in

Equation 2.12, are

$$
\begin{aligned}
M_{i,j} &= \frac{n}{2\pi^2}\int_0^{\pi}\int_0^{2\pi/n} \phi_i(x,y)\nabla^2\phi_j(x,y)\mathrm{d}x\,\mathrm{d}y = -\delta_{ij}m_i^2 \\
O_{i,j,m} &= \frac{n}{2\pi^2}\int_0^{\pi}\int_0^{2\pi/n} \phi_i(x,y)J\left(\phi_j(x,y),\phi_m(x,y)\right)\mathrm{d}x\,\mathrm{d}y \\
C_{i,j,m} &= \frac{n}{2\pi^2}\int_0^{\pi}\int_0^{2\pi/n} \phi_i(x,y)J\left(\phi_j(x,y),\nabla^2\phi_m(x,y)\right)\mathrm{d}x\,\mathrm{d}y \\
N_{i,j} &= \frac{n}{2\pi^2}\int_0^{\pi}\int_0^{2\pi/n} \phi_i(x,y)\frac{\partial}{\partial x}\phi_j(x,y)\mathrm{d}x\,\mathrm{d}y \\
d_{i,j} &= \frac{n}{2\pi^2}\int_0^{\pi}\int_0^{2\pi/n} F_i(x,y)\nabla^2\phi_j(x,y)\mathrm{d}x\,\mathrm{d}y \\
K_{i,j} &= \frac{n}{2\pi^2}\int_0^{\pi}\int_0^{2\pi/n} \phi_i(x,y)\nabla^2F_j(x,y)\mathrm{d}x\,\mathrm{d}y \\
W_{i,j} &= \frac{n}{2\pi^2}\int_0^{\pi}\int_0^{2\pi/n} \phi_i(x,y)F_j(x,y)\mathrm{d}x\,\mathrm{d}y = s_{j,i}
\end{aligned}
\tag{2.18}
$$

2.5.4 Nonlinear Radiation Terms Modification

Nonlinear dynamics can lead to tipping points or unpredictable responses to parameter changes [Ashwin et al., 2012]. To investigate the sensitivity of the qgs model to the linearisation of the longwave radiation terms, we introduce methods of solving the system, that alter how the linearisation $T_{\mathrm{a}}(t,x,y) = T_{\mathrm{a},0} + \delta T_{\mathrm{a}}(t,x,y)$ is implemented.

This requires the reference temperature $T_{\mathrm{a},0}$, and $T_{\mathrm{o},0}$ or $T_{\mathrm{g},0}$, to be time-varying quantities in the linearisation. To allow the average temperature across the atmosphere and ocean to change dynamically with time, we introduced two new basis modes, corresponding to constant spatial modes: $F_0(x,y) = 1$ and $\phi_0(x,y) = 1$. These modes were added to the list of basis modes that were introduced in Equations 2.1 and 2.16

$$
\begin{aligned}
F_0 &= 1 & \phi_0 &= 1 \\
F_1 &= \sqrt{2}\cos(y) & \phi_1 &= 2\sin(nx/2)\sin(y) \\
F_2 &= 2\cos(nx)\sin(y) & \phi_2 &= 2\sin(nx/2)\sin(2y) \\
&\vdots & &\vdots
\end{aligned}
\tag{2.19}
$$

These additional basis modes now allow us to express the expanded temperature variables as $T_{\mathrm{a}}(t,x,y) = \sum_{i=0}^{n_{\mathrm{a}}} T_{\mathrm{a},i}(t)F_i(x,y)$, and similarly for the ocean or ground.

Only the temperature equations are projected onto these new basis modes, as these are the variables linearised in the original land-atmosphere or ocean-atmosphere models. Due to the additional basis modes introduced, we obtain an additional ODE for the atmospheric baroclinic streamfunction (as this variable replaces the atmospheric tempera-

ture variables) and for the ocean temperature or ground temperature, depending on which model flavour is used. Thus increasing the number of model equations by two.

We now have a choice whether to project the quartic Stefan-Boltzmann equations directly onto the basis modes, thus retaining the non-linear longwave radiation terms, or to use the same linearisation, but allow the reference temperature $T_{\mathrm{a},0}$ to change with time (it was set to a constant in the original model version). We introduce these new model variations in the following sections. Here we focus on the ocean-atmosphere version of the model, as this version is the focus of Chapter 5, but the land-atmosphere model can be altered with almost identical modifications.

Non-Linear Version

Instead of taking a linearisation of the Stefan-Boltzmann law terms, we directly project the model equations onto the set of basis modes. Taking the equation for the atmospheric temperature (Equation 2.15), and substituting the variables with the those decomposed on the basis modes, the modified atmospheric temperature equation is given by

$$\begin{aligned}\gamma_{\mathrm{a}}\left(\frac{\partial}{\partial t}\sum_{j=0}^{n_{\mathrm{a}}} T_{\mathrm{a},j}\,F_j + J\left(\sum_{m=1}^{n_{\mathrm{a}}}\psi_{\mathrm{a},m}\,F_m, \sum_{j=0}^{n_{\mathrm{a}}} T_{\mathrm{a},j}\,F_j\right) - \sigma\omega\frac{p}{R}\right) = \\ -\lambda\left(\sum_{j=0}^{n_{\mathrm{a}}} T_{\mathrm{a},j}\,F_j - \sum_{j=0}^{n_{\mathrm{o}}} T_{\mathrm{o},j}\,\phi_j\right) + \varepsilon_{\mathrm{a}}\sigma_B\left(\sum_{j=0}^{n_{\mathrm{o}}} T_{\mathrm{o},j}\,\phi_j\right)^4 \\ -2\varepsilon_{\mathrm{a}}\sigma_B\left(\sum_{j=0}^{n_{\mathrm{a}}} T_{\mathrm{a},j}\,F_j\right)^4 + R_{\mathrm{a}}\end{aligned}$$

as before, we use the identity $T_{\mathrm{a},i} \equiv 2\frac{f_0}{R}\theta_{\mathrm{a},\,i}$ to remove a variable, and we introduce the new tensors to simplify writing the equations

$$\begin{aligned}\sum_{j=0}^{n_{\mathrm{a}}} u_{i,j}\,\dot{\theta}_{\mathrm{a},j} = -\sum_{j,k=1}^{n_{\mathrm{a}}} g_{i,j,m}\,\psi_{\mathrm{a},j}\,\theta_{\mathrm{a},m} + \frac{\sigma}{2}\sum_{j=1}^{n_{\mathrm{a}}} u_{i,j}\,\omega_j - \lambda'_{\mathrm{a}}\sum_{j=0}^{n_{\mathrm{a}}} u_{i,j}\,\theta_{\mathrm{a},j} \\ - S_{B,\mathrm{a}}\sum_{j,k,l,m=0}^{n_{\mathrm{a}}} z_{i,j,k,l,m}\,\theta_{\mathrm{a},j}\theta_{\mathrm{a},k}\theta_{\mathrm{a},l}\theta_{\mathrm{a},m} + \frac{\lambda'_{\mathrm{a}}}{2}\sum_{j=0}^{n_{\mathrm{o}}} s_{i,j}\,T_{\mathrm{o},j} \\ + S_{B,\mathrm{o}}\sum_{j,k,l,m=0}^{n_{\mathrm{o}}} v_{i,j,k,l,m}\,T_{\mathrm{o},j}T_{\mathrm{o},k}T_{\mathrm{o},l}T_{\mathrm{o},m} + \sum_{j=0}^{n_{\mathrm{a}}} u_{i,j}\,C'_{\mathrm{a},j}\end{aligned}$$

where $S_{B,\mathrm{a}} = 16\varepsilon_\mathrm{a}\sigma_B L^6 f_0^5/(\gamma_\mathrm{a} R^3)$ and $S_{B,\mathrm{o}} = \varepsilon_\mathrm{a}\sigma_B L^6 f_0^5/(2\gamma_\mathrm{a} R)$, and the new tensors correspond with the following inner products

$$
\begin{aligned}
u_{i,j} &= \frac{n}{2\pi^2}\int_0^{\pi}\int_0^{2\pi/n} F_i(x,y)\; F_j(x,y)\,\mathrm{d}x\;\mathrm{d}y \\
v_{i,j,k,l,m} &= \frac{n}{2\pi^2}\int_0^{\pi}\int_0^{2\pi/n} F_i(x,y)\;\phi_j(x,y)\;\phi_k(x,y)\;\phi_l(x,y)\;\phi_m(x,y)\,\mathrm{d}x\;\mathrm{d}y \\
z_{i,j,k,l,m} &= \frac{n}{2\pi^2}\int_0^{\pi}\int_0^{2\pi/n} F_i(x,y)\; F_j(x,y)\; F_k(x,y)\; F_l(x,y)\; F_m(x,y)\,\mathrm{d}x\;\mathrm{d}y
\end{aligned}
$$

The equations for the atmospheric flow (Equation 2.14) are unchanged, and again the vertical velocities can be eliminated to obtain a single equation for the baroclinic streamfunction

$$
\begin{aligned}
\frac{\sigma}{2}\sum_{j=1}^{n_\mathrm{a}} a_{i,j}\,\dot\theta_{\mathrm{a},j} - \sum_{j=0}^{n_\mathrm{a}} u_{i,j}\,\dot\theta_{\mathrm{a},j} = \frac{\sigma}{2}\Bigg\{ &- \sum_{j,m=1}^{n_\mathrm{a}} b_{i,j,m}\,(\psi_{\mathrm{a},j}\,\theta_{\mathrm{a},m} + \theta_{\mathrm{a},j}\,\psi_{\mathrm{a},m}) \\
&- \beta\sum_{j=1}^{n_\mathrm{a}} c_{i,j}\,\theta_{\mathrm{a},j} + \frac{k_d}{2}\sum_{j=1}^{n_\mathrm{a}} a_{i,j}\,(\psi_{\mathrm{a},j} - \theta_{\mathrm{a},j}) \\
&- \frac{k_d}{2}\sum_{j=1}^{n_\mathrm{o}} d_{i,j}\,\psi_{\mathrm{o},j} - 2\,k_d'\sum_{j=1}^{n_\mathrm{a}} a_{i,j}\,\theta_{\mathrm{a},j}\Bigg\} \\
+\Bigg\{ &\sum_{j,k=1}^{n_\mathrm{a}} g_{i,j,m}\,\psi_{\mathrm{a},j}\,\theta_{\mathrm{a},m} + \lambda_\mathrm{a}'\sum_{j=0}^{n_\mathrm{a}} u_{i,j}\,\theta_{\mathrm{a},j} \\
&+ S_{B,\mathrm{a}}\sum_{j,k,l,m=0}^{n_\mathrm{a}} z_{i,j,k,l,m}\,\theta_{\mathrm{a},j}\theta_{\mathrm{a},k}\theta_{\mathrm{a},l}\theta_{\mathrm{a},m} \\
&- S_{B,\mathrm{o}}\sum_{j,k,l,m=0}^{n_\mathrm{o}} v_{i,j,k,l,m}\,T_{\mathrm{o},j}T_{\mathrm{o},k}T_{\mathrm{o},l}T_{\mathrm{o},m} \\
&- \frac{\lambda_\mathrm{a}'}{2}\sum_{j=0}^{n_\mathrm{o}} s_{i,j}\,T_{\mathrm{o},j} - \sum_{j=0}^{n_\mathrm{a}} u_{i,j}\,C'_{\mathrm{a},j}\Bigg\}
\end{aligned}
\tag{2.20}
$$

For the ocean temperature we do the same. The equation for the ocean barotropic stream functions is unchanged. We now input the expanded variables directly into the

temperature equation for the ocean (Equation 2.15), which results in

$$\begin{aligned}\sum_{j=0}^{n_\mathrm{o}} U_{i,j}\,\dot{T}_{\mathrm{o},j} = &-\sum_{j,k=1}^{n_\mathrm{o}} O_{i,j,m}\,\psi_{\mathrm{o},j}\,T_{\mathrm{o},m} - \sum_{j=0}^{n_\mathrm{o}} \lambda'_\mathrm{o}\,U_{i,j}T_{\mathrm{o},j} \\ &- s_{B,\mathrm{o}} \sum_{j,k,l,m=0}^{n_\mathrm{o}} V_{i,j,k,l,m}\,T_{\mathrm{o},j}T_{\mathrm{o},k}T_{\mathrm{o},l}T_{\mathrm{o},m} + 2\lambda'_\mathrm{o} \sum_{j=0}^{n_\mathrm{a}} W_{i,j}\,\theta_{\mathrm{a},j} \\ &+ s_{B,\mathrm{a}} \sum_{j,k,l,m=0}^{n_\mathrm{a}} Z_{i,j,k,l,m}\,\theta_{\mathrm{a},j}\theta_{\mathrm{a},k}\theta_{\mathrm{a},l}\theta_{\mathrm{a},m} + \sum_{j=0}^{n_\mathrm{o}} W_{i,j}\,C'_{\mathrm{o},j}\end{aligned} \tag{2.21}$$

where $s_{B,\mathrm{o}} = \sigma_B f_0^5 L^6/(\gamma_\mathrm{o} R^3)$ and $s_{B,\mathrm{a}} = 16\varepsilon_\mathrm{a}\sigma_B f_0^5 L^6/(\gamma_\mathrm{o} R^3)$, and the tensors represent the following inner products

$$\begin{aligned}U_{i,j} &= \frac{n}{2\pi^2}\int_0^\pi\int_0^{2\pi/n} \phi_i(x,y)\;\phi_j(x,y)\,\mathrm{d}x\,\mathrm{d}y \\ V_{i,j,k,l,m} &= \frac{n}{2\pi^2}\int_0^\pi\int_0^{2\pi/n} \phi_i(x,y)\;\phi_j(x,y)\;\phi_k(x,y)\;\phi_l(x,y)\;\phi_m(x,y)\,\mathrm{d}x\,\mathrm{d}y \\ Z_{i,j,k,l,m} &= \frac{n}{2\pi^2}\int_0^\pi\int_0^{2\pi/n} \phi_i(x,y)\;F_j(x,y)\;F_k(x,y)\;F_l(x,y)\;F_m(x,y)\,\mathrm{d}x\,\mathrm{d}y\end{aligned} \tag{2.22}$$

Dynamic Equilibria Version

They dynamic equilibria version allows the same linearisation as in the original model, but allows the zero order reference temperature to be dynamic in time. The reference temperatures $T_{\mathrm{a},0}$ and $T_{\mathrm{o},0}$ are spatially uniform in space, but can alter with time. This differs to the original version, where these reference temperatures were also fixed in time.

For this model version, we take the temperature equations, as shown in Equation 2.20 and 2.21, and linearise the quartic terms in the longwave radiation terms by setting the indices j, k, and l to zero, hence dropping the higher-order dependencies in the perturbations. The dynamic equilibria equation for the atmospheric temperature, or baroclinic streamfunctions is therefore given by

$$\begin{aligned}\frac{\sigma}{2}\sum_{j=1}^{n_\mathrm{a}} a_{i,j}\,\dot{\theta}_{\mathrm{a},j} - \sum_{j=0}^{n_\mathrm{a}} u_{i,j}\,\dot{\theta}_{\mathrm{a},j} = \frac{\sigma}{2}\Bigg\{ &- \sum_{j,m=1}^{n_\mathrm{a}} b_{i,j,m}\,(\psi_{\mathrm{a},j}\,\theta_{\mathrm{a},m} + \theta_{\mathrm{a},j}\,\psi_{\mathrm{a},m}) \\ &- \beta\sum_{j=1}^{n_\mathrm{a}} c_{i,j}\,\theta_{\mathrm{a},j} + \frac{k_d}{2}\sum_{j=1}^{n_\mathrm{a}} a_{i,j}\,(\psi_{\mathrm{a},j} - \theta_{\mathrm{a},j}) \\ &- \frac{k_d}{2}\sum_{j=1}^{n_\mathrm{o}} d_{i,j}\,\psi_{\mathrm{o},j} - 2\,k_d'\sum_{j=1}^{n_\mathrm{a}} a_{i,j}\,\theta_{\mathrm{a},j}\Bigg\} \\ + \Bigg\{ &\sum_{j,k=1}^{n_\mathrm{a}} g_{i,j,m}\,\psi_{\mathrm{a},j}\,\theta_{\mathrm{a},m} + \lambda_\mathrm{a}'\sum_{j=0}^{n_\mathrm{a}} u_{i,j}\,\theta_{\mathrm{a},j} \\ &+ S_{B,\mathrm{a}}\sum_{m=0}^{n_\mathrm{a}} z_{i,0,0,0,m}\,\theta_{\mathrm{a},0}^3\theta_{\mathrm{a},m} \\ &- S_{B,\mathrm{o}}\sum_{m=0}^{n_\mathrm{o}} v_{i,0,0,0,m}\,T_{\mathrm{o},0}^3 T_{\mathrm{o},m} \\ &- \frac{\lambda_\mathrm{a}'}{2}\sum_{j=0}^{n_\mathrm{o}} s_{i,j}\,T_{\mathrm{o},j} - \sum_{j=0}^{n_\mathrm{a}} u_{i,j}\,C_{\mathrm{a},j}'\Bigg\}\end{aligned} \tag{2.23}$$

and similarly for the ocean temperature

$$\begin{aligned}\sum_{j=0}^{n_\mathrm{o}} U_{i,j}\,\dot{T}_{\mathrm{o},j} = &- \sum_{j,k=1}^{n_\mathrm{o}} O_{i,j,m}\,\psi_{\mathrm{o},j}\,T_{\mathrm{o},m} - \sum_{j=0}^{n_\mathrm{o}} \lambda_\mathrm{o}'\,U_{i,j}T_{\mathrm{o},j} \\ &- s_{B,\mathrm{o}}\sum_{m=0}^{n_\mathrm{o}} V_{i,0,0,0,m}\,T_{\mathrm{o},0}^3 T_{\mathrm{o},m} + 2\lambda_\mathrm{o}'\sum_{j=0}^{n_\mathrm{a}} W_{i,j}\,\theta_{\mathrm{a},j} \\ &+ s_{B,\mathrm{a}}\sum_{m=0}^{n_\mathrm{a}} Z_{i,0,0,0,m}\,\theta_{\mathrm{a},0}^3\theta_{\mathrm{a},m} + \sum_{j=0}^{n_\mathrm{o}} W_{i,j}\,C_{\mathrm{o},j}'\end{aligned} \tag{2.24}$$

More information about how these modifications were made can be found in the model manual [Demaeyer et al., 2022].

2.6 Symbolic qgs

The qgs model introduced in this chapter originally was a purely numerical model, meaning that once the parameters were set and the model equations were built the only way to tweak the parameters was to re-build the equations from scratch. This meant that continuation or ramping experiments was not possible. To overcome this limitation we developed the symbolic qgs model, using the symbolic python library SymPy [Meurer et al., 2017a]. This required restructuring the code base to allow for the calculation of the inner products, the building of the tensor, the subsequent tensor contraction, and finally the construction of the model equations from the contracted tensor, all in symbolic python. As all the variables

are now held as a symbolic python object, it now allows for the model equations to be built in any programming language, thus opening the door for the qgs framework to feed into FORTRAN or julia workflows. This work facilitated the majority of follow on work for this thesis, as the model equations and the model Jacobian were required with the option to vary any parameter for calculating UPOs, and using continuation software.

As part of this thesis we introduce a significantly modified version of the qgs framework, which uses a symbolic Python library (SymPy) to return the model equations including parameter values [Meurer et al., 2017b]. This is instead of fixing the numerical values of parameters, as was the case in the original framework, when the equations of the model are generated. The modified qgs framework (qgs v1.0) provides two key improvements over the previous version. The first is that selected parameters can now be left as an undefined variable [Meurer et al., 2017b] when generating the model tendencies, i.e. the model tendencies become a function of the selected parameters (in addition to being a function of the state space). Second, the model equations can now be returned in any desired programming language. Combined together, these two features allowed us to create a pipeline that directly feeds the model equations into continuation software to study the dynamics of the model. This version was developed as part of the work presented in Chapter 3.

3

Using Unstable Periodic Orbits to Understand Blocking Behaviour in a Low Order Land-Atmosphere Model

---

This chapter is based on the following paper, published in Chaos:

Oisín Hamilton, Jonathan Demaeyer, Michel Crucifix, Stéphane Vannitsem (2025) Using unstable periodic orbits to understand blocking behavior in a low order land–atmosphere model. *Chaos*, 35 (8): 083126. 10.1063/5.0268852

Abstract

Unstable Periodic Orbits (UPOs) were used to identify regimes, and transitions between regimes, in a reduced-order coupled atmosphere-land spectral model. In this paper we describe how the chaotic attractor of this model was clustered using the numerically derived set of UPOs. Using continuation software, the origin of these clusters were also investigated. The flow of model trajectories can be approximated using UPOs, a concept known as shadowing. Here we extend that idea to look at the number of times a UPO shadows

a model trajectory over a fixed time period, which we call cumulative shadowing. This concept was used to identify sets of UPOs that describe different life cycles of each cluster. The different regions of the attractor that were identified in the current work, and the transitions between these regions, are linked to specific atmospheric features known as atmospheric blocks.

Atmospheric blocking describes particular weather patterns that can cause prolonged extreme weather, such as heat waves or cold spells, in the midlatitudes. Currently, the physical mechanisms behind atmospheric blocking are not fully understood. In this paper, we study atmospheric blocking events - specifically their onset and decay - using a simple climate model. Such models can play a useful role in identifying the key physical behaviours that lead to blocking.

In this model, specific regimes in state space correspond to different atmospheric blocking conditions. We focus on solutions of the system that can explain why these regimes exist in the chaotic attractor. These solutions are known as unstable periodic orbits (UPOs), which are densely distributed in the chaotic attractor. This means that any trajectory is finitely close to a UPO at any given time. UPOs, therefore, provide a means of describing properties of the attractor and, by extension, the model climate.

In this paper, we use UPOs to classify the regimes in the model climate and to identify the transitions between them. We then link these regimes and transitions to specific blocking patterns in the model, showing that persistent visits of the trajectory to regions of state space associated with blocking events occur through well-defined channels. The resulting behaviour in the model climate indicates that the onset and decay of persistent blocks produce predictable weather patterns. We also show that UPOs can serve as a simple early warning indicator for the onset and decay of such persistent blocking events.

3.1 Introduction

The atmosphere, while characterised by chaotic behaviour, can exhibit some level of repetition over time spans of weeks or months [Holton, 2004]. This quasi repeating behaviour is called Low Frequency Variability (LFV). One example of LFV is midlatitude atmospheric blocking (from here referred to as blocks or blocking). Blocking causes the jet stream to be deflected, and in the midlatitudes this deflects the eastward moving low pressure systems, while the area in the trough of the deflection experiences persistent weather [Boyd, 2015]. This usually leads to heat waves and cold snaps in the midlatitudes. Heat waves are responsible for tens of thousands of excess deaths across the midlatitudes [Ballester et al., 2023; Vautard et al., 2023], and numerical weather prediction methods still struggle with predicting the onset and decay of such events [Davini and D'Andrea, 2020]. This is believed to be caused by missing subgrid processes and regional specific features, but there

is still no clear consensus on the exact key physical processes that cause blocking [Badza and Froyland, 2024; Pinheiro et al., 2019; Tibaldi and Molteni, 2018].

Climate change will increase the intensity, frequency, and duration of heat waves [Intergovernmental Panel On Climate Change (IPCC), 2023]. However, it is not clear what the impact of climate change will be on blocking events [Kautz et al., 2022; Davini and D'Andrea, 2020; Nabizadeh et al., 2019; Tibaldi and Molteni, 2018]. This is due to the lack of a comprehensive theory of blocking [Woollings et al., 2018] and because climate change is expected to alter the magnitude of baroclinic instability at different levels of the atmosphere [Shaw, 2019], resulting in opposing influences on the atmospheric circulation [Shaw et al., 2016; Shaw and Voigt, 2015]. Therefore, to fully understand the nature of blocking, it should also be studied from a conceptual point of view.

One way to tackle this problem conceptually is to use reduced order models to look at new approaches to describe and predict the dynamical properties of the atmosphere. This is the core concept of "bottom-up" analysis, which tries to identify fundamental dynamical mechanisms from fluid mechanics, thermodynamics, and dynamical system theory. Low-order models build upon a minimal set of key physical ingredients believed to be at the origin of the mechanisms of interest. They can, therefore, act as a testing ground to investigate new concepts for understanding and predicting LFV (see Vautard and Legras [1988]; Mak [1989]; Nauw and Dijkstra [2001]; Vannitsem et al. [2015, 2021] for some examples). These models provide a cheap and flexible platform upon which to test concepts, and can be simple enough to understand the underlying dynamics which produce the climatological behaviour. Once such behaviour is understood, the aim is to then test whether similar behaviour exists in more complex models, and whether the same dynamical processes are present. Thus, helping isolate and understand the key dynamical processes in the governing equations [Maher et al., 2019; Randall et al., 2007].

Consistent with this strategy, we aim study the onset and decay of blockings from a dynamical systems perspective, by using the qgs (quasi-geostrophic spectral) model framework [Demaeyer et al., 2020], which we describe below. Our objective is to link features of the state space of the attractor, to the climatology of the model, with the aim of then describing the atmospheric behaviour that we see from the dynamics of the model.

Weather regimes and LFV have been studied from a dynamical systems perspective in low order models since the early days of numerical weather prediction [Lorenz, 1963b; Veronis, 1963]. However, caution needs to be taken when interpreting results from low order models. On top of the obvious fact that these models only reproduce select behaviour of the real atmosphere, they can also be highly susceptible to which wave modes (or model resolution) are included. This means that the resulting chaotic attractor, and in turn repeating behaviour in the attractor, can differ wildly [Cehelsky and Tung, 1987]. Convergence of the structure of the attractor with model resolution should therefore be checked [De Cruz et al., 2016b].

Work on reduced order models led to the hypothesis that persistent weather phenomena, and different weather regimes, could be explained by proximity of the trajectory to

different fixed points with differing stability properties [Charney and DeVore, 1979; Charney and Straus, 1980; Reinhold and Pierrehumbert, 1982]. These fixed points correspond to different weather regimes, and as the trajectory is attracted to particular fixed points, the trajectory may remain in these regimes for some time before the unstable manifold repels the trajectory, and it continues its path on the chaotic attractor. The idea has since been expanded to look at areas of periodically repeating behaviour [Kazantsev, 1998], and other regions of quasi-stationary, or very slowly altering behaviour [Badza and Froyland, 2024]. Our aim is to better understand how trajectories evolve through these systems, and how parameter changes will alter the chaotic attractor. These questions can be addressed using periodic orbit theory, which considers the periodic orbits of a dynamical system as building blocks of its attractor, helping to construct a skeleton of the dynamics [Cvitanović et al., 2020].

It was conjectured by Poincaré in the 19th century that chaotic systems could be approximated by periodic motions that are densely distributed within the attractor [Birkhoff, 1927]. Unstable Periodic Orbits (UPOs) are closed loops in state space that provide a kind of topological invariant characterisation of the attractor [Cvitanović, 1988]. This means that they preserve topological relations between periodic orbits, such as their relative interwindings, allowing for at least a partial organisation of the state space. The use of these orbits to investigate the state space has since been called periodic orbit theory [Cvitanović et al., 2020], and has been used in a wide range of fields to help describe properties of the attractor [Grebogi et al., 1988; Pughe-Sanford et al., 2023; Crane et al., 2025], in particular, in the study of turbulent flows [Sasaki et al., 2021; Chandler and Kerswell, 2013; Kreilos and Eckhardt, 2012; Kawahara et al., 2006; Kawahara and Kida, 2001; Kato and Yamada, 2003].

Though numerically finding all of the UPOs in the chaotic attractor of a system is impossible, as they form a dense set, it has been found that usually a limited number of them - likely of low period [Hunt and Ott, 1996a,b] - can be used to describe the predominant behaviour of the system. In simple systems Maiocchi et al. [2022] found that UPOs could help predict transitions between wings of the Lorenz 1963 attractor, among other important stability properties of the attractor. This work was expanded to the Lorenz 96 model in Maiocchi et al. [2024], where the authors suggest that Lyapunov analysis should be complimented with the use of UPOs to provide a global picture of the attractor.

UPOs have also been used in reduced order models of the climate. Using a barotropic ocean model Kazantsev [1998] found that, even with only a few low order UPOs, some key properties of the attractor, such as the PDF of model trajectories, could be predicted. This work was built on by Selten and Branstator [2004], using the Lorenz 84 model, who found that particular transition paths exist between weather regimes, and they hypothesis that the cycle seen in the weather patterns corresponds to a particular periodic orbit. Later Gritsun [2013], using a more realistic barotropic atmosphere model, found that the most common paths of trajectories could also be explained in terms of particular orbits.

Kazantsev [2001] investigated the impact of forcing on the model, by analysing the impact of the forcing on a small set of UPOs ($\sim 20 - 30$). This method allowed them to find

the magnitude of forcing that caused the largest change in the averaged dynamics, allowing them to identify which forcings would have the largest impact on the climate of the model. Gritsun [2008], using a barotropic atmosphere model, attempted to use UPOs to calculate the response of the system to small external forcings. They concluded that the method could be utilised for understanding local sensitivity on specific orbits, but likely cannot be used to understand the global behaviour. This is a result of the computational cost in finding the UPOs, and the fact that it is impossible to know in more complex systems if all UPOs up to a period of T have been found.

Lucarini and Gritsun [2019] extended the approach of using UPOs to structure the state space in an intermediate complexity model. They found that blockings occur when the model trajectory is in the neighbourhood of a particular set of UPOs, and that these UPOs generally have higher instability compared to the set of UPOs that describe zonal flows. This result could explain the local instability associated with blocking events. However, these promising results from periodic orbit theory become challenging to use in high Lyapunov dimensional systems (or the Kaplan-Yorke dimension) [Crane et al., 2025]. Therefore the requirement for the orbits to be closed has been relaxed in some studies and extended to quasi recurrent patterns in the attractor [Badza and Froyland, 2024].

In this paper we use UPOs to provide an explanation to the structure of the chaotic attractor of a reduced-order land-atmosphere model, and explain the persistence seen in different parts of the attractor. We use the UPOs to also define transition regions in the attractor. The onset and decay of blockings is also investigated to see whether collections of UPOs can be used to identify these events. In Section 3.2.1 we introduce the model used, and then discuss, in Section 3.2.3, how we numerically found the UPOs. In Section 3.3.2 we describe the UPOs found in the model and how they appear to centre around two clusters, then in Section 3.3.3 we describe the origin of these clusters for certain parameter values. In Section 3.3.4 we describe how we use the UPOs to cluster the attractor, the transitions between these clusters (Section 3.3.5), and lastly how we can use the UPOs to predict transitions (Section 3.3.6).

3.2 Methods

3.2.1 Model

This chapter uses the land-atmosphere model, introduced in Section 2.4, as well as the symbolic equation building pipeline, that we discussed in Section 2.6. The resulting equations track the barotropic and baroclinic streamfunctions $\psi_{\mathrm{a},\,i}$ and $\theta_{\mathrm{a},\,i}$, and the ground temperatures $\delta T_{\mathrm{g},\,i}$, projected on the basis functions F_i. In this chapter we configure the model as described in Xavier et al. [2024], where we set the model resolution to be of wavenumber 2 in the x and y direction, resulting in 10 basis functions. The land and atmosphere use the same basis. The key parameter values used are given in Table 3.1.

Zonal flow corresponds to times when the flow is directed from west to east. The atmosphere is considered blocked where a high amplitude ridge exists either to windward

or leeward of the idealised orography, which is analogous to blocking patterns seen in the North Pacific [Ghil et al., 2019]. Here, the orography is modelled as a mountain and valley, using the $F_2 = 2\cos(nx)\sin(y)$ mode, where the resulting orography profile is shown in Figure 3.9. As in Charney and DeVore [1979], specific barotropic streamfunction modes can provide a description to determine the atmospheric state of the atmosphere. Blocking in the atmosphere, or the presence of a large amplitude wave, points towards an east-west orientated double gyre in the barotropic streamfunctions. Given the highly truncated nature of this model, this points towards high amplitudes of the barotropic modes $\psi_{\mathrm{a},\,2}$ and/or $\psi_{\mathrm{a},\,3}$, which correspond to modes F_2 and $F_3 = 2\sin(nx)\sin(y)$. On the other hand, zonal flow is expected to have low magnitudes over these modes.

Further information, on the bifurcation structure of the fixed points and sensitivity to model properties can be found in Li et al. [2018]. For further information on predictability of the different regimes for altering parameter values see Xavier et al. [2024].

3.2.2 Lyapunov Analysis

To analyse the stability properties of the chaotic attractor, we have calculated the Lyapunov exponents of the system. In this study we calculate the backwards Lyapunov exponents, using QR factorisation of the tangent linear propagator [Kuptsov and Parlitz, 2012], or orthogonalisation, as discussed in Section 1.5.2, and in Appendix A.4.

The instantaneous Lyapunov horizon can be used to understand the regions of the state space that display greater levels of predictability, compared with the remainder of the chaotic attractor. The instantaneous Lyapunov horizon is calculated by taking the inverse of the instantaneous Lyapunov exponent, and is therefore measured in units of time. The Kaplan-Yorke dimension [Kaplan and Yorke, 1979] measures the dimension of the chaotic attractor. Here we define an instantaneous (or local) Kaplan-Yorke dimension as $D = j + \sum_{i=1}^{j} \tilde{\lambda}_i / |\tilde{\lambda}_{j+1}|$ where j is the largest index, such that $\sum_{i=1}^{j} \tilde{\lambda}_i > 0$. The dimension of the attractor provides information about the number of expanding dimensions, and thus provides a way of quantitatively characterising the stretching and contracting regions of state space [Kuznetsov, 2012].

3.2.3 Numerically Finding UPOs

In this chapter we have used two methods for finding UPOs: the Newton-Raphson method, as described in Section 1.6.2 and Appendix A.5, as well as the continuation software AUTO [Doedel and Oldeman, 2012]. The Newton-Raphson method [Mestel and Percival, 1987; Parker and Chua, 1989] aims to solve the equation $S^t(\mathbf{x}_0) = \mathbf{x}_0$, where the unknowns are the starting location in state space ($\mathbf{x}_0$), and the time t. Following Gritsun [2008] we have used the second order tensor method, which aids in finding UPOs in this system where there are a large number of close to zero Lyapunov exponents [Gritsun, 2010]. In this case, due to unstable dimensions variability [Kostelich et al., 1997], or a breakdown in hyperbolicity, the region of convergence can be very small and the second

Parameter	Value	Description
ε_{a}	0.76 [non dim]	Atmospheric emissivity
k_d	0.085 [non dim]	Friction between the atmosphere and the ground
$k_d^{'}$	0.02 [non dim]	Internal friction between the two layers of the atmosphere
$C_{\mathrm{g},1}$	$300\mathrm{Wm}^{-2}$	North-south gradient of solar forcing on ground
$C_{\mathrm{a},1}$	$\frac{4}{10}C_{\mathrm{g},1}\mathrm{Wm}^{-2}$	North-south gradient of solar forcing on atmosphere
γ_{a}	$1 \times 10^7 \mathrm{Jm}^{-2}\mathrm{K}^{-1}$	Heat capacity of atmosphere
γ_{g}	$1.6 \times 10^7 \mathrm{Jm}^{-2}\mathrm{K}^{-1}$	Heat capacity of ground
λ	$10\mathrm{Wm}^{-2}\mathrm{K}^{-1}$	Sensible and turbulent heat transfer
σ_{B}	$5.67 \times 10^{-8} \mathrm{Jm}^{-2}\mathrm{s}^{-1}\mathrm{K}^{-4}$	Stefan-Boltzmann constant
σ	0.2 [non dim]	Static stability of the atmosphere
n	1.3 [non dim]	Aspect ratio $(n = 2L_y/L_x)$
f_0	$1.032 \times 10^4 \mathrm{s}^{-1}$	Coriolis parameter
β	$1.3594 \times 10^{-11} \mathrm{m}^{-1}\,\mathrm{s}^{-1}$	$2\mathbf{\Omega}\cos(\phi_0)/a$ (ϕ_0: reference latitude, a: radius of the Earth)
Δp	$500\mathrm{hPa}$	Difference in pressure between the two layers

Table 3.1: Unless otherwise stated, the model is set with the above parameter values.

order method, though approximately 10 times more computationally expensive, can aid with finding UPOs [Crofts and Davidchack, 2009] in these circumstances.

We also used the software AUTO to find UPOs via continuation across parameters. This software was chosen for its extensive track record for bifurcation analysis in relatively high dimensional systems, but several other suitable continuation software options are available (for example Veltz [2020]; Clewley et al. [2007]). This was done by first numerically finding the fixed points of the model. We tracked these fixed points for several key parameter values. At any Hopf bifurcation points we then branched and followed the periodic orbit branches. We continued to follow branches at branching points or period doubling from these periodic branches. This process was done for up to 50 branches deep. This process was aided by the auto-AUTO Python package [Demaeyer and Hamilton, 2025]. This package acts as a layer on top of AUTO, and automates the branching and identifies which branches to follow.

3.3 Results

3.3.1 Model Behaviour

The model climate displays both zonal, as well as blocked weather regimes. These differing weather regimes occur quasi-periodically, as the trajectory travels around the single attractor. The blocked regimes consist of two distinct behaviours, one where the blocking occurs to windward of the orography, and the other to leeward. The model is chaotic, and has three positive Lyapunov exponents (Figure 3.1a), but is dissipative with large negative exponents. There exists a plateau of close to zero Lyapunov exponents, likely resulting from the longer timescales in the ground heat capacity, compared with the atmosphere [Xavier et al., 2024]. This plateau results in regions of the attractor that display significant differences in instantaneous Kaplan-Yorke dimension. This, along with information about the the instantaneous Lyapunov exponents, shows that regions of the chaotic attractor display differing rates of convergence and divergence, and as a result, persistence.

There are particular projections of the 30 dimensional state space that make intuitive sense for studying atmospheric blocking regimes. As discussed in Section 3.2.1, we are interested in the magnitudes of the barotropic streamfunctions $(\psi_{\mathrm{a},\,2},\ \psi_{\mathrm{a},\,3})$. By analysing the climatology of the model, we found that there is a temperature anomaly in the ground, which displays a low frequency variability, moving from east to west with a quasi periodic behaviour. This anomaly results in, on average, a greater level of blocking in the region of the atmosphere above the temperature anomaly. This can be tracked by observing the magnitude of the variable $\delta T_{\mathrm{g},\,3}$. When the temperature anomaly transitions from one side of the domain to another, the atmosphere can display zonal atmospheric behaviour, or transitions between leeward and windward blocking regimes. A projection on the variables $(\psi_{\mathrm{a},\,2}, \psi_{\mathrm{a},\,1})$ has been used before for studying similar baroclinic two layer atmospheres [Reinhold and Pierrehumbert, 1982]. This projection identifies particular large magnitude barotropic streamfunction that correspond to blocking systems. However, this projection does not cleanly present the low frequency variability in the ground tempera-

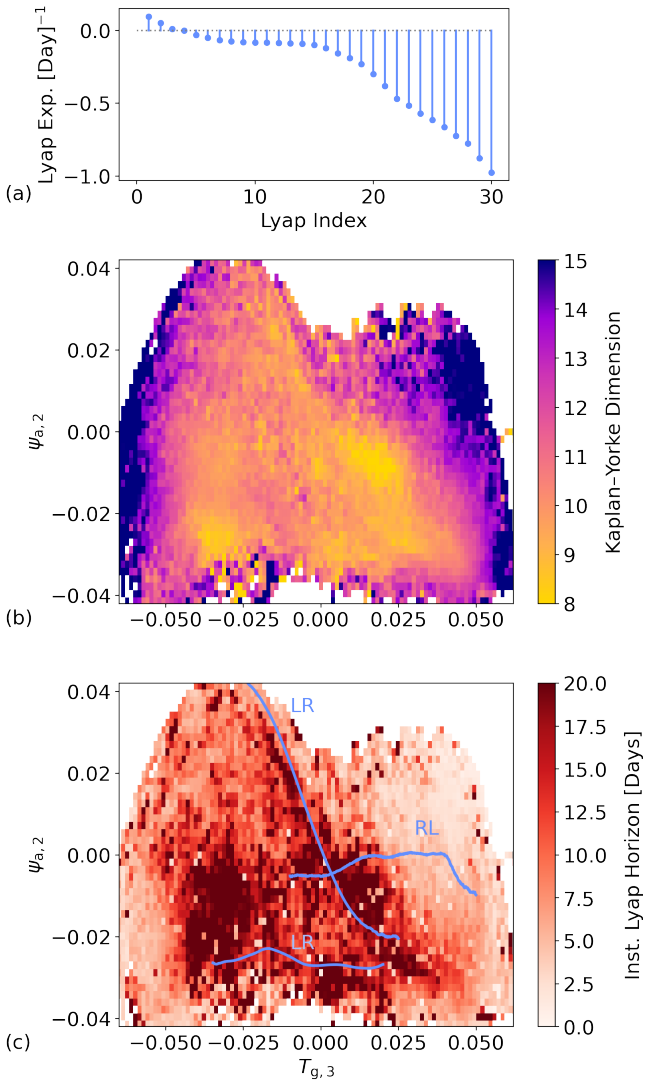


Figure 3.1: Lyapunov analysis of the chaotic attractor. Subplot a: The Lyapunov spectra. Subplot b: Instantaneous Kaplan-Yorke dimension. Subplot c: Binned instantaneous Lyapunov horizon, or the inverse of the binned instantaneous Lyapunov exponents, averaged over each pixel. The averaged transition trajectories (see Section 3.3.5) are shown, with two transitions from the left to right cluster (LR) and one from right to left (RL).

ture. When the chaotic attractor is projected onto the variables $(\delta T_{\mathrm{g},\,3}, \psi_{\mathrm{a},\,2})$, shown in Figure 3.2a, two main clusters are visually present. The clusters seen on the left and right designate regions where averaged behaviour displays, on average, atmospheric blocking behaviour, driven by the orography and the temperature in the ground. Lastly, we also analysed the results using the projection $(\delta T_{\mathrm{g},\,3}, \psi_{\mathrm{a},\,1})$, and while we found the same two distinct clusters, the transitions between these clusters could not be as cleanly disentangled.

3.3.2 Key Unstable Periodic Orbits

We found 6818 UPOs in total, using the methods described in Section 3.2.3. These UPOs are primarily centred on top of the two dense clusters, designating a high temperature anomaly in the ground, which results in one of the two key weather regimes described above. The Newton method primarily found UPOs in regions where model trajectories remain for extended time periods. This is likely due to adequate initial conditions being more probably to encounter. We could not find any UPOs that link the two central clusters. This is likely because such orbits would either have periods longer than the maximum searched for (set to 225 days as beyond this the algorithm converged extremely slowly), or either because no such orbits exist or they exist in a narrow band in space and period length making it difficult to find numerically.

In Figure 3.2b we show the projection of the UPOs that we found on the attractor. This shows how the UPOs appear to form dense sets over the dense areas in the attractor. It is expected that such numerical searches for UPOs will be biased towards short period UPOs, as long period UPOs are numerically more difficult to find [Cvitanović et al., 2020]. In our case, however, we have found a similar number of UPOs between periods of 4-100 days, as shown in Figure 3.2c. In addition, we see a large range in the largest Floquet exponent (Figure 3.2d), meaning that there is a large range in the stability properties of the clusters. This is clearly not a complete set of UPOs for these periods, and the skew in the period of the resulting UPOs found is likely due to the most common repeating cycles in the key variables $(\delta T_{\mathrm{g},\,3},\ \psi_{\mathrm{a},\,2})$. This is not unexpected, as the numerical method we employ is highly sensitive to the initial conditions used. In our case, the initial conditions were primarily found by looking for close recurrences in the trajectory, which in turn is driven by natural cycles in these variables.

3.3.3 Origin of Blocking Clusters

To understand why our model contains these two regimes, we undertook a bifurcation analysis of the model for varying k_d and $C_{\mathrm{g},1}$, as varying these parameters resulted in the finding of stable periodic solutions in the centre of these clusters, in the work by Xavier et al. [2024]. We have developed on this previous work by using AUTO [Doedel and Oldeman, 2012] to investigate the bifurcation structure that originates from these two stable windows. Figure 3.3 shows the bifurcation diagram as a function of k_d. The same analysis for altering $C_{\mathrm{g},1}$ is presented in Appendix B.2. These bifurcation diagrams were produced by numerically finding fixed points of the model and continuing along all branches, and following any subsequent branching points. We branched at any detected Hopf bifurcation points,

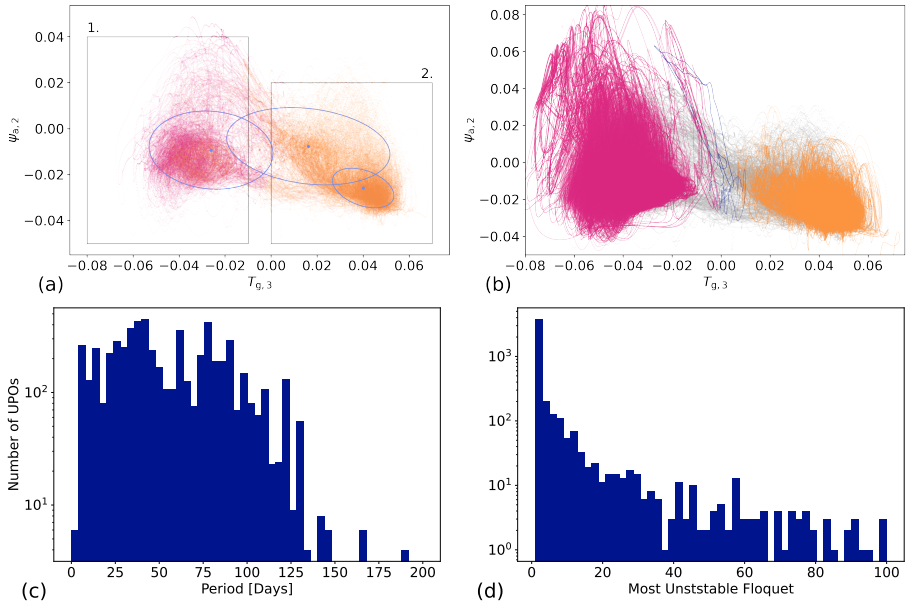


Figure 3.2: Key UPO properties, for all UPOs found. Subplot a) shows the chaotic attractor of the model, with points showing the time steps of a trajectory, where the two colours (pink and orange) show the clustering of the attractor using the distance from UPOs. The Gaussian mixture clustering clusters are shown in blue, calculated as described in Xavier et al. [2024]. In Appendix B.1 we present the climatology of the three centroids in Figure B.1. The grey inset boxes display the extends of $1)$: Figure 3.4, and $2)$: is shown in Appendix B.2 in Figure B.2. Subplot b) shows the UPOs projected on top of the attractor, again coloured based on the clusters. Subplot c) and d) show compiled information on the periods and largest Floquet exponents of the identified UPOs. The number of unstable dimensions of the collection of UPOs range between 1 and 6, pointing to violations of hyperbolicity [Maiocchi et al., 2024]. Subplot a) was modified from “Xavier, A K., Demaeyer, J., and Vannitsem, S., Variability and Predictability of a Reduced-Order Land–Atmosphere Coupled Model, Earth System Dynamics 15 (4), 893-912, 2024 [Xavier et al., 2024]; licensed under a Creative Commons Attribution (CC BY) license."

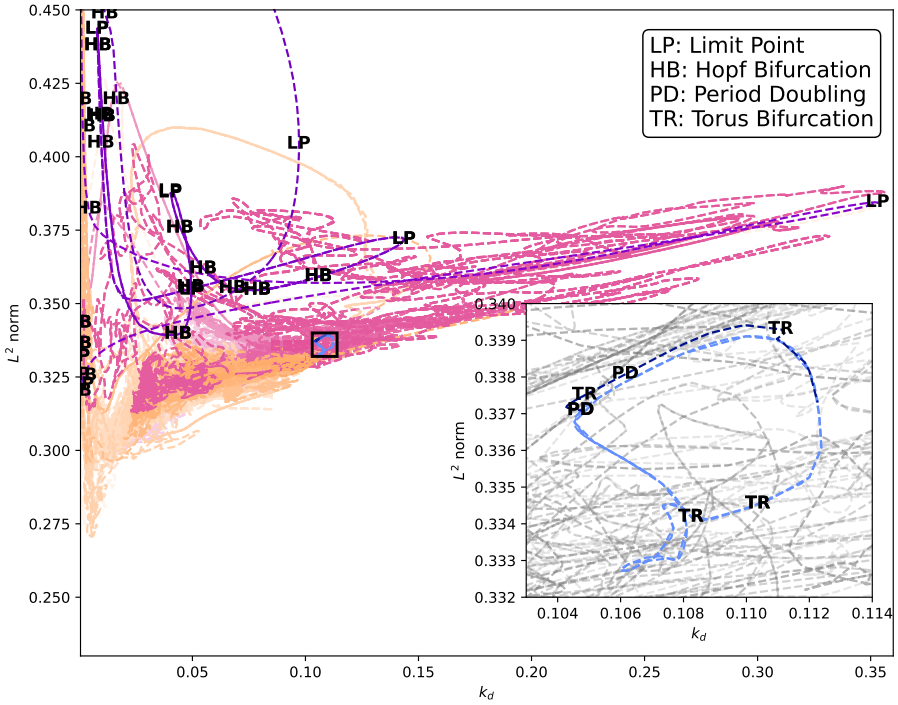


Figure 3.3: Bifurcation diagram of all fixed points (shown in purple) and the branching periodic orbits (shown in orange and pink to visualise the two separate clusters) of the model for varying k_d with a value of $C_{\mathrm{a},1} = 300\mathrm{W\,m^{-2}}$. Dotted lines represent unstable regions and solid lines represent stable regions. Bifurcation points are shown for the fixed points continuations. The black rectangle is zoomed in on and shown in the inset, and focuses on two key branches shown in blue. These two periodic branches were found by continuing periodic orbits that have a small window of stability. The light blue branch being stable at $k_d \approx 0.112$ and the dark blue at $k_d \approx 0.1045$.

again continuing along branches originating from periodic orbit branching points or period doubling bifurcations. This process was automated using the auto-AUTO package. Lastly, we also continued the periodic orbit branches, from the UPOs found numerically using the Newton-Raphson method, described in Section 3.2.3, and included these in the bifurcation diagram.

There exists a window, at approximately $k_d \approx 0.1045$, and $k_d \approx 0.115$, where periodic orbits living in the LHS cluster becomes stable. We used AUTO to track these orbits to investigate how they destabilise and whether they can give a hint at how chaos emerges.

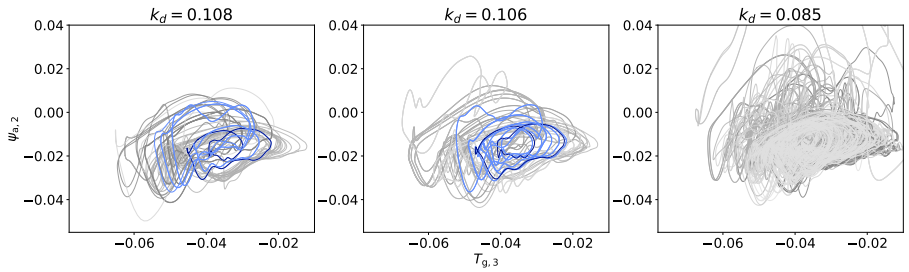


Figure 3.4: State space for variables ($\delta T_{\mathrm{g},3},\ \psi_{\mathrm{a},2}$), for decreasing values of k_d. The orbits shown in blues correspond to the branches shown in the inset plots in Figure 3.3. Grey orbits show the other branches found, that do not directly branch from the key orbits. On the left we show the parameter values where a stable orbit was found, we then decrease the parameter values to end up with the clusters, as shown in Figure 3.2b). Extents, relative to the entire attractor, are shown in Figure 3.2a).

In Figure 3.3 we show these regions of stability on the bifurcation diagram. The continuation parameter is plotted against the maximum L^2-norm. The L^2-norm ($|x_i| = \sqrt{\sum_j [\overline{S}_i^T]_j^2}$, where j is an index over the dimension) was chosen to retain continuity with previous studies [Vannitsem et al., 2015]. We see that there is a closed branch (shown in light blue) which goes through a period doubling bifurcation, and leads to another branch (shown in dark blue) that has a small window of stability before destabilising through a torus bifurcation. The bifurcation diagram shows that this structure has a similar value in L^2 norm space to the other periodic orbit branches. This means that while we cannot see how these key branches connect to the rest of the bifurcation diagram, we hypothesise that these branches originate from a torus bifurcation of another branch, a guess that is reinforced by the visual similarity between these orbits and other orbits that we found in this cluster.

In Figure 3.4 we show key UPOs, from the left hand cluster, for decreasing values of k_d. Two particular UPOs are coloured to match the colouring in the bifurcation diagram shown in Figure 3.3, all other periodic orbits are shown in grey. The blue UPOs appear to occupy the central section of the cluster defined by the UPOs, and we see that this structure remains even once the coloured periodic orbit branches go through a fold bifurcation and disappear for lower values of k_d. Similar analysis for the right hand side cluster is provided in Appendix B.2, with the bifurcation diagram for $C_{\mathrm{a},1}$ shown in Figure B.3 and the change in UPOs as a result of altering the value of this parameter shown in Figure B.2. This analysis shows that key branches provide a hint at the origin of the cluster dynamics that we find in this model.

3.3.4 Clustering the Attractor

In this study we use the UPOs to assign each point of a trajectory into the left and right hand clusters identified, and shown on Figure 3.2a). We are interested in doing this, as it provides a classification of whether we are in a windward or leeward blocking regime, and allows us to identify the onset and decay, or transitions, between these regimes. This is done by first splitting the UPOs into two clusters dependent on if they have positive or negative values of $\delta T_{\mathrm{g},\,3}$. More precisely, we analyse the maximum and minimum values of each UPO on the variable $\delta T_{\mathrm{g},\,3}$, which is the ground heat projected onto the mode $F_3 = 2\sin(nx)\sin(y)$

$$\text{LHS Cluster UPOs}: \; C^{\text{UPO}}_{\text{LHS}} = \{\overline{S}^T_i \; : \; \max_{\delta T_{\mathrm{g},\,3}} \overline{S}^T_i < 0, \; i \in I\}$$
$$\text{RHS Cluster UPOs}: \; C^{\text{UPO}}_{\text{RHS}} = \{\overline{S}^T_i \; : \; \min_{\delta T_{\mathrm{g},\,3}} \overline{S}^T_i > 0, \; i \in I\}$$

where $\overline{S}^T_i$ is a UPO with a period T, and an index i, and I is an indexing of all UPOs found. This results in 3425 UPOs in the left hand cluster, and 3361 on the right (32 UPOs do not fall into either cluster and are ignored). Next, for a given trajectory $S^t(\mathbf{x}_j)$ with initial condition $\mathbf{x}_j$, we cluster the points of the trajectory ($S^{t_k}(\mathbf{x}_j)$) by calculating which cluster the UPO, that is closest to the trajectory point, is a member of

$$\text{LHS Cluster Trajectory}: \; C^{S^t}_{\text{LHS}} = \{S^{t_k}(\mathbf{x}_j) : \min_{i\in I} \left\| S^{t_k}(\mathbf{x}_j) - \overline{S}^T_i \right\|, \; \overline{S}^T_i \in C^{\text{UPO}}_{\text{LHS}}\}$$
$$\text{RHS Cluster Trajectory}: \; C^{S^t}_{\text{RHS}} = \{S^{t_k}(\mathbf{x}_j) : \min_{i\in I} \left\| S^{t_k}(\mathbf{x}_j) - \overline{S}^T_i \right\|, \; \overline{S}^T_i \in C^{\text{UPO}}_{\text{RHS}}\}$$

$$\text{LHS Cluster Trajectory}: \; C^{S^t}_{\text{LHS}} = \{S^{t_k}(\mathbf{x}_j) : \min_{i\in I} \left\| S^{t_k}(\mathbf{x}_j) - \overline{S}^T_i \right\|, \; \overline{S}^T_i \in C^{\text{UPO}}_{\text{LHS}}\}$$
$$\text{RHS Cluster Trajectory}: \; C^{S^t}_{\text{RHS}} = \{S^{t_k}(\mathbf{x}_j) : \min_{i\in I} \left\| S^{t_k}(\mathbf{x}_j) - \overline{S}^T_i \right\|, \; \overline{S}^T_i \in C^{\text{UPO}}_{\text{RHS}}\}$$

where the notation $\|\cdot\|$ stands for the Euclidean norm.

The clustering is visualised by the color scheme (pink and orange) in Figure 3.2b). As we see, this is not as simple as just clustering the points of the trajectory by value of $\delta T_{\mathrm{g},\,3}$ as in other projections the UPOs are not neatly separated. We think this clustering method is optimal as the UPOs form a dense skeleton in dense region of the attractor, and by clustering on which UPO a trajectory point is closest to, it is expected that the UPO should provide some description as to the flow in that neighbourhood. Of course this approach is dependent on the number of UPOs found and how close the trajectory is to a given UPO. If few UPOs are found, the attractor is not described in any real detail and if the trajectory is far from a UPO then there is no reason to believe that the closest UPO will have any influence on the trajectory.

We expect that our approach is robust to the above concerns. It has been found in that a surprising low number of UPOs still provides reasonable results [Hunt and Ott, 1996a]. In our case there is clearly multiple distinct regimes within the single attractor [Xavier et al.,

2024], and the clusters found here overlap well with those found in this earlier study. We believe that our clustering method provides a cleaner method for isolating transitions as it is not a probabilistic clustering method and provides information influenced by the system dynamics. In addition, it provides a measure between a point of the trajectory and the cluster of UPOs that covers the dense regions of the attractor. This distance therefore provides a useful metric for identifying transitions, as well as providing information on how much we expect the cluster of UPOs to affect the behaviour of a trajectory.

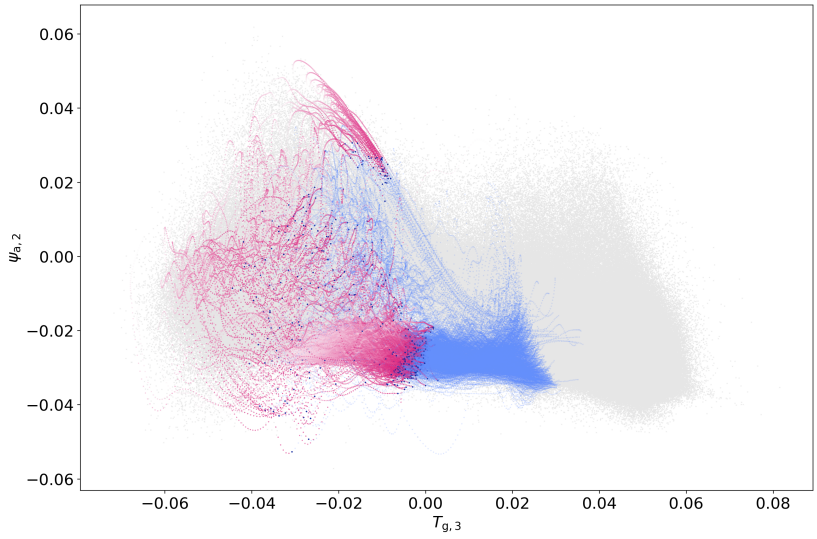
On average, trajectories in the pink regime of the attractor correspond to a windward blocking pattern in the atmosphere, which can be visualised in the first panel of Figure 3.9a, and the last panel of Figure 3.9c. The orange regime corresponds to leeward blockings, which can be see in the last panel of Figure 3.9a and the first panel of Figure 3.9c.

3.3.5 Transition paths

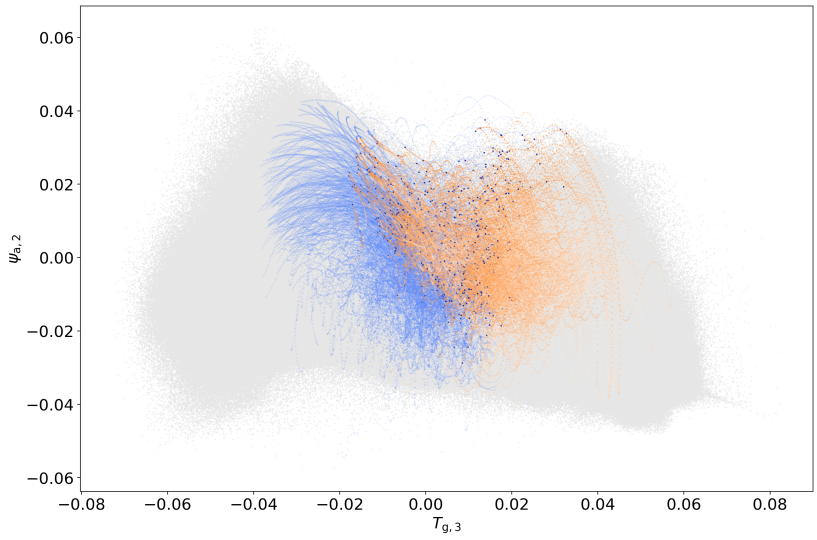
Transitions between the two regimes of the attractor occur through specific regions, or channels, of the state space, shown in Figures 3.5a and 3.5b. These transitions correspond to a shift in the ground temperature anomaly, and thus whether the climate displays windward or leeward blocking behaviour. The transitions are identified by the points in state space where a trajectory passes from one cluster to another, and by analysing the points on the trajectory that precede and follow the transition. To analyse the properties of these transitions we began by running a long trajectory, and then isolating the occurrences where a transition occurs. To ensure we are capturing transitions between the regimes we filter the points to ensure that a trajectory remained in one cluster for at least 56 days before, and 56 days in the other cluster after transitioning. This threshold is set to remove points that are in between the two sets of UPOs and are therefore not described well by our clustering method (approximately 0.07% of points).

By parametrising on $\delta T_{\mathrm{g},\,3}$ we created averaged transition trajectories to analyse the climatology of these paths. Transitions from the LHS (left hand side) to RHS cluster appear to pass through two regions, and the averaged trajectories shown are the transitions between two blocking regimes. This is primarily driven by the ground temperature anomaly shifting between the east and west. The transition in the lower portion of the attractor, shown in Figure 3.6a displays the blocking regime moving to the west, which can be seen in the model climatology shown in Figure 3.9a. The other left to right transition taking place in the upper part of the attractor (Figure 3.7a) shows the blocking regime moving to the east (Figure 3.9b).

Transitions from the RHS to LHS are not as clearly defined in state space (shown in Figure 3.5b), but the averaged transition (Figure 3.8a) shows that the transitions between the two blocking regimes result in averaged zonal behaviour in the atmosphere. This is not surprising as the transitions paths pass close to the Hadley circulation, or the origin. In Xavier et al. [2024] the zonal regime was identified as a separate cluster, but in our analysis we find that this atmospheric regime primarily occurs during transitions between the RHS cluster to the LHS cluster, as shown in Figure 3.9c. The difference between transitions types has been observed before by Grafke and Vanden-Eijnden [2019], who



(a)



(b)

Figure 3.5: Transitions from one cluster to the other, Figure 3.5a shows transitions from left to right, and Figure 3.5b from right to left. The trajectory is shown 11 days before the transition (in pink or orange, where the saturation increases towards the transition). The transition points are shown in navy blue, and the post transition trajectory is shown in light blue for 11 days after the transition.

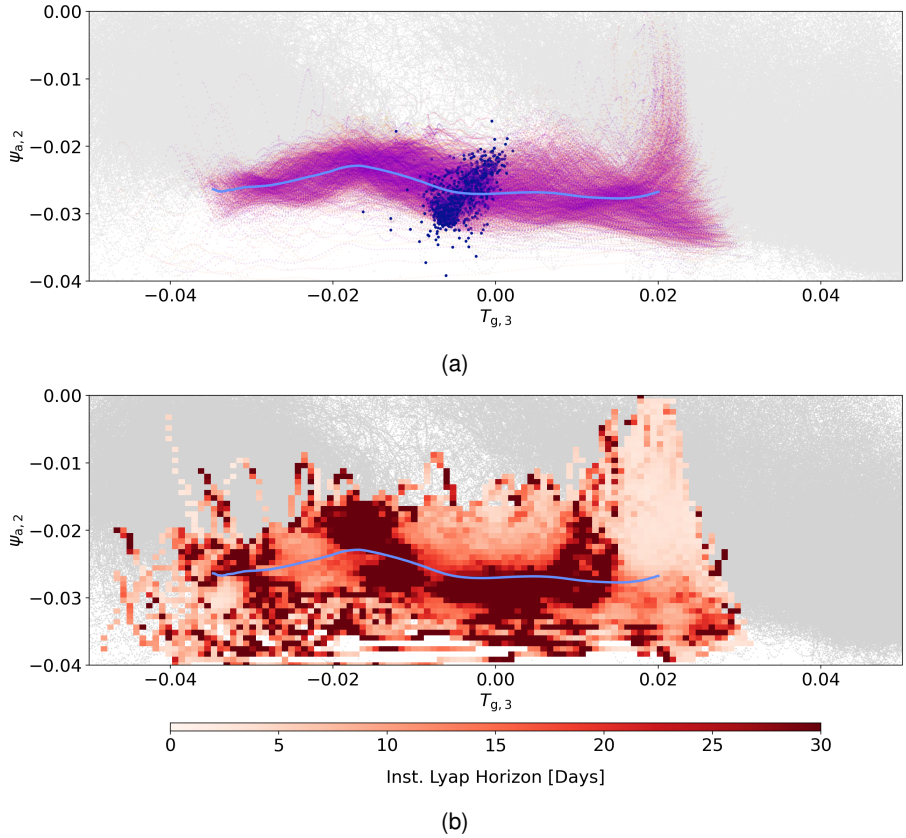


Figure 3.6: Left to right transitions, taking place in the lower section of the attractor. Figure 3.6a shows the filtered trajectories that transition from left to right in the lower portion of the attractor. The mean of these trajectories is shown in light blue. The transition points are shown in navy blue. Figure 3.6b displays the binned instantaneous Lyapunov horizon, calculated by taking the inverse of the binned instantaneous Lyapunov exponent.

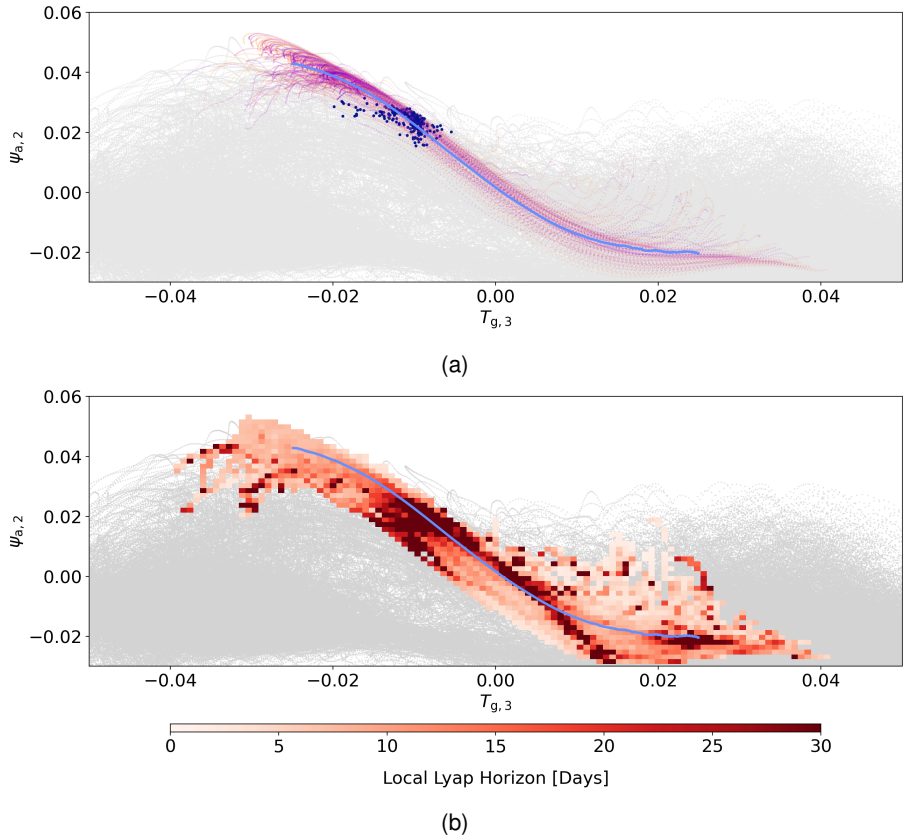
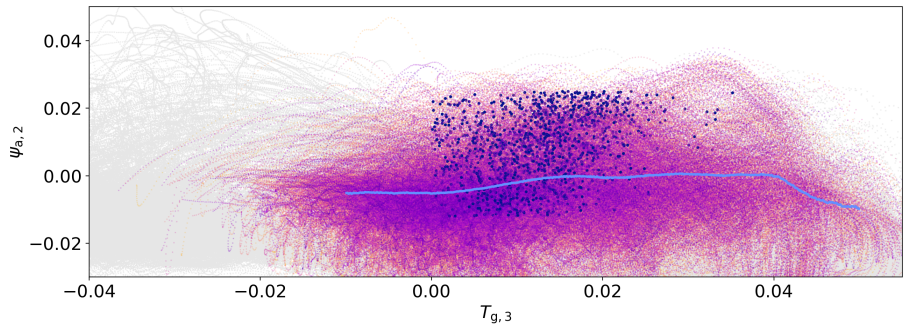
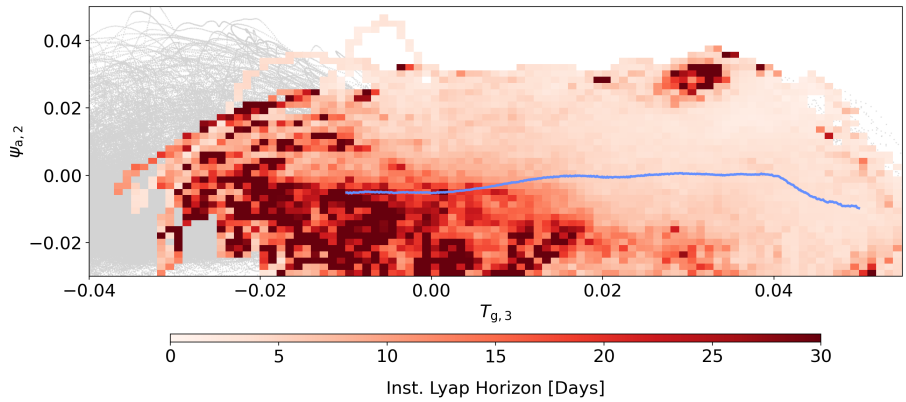


Figure 3.7: Upper left to right transition. Figure 3.7a shows the filtered trajectories that transition from left to right in the upper section of the attractor, shown in Figure 3.5a, with the same colour scheme. Figure 3.7b shows the same as Figure 3.6b, but again for the upper left to right transition.

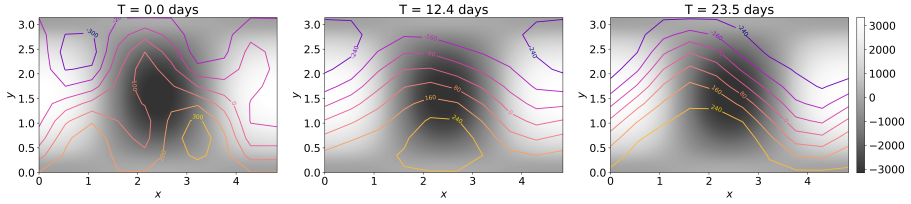


(a)

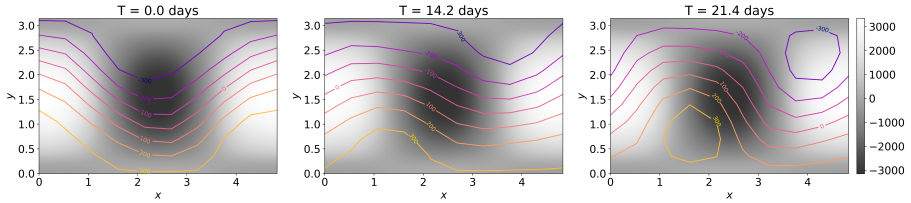


(b)

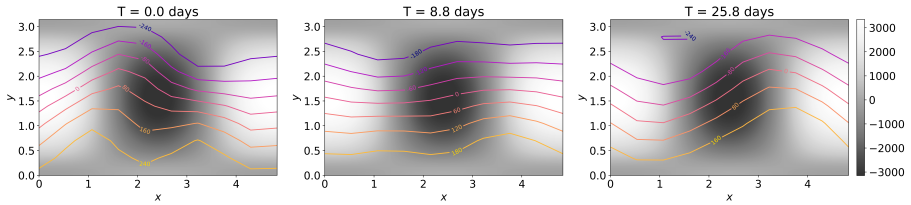
Figure 3.8: Right to left transition. Figure 3.8a shows filtered transition trajectories. The mean of these trajectories is shown in light blue. The transition points are shown in navy blue. Figure 3.8b displays the same as Figure 3.6b, but for the right to left transition.



(a) Transition from left to right in the lower portion of the attractor, shown in Figure 3.6a. Here the average blocking behaviour transitions from the windward side of the orography to the leeward side by travelling to the west.



(b) Transition from left to right in the upper portion of the attractor, shown in Figure 3.7. The blocking transitions from above the orography to the leeward side by travelling to the east.



(c) Transition from right to left, as in Figure 3.8a. Here the blocking moves from the leeward side of the orography to the windward side through zonal atmospheric behaviour.

Figure 3.9: Snap shots of the climatology of the averaged transition trajectories. The model time of each snap shot is shown in the title. The contours show the 500hPa height anomaly, and the greyscale shading shows the relative height of the orography in metres. The 500hPa height anomaly is commonly used to determine regions of blocking, as higher anomalies correspond to high pressure systems [Tibaldi and Molteni, 2018].

used an action minimisation algorithm to find the most likely noise induced transition paths between blocked and zonal states in the barotropic model of Charney and DeVore [1979]. They found that transitions from blocked to zonal, and zonal to blocked regimes are not merely the time-reversed forward transition, implying that time-reversal symmetry is broken and highlighting the nonequilibrium nature of the transition.

Finally, 55 percent of transitions between regimes do not occur through the regions described above. These transitions occur for trajectories that spend short time in a given regime (less than 56 days). These transitions do not appear to follow predictable behaviour and are probably due to the trajectory making diversions in other dimensions and the transitions only appear to occur due to the projection we make onto two dimensions.

The paths of the transitions were found to occur through relatively stable regions of the state space. This is shown in Figures 3.6b, 3.7b, 3.8b which show the Lyapunov horizon, calculated by taking the instantaneous Lyapunov exponent for each transition, binning the results in state space, and then taking the inverse of the results. This shows that while the onset of the transition occurs through an unstable region, once the trajectory begins transitioning from one regime to another, the path it takes, and therefore the atmospheric behaviour, is more predictable.

The transition paths identified in this study have qualitative similarities with transition channels seen in other systems with self induced switching behaviours. Ansmann et al. [2016] found that, in a network of diffusively coupled FitzHugh-Nagumo oscillators, switching between different dynamics was facilitated by channel-like structures on a chaotic saddle [Ansmann et al., 2013], and the opening of the channel can be studied by computing the stable and unstable manifolds of the fixed point associated with the mechanism of the emergence [Karnatak et al., 2014; Altmann et al., 2013]. In the context of climate models, similar channels have been found in paths of extreme events in an ENSO model [Ray et al., 2020].

3.3.6 UPO Shadowing

The trajectory moves between the two clusters, sometimes spending a long time in one regime (up to 1000 days in the RHS cluster and 600 days in the LHS), other times quickly returning back to the previous regime. Above, we showed that when a trajectory spends long times in one regime and then transitions to the other regime, it tends to pass through a well-defined region in the state space. We now look at which collection of UPOs the trajectory passes close to during its visit to a cluster. The idea being that if the transition path appears to be confined in state space, the trajectory must pass close to a specific set of UPOs while transitioning. As UPOs are dense in the attractor, the UPOs can provide an arbitrarily accurate approximation for a given trajectory [Maiocchi et al., 2022]. The idea of looking at UPOs close to the trajectory, to gain some understanding of the future path the trajectory will take, is referred to as UPO shadowing. In our case, we have only found a small selection of UPOs so the accuracy of any shadowing will be limited, but the idea remains the same; a UPO will shadow a trajectory if they are close to one another, and for some limited time the evolution of the trajectory is similar to that of the UPO.

More concretely, a UPO $\overline{S}_i^T$ shadows the trajectory at time t if it is the closest UPO, of all UPOs found, to the location of the trajectory at time t: $\min_{i \in I} \left\| \overline{S}_i^T - S^t(\mathbf{x}_j) \right\|$, where I is an index of all the UPOs. Here we are assuming that we can create an index of the UPOs as numerically we can only find a finite number of UPOs, the method of indexing the UPOs is arbitrary. We are interested in which UPO is the closest at a given time, so we define a function ind$(S^t(\mathbf{x}_j))$ which returns the index of the UPO, given the trajectory point $S^t(\mathbf{x}_j)$, where ind : $\mathbb{R}^n \to I$, and I is the indexing set of the UPOs.

We define the number of times that a given UPO shadows a trajectory over a set period of time, which we call cumulative shadowing (CS). This is done by counting the number of times a given UPO $\overline{S}_i^T$ shadowed the trajectory in the time range $(t_1,\ t_2)$, expressed as

$$\Omega(\overline{S}_i^T,\ t_1,\ t_2) = \sum_{t \in [t_1,\ t_2]} \delta\Big(i,\ \text{ind}(S^t(\mathbf{x}_0))\Big) \tag{3.1}$$

where δ is the Kronecker delta, and returns 1 if the closest UPO has index i, otherwise returns 0.

Looking at trajectories that spend long time periods (at least 110 days) in only one cluster, we found at least three distinct sets of UPOs: one where the the CS increases primarily when the trajectory first enters the cluster (called Pre-Blocking), another set where the CS mainly increases before a transition (called Transition), and a final set where the CS mainly increases in between entering and transitioning from the regime (called Blocking). We show these three distinct sets of UPOs for the LHS cluster in Figure 3.10. In this figure we also show the CS for each set of UPOs, during the time period just after a transition, and just before a transition. We see that there is a step change in the slope of the CS for the different sets, depending on the proximity to a transition. We present similar analysis for the RHS in Appendix B.3, in Figure B.4. We set a minimum time for the trajectory to spend in one cluster because, as we showed in Section 3.3.5, trajectories that do not spend enough time in either cluster tend to not transition through the specified regions, meaning that one cannot predict these transitions with only three groups of UPOs.

In Figure 3.11 we show three example time series of the trajectory, and the CS for each one. We see in these examples that before the transition there is a clear increase in the CS of the Transition set of UPOs, while the CS of the Blocking set plateaus. In addition, we show the CS of the Pre-Blocking set shows that largest increase before the trajectory settles onto the set of Blocking UPOs. This method is dependent on the trajectories travelling along the described channels in state space. Transitions of trajectories that do not remain in one cluster for long periods of time transition through other, less predictable, regions and this method cannot be used to provide a warning signal. In addition, depending on where the trajectory exits the cluster of UPOs, the early warning indicator provides more or less warning of the impending transition. An example of this can be seen in Figure 3.11, where the Transition set increases at a different number of days before the transition occurs, thus not providing a regular warning. Lastly, the accuracy of this method is dependent on the

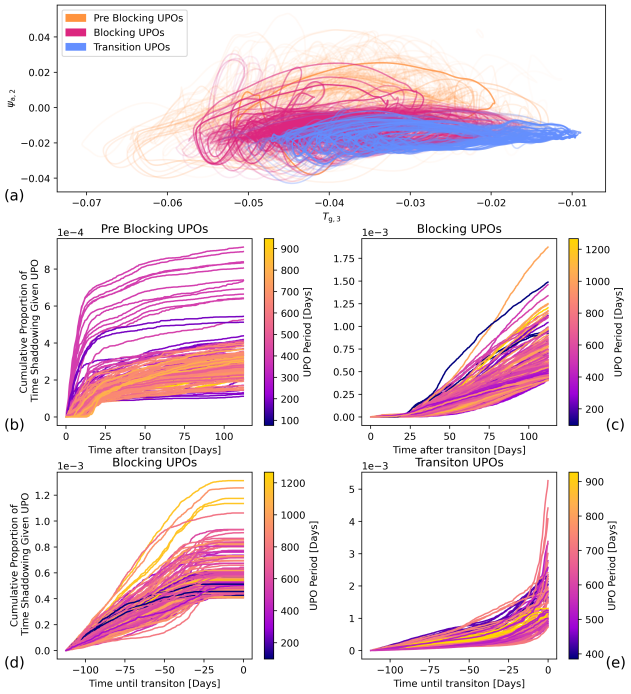


Figure 3.10: Figure (a) shows the three sets of UPOs, colour coded by which set they are in, the shade of the colour displays the magnitude of CS overall, with darker shades representing UPOs that are shadowed more frequently. (b) each curve represents a UPO, and the y-axis shows the proportion of time that the UPO shadows the trajectory. The shading is the UPO period, showing that there is a wide range in the period of the UPOs shadowing the trajectory. This subplot shows the CS of the UPOs in the Pre-Blocking set (those in orange in (a)), for the first 100 days of the time in the cluster, where we see that the CS increases mainly in the first 25 days. Subplot (c) is for the same time period as (b), but showing the CS of the Blocking set of UPOs, shown in pink in (a). Here we see that the CS increases relatively linearly after 25 days. Subplot (d) shows the CS of the set of Blocking UPOs for the final 100 days before transitioning. We see that the CS plateaus approximately 25 days before the transition. Finally, (e) shows the same as (d), but for the Transition set of UPOs, shown in blue in (a). Here we see that the transition is captured by the exponential increase in the CS.

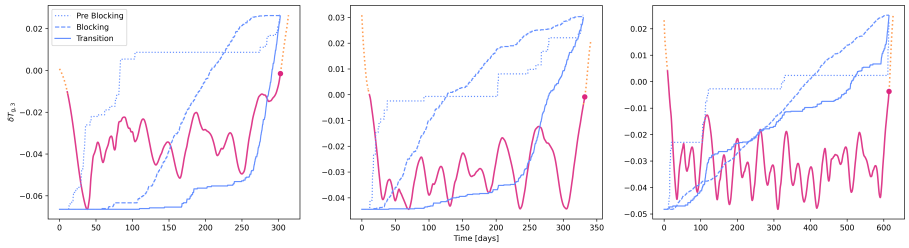


Figure 3.11: Examples of CS of three trajectories in the left hand cluster. A time series of $\delta T_{\mathrm{g},3}$ is shown in pink when in the left hand cluster and orange when in the other cluster, a dot is shown where this transitions to the RHS cluster. The blue lines are the sum of the individual cumulative shadowing curves presented in Figure 3.10b)-e). The solid blue line shows the CS of the transition set, the dashed line shows the CS of the set associated with blocking, and the dotted line shows the CS of the pre-blocking set. We see before the transition the blocking set flattens out, while the CS of the transition set begins to increase considerably. All three CS curves are normalised and scaled for visualisation purposes.

number of UPOs used, and it is possible that we are missing some orbits that would further improve the accuracy. Overall the proposed method of using CS could provide a useful early warning indicator for transitions between clusters of the attractor.

3.4 Conclusions

In this paper, identification of unstable periodic orbits and continuation methods were used to explain the dynamical behaviour of a reduced order land-atmosphere model. While the use of UPOs to characterise atmospheric blocking has been studied before [Gritsun, 2008; Lucarini and Gritsun, 2019], in both barotropic and baroclinic models, this study has built on this by using the UPOs to cluster the attractor into specific regions. These clusters were then used to identify transition regions, and link these with atmospheric behaviour.

The clusters in this model are of interest as they represent areas where the ground heat shows an anomaly in either the east or west regions of the domain. Through the heat transfers between the land and the atmosphere, this anomaly causes, on average, higher temperatures in the atmosphere, which can reinforce atmospheric blocking situations, that result from Rossby wave deflections induced by the orography.

This paper has also introduced a significant modification of the qgs framework [Demaeyer et al., 2020], which uses symbolic Python to construct the model equations. This modification allowed us to export the model equations in Julia (the language used for numerically finding the UPOs) and Fortran (formatted for using in the AUTO continuation software). In addition, it facilitated exporting certain parameter values as variables.

Through the use of continuation software we have also been able to provide a more comprehensive understanding of the origin of the structure of the attractor that lead to atmospheric blocking. We found the paths to chaos from two stable orbits (for parameter values found in Xavier et al. [2024]).

Finally, we explored the possibilities offered by the concept of shadowing of UPOs [Maiocchi et al., 2022] to define cumulative shadowing (CS), and identification of three sets of UPOs associated with different times of the blocking regime lifecycle. As the accuracy of numerical weather prediction's ability to forecast the onset and decay of atmospheric blocks still lags behind other features of the atmosphere, other methods that can forecast the onset or decay are of particular interest. While the approach that we used here is somewhat simplistic, we believe that proximity to particular UPOs or the rate of change of the CS could be useful as a training parameter in a machine learning, or more traditional forecasting approach, for forecasting transitions in state space.

Shadowing has been used with success in simple models to understand transitions [Maiocchi et al., 2024], and we believe that there is untapped potential to do similar for more complex models. In higher dimensional models, however, it could be more fruitful to analyse the shadowing of collections of UPOs rather than individual UPOs. This is because in higher dimensional systems we will usually have fewer UPOs to study, and there are a larger number of unstable directions that the trajectory could diverge from the UPO.

Future work is required to investigate if similar techniques to those shown in this paper can expand to more complex models that more accurately model atmospheric blocking. In addition with the increase of global temperatures, and the change in north-south temperature gradients as a result of anthropogenic climate change, such models and techniques could help understand how atmospheric blocking events will differ in the future, a topic that models and observations still differ largely on [Riboldi et al., 2020; Davini and D'Andrea, 2020].

4

Climate Change Forcings in a Reduced Order Coupled Atmosphere Model

4.1 Introduction

Climate change is expected to have impacts on the midlatitude jet stream and storm track [Shaw et al., 2024]. Even small changes to these features of the atmosphere could lead to widespread alterations in regional climates [Vallis et al., 2015]. There is also concern that climate change could lead to abrupt, irreversible changes in the climate system, known as tipping points [Armstrong McKay et al., 2022]. Understanding the future behaviour of jet streams and powerful cyclonic eddies is of major importance for adapting to climate change. Storm tracks, regions where there is large eddy kinetic energy [Shaw et al., 2016], cover large population centres, such as Western Europe, Eastern Asia, and Western North America and could therefore impact a large number of people [Shaw et al., 2016].

Changes to the midlatitude climate, due to anthropogenic climate change, are still not well understood [Keel et al., 2024; Harvey et al., 2015]. One hypothesis is that increasing polar temperatures will weaken the north south temperature gradient, leading to a weaker jet stream and more persistent atmospheric blocking [Francis and Vavrus, 2012]. This could lead to longer lasting heat waves and cold snaps. Heat exposure accounts for, on average, tens of thousands of deaths in Europe per year, and this number would likely increase with an increase in extreme events [Delforge et al., 2025; Ballester et al., 2023]. On the other hand, the meridional temperature gradient in the upper atmosphere is expected to increase, enhancing storm tracks and baroclinic instability, leading to stronger midlatitude storms [Shaw and Miyawaki, 2024]. These storms exacerbate the threat to coastal communities due to rising sea levels [Muis et al., 2023], with these storms already accounting for damages amounting to several billion euro per year [Flynn et al., 2024]. Policy makers

and infrastructure planners need to know how to plan for the changing future, and these two possible future climates would require different infrastructure and policy responses.

The response of the midlatitudes to climate change remains difficult to predict because of the many interacting components in the system [Ossó et al., 2024; Woollings et al., 2023a; Blackport and Fyfe, 2022]. High resolution general circulation models are a standard approach to studying but they suffer from biases and they are computationally expensive to run. Furthermore, to have confidence in the response of the midlatitude circulation to climate change it is important to have a physically based explanation of the underlying mechanisms [Shaw, 2019]. Due to the complexity of the models this is not an easy task. This motivates the present study. We aim to investigate key changes originating from climate change using an idealised climate model to test the theory behind these concepts and to help develop a physical understanding.

As discussed in Section 1.4, low order models can be used to identify key dynamical mechanisms by incorporating a minimal set of key physical ingredients, believed to be at the origin of the physical behaviour. This study aims to provide a step above the 'bottom-rung' of this ladder, building upon theoretical arguments that connect the meridional temperature gradient and baroclinic instability [Charney, 1947]. More recently, studies have used reduced order models to investigate the key dynamical responses to climate change. These studies have primarily focused on investigating the impact of the meridional temperature gradient on barotropic eddies and jets [Kobras et al., 2024; Moon et al., 2022a,b; Kidston and Vallis, 2012], the impact of climate change on non-linear dynamics [Hamilton et al., 2023; Palmer, 1999, 1993], and other impacts on the circulation from simplified processes [Laîné et al., 2011; Schneider et al., 2010].

However, the studies described above focus on primarily the atmosphere, and neglect the coupled climate system. As we discussed in Section 1.4, coupled models are crucial for helping understand the impacts of land or ocean coupling in the development of low frequency variability (LFV). The response to coupled behaviour and feedbacks in the atmosphere to climate change is another area where there is still large uncertainty [Gu et al., 2024].

One of the difficulties in using idealised models is in accurately incorporating changes brought about by climate change, because the radiative transfer is not explicitly computed as a function of atmospheric composition, as it is in general circulation models. We therefore need to account for the consequences of anthropogenic forcing by altering drivers, chosen here due to their importance in affecting the circulation dynamics [Ossó et al., 2024; Catto et al., 2019; Shaw et al., 2016]. We provide a summary of the current understanding of how these changes could impact the climate, based on state of the art climate modelling. The three drivers that we will focus on are:

- **Arctic Amplification:** Decrease in baroclinic instability due to Arctic Amplification [Screen and Simmonds, 2013]
- Increase in baroclinic instability in the upper atmosphere dues to tropical expansion, or **temperature exchanges** [Shaw et al., 2016].

- **Static Stability:** The increase in moisture that the atmosphere can contain, or an increase in the saturation specific humidity with increasing temperature [Catto et al., 2019]

4.1.1 Arctic Amplification and Tropical Expansion

The Arctic is warming at a faster rate than the rest of the world [Francis and Vavrus, 2012; Cohen et al., 2020], warming about four times faster than the midlatitudes over the last forty years Rantanen et al. [2022]. This is called Arctic Amplification (AA) This has the impact of reducing the surface temperature gradient between the tropics and the polar regions, leading to a decrease in baroclinic instability. This is turn would reduce the speed at which Rossby waves propagate, moving the jet towards the equator, leading to a 'wavier' jet stream and increasing the frequency of stationary extreme weather events such as heat waves [Riboldi et al., 2020; Moon et al., 2022a; Shaw and Miyawaki, 2024].

At the same time, the temperature of the upper troposphere is increasing faster over the tropics compared with the pole [Staten et al., 2018; Lu et al., 2007], which is called Tropical Expansion (TE). This increases the baroclinic instability at the top of the troposphere, moving the jet poleward. It is not clear which of these two opposing changes in the atmosphere will be dominant [Shaw et al., 2016; Butler et al., 2010]. Recently the influence of Arctic amplification on the jet behaviour has been debated [Blackport and Screen, 2020]. Modelling appears to predict a weak poleward shift in the jets hinting at tropical warming being dominant, and observations seem to have started to support this, though the significance of these studies is still weak and is likely dominated by internal and LFV [Woollings et al., 2023a; Vallis et al., 2015].

4.1.2 Atmosphere-Ground Temperature Transfers

Climate change will increase the heating in certain parts of the atmosphere. The tropical troposphere will become warmer through increased latent heating from water vapour following the Clausius- Clapeyron relation [Shaw, 2019]. At the same time polar regions will experience an increase in surface heating due to the reduction of ice albedo reflection (Arctic amplification). For this reason, we want to investigate the impact of temperature exchanges between the atmosphere and land in this model.

Modelling suggests that the heating of the tropical troposphere drives a robust poleward contraction of the extratropical storm track [Woollings et al., 2023a; Butler et al., 2010]. In the North Atlantic, the winter storm track is expected to strengthen and widen, with the opposite response in the summer [Shaw et al., 2018]. The response of the North Atlantic storm track is reflected in the change in the North Atlantic jet stream, which also strengthens and extends further into Europe [Harvey et al., 2020].

4.1.3 Static Stability

Static stability is the measure of stability that a parcel of air in the atmosphere experiences to vertical or adiabatic perturbations. The atmosphere is stable if a pocket of air that is moved vertically returns to its original altitude, and unstable if it continues to change altitude, or oscillates around a given altitude [Holton, 2004]. If the temperature of the upper atmosphere increases this leads to an increased static stability, while if the lower atmosphere warms, this decreases the static stability. Arctic Amplification (AA) is expected to increase the temperature of the lower atmosphere in the North Polar regions, and it is therefore expected that AA will lead to an increased gradient in the meridional static stability.

Frierson [2006] used coupled climate models from the ERA4 archive to find that overall there was a clear increase in static stability in the midlatitudes, with the upper troposphere warming by up to 2K over the lower atmosphere. They expanded on this work [Frierson, 2008], using aqua-planet models, to show that land surfaces complicate the determination of the static stability in midlatitudes in the Northern Hemisphere.

4.2 Methodology

4.2.1 Model

While numerous studies have investigated the expected changes to the midlatitude circulation, it is still not clear what the large scale impact will be, due to multiple drivers being altered at once [Woollings et al., 2023b; Lorenz, 2022; Stendel et al., 2021; Shaw, 2019; Woollings et al., 2018; Staten et al., 2018; Francis, 2017; Vallis et al., 2015]. We want to investigate the impact in a reduced order model framework to help understand the impact on the dynamics and the chaotic attractor. As discussed in Section 1.2, the atmosphere model used is the minimal set of equations that produce synoptic scale behaviour. In this chapter we used the land-atmosphere model, as introduced in Section 2.4 and used in Chapter 3. The parameter values used in this study, unless otherwise stated, are given in Table 4.1.

The model equations are projected onto a set of basis modes, shown in Equation 2.1, and in this study we use the following model resolutions, where $n_x \times n_y$ (number of wavenumbers in x and y directions): 2×2, 4×4, and 6×6. These have 30, 108, and 234 degrees of freedom respectively. These resolutions are selected to investigate the impact of the forcings on incremental increases in the model resolution, and to allow us to verify whether dynamics in the base 2×2 model, which has been the most widely studied, remains in higher resolution versions [Cehelsky and Tung, 1987].

Previous studies have focused on the LFV in the model that governs the transitions between different ground temperature anomalies [Hamilton et al., 2025; Xavier et al., 2024; Li et al., 2018]. The clearest behaviour is seen in the $\delta T_{\mathrm{g},\,3}$ mode, which describes a positive ground heat anomaly that oscillated between the west and east of the domain. In this study, we focus on altering parameters projected onto the specific mode $F_1 = \sqrt{2}\cos y$, which captures the meridional gradient. In the following sections, we outline the modifications made to the coupled land-atmosphere model.

Parameter	Value	Description
n	1.3 [non dim]	Aspect ratio of the model domain.
ε_{a}	0.76 [non dim]	Atmospheric emissivity.
k_d	0.085 [non dim]	Friction between the atmosphere and the ground.
$k_d^{'}$	0.02 [non dim]	Internal friction between the two layers of the atmosphere.
$C_{\mathrm{g},1}$	300W m^{-2}	Solar forcing on ground layer.
$C_{\mathrm{a},1}$	$\frac{4}{10}C_{\mathrm{g},1}$W m^{-2}	Solar forcing on the atmosphere.
λ_0	10W m^{-2} K^{-1}	Latent, sensible and turbulent heat coupling.
σ_0	0.2 [non dim]	Static stability of the atmosphere.

Table 4.1: Base model parameters used in this study.

4.2.2 Modifications

4.2.2.1 Baroclinic Instability

We can attempt to model AA and TE, described in Section 4.1.1, in the qgs model by altering the incoming solar forcing in the model. To simulate AA we could reduce $C_{\mathrm{g},1}$, which is the solar forcing projected on the ground mode F_1. To model TE we could increase the atmospheric solar forcing $C_{\mathrm{a},1}$, which is the equivalent atmospheric mode. Currently the atmospheric forcing is defined as a proportion of the ground heating: $C_{\mathrm{a},1} = \alpha C_{\mathrm{g},1}$, where previous studies have used $\alpha = 0.4$ [Li et al., 2018].

We will investigate the impact of altering α while keeping the value of $C_{\mathrm{g},1}$ constant. We took this decision as it simplifies the analysis to only investigate a single parameter. However, more importantly, numerous studies have investigated the impact of altering $C_{\mathrm{g},1}$ before [Vannitsem et al., 2015; Xavier et al., 2024; Hamilton et al., 2025]. From studies using aqua-planet models [Shaw et al., 2016; Voigt and Shaw, 2015], the increase in the gradient due to climate change could be up to 18%, assuming a base value of 120W m^{-2} in the atmosphere.

4.2.2.2 Atmosphere-Ground Temperature Transfers

With increased temperature comes the increase in moisture that the atmosphere can hold, and the additional energy that is released through latent heat. We cannot model this directly in the dry atmosphere qgs framework, but an approximation of these changes can be captured by λ, which controls the heat transfer coefficient between the land and the atmosphere, and combines both the latent and sensible heat fluxes [Vannitsem et al., 2015].

We argue that this value will not be uniform across the planet, and should be larger at in the tropics where convection and latent heating will more quickly restore temperature differences between the ground and the atmosphere [Shaw and Miyawaki, 2024]. We introduce this gradient in the parameter by decomposing the parameter onto a set of basis modes $\lambda = \lambda_0 \cdot F_0 + \lambda_1 \cdot F_1$, where $F_0 = 1$. This process is described in Appendix C.1.

4.2.2.3 Static Stability

AA and TE will alter the vertical temperature profile of the atmosphere, in addition to the horizontal temperature gradients [Frierson, 2006]. The vertical temperature structure will impact the static stability of the atmosphere in these regions [Ossó et al., 2024; Dai and Nie, 2022; Lorenz, 2022; O'Gorman, 2010]. In the qgs model, there is an explicit parameter for the atmospheric static stability (σ). To model the local changes, we use the same approach as for the temperature transfers, and we project σ onto the basis mode F_1. This is done by decomposing the variable $\sigma = \sigma_0 \cdot 1 + \sigma_1 \cdot F_1$, with further details in Appendix C.1.

4.2.3 Other Key Drivers

Here we have narrowed down the parameters to the key drivers that can be altered in the model. However, there are of course key processes that we cannot implement in this simplistic model. Here we briefly outline some of these processes and discuss the impact that not including them may have.

We neglect moisture, which is a a crucial element of climate change. As the temperature of the atmosphere increases, the amount of water vapour that it can hold also increases [Held and Soden, 2006]. More specifically, the saturation specific humidity increases with temperature (also called the Clausius-Clapeyron relation) [Booth et al., 2013; Bembenek et al., 2020]. On a warming planet this causes the low level air to become moister and a greater amount of latent heat to be released in the upper troposphere in the tropics from, in turn increasing the baroclinic instability Shaw et al. [2016]. Neglecting moisture can lead to underestimating the speeds of storm tracks and jets [Rantanen et al., 2019; Chang, 2006]. In addition, it has been found in idealised models that moisture plays a complicated and non-monotonic role in anticylonic eddy growth [Tierney et al., 2018].

Clouds also have a vitally important influence in the real climate. First, they act as a greenhouse gas, further increasing the capture of long-wave radiation [Watt-Meyer and Frierson, 2017]. However, they can also have cooling effects depending on density and altitude [Voigt and Shaw, 2015] and any long term movement of the jet to the north or south will impact the height of clouds in specific regions, and can in turn alter the localised capture of longwave radiation, potentially causing positive or negative feedback loops [Voigt et al., 2021].

Finally, we have taken an overly simplified approach to warming in the atmosphere. In particular, we ignore the cooling of the Polar stratosphere. The latter is expected to cause a robust poleward contraction of the midlatitude storm track and its associated fluxes of heat

and momentum Butler et al. [2010]. However, studies suggest that this is dependent not only on the height but also the vertical scale of the cooling.

4.2.4 Atmospheric Blocking

In this study, we identified regions of atmospheric blocking using the reversal in geopotential gradient, as introduced in Scherrer et al. [2006], which is a generalisation of the original gradient reversal index in Tibaldi and Molteni [1990]. This index has since been expanded on, notably in Davini et al. [2012], to capture both larger scale and persistent events. We have taken a simplified approach to identify gradient reversal, using a weaker criteria than Davini et al. [2012], as the atmosphere in this model does not have exactly the same timescales as the real atmosphere. As the model used in this study uses a sever truncation of Fourier modes, there are limited atmospheric states that can lead to blocking. As we will see, the jet in this model was found to oscillate between different states faster than the real atmosphere, potentially due to the baroclinic nature of the model [Reinhold and Pierrehumbert, 1982], requiring a reduction in the persistence of blocking.

The blocking index is calculated by calculating the meridional gradient of the geopotential height at 500hPa (Z_{500}) between a northern and southern latitude (Φ_N and Φ_S) and a central latitude (Φ_0), for a given line of longitude λ_0 at time t. From here on all references to geopotential height are referring to this definition. These gradients must satisfy conditions given in Scherrer et al. [2006]

$$\frac{Z_{500}(t,\lambda_0,\Phi_N) - Z_{500}(t,\lambda_0,\Phi_0)}{\Phi_N - \Phi_0} > 0\,\text{m}\,{}^\circ\text{lat}^{-1}$$
$$\frac{Z_{500}(t,\lambda_0,\Phi_0) - Z_{500}(t,\lambda_0,\Phi_S)}{\Phi_0 - \Phi_S} < 10\,\text{m}\,{}^\circ\text{lat}^{-1}$$

We then centre a box of 10° latitude and 20° longitude on each grid point, for each day. If a reversal in the gradient occurs somewhere inside this box, for at least 3 further days, we say that the grid point is blocked at the given day.

We will compare the differences in the blocking index in different model runs, with different forcings. To do this we take the difference in blocking index between the two scenario runs, and divide this by the blocking indices of the control run. This provides a proportion of increase or decrease in blocking index. We call this the proportional change in blocking index, or the change in blocking for short.

4.3 Results

The results are broken into three main sections: Section 4.3.1 introduces the 2×2 resolution model using the base set of parameters, as in Section 4.2.1, and the citations given in that section. In particular, we present the dynamical origin of atmospheric blocking in the low resolution version of the model. Section 4.3.2 will discuss the impact of climate change forcing on the 2×2 model. Finally, Section 4.3.3 will present the impact of climate change forcings on higher resolution versions of the model.

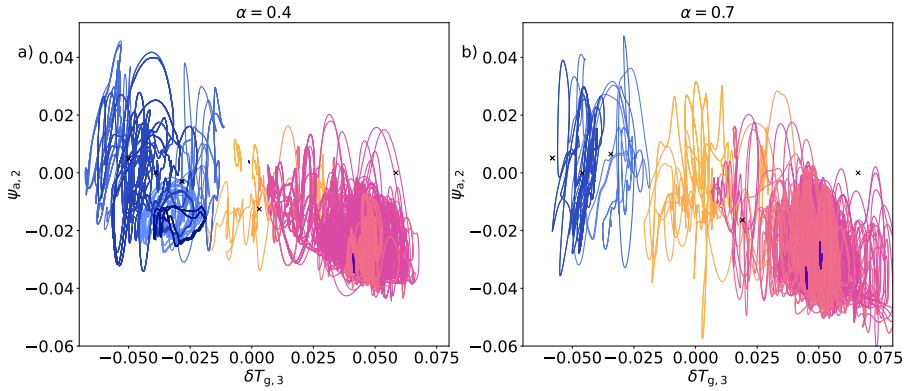


Figure 4.1: Projection of the periodic and fixed point solutions (crosses), onto the modes $(\delta T_{\mathrm{g},\,3},\ \psi_{\mathrm{a},\,2})$ for two different values of α. The LHS periodic solutions are shown in blues, the RHS are shown in pinks, and any solutions not falling into either of these clusters are in yellows. The shading within these colours are just to differentiate the different orbits. The solutions of the branch that is stable for some values of α are shown in purple. For higher values of α the main cluster of periodic orbits on the LHS cluster no longer exist, which means that trajectories favour the RHS.

4.3.1 Low Resolution Model Behaviour

The 2×2 model displays both zonal flow, and blocking behaviour where the zonal flow is deflected due to a persistent eddy. In this model, the addition of a coupled land layer introduces a longer time scale from the larger heat capacity of the land compared with the atmosphere, and through heat transfers this leads to a LFV pattern in the land temperature anomaly. This temperature anomaly appears to further strengthen/weaken the eddies in the atmosphere, resulting in increased/decreased blocking over certain regions of the model [Hamilton et al., 2025] (Chapter 3). The temperature anomaly, particularly over the mode $\delta T_{\mathrm{g},\,3}$, has been found to explain the three prominent types of behaviour found in this model.

In Figure 4.1a we present a set of unstable periodic orbits (UPOs) of the model, which provide a sketch of the behaviour of the chaotic attractor. As discussed in Chapter 3 the LHS set of UPOs is associated with windward blocking, the RHS cluster with leeward blocking, and the transition zones (not shown in the image) with zonal flow.

While clusters in the attractor explain average blocking behaviour, blocking events sometimes occur on the opposite domain side, due to faster atmospheric variability. To show this we divided the domain into left ($0 \leq x \leq \pi$) and right ($\pi \leq x \leq 2\pi$) sections[1]. For each time

[1] This is similar to the approach taken in a study by Xavier et al. [2025], which is under review.

step, we calculated the spatially averaged blocking index for each region, where 0 indicates no blocking and 1 indicates complete subdomain blocking. We matched each time step to its corresponding state space position, enabling comparison between regional blocking and system state, as shown in Figure 4.2. We now focus on the right-hand side cluster (corresponding to left-side domain blocking, Figure 4.2b), though the same arguments apply to the left-hand side cluster (right-side domain blocking, Figure 4.2a) with flipped variable signs.

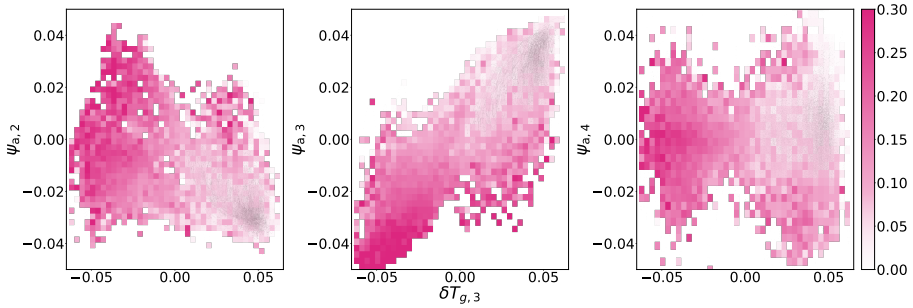
In Figure 4.2a, in projection $(\delta T_{\mathrm{g},3}, \psi_{\mathrm{a},2})$ (left panel), positive $\delta T_{\mathrm{g},3}$ values generally produce high average blocking indices as expected, though some left-hand cluster points show non-zero blocking indices. The projection $(\delta T_{\mathrm{g},3}, \psi_{\mathrm{a},3})$ (middle panel) reveals that non-zero blocking indices occurring for negative $\delta T_{\mathrm{g},3}$ correspond to near-zero or positive $\psi_{\mathrm{a},3}$ values, consistent with this mode's shape and resulting barotropic flow that it produces. Large negative magnitudes of $\psi_{\mathrm{a},3}$ typically occur after trajectory transitions from the right-hand side, when left-side blocking eddies are advected rightward by mean flow into the right subdomain where they decay. The projection $(\delta T_{\mathrm{g},3}, \psi_{\mathrm{a},4})$ (right panel) shows that non-zero blocking indices for negative $\delta T_{\mathrm{g},3}$ tend to correspond to large $\psi_{\mathrm{a},4}$ magnitudes. This mode categorizes jet behaviour (detailed in Appendix C.2) large $\psi_{\mathrm{a},4}$ magnitudes indicate high or low latitude jets, while near-zero values indicate a 'wavy' jet. This suggests atmospheric jet position may explain blocking presence in the model, resembling real atmospheric behaviour.

4.3.2 Climate Change Forcings - Low Resolution

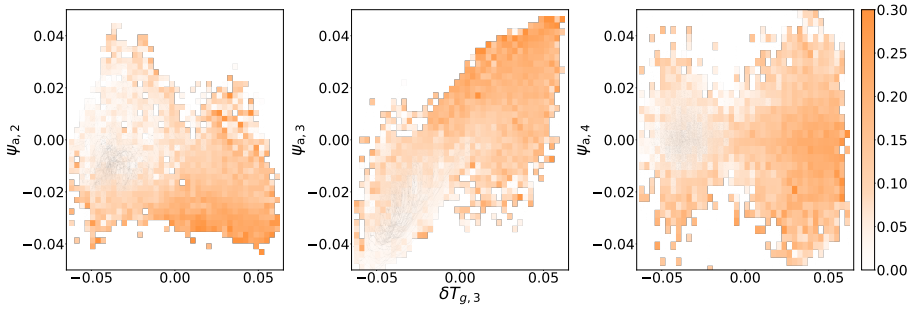
Insolation Gradient

In this section we alter the ratio between insolation ($\alpha = C_{\mathrm{a},1}/C_{\mathrm{g},1}$), as discussed in Section 4.1.1, while keeping the ground insolation constant. The resulting bifurcation diagram is shown in Figure 4.3. As the value of α is increased we see that the branches of orbits that exist for negative values of $\delta T_{\mathrm{g},3}$ disappear through fold bifurcations (shown in blues in the bifurcation diagram). This results in trajectories favouring positive values of $\delta T_{\mathrm{g},3}$. Figure 4.1 shows the value of α impacts the distribution of unstable periodic orbits between the two clusters.

UPO distribution changes could be the cause of trajectory distribution shifts, resulting in stronger western domain ground temperature anomalies. This increases atmospheric blocking on the orography's leeward side, as shown in Figure 4.4. For large atmospheric insolation ($\alpha \in [0.68, 0.8]$), the system stabilizes to a periodic orbit creating a standing wave of the jet around the orography. However, this behaviour disappears in higher resolution models, discussed in Section 4.3.3. Increasing α enhances baroclinic instability, strengthening the wind as evidenced by increased geopotential height (GPH) gradients in the domain center.



(a) The blocking index of the right hand side of the domain, shown in pink. Note that a temperature anomaly on the right hand side of the domain corresponds to a negative value of $\delta T_{\mathrm{g},3}$. In the left panel, we see that nonzero average blocking indices are primarily located for positive values of $\delta T_{\mathrm{g},3}$.



(b) The averaged blocking index of the left hand side of the domain, shown in orange. Note that a temperature anomaly on the left hand side of the domain corresponds to a positive value of $\delta T_{\mathrm{g},3}$. In the left panel, we see that nonzero average blocking indices are primarily located for positive values of $\delta T_{\mathrm{g},3}$. Where this is not the case, we argue in the text that this can be explained by either the values of other modes (such as $\psi_{\mathrm{a},3}$), the advection of eddies, or the location of the jet.

Figure 4.2: The blocking index for either the left or right hand side of the domain, projected onto the attractor. The attractor is shown in grey, with the blocking index, binned and averaged, shown in colour. The colour bar shows the spatially average blocking index for either the left or right hand side of the domain. All panels project the ground temperature anomaly on the x axis, with the projection on the y axis being $\psi_{\mathrm{a},2}$ (left), $\psi_{\mathrm{a},3}$ (middle), and $\psi_{\mathrm{a},4}$ (right).

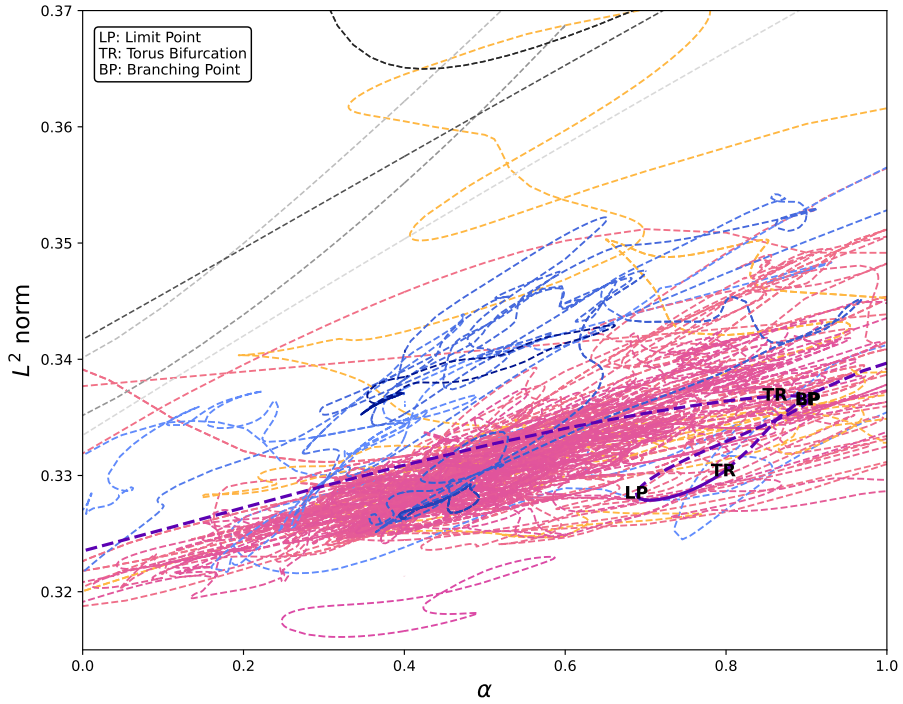


Figure 4.3: Bifurcation diagram of the periodic and fixed point solutions, for varying α. The fixed points are shown in shades of grey, the branches of periodic solutions that exist only in the LHS cluster are shown in shades of blue, the RHS cluster shown in pinks, with the other branches shown in yellows. The purple branch displays a stable periodic behaviour for values $\alpha \in [0.68, 0.8]$. This solution becomes unstable through a fold and a torus bifurcation. At approximately $\alpha \geq 0.65$ fold bifurcations occur on the blue branches, resulting in many of the solutions in the LHS cluster disappearing. In all bifurcation diagrams in this study, dotted lines refer to unstable solutions, and solid lines to stable solutions.

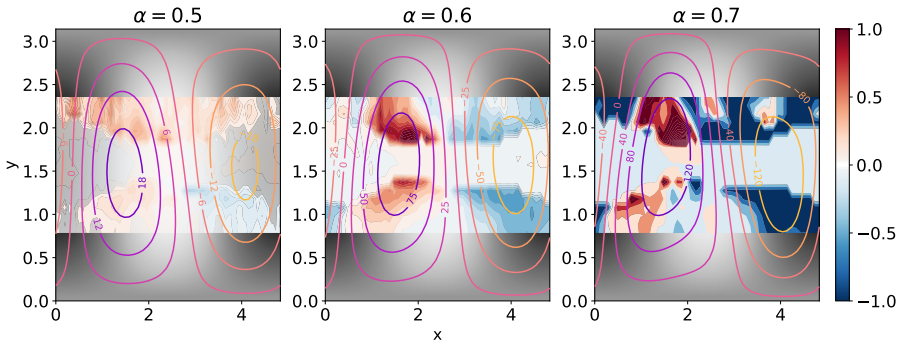


Figure 4.4: The anomaly of the GPH (shown as contour lines with the anomaly shown in m). The change in blocking index, compared with the reference case of $\alpha = 0.4$, is shown by the coloured heat map. The grey colouring shows the height of the orography, with darker colours representing the high ground.

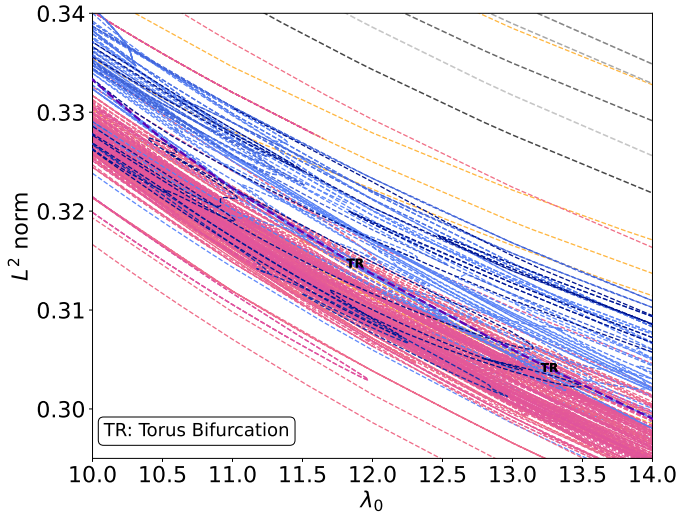
Heat Exchanges

The latent, sensible, and turbulent heat exchange (λ_0) controls atmosphere-land heat transfer rates, as summarised in Section 4.1.2. Since the land has greater heat capacity than the atmosphere, the temperature of the land changes more slowly. The uneven ground heating, via gradient $C_{\mathrm{g},1}$, is transferred to the atmosphere faster as λ_0 increases, enhancing baroclinic instability and atmospheric variability, which increases poleward heat transport [Vannitsem et al., 2015].

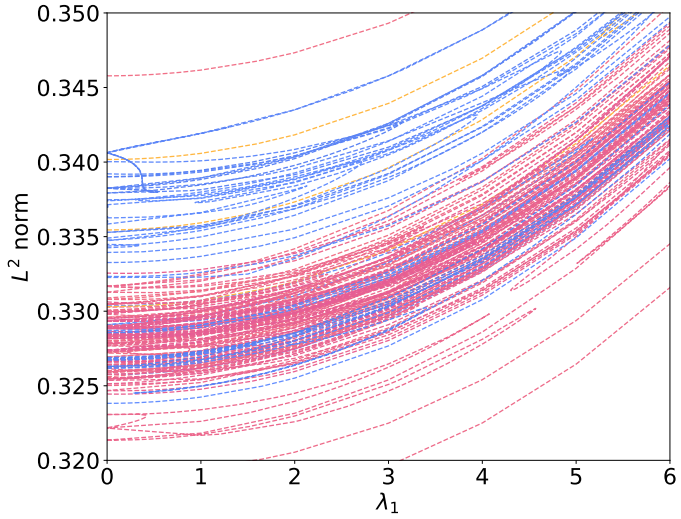
The bifurcation diagram for λ_0 (Figure 4.5a) and unstable orbit projections (Figure 4.7a, $\lambda_0 = 14$) show that low heat exchange values ($\lambda_0 \in [0, 2]$) produce stable orbits that destabilize through a torus bifurcation, leading to chaos. This parameter causes minimal change in positive/negative $\delta T_{\mathrm{g},\,3}$ solution distributions (Figure 4.7a), resulting in small change in the locations where atmospheric blocking occurs. Changes in blocking index, compared to $\lambda_0 = 10$ are shown in Figure 4.8a. Overall, there is a small increase in the average GPH over the windward side of the orography, resulting in a slight increase in the blocking indices. A similar increase is seen in the upper latitudes of the domain, but this response is small.

In this study, we have incorporated a gradient of the temperature exchanges (λ_1) to model uneven temperature exchange rates over the model domain. We present the bifurcation diagram for this variable in Figure 4.5b. As described in Appendix C.1, this parameter has a set of symmetries around $\lambda_1 = 0$. This results in a symmetric bifurcation diagram. In addition, the projection of the UPOs ($\delta T_{\mathrm{g},\,3},\ \psi_{\mathrm{a},\,2}$) are unchanged by the sign of the parameter. We present the projection of the orbits in Figure 4.7b.

Figure 4.7b shows that as the value of λ_1 increases, the distribution of UPOs does not alter significantly though the cluster locations shift. This results in a similar response in

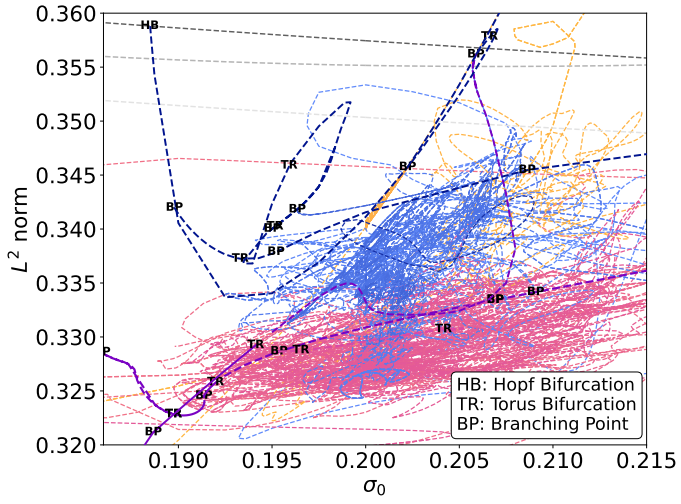


(a)

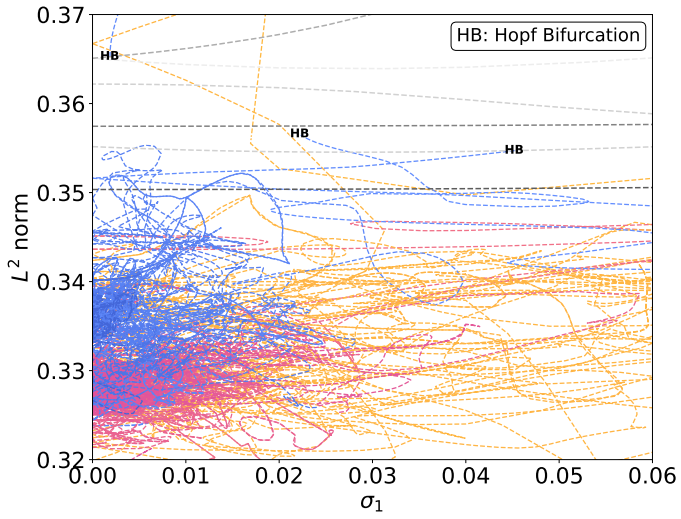


(b)

Figure 4.5: Bifurcation diagrams of the parameters λ_0 and λ_1. The colour coding is the same as used in Figure 4.3. Panel 4.5a shows the bifurcation diagram for λ_0 and Panel 4.5b shows the bifurcation diagram for λ_1. For both of these variables we see that the proportion UPOs in each cluster remain approximately equal.



(a)



(b)

Figure 4.6: Bifurcation diagrams of the parameters, σ_0 and σ_1. Panel 4.6a shows two stable periodic orbits for low levels of $\sigma_0 \approx 0.19$. These destabilise through torus bifurcations. Interestingly these stable orbits both appear for certain parameter values, and they exist in each cluster. Panel 4.6b shows that as the value of σ_1 increases (or decreases as it is symmetric around 0), the solutions that designate each cluster go through fold bifurcations, leaving primarily the solutions that do not fall into one cluster or another, meaning that the LFV is likely destroyed.

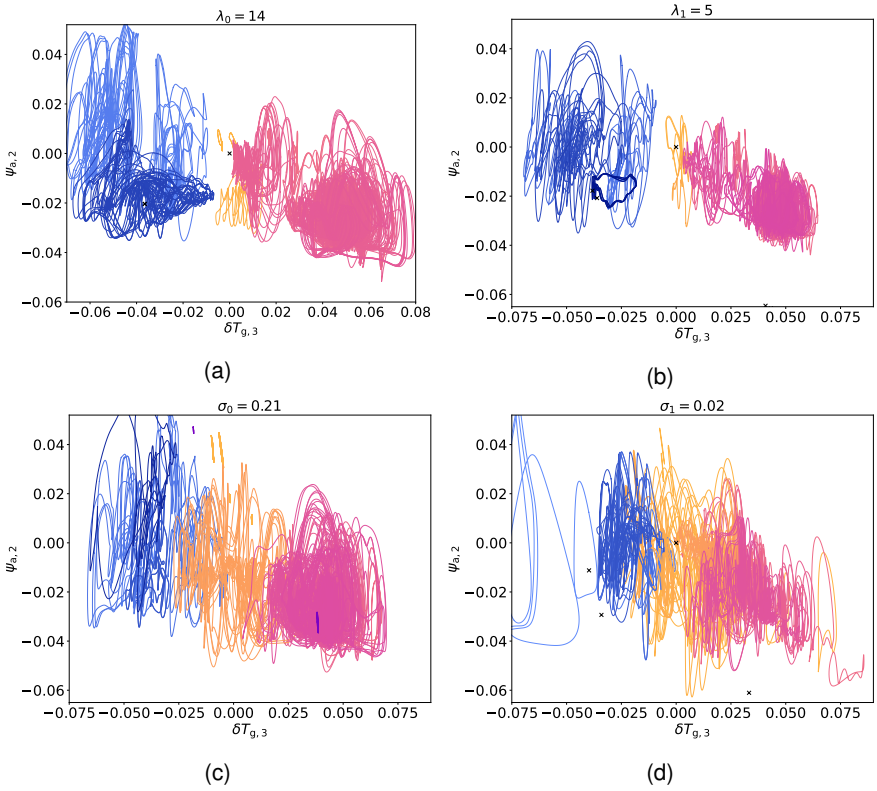
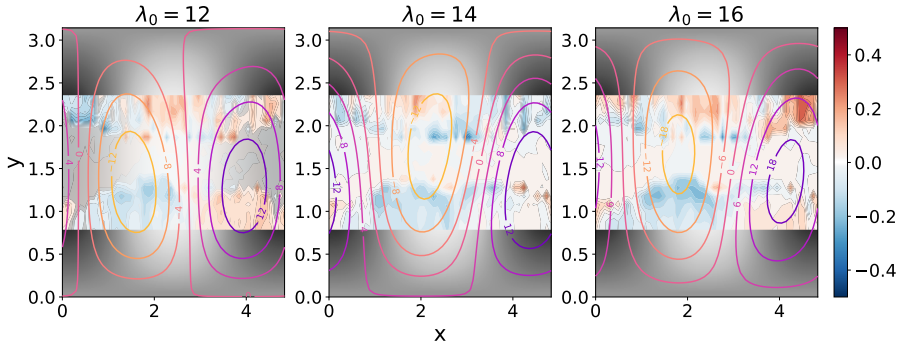
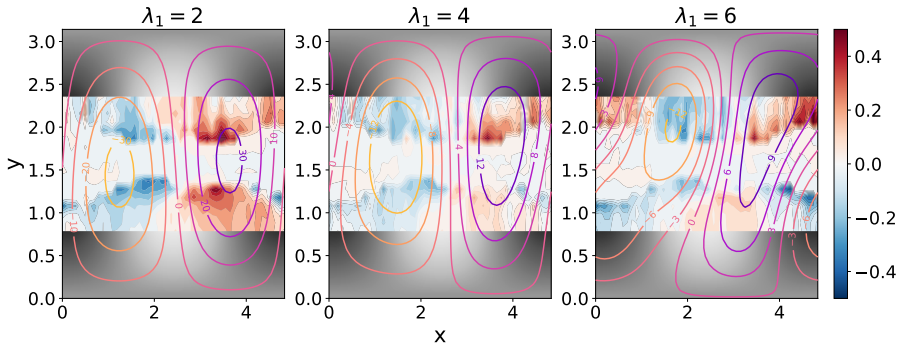


Figure 4.7: Projection of the orbits and fixed points for different parameter values. In this plot only one parameter is changed at each time. The colour coding of orbits is the same as described in Figure 4.1. We see that for increases in λ_0 and λ_1 (Panels 4.7a and 4.7b) that the two clusters of UPOs remain, while for increases in σ_0 and σ_1 (Panels 4.7c and 4.7d) the distribution of UPOs not in either of the LHS or RHS clusters increases.

blocking location, as seen for altering λ_0, and this is shown in Figure 4.8b. However, the new gradient introduced by this variable shows a skew in the position of the anomalies. Interestingly, increasing this parameter does not appear to increase the response in the GPH, but increases the skew in the geopotential anomaly.



(a) Same colouring as in Figure 4.4, but for varying λ_0. Here we see a weak response, appearing to show an increase in GPH over the windward side of the orography. This produces a weak increase in blocking in the same region.



(b) Same as Figure 4.8a, but for λ_1. The magnitude of λ_1 appears to increases the slant of the anomaly, pointing towards altering behaviour in the north and south regions of the domain, introduced by the gradient in heat exchange.

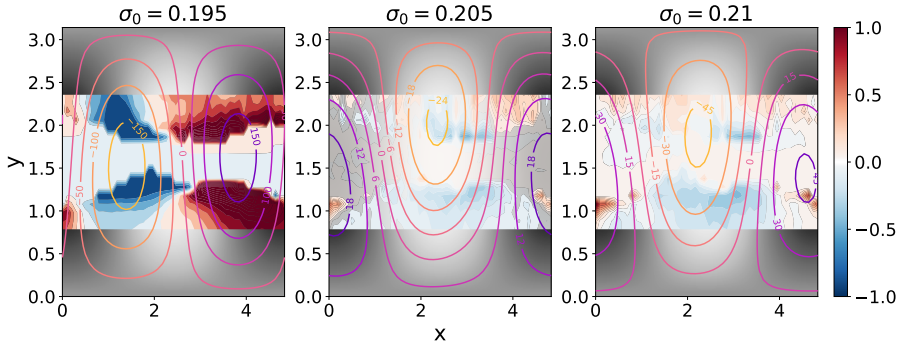
Figure 4.8: The change in blocking index for varying the temperature exchanges $\lambda = \lambda_0 + \lambda_1 F_i$. Note that the heat map scale has been altered due to a reduced response.

.

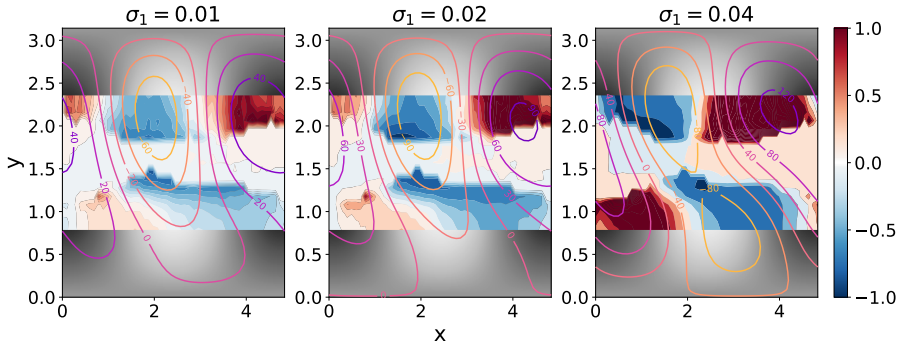
Static Stability

The bifurcation diagram for σ_0, or static stability discussed in Section 4.1.3, (Figure 4.6a) shows two stable periodic orbits, for negative and positive $\delta T_{\mathrm{g},\,3}$ values, when decreasing

σ_0. Increased static stability reduces the number of orbits for negative $\delta T_{\mathrm{g},\,3}$ (blue, Figure 4.7c, $\sigma_0 = 0.21$), indicating decreased windward blocking. Resulting blocking anomalies (Figure 4.9a) show weaker responses than insolation changes. For decreased static stability, windward blocking increases, which is expected as this decreasing the value of σ_0 further creates a stable orbit. The orbit destabilises through a torus bifurcation with increasing σ_0. At $\sigma_0 = 0.195$, the system is chaotic but lacks the LFV, seen at higher σ_0 values, producing trajectories with persistent negative $\delta T_{\mathrm{g},\,3}$. Beyond $\sigma_0 = 0.195$ the proportion of time spent in the LHS cluster continued to reduce.



(a) Same colouring as in Figure 4.4, but for varying σ_0. A weak response is seen, similar to increasing λ_0. Note that the first plot shows a decrease in static stability to highlight the sensitivity of this parameter, especially when the parameter value comes close to a value where stable periodic solutions exist.



(b) Same as Figure 4.9a, but for varying σ_0. We see that the change in gradient of the static stability causes a slant in the geopotential anomaly.

Figure 4.9: The change in blocking for varying the static stability $\sigma = \sigma_0 + \sigma_1 F_i$.

.

As with heat exchange λ, we project static stability onto a meridional gradient, designated σ_1. Increasing this value enhances the gradient of static stability, altering the mass

transfer across the model domain. The bifurcation diagram (Figure 4.6b) and orbit projections (Figure 4.7d) show that increasing σ_1 magnitude causes orbits associated with a cluster (blues and pinks) to disappear through fold bifurcations. This eliminates the system's LFV, likely due to reduced meridional flow preventing effective ground temperature distribution across the atmosphere.

In summary, increased atmospheric insolation gradient produces opposite responses to increased heat exchange and static stability. The insolation gradient's impact on GPH anomalies is an order of magnitude larger than other parameters, indicating insolation and resulting temperature gradients have prominent influence on simple baroclinic atmospheres.

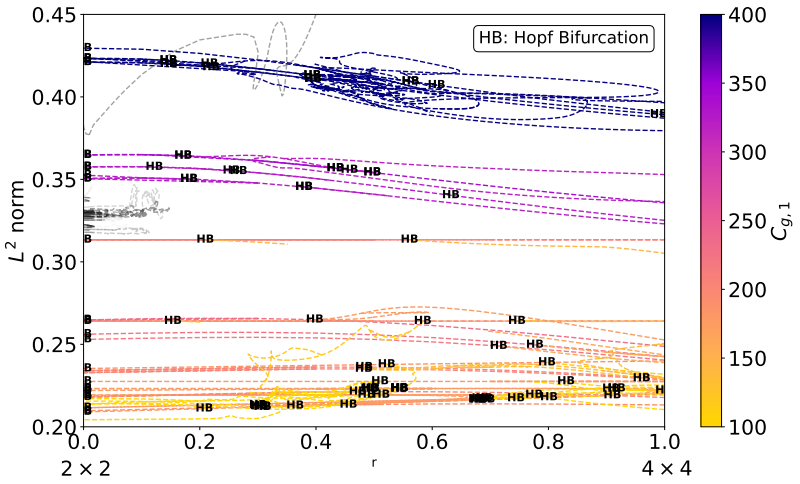
4.3.3 Climate Change Forcings - Higher Resolutions

To investigate the impact of model resolution our findings, we now present results using the 4×4 and 6×6 resolution model (108 and 234 degrees of freedom respectively). Numerically finding UPOs becomes exponentially more difficult with increasing model dimension [Lucarini and Gritsun, 2019]. Instead of finding the UPOs for these models, we chose to use the existing UPOs that we had found for the 2×2 model, and use continuation software to investigate the impact on these orbits as we increase resolution.

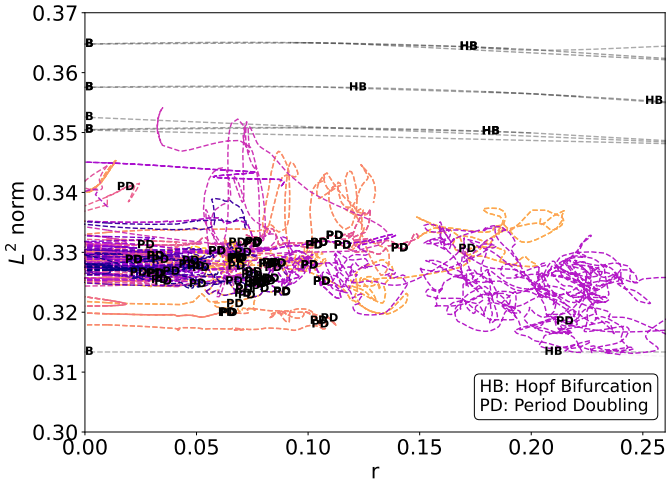
This involved creating a qgs model version which enabled continuous transition between the 2×2 and 4×4 models. We included a new parameter r as a coefficient for every term in model equations, except those appearing in the 2×2 version, creating system $\dot{x} = f(x, r)$ where $F(f(x, r = 0)) = f_{2\times2}(x)$ and $f(x, r = 1) = f_{4\times4}(x)$. Here $f(x, r)$ maintains 4×4 system dimensions, with function F projecting 4×4 outputs to lower 2×2 dimensions. This parameter introduces higher order terms, which appear only in the 4×4 version, in a continuous manner with $r \in (0, 1)$ introducing intermediate resolution models.

To track the UPOs found in the 2×2 model, we increased their dimensions to match the 4×4 model using the UPO searching algorithm [Gritsun, 2008]. Initial conditions matched the original UPO for dimensions existing in both models, with small random numbers for other dimensions. The period was assumed identical to the original UPO. We slightly perturbed r since at $r = 0$, the 4×4 model tendencies, absent in the 2×2 model, equal zero, preventing the Newton method to reduce the error. After algorithm convergence, we used AUTO to track UPOs back to $r = 0$, verifying retention of original UPOs. The resulting bifurcation diagram appears in Figure 4.10a.

This method failed for tracking most of the original UPOs, with Newton algorithm convergence failing in higher dimensions for approximately 90% of the original set. Possible causes include: random initial conditions in new dimensions falling outside convergence neighbourhoods, the small perturbation we made in r was 'too large' meaning that the period of some UPOs were no longer accurate for the altered parameter value, or UPOs not existing at perturbed r values. The method could be improved by running Newton algorithm multiple times with additional random initial conditions or reducing r size. Future work should be done to enhance the robustness of this approach.

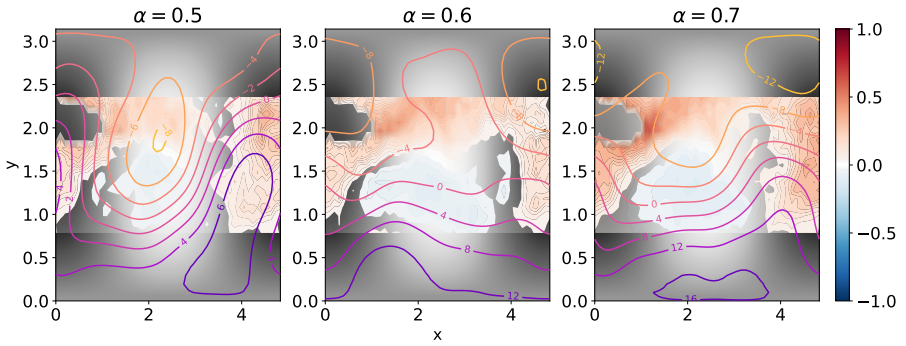


(a) Fixed points and the first level of branching points were continued for values $0 \leq r \leq 1$, where $r = 0$ is the 2×2 version, and $r = 1$ is the 4×4 version. The colour coding shows the values of $C_{g,1}$. In grey, the collection of UPOs are shown, with a zoomed in image in Figure 4.10b. The diagram shows that the majority of fixed points continue across the resolution gap, but all of the UPOs go through fold bifurcations below values of $r < 0.2$.

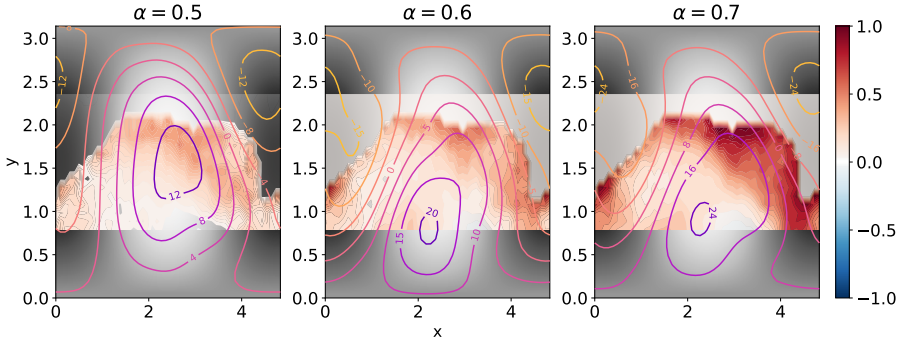


(b) The UPO branches, which are shown in grey in the above image, are shown in colour to differentiate the branches, the grey branches show the fixed points. All of the branches go through fold bifurcations for values of $r < 0.3$. Thus it is not possible to track particular instances of LFV across the intermediate model resolution.

Figure 4.10: Bifurcation diagrams of altering model resolution r. This diagram includes fixed points, the first level of branching points, and a collection of UPOs.



(a) The change in blocking index for 4×4 model, for varying α.



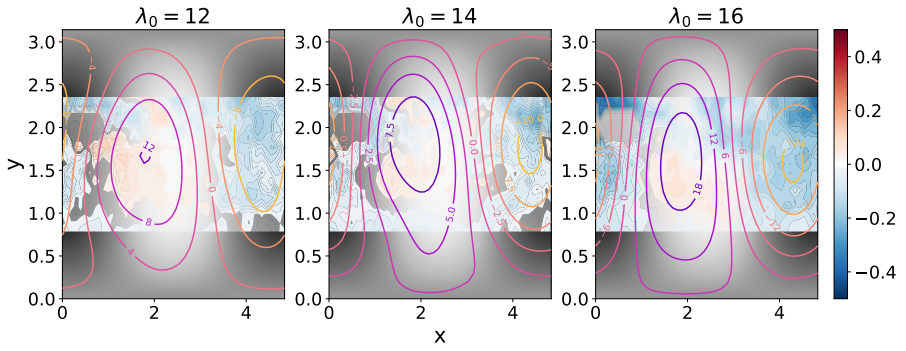
(b) The change in Blocking index for 6×6 model, for varying α.

Figure 4.11: High resolution runs for α. Figure 4.4 describes the plot colourings.

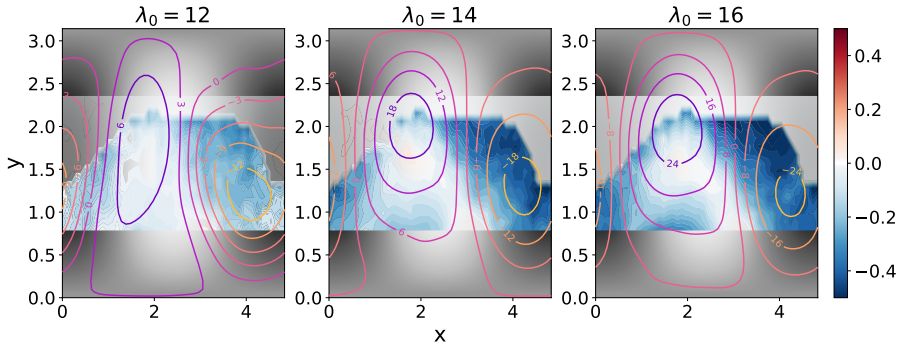
Generally, increased resolution destroys the LFV visible in the 2×2 model, evident in the bifurcation diagram where all but one branch extends beyond $r = 0.25$, in Figure 4.10a. This aligns with previous studies showing low-order spectral method solution sensitivity to model resolution [Cehelsky and Tung, 1987]. The remainder of this section presents higher resolution model responses to climate change-like forcings, investigating shared statistical or dynamical properties with the lower resolution version.

Insolation Gradient

First we analyze the impact of increasing α, shown in Figure 4.11. Higher resolution models show weak GPH increases in the domain center, over the low lying section of the orography. This is more pronounced in the 6×6 model, and results in a larger increase in atmospheric blocking in the region surrounding this increase in GPH. The 4×4 version we see a slight decrease in blocking in the lower centre of the domain, attributed to greatest GPH increases occurring at very low latitudes. The blocking identification method requires GPH



(a) The change in blocking index for 4×4 model, for varying λ_0.



(b) The change in blocking index for 6×6 model, for varying λ_0.

Figure 4.12: Same as Figure 4.11, but altering λ_0.

comparisons between low and high latitudes. As this is a midlatitude model, the domain is restricted in latitude, thus preventing the comparisons between more extreme latitudes. Consequently, expected blocking increases at higher GPH anomaly regions are not captured.

Comparing these results with the 2×2 model resolution, at higher resolutions we no longer get a clear windward/leeward response. This is believed to be due to the lack of a clear LFV behaviour in the higher resolution versions. We saw that in the 2×2 model this behaviour could be described by the presence of particular UPOs in the attractor.

Heat Exchanges

While large dynamical changes occur between 2×2 and 4×4 resolution models, climatology differences between 4×4 and 6×6 models appear similar for increasing λ_0 (Figure 4.12). The similarity between the high resolution models may be a result of convergence of the dy-

namics with the addition of non linear terms, or because the 4×4 model contains sufficient degrees of freedom to avoid stable cycles seen in the 2×2 model. These hypotheses align with De Cruz et al. [2016a], who found atmospheric mode variance changes little between resolutions above 4×4 in the MAOOAM model (atmosphere-ocean coupled rather than atmosphere-land). Beyond 6×6 resolution, added modes may minimally impact dynamics due to the high proportion of stable modes added [De Cruz et al., 2018]. Higher resolution model responses to increased heat exchange gradient (λ_1) were weak.

The 2×2 resolution model shows the opposite geopotential anomaly response when compared to the higher resolution versions. This clearly shows that the low resolution model is influenced by differing dynamics in higher order modes when it comes to the heat exchange. Further work is needed to identify the possible dynamical causes for this.

Static Stability

Higher resolution model responses to static stability broadly resemble heat exchange responses from the previous section. When increasing the zero-order static stability σ_0, the two higher resolution models show similar behaviour (Figure 4.13). However, the high resolution model responses to σ_1 parameter increases were very weak.

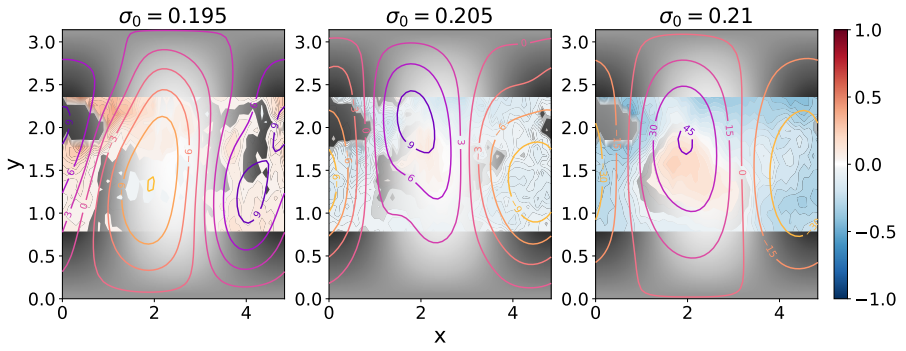
This could result from insufficient parameter value increases. Testing higher σ_1 values produced slightly increased responses. Parameter values here were selected based on 2×2 model responses, which may poorly represent higher resolutions due to the 2×2 model's tendency toward stable regimes. Further work could investigate parameter value sensitivity based on model resolution in higher resolution models.

4.4 Conclusions

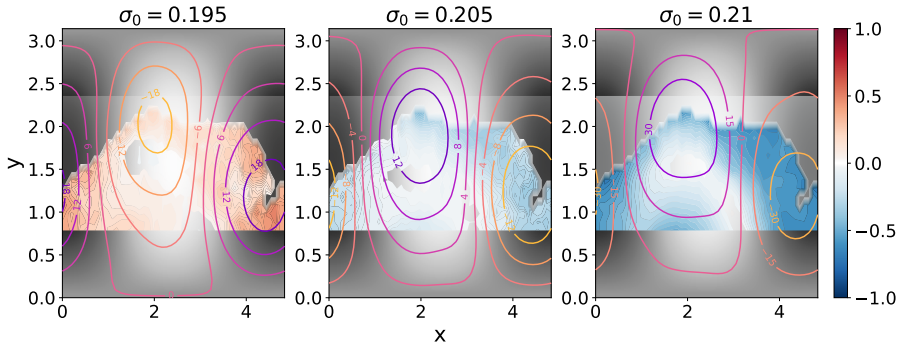
In this chapter we modified the qgs model to implement gradients in two parameters, examining model responses to potential climate change impacts. This was done across three resolutions to investigate the impact of the Fourier truncation on the model climate. We also introduced a model version allowing intermediate resolutions, aiming to use continuation software for investigating solution changes with model resolution.

In summary, the 2×2 model shows significant changes in the GPH and blocking position/frequency, depending on parameter values. We used unstable periodic orbits to track state space structures via continuation software. The largest changes to the attractor and model climate occurred when altering the ground-to-atmospheric insolation ratio, mimicking tropical expansion or increased baroclinic instability from tropospheric warming at lower latitudes. Increasing this parameter increased leeward orography geopotential height in the 2×2 model. Higher resolution versions showed weaker responses with general geopotential height increases over the domain's 'valley' region.

When altering heat exchange, we found generally the opposite, and weaker, responses compared to increased atmospheric insolation. The higher resolution models present similar results, apart from the temperature exchange, where the 2×2 model shows opposite



(a) Blocking anomaly for 4×4 model, for varying σ_0.



(b) Blocking anomaly for 6×6 model, for varying σ_0.

Figure 4.13: Same as Figure 4.11, but altering σ_0.

geopotential responses compared to higher resolution versions. Finally, increasing static stability had broadly similar geopotential height anomaly impacts as temperature exchange. These results support the existing literature, which finds that the response of the midlatitude flow as a result of climate change is difficult to determine due to competing responses, or a 'tug of war'. In these simple models the increasing gradient of atmospheric insolation appears to be the dominant response.

Different model resolutions show varying agreement depending on altered parameters. The 4×4 and 6×6 models present similar behaviour for tested parameters, while the 2×2 model sometimes shows different responses. For atmospheric insolation, models generally show increased north-south GPH gradients, with weaker responses in higher resolutions. Heat exchange parameter responses differ between low and higher resolution models, where increased geopotential anomaly occurs over orography in low resolution, but over valleys in higher resolution models, producing opposite atmospheric blocking responses. Increased heat exchange gradient creates a shear in the 2×2 model atmosphere,

while higher resolution models show weak responses without clear patterns. In general, increasing static stability impacts all resolutions similarly to increases in the heat exchange parameter. Clearly there is a discrepancy in the understanding of why the behaviour in the atmospheric response alters greatly, for certain parameter values, between primarily the 2×2 and 4×4 resolution models.

More work is required to understand the dynamical response to including further modes. Here we have begun that work by introducing a method for continuously transitioning between the model resolutions. Further work could build on this by investigating the bifurcation structure in more detail, by fleshing out the bifurcation diagram. Another option to understand the structure of the chaotic attractor would be to numerically find unstable periodic orbits for the higher resolution versions of the model, though as mentioned this is computationally challenging.

5

Multistability in a Coupled Ocean–Atmosphere Reduced-Order Model: Nonlinear Temperature Equations

---

This chapter is based on the following paper, published in the Quarterly Journal of the Royal Meteorological Society:

Hamilton, O., Demaeyer, J., Vannitsem, S. & Crucifix, M.(2023) Multistability in a coupled ocean–atmosphere reduced-order model: Nonlinear temperature equations. Quarterly Journal of the Royal Meteorological Society, 1–17. https://doi.org/10.1002/qj.4564

Abstract

Multistabilities in the ocean-atmosphere flow were found in a reduced order ocean-atmosphere coupled model, by solving the non-linear temperature equations numerically. In this chapter we explain how the full non-linear Stefan-Boltzmann law was numerically implemented, and the resulting change

to the system dynamics compared to the original model where these terms were linearised. Multiple stable solutions were found that displayed distinct ocean-atmosphere flows, as well as different Lyapunov stability properties. In addition, distinct Low Frequency Variability (LFV) behaviour was observed in multiple attractors. We investigated the impact on these solutions of changing the magnitude of the ocean-atmospheric coupling, as well as the atmospheric emissivity to simulate an increasing green-house effect. Where multistabilities exist for fixed parameters, the possibility for tipping between solutions was investigated, but tipping did not occur in this version of the model where there is a constant solar forcing. This study was undertaken using a reduced-order coupled quasi-geostrophic ocean-atmosphere model.

5.1 Introduction

Due to non-linear processes in the climate system a global temperature increase could lead to tipping points, causing rapid or irreversible changes to the climate [Lenton et al., 2008]. In the North Atlantic the jet stream has been identified as a potential tipping element [Steffen et al., 2018; Armstrong McKay et al., 2022], potentially causing long term climate patterns to be fundamentally altered. Low Frequency Variability (LFV) describes climate processes that slowly vary on interannual to multidecadal time scales. An example of LFV is the North Atlantic Oscillation (NAO), which is the sea-surface pressure difference between the subtropical and subpolar gyres. Accurate modelling of LFV could also help extend the typical two-week weather forecast horizon, which is caused by the sensitivity to initial conditions, in the midlatitudes.

Potential mechanisms for LFV in the midlatitudes include coupling of the ocean with the atmosphere where temperature, wind stresses, and moisture are transferred from one to another [Holton, 2004]. This coupling has been observed in data [Årthun et al., 2021; Wu and Liu, 2005; Czaja and Marshall, 2001]. Studies have attempted to reproduce this LFV using models of varying complexity. In this chapter we focus on modelling LFV using reduced order dynamical models, and the impacts of linearisations on these dynamics. These models purposely sacrifice the required complexity to accurately model the real climate and they instead focus on the minimum set of conditions necessary to generate a qualitatively similar variability.

Simplifying atmospheric models began with Lorenz [1963b] and Veronis [1963] with reduction of the quasi-geostrophic equations using a harsh spectral truncation and removal of small scale processes. These simplified the governing equations to allow for multiple solutions to be found explicitly. Charney and DeVore [1979] developed a land-atmosphere model, using a two layer QG atmosphere (adapting the one layer model of Egger [1978]), with a simple topography. The forcing of the zonal flow over topography led to multiple stable equilibria, or distinct atmospheric flows, and they believed it was the small scale perturbations or baroclinic instability that caused the transitions between solutions.

This claim was analysed by Charney and Straus [1980] who found that the transitions were caused by baroclinic instability instead of zonal flow perturbations, when using a baroclinic model. Reinhold and Pierrehumbert [1982] increased the zonal resolution of this model to better represent the synoptic scale baroclinic instability. They found that the atmospheric flow oscillated between two regimes, but these were not in the region of the equilibria. They conclude that understanding the overall variability in the climate system requires understanding the behaviour of these "regime-equilibrium". Further work has been undertaken to further understand multiple regimes present in these systems to investigate bifurcations [Legras and Ghil, 1985], and to show that these multiple attractors are resilient to the presence of noise [Itoh and Kimoto, 1996].

Studies have investigated the role of the ocean dynamics on LFV in the ocean [Chen and Dewar, 1993]. Weng and Neelin [1998]; Cessi [2000] implemented coupled versions of similar ocean models where the zonal wind was in turn impacted by ocean temperature gradients. Such studies found that the wind forcing was capable of generating LFV from the baroclinic exchange between gyres, as well as inter-decadal modes. LFV was also found in more complex ocean models [Nauw and Dijkstra, 2001; Dewar, 2001; Spydell and Cessi, 2003; Pierini, 2011]. These studies included a greater number of QG layers in the ocean models, and found that the intrinsic variability in the solutions comes from gyre modes. Together, these studies showed that intrinsic ocean modes could be sources of LFV in the coupled ocean-atmosphere system through time separation in heat transfers, or ocean gyres generated by wind stresses.

Models using more complex atmospheres coupled to the ocean were developed to further study LFV [Goodman and Marshall, 1999; Ferreira et al., 2001]. These studies used a linearised version of the two layer model introduced in [Charney and Straus, 1980], and a quasi-geostrophic two layer ocean, coupled through thermal and stress forcings. They analytically found that such models contain coupled modes, which were broadly consistent with the NAO, created and maintained by atmospheric Rossby waves moving over sea temperature anomalies. van der Avoird et al. [2002] showed that the coupling strength in such models can dictate the presence and strength of coupled modes and alters the behaviour of LFV. However, due to a discrepancy between the NAO variability and the behaviour of the LFV in this model, they concluded the model was likely missing key dynamics or that the coupled modes play no role in the observed variability. Further work was undertaken to understand the impact of the Atlantic gyre system [Kravtsov and Robertson, 2002], the sensitivity to non-linear dynamics and interactions between the layers [Kravtsov et al., 2006], and the impacts of ocean eddies on the variability [Berloff et al., 2007].

Multiple attractors in the coupled ocean-atmosphere system have been found in more complex models. Saravanan and Mc Williams [1995] modelled the atmosphere and ocean with the primitive equations and Boussinesq equations respectively, over a greatly simplified land or ocean base. This model presented multiple coupled attractors as well as coupled LFV. The authors studied the impacts of increasing CO_2 in the model by altering the longwave radiation leaving the grey body atmosphere. They found as CO_2 was increased the solutions seemed to collapse to a single attractor, due to the weakened jet stream and the ocean overturning.

Lorenz [1984] also developed a coupled ocean-atmosphere model based on the primitive equations for the atmosphere and a heat bath (slab) for the ocean. Using a fully nonlinear energy balance scheme, he was able to show the presence of attractors at different mean temperatures. This model was then extended by Nese and Dutton [1993] in order to incorporate a quasi-geostrophic transport in the ocean. Hogg et al. [2006] (following from Hogg et al. [2003]) used an intermediate complexity model to investigate ocean temperatures on LFV. They found that the ocean heat flux modified the behaviour and period of the existing LFV in the atmosphere but was not the cause of the variability.

These previous works have provided considerable hints on the development of multiple solutions in atmospheric and climate models, together with the possibility of the emergence of LFV. These studies, however, have shown limitations in terms of configuration flexibility and modularity. To alleviate these limitations, and provide a framework to investigate the emergence of coupled LFV modes, the Modular Arbitrary Order Ocean-Atmosphere Model (MAOOAM) [De Cruz et al., 2016a; Demaeyer et al., 2020] was developed. To do this, the atmosphere model of Charney and Straus [1980] was coupled with the simplified ocean model of Pierini [2011], as described in Vannitsem and De Cruz [2014]. It was shown that the combination of an energy balance model and a wind stress ocean forcing was essential in the development of the LFV [Vannitsem et al., 2015]. This model thus reduces the complexity of previous atmosphere-ocean coupled models, provides a flexible framework in which the domain size and the number of retained modes can be easily modified, and produces coupled LFV while retaining a good representation of the large scale ocean and dry atmosphere dynamics.

A source of non-linearity in this model comes from the longwave radiation modelled using the Stefan-Boltzmann law ($\sigma_{\mathrm{B}} T^4$, where σ_{B} is the Stefan Boltzmann constant). In the MAOOAM model the quartic radiation terms are linearised to simplify the numerical integration. This linearisation is justified as the perturbations in temperature are small relative to the average temperatures [De Cruz et al., 2016a]. However, this linearisation removes the possibilities of non-linear interactions from the temperature terms.

We will show that relaxing the linearisation leads to multiple stable flow patterns in the atmosphere and ocean, for certain parameter values. These flow patterns are qualitatively distinct and result in multiple average temperatures, for the same model parameters. The MAOOAM model is well suited to studying this due to its simplified dynamics, while retaining non-linear longwave radiation terms for both the ocean and atmosphere layers. Section 5.2 describes the reduced order model used in this study. This section also gives a description of the model configurations used in this study. The results are split into three sections, where we first look at the results from altering the ocean-atmosphere coupling (Section 5.3.1), then the impact of atmospheric emissivity (Section 5.3.2). We also look at the impact of altering theses two parameters on the stability and predictability of the system. In the last results section we present the impact of model resolution on the previous results (Section 5.3.3). Section 5.4 summarises the main results and discusses the general implications of these findings.

5.2 Model

In this chapter we use the ocean-atmosphere model (MAOOAM), as discussed in Section 2.5, using a model resolution of wavenumber 2×4 in the x and y directions. We track the barotropic and baroclinic streamfunctions $\psi_{\mathrm{a},\,i}$ and $\theta_{\mathrm{a},\,i}$, as well as the ocean streamfunctions and temperature $\psi_{\mathrm{o},\,i}$ and $\delta T_{\mathrm{o},\,i}$. The atmosphere equations are projected onto the basis functions F_i and the ocean onto the basis functions ϕ_i, as defined in Equations 2.1 and 2.16 respectively. Over the given model resolution, this results in 38 ordinary differential equations. The parameter values used in this study are presented in Table 5.1.

There are three basis modes of particular interest, as they have real world analogies: $F_1(x,y) = \sqrt{2}\cos(y)$ represents the solar insolation imbalance between the north and south. $\phi_1(x,y) = 2\sin(x/2)\sin(y)$ represents average temperature fluctuations in the ocean. $\phi_2(x,y) = 2\sin(x/2)\sin(2y)$ is the double gyre, orientated so the peak is either to the north or south of the trough. This loosely approximates the NAO, which is defined by the difference in surface pressure anomalies between northern and southern locations (often the Azores and Iceland) [Hurrell et al., 2003]. The prevailing clockwise winds around the Azores high, and the counter clockwise winds around the northern low pressure can be broadly simulated by projecting the atmospheric streamfunction anomalies on this mode, thus simulating the impact on the wind and heat transport caused by the NAO.

This study studied the impact of the linearisation of the longwave radiation terms, and this required significant modification of the qgs framework, as discussed in Section 2.5.4. The modifications have resulted in the creation of two new model frameworks, alongside the original linearised version. In this chapter we use all three versions, which are introduced in Section 2.5.4, and outlined below:

Linear Model: this refers to the original model version, as outlined in Section 2.5. Here, the temperature in the atmosphere and ocean are linearised, where the equilibrium temperature is fixed across the domain and time, so that any temperature fluctuations are controlled by the anomaly: $T(t,x,y) = T_0 + \delta T(t,x,y)$.

Dynamic Equilibria: this version of the model includes the same linearisation as the linearised version of the model, but the equilibrium temperature is dependant on time: $T(t,x,y) = T_0(t) + \delta T(t,x,y)$. We will refer to this version as DE.

Non-Linear T4: this version does not involve the linearisation of the Stefan-Boltzmann law terms and the equations are projected directly onto the basis modes. This retains the quartic radiation terms. We will refer to this version of the model as T4.

This results in three model versions:

Linear Model (LM) Dynamic Equilibria (DE) Non-Linear (T4)

Parameter	Value	Description
β	1.62×10^{-11} $\mathrm{m}^{-1}\mathrm{s}^{-1}$	The meridional gradient of the Coriolis parameter at a given latitude
f_0	1.032×10^{4} s^{-1}	Coriolis parameter
k_d	$\mathrm{g}C/\Delta p$ s^{-1}	Atmosphere-surface friction
k_d'	$\mathrm{g}C/\Delta p$ s^{-1}	Internal atmosphere friction
r	1×10^{-7} s^{-1}	Ocean bottom Rayleigh friction
L_R	1.9934×10^{4} [non dim]	Reduced Rossby deformation radius
h	136.5 m	Depth of the ocean layer
d	$C/(\rho_{\mathrm{o}} h)$ s^{-1}	Coefficient of mechanical ocean atmosphere coupling
γ_{a}	1×10^{7} $\mathrm{Jm}^{-2}\mathrm{K}$	Specific heat capacity of the atmosphere
γ_{o}	5.46×10^{8} $\mathrm{Jm}^{-2}\mathrm{K}^{-1}$	Specific heat capacity of the ocean
σ	0.2 [non dim]	Static stability of the atmosphere
λ	$1004C$ $\mathrm{Wm}^{-2}\mathrm{K}^{-1}$	Sensible and turbulent heat exchange between ocean and atmosphere
R	287.058 $\mathrm{Jkg}^{-1}\mathrm{K}^{-1}$	Gas constant in dry air
σ_{B}	5.67×10^{-8} $\mathrm{Jm}^{-2}\mathrm{s}^{-1}\mathrm{K}^{-4}$	Stefan-Boltzmann constant

Table 5.1: MAOOAM Model Parameters used in this study. Here C is a variable that we alter to investigate the impact of the ocean-atmosphere coupling. As in Charney and Straus [1980] we assume $k' = k_d$ and as in Vannitsem [2015] that gravity $\mathrm{g} = 10\mathrm{ms}^{-2}$.

5.3 Results

The results section is split into two main parts. We first describe the system dynamics when the ocean atmosphere coupling is altered, and second we alter the atmospheric emissivity. We focus on values of these parameters that result in multiple distinct ocean-atmosphere flows, which are described by distinct attractors. Multiple stationary attractors, for given parameter values, provide the possibility for model solutions to transition from one attractor to another, provided appropriate forcing is imposed. Such transitions between attractors could represent tipping points, abrupt changes, or switching of flows. We are particularly interested in flows that present LFV, generated by the coupling between ocean and atmosphere variables, due to the increased predictability of the system dynamics that these solutions provide.

5.3.1 Ocean-Atmosphere Coupling

This section presents the results where the magnitude of ocean-atmosphere coupling is varied for the three model versions. Increasing the ocean-atmosphere coupling has the effect of increasing the heat transfer between the ocean and atmosphere. This reduces the ocean temperature (which has a higher equilibria temperature than the atmosphere) and increases the atmospheric temperature, which has an impact on the baroclinic streamfunctions. The ocean temperature anomalies cause uneven temperature exchanges in the atmosphere that require the heat energy to be transported by atmospheric winds. At the same time, increasing the ocean-atmosphere coupling increases the friction felt by the atmosphere from the surface wind stresses with the ocean. In turn, this causes the atmospheric wind to have a greater impact on the movement of the sea temperature anomalies. Together, this reduces the fast moving timescales of the atmosphere through coupling to the ocean, which has a slower timescale relative to the atmosphere.

We alter the ocean-atmosphere coupling C by altering the following parameters: the strength of the ocean-atmosphere coupling d, the ocean-atmosphere friction k_d, the internal atmosphere friction k_d', and the direct heat transfer between the ocean and atmosphere λ [Vannitsem, 2015]. These parameters are controlled using a single friction coefficient C, where the relationship between C and the above parameters is given in Table 5.1. In this study we focus on values of C that are deemed to be within a realistic range ($C \in [0.008\text{kgm}^{-2}\text{s}^{-1},\ 0.02\text{kgm}^{-2}\text{s}^{-1}]$) for the real world coupling of the ocean and atmosphere [Houghton, 1986; Nese and Dutton, 1993; Vannitsem, 2017].

5.3.1.1 State Space Probing

The effect of the ocean-atmosphere coupling on the system dynamics was investigated by fixing the coupling value C and running many trajectories with random initial conditions. Once these trajectories had appeared to settle onto an attractor, the initial transient section of the trajectories was discarded and we continued to run the trajectories for long run times (1×10^7 model days). This was done to ensure that the attractors remain attracting and trajectories remain on the attractor. For these experiments, the atmosphere emissivity was

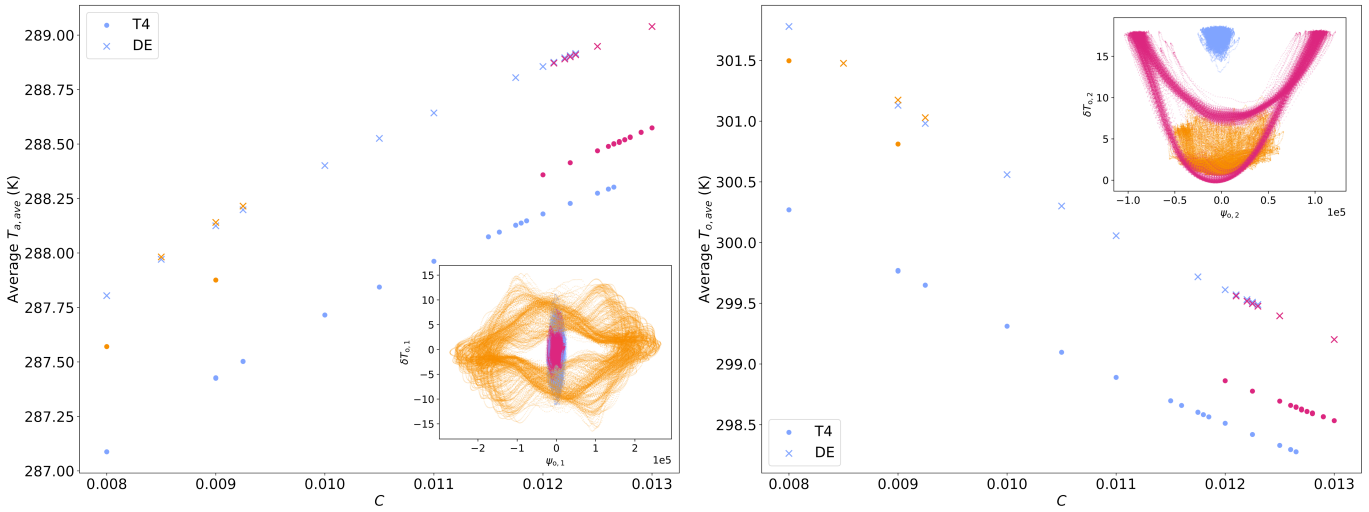


Figure 5.1: The Temperature-C diagrams for the averaged atmosphere (left), and ocean (right) temperatures for the DE model (crosses), and the T4 mode (dots), of the attractors. The branches were colour coded by qualitatively investigating the behaviour of each attractor. The attractors are projected onto the planes $(\psi_{o,1}, T_{o,1})$ (left) and $(\psi_{o,2}, T_{o,2})$ (right), to display how the behaviour differs between the three attractors. The projection of the orange attractor is shown for $C = 0.009\text{kgm}^{-2}\text{s}^{-1}$ and the other two projections (blue and pink) of the attractors are shown for $C = 0.0125\text{kgm}^{-2}\text{s}^{-1}$.

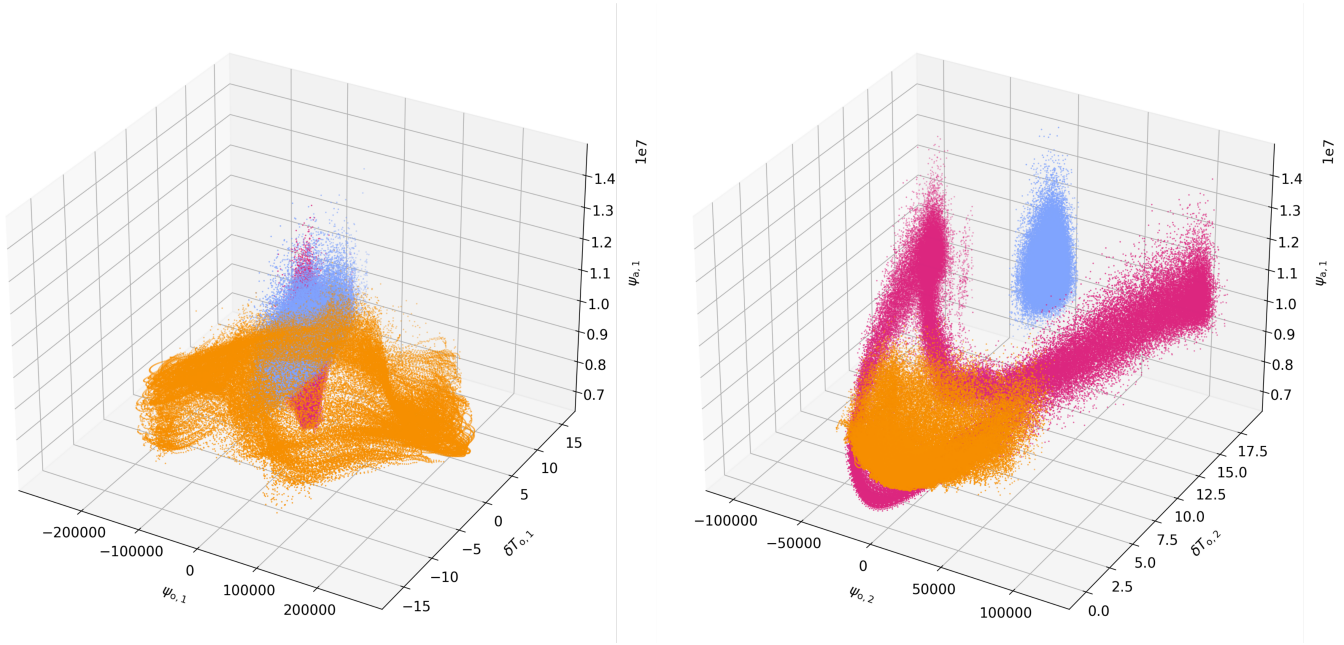


Figure 5.2: The distinct attractors for the T4 runs are projected onto $(\psi_{\mathrm{a},1}, \psi_{o,1}, T_{o,1})$ (left) and $(\psi_{\mathrm{a},1}, \psi_{o,2}, T_{o,2})$ (right), to present the level of ocean-atmosphere coupling. The orange attractor is shown for $C = 0.009\mathrm{kgm}^{-2}\mathrm{s}^{-1}$ and the other two attractors are shown for $C = 0.0125\mathrm{kgm}^{-2}\mathrm{s}^{-1}$. Here we only present the T4 runs as the dynamics over these three variables are identical between the T4 and DE model runs.

set to $\varepsilon = 0.7$ as the model default [De Cruz et al., 2016a]. This process was repeated for different values of C.

The average temperatures of the ocean and atmosphere were calculated by projecting the trajectories, that were embedded within an attractor, onto the basis modes to obtain the temperature profiles for each time step. We then took the average across the spatial domain to obtain a single average temperature for each time step. Finally we took the average across time to obtain a single temperature, which represents the average temperature associated with a given attractor. This process is shown for the temperature of the ocean, with a similar process taken to calculate the average atmospheric temperatures

$$\langle T_o(t)\rangle_{\text{space, time}} = \frac{1}{n_\tau n_x n_y}\sum_{\tau=0}^{n_\tau}\sum_{i=0}^{n_x}\sum_{j=0}^{n_y}\sum_{k=0}^{n_o} T_{o,k}(t_\tau)\phi_k(x_i, y_j)$$

Where n_o are the number of ocean modes, n_x and n_y are the number of spatial grid points being averaged across, and n_τ is the number of time steps in the numerical solution.

5.3.1.2 Multistabilies in Temperature - C

The average spatial and temporal temperatures are presented on a Temperature-C diagram. These diagrams are not bifurcation diagrams, as we only have information about the attracting branches that we could find using the described method. The resulting figures for the average atmosphere and ocean temperatures, where the value of the ocean-atmosphere coupling is altered, are shown in Figure 5.1. In these figures, the branches are colour coded depending on the qualitative behaviour of the attractor. The figures show there are two intervals of C where there are multistabilities in the temperature. These intervals are approximately $C \in [0.008, 0.009]$ and $C \in [0.012, 0.0127]$ (units of $\text{kgm}^{-2}\text{s}^{-1}$). These figures also show that there exists a single attracting branch that bridges the two intervals (shown in blue). We plot the results of the dynamic equilibria (DE) and non-linear (T4) model runs on the same plot.

We found two differences between the T4 and DE runs. The first is that the difference in average temperatures between the attracting branches in the DE runs are smaller than in the T4 runs. The small temperature differences between the attractors in the DE runs occurs due to the zeroth order temperature equations controlling the equilibria temperature $(T_{\text{a},0},\ T_{o,0})$ having only one real stable solution. This means that the difference in average temperatures in the stationary dynamics is caused by only higher order terms. In the T4 model, there are additional terms in the zeroth order temperature equations that result in larger differences between the zeroth order temperatures. This difference in the equations occurs in the non-linear longwave radiation terms, and is sketched be-

low for the ocean temperature equation. In the below expressions we introduce the tensor $v_{i,j,k,l,m} = \langle F_i,\, \phi_j,\, \phi_k,\, \phi_l,\, \phi_m \rangle$.

	Full Term	Zero Order Term
DE	$T_{o,0}^4 + 4T_{o,0}^3 \sum_{m=1}^{n_o} v_{i,0,0,0,m} T_{o,m}$	$T_{o,0}^4$
T4	$\sum_{j,k,l,m=0}^{n_o} v_{i,j,k,l,m} T_{o,j} T_{o,k} T_{o,l} T_{o,m}$	$T_{o,0}^4$ $+ \sum_{j,k,l,m=1}^{n_o} v_{0,j,k,l,m} T_{o,j} T_{o,k} T_{o,l} T_{o,m}$

The second difference between the model runs is that the T4 runs show a wider region of multistability in the interval $C \in [0.012\text{kgm}^{-2}\text{s}^{-1}, 0.0127\text{kgm}^{-2}\text{s}^{-1}]$. This is again assumed to be a result of higher order terms interacting in the T4 model equations, when compared to the DE runs, where the linearisation removes the higher order terms.

To investigate the properties of the attractors in the regions of multiple stability, the attractors were projected onto the ocean variables $(\psi_{o,1}, T_{o,1})$ and $(\psi_{o,2}, T_{o,2})$ to visualise the behaviour. Looking at these projections we can see that there are three qualitatively distinct attractor behaviours, which correspond to three distinct flow behaviours in the ocean. We project all three attractors onto the same figure for comparison, shown in Figure 5.1, with the orange attractor shown for $C = 0.009\text{kgm}^{-2}\text{s}^{-1}$, and the other two attractors shown for $C = 0.0125\text{kgm}^{-2}\text{s}^{-1}$. In the interval $C \in [0.008\text{kgm}^{-2}\text{s}^{-1}, 0.009\text{kgm}^{-2}\text{s}^{-1}]$, there exists two attractors, where the attractor shown in orange displays LFV with respect to the variables $(\psi_{o,1}, T_{o,1})$. The orange attractor becomes unstable when $C > 0.009\text{kgm}^{-2}\text{s}^{-1}$. This multistability has not been found in other studies using the linear MAOOAM model. The LFV in the first ocean modes suggests that the variability in the ocean temperature and streamfunctions is prominently impacted by the single gyre oscillation in this case.

The pink attractor, which becomes attracting for values $C > 0.012\text{kgm}^{-2}\text{s}^{-1}$, presents LFV over the variables $(\psi_{o,2}, T_{o,2})$, signifying that the dynamics of the flow are impacted by the double gyre dynamics. The other attractor (blue) present does not show LFV with any of the modes and this signifies that flows associated with this attractor do not present the same LFV or the same ocean dynamics as the other two attractors. The blue attractor disappears for values $C > 0.01275\text{kgm}^{-2}\text{s}^{-1}$. This second bifurcation was found in Vannitsem [2017] using the linear version of the model, however the region of multistability in this interval was not found using the linear model. We have conducted long model runs to ensure the stability of both attractors in this interval and found that both attractors remain stable for at least 3×10^7 model days. This region of multistability was found in both the T4 and DE model runs, however it was found that the region of multistability is extended in the T4 model, when compared with the DE model.

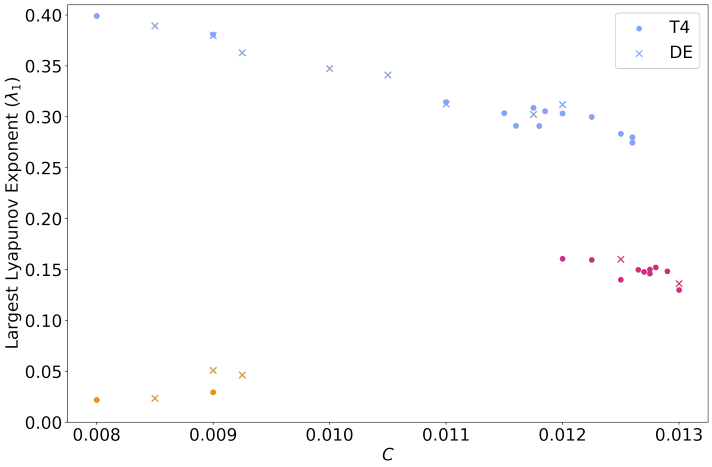
Following the analysis of [Vannitsem et al., 2015], we project the attractors onto the variables $(\psi_{\mathrm{a},1}, \psi_{o,1}, T_{o,1})$ and $(\psi_{\mathrm{a},1}, \psi_{o,2}, T_{o,2})$ to visualise the degree of ocean-atmosphere coupling in the attractors. In Figure 5.2 we show all three attractors, for the same values of C as before. In each image there is one attractor that develops around an unstable orbit that varies across all three variables over a decadal time scale. The image displaying $(\psi_{\mathrm{a},1}, \psi_{o,2}, T_{o,2})$ shows that the attractor coloured in pink presents the same oscillating behaviour over the three variables as the attractor found in Vannitsem [2017]. Unlike in this paper, however, here the distinct attractors coexist for the same parameter values. In addition, we also recover the attractor found by Vannitsem that does not present LFV (blue). The novel result here is that we have found an additional attractor (orange), for lower values of C, that also displays LFV in the coupled ocean-atmosphere system, but across the ocean-atmosphere modes $(\psi_{\mathrm{a},1}, \psi_{o,1}, T_{o,1})$.

To visualise the resulting flow in the ocean, given the attractor behaviour, we have created videos showing the ocean streamfunction and temperature profiles, given the location in the projected 2D state-space, which can be found in Appendix D.1. The attractor coloured in blue shows a persistent positive value for the $T_{o,2}$ variable, leading to a persistent double gyre temperature anomaly in the ocean temperature. In addition no clear LFV is present in the videos, which can be accessed from links in Appendix D.1. The pink attractor shows oscillating behaviour over the variables $T_{o,2}$ and $\psi_{o,2}$ with timescales of approximately 70 model years, leading to transitions between a double and quadruple gyre temperature anomaly in the ocean. Similarly, a clear oscillation is seen in the ocean streamfunction where the most prominent variables oscillate between $\psi_{o,2}$ and $\psi_{o,6}$ over the same time period. Lastly, in the case of the orange attractor, no clear double gyre appears in the ocean temperature profile, and the LFV instead manifests in the first ocean mode $\phi_{o,1}$. This leads to LFV with a timescale of 80-100 model years over the temperature variables $T_{o,1}$, $T_{o,5}$, and $T_{o,7}$.

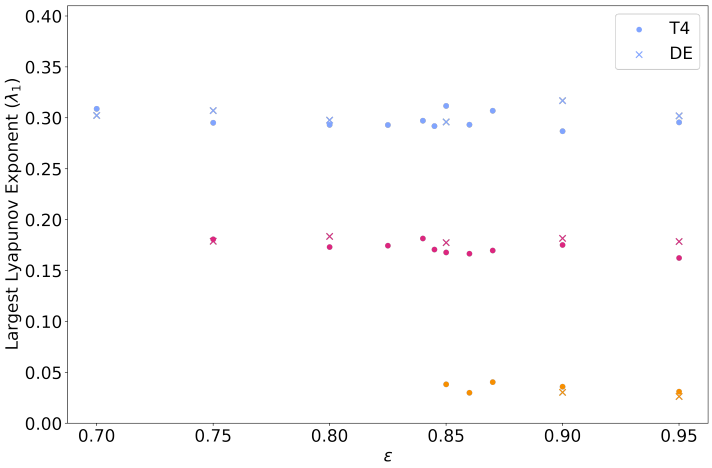
5.3.1.3 Lyapunov Stability - C

To analyse the stability properties, as introduced in Section 1.5.2, of the attractors that were found we calculated their Lyapunov properties, focusing on values of C identified in the previous section where multiple attractors exist.

We present the largest Lyapunov exponents (LLE) in Figure 5.3 (a), as a function of C, where again there is a multistability present in the two intervals identified. We have used the same colour coding as in Section 5.3.1.2 to display which Lyapunov exponent is associated with which attractor. Approximately, the midlatitudes have a synoptic forecast time scale of less than two week [Lorenz, 1982], with larger scale process having a larger forecasting time [Lorenz, 1969]. At the synoptic scale, this would correspond to LLE of approximately 0.2-0.3 days^{-1}. In the MAOOAM model there is a general decrease in the magnitude of the LLEs as C increases due to the increase in coupling between the ocean and atmosphere, resulting in the flow instabilities from the atmospheric dynamics being reduced [Vannitsem, 2017]. However, it is clear that the orange branch displays significantly smaller LLEs than the other two branches, for relatively small values of C. Other studies have shown that for



(a) LLE of the DE and T4 model runs, for varying C and $\varepsilon = 0.7$.



(b) LLE of the DE and T4 model runs, for $C = 0.01175\text{kgm}^{-2}\text{s}^{-1}$ and varying ε.

Figure 5.3: The Largest Lyapunov Exponents (LLE), shown in days^{-1}, where the results are colour coded based on the attractor behaviour, as described in Sections 5.3.1.2 and 5.3.2.1.

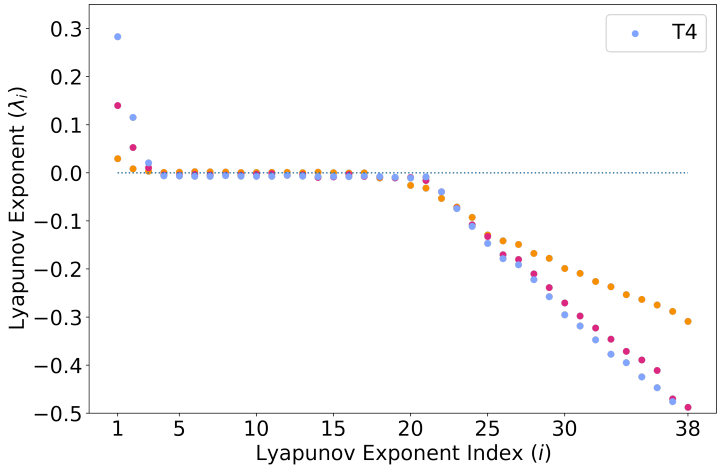
low values of C the magnitude of LLEs do decrease [Vannitsem, 2017], however this was observed for values $C \leq 0.0015\text{kgm}^{-2}\text{s}^{-1}$, and we did not carry out runs for values of C this low due to these ocean-atmospheric coupling values being unrealistic in the real earth system.

In Figure 5.4 (a) we present the Lyapunov spectra of the three distinct attractors identified while varying the level of ocean-atmosphere coupling. The figure shows that the two attractors at $C = 0.0125\text{kgm}^{-2}\text{s}^{-1}$ (blue and pink), both have 18 near zero Lyapunov exponents, 17 negative exponents, and three positive exponents. However the positive Lyapunov exponents are approximately double in one of the attractors compared with the other, showing that the rate of divergence of initial conditions will be much greater in the blue attractor. The novel attractor found in this study (orange), presents significantly smaller magnitude positive Lyapunov exponents than the other attractors, and has a lower number of near zero Lyapunov exponents, implying that the attractor exists on a lower dimensional chaotic manifold than the other attractors. The smaller positive magnitude Lyapunov exponents for two of the three attractors occurs due to these attractors existing around unstable periodic orbits that produce the LFV on decadal timescales and therefore increases the predictability.

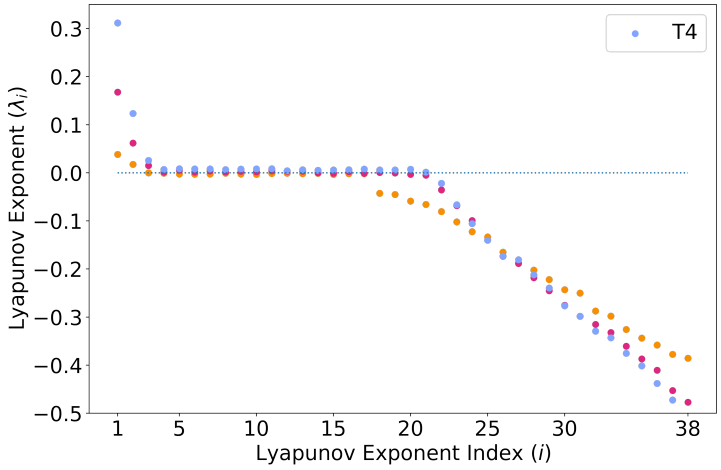
The extent to which coupling between the ocean and atmosphere is responsible for the LFV can be visualised using the variance of Covariant Lyapunov Vectors (CLVs) [Vannitsem and Lucarini, 2016]. The CLVs provide a covariant basis of the tangent linear space of the system. In other words, the CLVs are vectors that form a basis and remain covariant with the flow, unlike forwards or backwards Lyapunov vectors [Kuptsov and Parlitz, 2012]. Each covariant Lyapunov vector is stretched by the system dynamics by the corresponding local Lyapunov exponent. Each CLV is made up of 38 components, one for every variable of the system. The CLVs were calculated at each time step, and we took the variance of each of the 38 vector components across time, for each of the 38 vectors. The variance measures the variability of the CLV component in the direction of a given variable. Variables from the atmosphere and ocean that both have high variance for the same CLV index implies that these variables are interacting, or influencing each other. Therefore variables that are coupled with one another will present higher variance for the same CLV index (horizontal rows on the diagram). This allows us to visualise which variables are coupled and have a greater impact on the system dynamics. In Figure 5.5 we present a heatmap of the variance ($\log_{10}$ scale) for the three distinct attractors. These plots show the CLV index on the y-axis, and the model variables on the x-axis. The variables are ordered as:

- Atmospheric barotropic streamfunctions ψ_{a} (Index: 1-10)
- Atmospheric baroclinic streamfunctions θ_{a} (Index: 11-21)
- Ocean barotropic streamfunctions ψ_{o} (Index: 22-29)
- Ocean temperature T_o (Index: 30-38)

As expected, the majority of the variance is seen in the atmosphere as these variables are the components that contribute to the fast timescale dynamics of the system. All three



(a) Lyapunov spectra where the orange attractor is shown for $C = 0.009\text{kgm}^{-2}\text{s}^{-1}$, and the other two for $C = 0.0125\text{kgm}^{-2}\text{s}^{-1}$, where $\varepsilon = 0.7$.



(b) Lyapunov spectra for $\varepsilon = 0.9$ and $C = 0.01175\text{kgm}^{-2}\text{s}^{-1}$.

Figure 5.4: The Lyapunov spectra, shown in days^{-1}, for the three distinct attractors found are plotted to compare the magnitude of the largest Lyapunov exponent λ_1, and the number of near zero Lyapunov exponents.

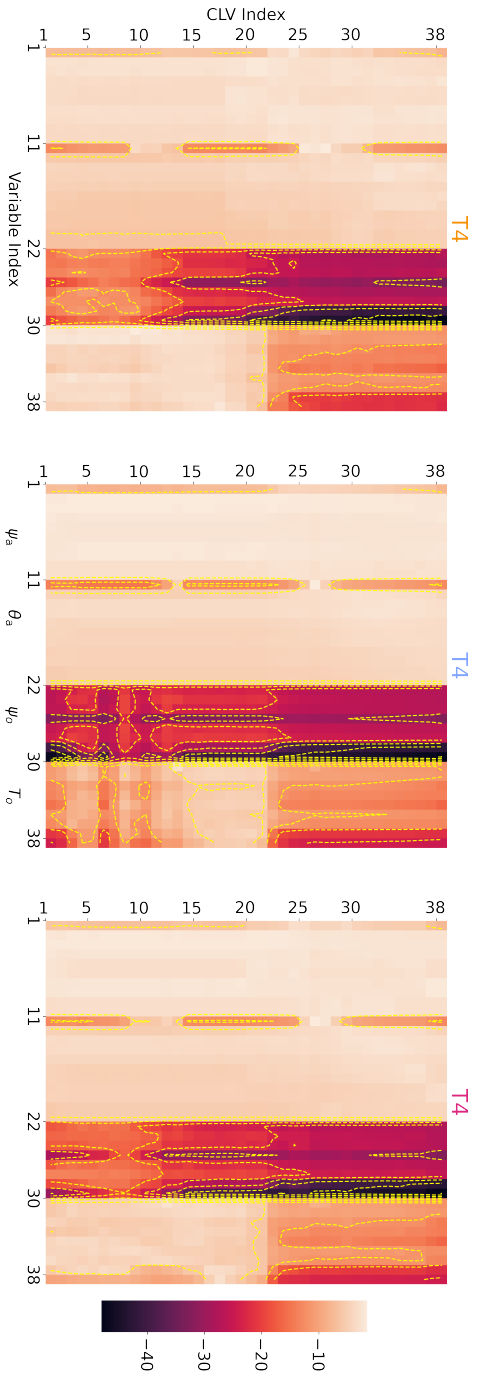


Figure 5.5: The variance of the CLVs (shown on a $\log_{10}$ scale), for each of the three distinct attractors shown in Figure 5.1. The attractors are designated by the colour of their title, which corresponds to the previous sections. The orange attractor CLVs are calculated for $\varepsilon = 0.7$, and $C = 0.009\text{kgm}^{-2}\text{s}^{-1}$, and the other two attractors' CLVs are calculated with $\varepsilon = 0.7$ and $C = 0.0125\text{kgm}^{-2}\text{s}^{-1}$.

attractors present coupling for CLV indices 13-22, where the ocean temperature variables present similar variability to the atmosphere variables. The near zero Lyapunov exponents (CLV index 4-22) in general have a larger projection on the ocean variables (columns 22-38). All three attractors present similar dynamics for the indices greater than 22, where the ocean components have low projection on the dynamics, implying that the large magnitude negative Lyapunov exponents are predominantly caused by the atmosphere dynamics. However, the attractors that present LFV have higher variance for the indices 1-12, implying that in these attractors the ocean temperature is having a stabilising impact on the atmosphere dynamics, and that there is a greater level of coupling between the ocean and atmosphere. In addition, the orange attractor (heat map on the left hand side) shows greater coupling between all four components of the model, as the ocean streamfunctions show higher variance for the indices 1-10. This explains the low magnitude of the positive Lyapunov exponents for this attractor as the unstable atmosphere components present high levels of coupling with the stable ocean.

5.3.2 Emissivity

To simulate the impact of climate change on the ocean-atmosphere dynamics in the MAOOAM model, the emissivity ε is increased. Increasing the emissivity acts as a proxy for rising levels of greenhouse gases, causing the atmosphere to 'trap' a larger proportion of the outgoing longwave radiation, thus increasing the average ocean and atmosphere temperatures. We picked a single value of ocean-atmosphere coupling $C = 0.01175\mathrm{kgm}^{-2}\mathrm{s}^{-1}$ to investigate. In the previous section this value of C resulted in a single stable attractor, for $\varepsilon = 0.7$.

5.3.2.1 Multistabilities in Temperature - ε

By using Temperature-ε diagrams, shown in Figure 5.6, that present the average spatial and temporal temperatures of stable attractors found numerically, we can see that as the emissivity increases bifurcations occur at two values, leading to an additional two attracting branches. We have coloured the attracting branches to display the attractors that present qualitatively distinct behaviour. On these images we only present the results from the T4 model runs as each of the T4 and DE model runs presented the similar trajectory behaviour, but the resulting average temperature of the three distinct branches in the DE runs were too close to be visible on the graph. This is because of the higher order non-linear terms being removed in the linearised version, as explained in Section 5.3.1.2.

We have taken the three attractors that we found at $\varepsilon = 0.9$ and projected these onto the planes $(\psi_{o,1}, T_{o,1})$ and $(\psi_{o,2}, T_{o,2})$, and these are also shown in Figure 5.6. We can see that two of the attractors (shown in pink and blue) present the same behaviour as seen in Section 5.3.1, in addition, the highest temperature branch (shown in orange) qualitatively appears to have similarities with the attractor that showed a periodic behaviour with respect to $(\psi_{o,1}, T_{o,1})$ that we also saw in the previous section. Therefore, increasing the value of ε appears to have the impact of providing stability to unstable branches. Figure 5.6 shows that the average temperatures in the atmosphere and ocean rise quickly as ε is increased, but

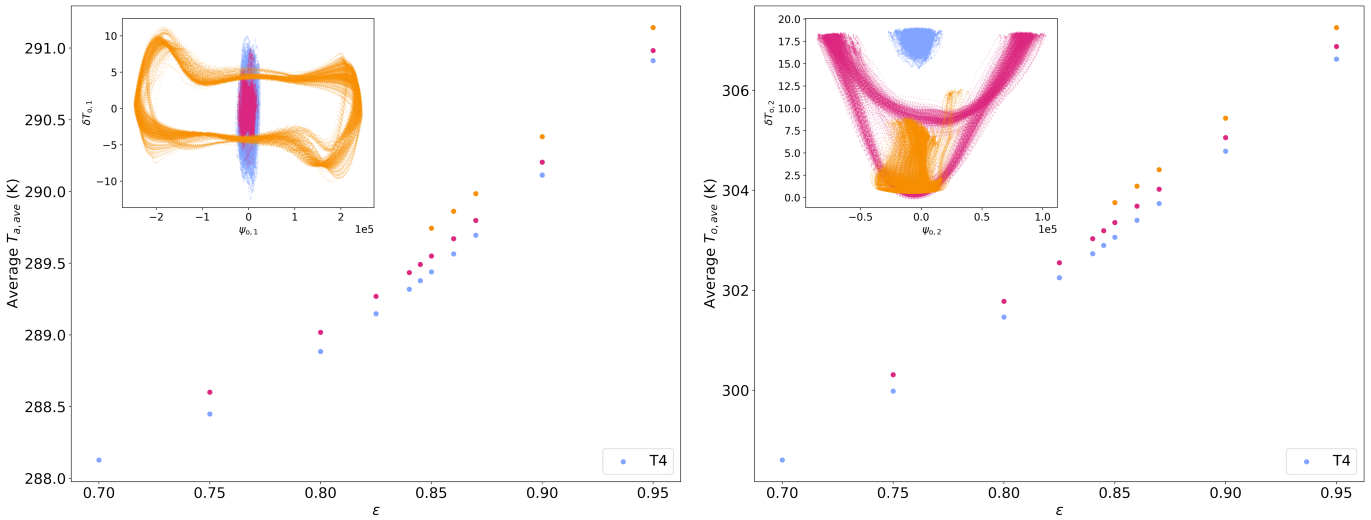


Figure 5.6: Temperature-ε diagrams showing the averaged atmosphere (left) and ocean (right) temperatures. The different colours represent stable branches that present qualitatively different attractors. Here we only present the T4 model run results as the DE results produce the same results, and the temperature differences between the three branches of the DE runs are too small to be visible on these graphs. As in Figure 5.1, the attractors are projected onto the plane of ocean variables with the single gyre (left) and double gyre (right) for $\varepsilon = 0.9$.

in addition there are multistabilies that are separated by up to $1^{\circ}K$ for the same emissivity values.

As in Section 5.3.1, we visualise the level of ocean-atmosphere coupling by projecting the three attractors onto the first atmosphere mode, and the single and double gyre ocean modes, which is shown in Figure 5.7. As with this previous section, we see that the orange attractor displays an oscillatory behaviour, coupling the barotropic streamfunctions and the single gyre variables, and the pink attractor displays LFV with the double gyre variables. Again, we see two distinct flows where there exists coupling between the ocean and atmosphere, over decadal time periods. These results show that in the MAOOAM model, rising emissivity leads to multistabilies in the ocean-atmosphere system, that were not present at low levels of emissivity. From our model runs we have not found examples of trajectories switching between the attracting branches, however all of our model runs were undertaken using a constant solar forcing. To understand the robustness of the attractors to forcing, further model runs will have to be undertaken.

Similar to Section 5.3.1.2, we have produced videos to show the resulting ocean streamfunction and temperature behaviour given the attractors. Links to these videos can be found in Appendix D.1. The qualitative behaviour of each of the attractors identified in this section is similar to that of the corresponding attractors (those sharing the same colours) in Section5.3.1.2. One minor difference in the results between the ocean-atmosphere coupling model runs and the emissivity model runs is that the LFV in the orange attractor over the first ocean mode $\phi_{o,1}$ is more clearly defined. This is shown by the projection of the attractor on the plane $(\psi_{o,1},\ T_{o,1})$, where the oscillating behaviour over these variables contains less noise and variation. This change in the orange attractor could be caused by the increase in ocean-atmosphere coupling between the two runs, where we used the value of $C = 0.009\text{kgm}^{-2}\text{s}^{-1}$ in Section 5.3.1.2, and $C = 0.01175\text{kgm}^{-2}\text{s}^{-1}$ in this section.

5.3.2.2 Lyapunov Stability - ε

Following the format of Section 5.3.1.3, we present the LLEs in Figure 5.3 (b), where ε is varied, and the ocean-atmosphere coupling is $C = 0.01175\text{kgm}^{-2}\text{s}^{-1}$. As the value of ε is increased we see additional attractors appear, however the value of the LLEs on each attracting branch does not alter with emissivity. This is because the emissivity has the impact of increasing the temperature of the layers evenly in space. The atmospheric layers in the model are driven from the meridional gradient in solar insolation, leading to baroclinic instability. In the current model set up the emissivity has no impact on this temperature gradient. A future study could look at linking the emissivity with the solar radiation gradient, to create a more holistic climate change impact on the coupled model.

We have presented the Lyapunov spectra of the three attractors at $\varepsilon = 0.9$, for $C = 0.01175\text{kgm}^{-2}\text{s}^{-1}$ in Figure 5.4 (b). Interestingly, the orange attractor, with the lowest magnitude LLE, shows a significantly lower number of near zero Lyapunov exponents, compared to the other two attractors and also the orange attractor presented in Section 5.3.1.3. There is a clear drop in the magnitude of the Lyapunov exponents at the index 18. This is an interesting result as it implies that the Lyapunov dimension of this attractor is significantly

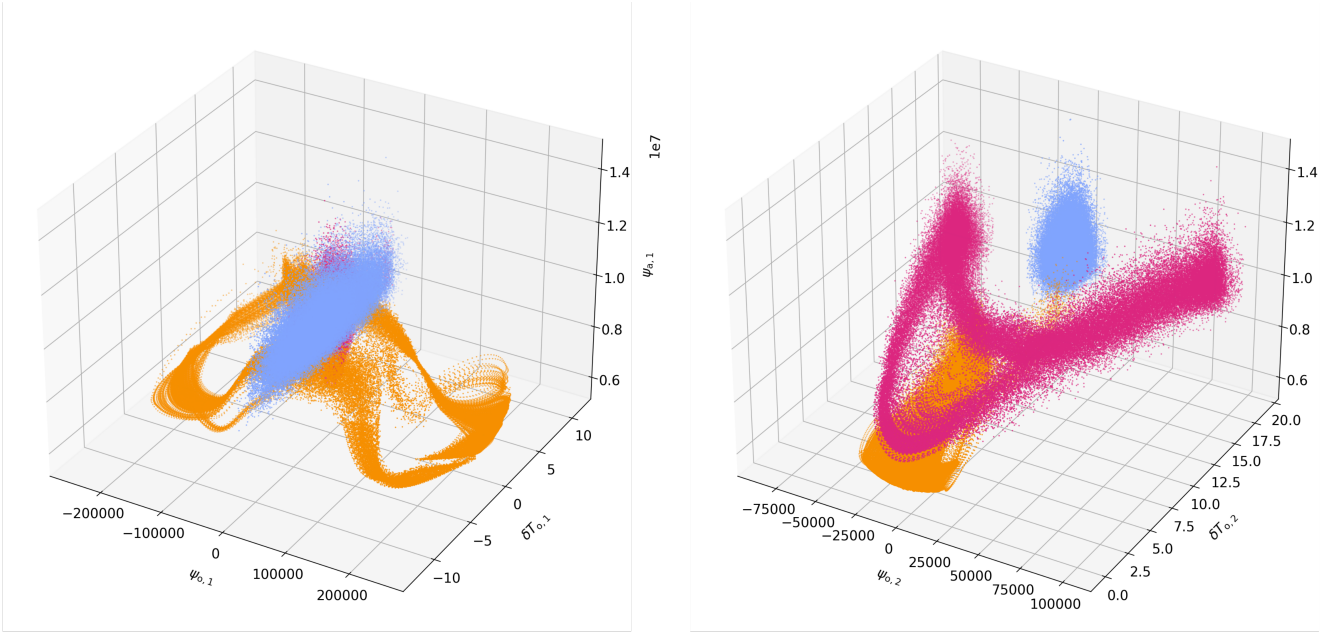


Figure 5.7: The three distinct attractors found at $C = 0.01175\text{kgm}^{-2}\text{s}^{-1}$ and $\varepsilon = 0.9$ are projected onto $(\psi_{\text{a},1}, \psi_{o,1}, T_{o,1})$ and $(\psi_{\text{a},1}, \psi_{o,2}, T_{o,2})$, left and right respectively. The attractors are coloured to match the diagrams shown in Figure 5.6.

lower than the other attractors. This difference between the Lyapunov spectra of the orange attractors in Figure 5.4 (a) and (b) could be caused by the increase in ocean-atmosphere coupling between the two model runs, from $C = 0.009\text{kgm}^{-2}\text{s}^{-1}$ to $C = 0.01175\text{kgm}^{-2}\text{s}^{-1}$ in this section.

5.3.3 Impact of Model Resolution

We investigated the impact of the model resolution on the results presented. The truncation (measured as the number of periods of a sine wave over the basin $x \in [0, 2\pi/n]$, $y \in [0, \pi]$) of the model was influenced by previous work using the MAOOAM model, which was set at (2×2) in the atmosphere and (2×4) in the ocean. This truncation in the atmosphere matches Reinhold and Pierrehumbert [1982], and the ocean truncation was chosen to more closely match the number of atmosphere modes, and provide a more realistic ocean temperature profile [Vannitsem, 2015]. As the number of modes used increases, the model resolution increases. However, as shown by Cehelsky and Tung [1987], for such models the accuracy is dependant on including certain modes that interact non-linearly that are inherent in the full system, and not necessarily dependant on the model resolution.

To test the impact of model resolution on the attractors we have run the Dynamic Equilibria (DE) model for key parameter values that we identified in the previous sections. The DE, rather than T4, model was used as the quartic term would result in model runs that take ages. Following the work of Cehelsky and Tung [1987] we have run the model at resolutions of (4×4) and (6×6) in both the ocean and atmosphere. In addition, the (6×6) resolution model approximately has the same scale as the Rhines scale (defined as $\sqrt{U/\beta}$, where U is the flow velocity and β is the gradient of the Coriolis parameter) in the model atmosphere, which marks the transition from wave dominated to turbulent dynamics [Rhines, 1975], and thus provides a resolution where we would expect the turbulent dynamics to impact the solutions. However, due to the order of magnitude difference between the flow velocity in the ocean and atmosphere the Rhines scale in the ocean is approximately an order of magnitude smaller than in the atmosphere, and as a result would require an ocean resolution of $\sim (60 \times 60)$ which would be computationally very expensive at this stage.

We ran higher resolution runs for $C = 0.009$ and $C = 0.0125$ while fixing $\varepsilon = 0.7$, to compare the results against those in Section 5.3.1. We found that the multi-stability for $C = 0.009$ collapsed into a single attractor, however we could still find two distinct attractors for $C = 0.0125$ (shown in Figure D.1(c)). There is a possibility that we did not find suitable initial conditions that would lead to multistability at $C = 0.009$, due to the increase in the dimension of the state space. These results are shown in Appendix D.2. The results here are similar to those of De Cruz et al. [2016a], where the LFV, while persisting, becomes less pronounced as the model resolution increases. Another very interesting result of the 6x6 formulation is that the range of values of the variable $\psi_{o,2}$ are now mostly positive, suggesting that the structure of the double gyres shows stronger similarities with the double gyres found in the North Atlantic basin.

We also ran higher resolution models for $\varepsilon = 0.9$ and $C = 0.01175$, to compare with the results shown in Section 5.3.2. For both the (4×4) and (6×6) resolution runs the

multiple attractors were no longer stable, and we found a single attractor. These results are shown in Figure D.1(e)-(f).

The higher resolution runs show that these novel attractors found are dependant on the model resolution, and specific non-linear interactions between the spectral modes. These results are in line with the results of Cehelsky and Tung [1987], who found that the multiple regime behaviour of the baroclinic model disappeared at higher resolutions. In our work, however, we do find a multistability persists for certain atmosphere-ocean coupling at the (4×4) resolution. Further studies are needed to investigate the values of coupling which this multistability exists for, to investigate the impact of the full quartic temperature term, and also the nature of the LFV emerging in a systematic way.

5.4 Discussion

We have described the novel multistabilities found in a reduced order atmosphere-ocean model, resulting from not linearising the longwave radiation terms. The modifications made to the MAOOAM model have resulted in several features that were not present in the original linearised version with fixed reference temperature. This study introduced two new versions of the model (the dynamic equilibria and non-linear versions), and compared the results of these versions with the existing linear model. The properties of the new attractor found, as well as the region of multistability, were analysed qualitatively and by using the Lyapunov properties of the attractors.

We have demonstrated in the reduced order ocean-atmosphere model, MAO-OAM, that by modifying the linearisation of the longwave radiation terms we can obtain three qualitatively distinct attractors, with intervals of multistability for certain parameters. Interestingly, the dynamic equilibria version of the model, which includes the same linearisation as the original model but allows the zeroth order equilibria temperature to change with time, presents similar dynamics as the fully non-linear version for most parameter values. All three distinct attractors can be obtained in the dynamic equilibria (DE) version, where there are two attractors that present LFV while representing largely different coupled ocean-atmosphere flows. In addition, the DE version of the model can be run in the same length of time as the fixed reference temperature version, which is almost an order of magnitude faster than the non-linear version of the model.

Two of the distinct attractors present LFV behaviour. One of the attractors, which displays LFV over the second ocean mode ϕ_2, has been identified in the linear model. In this study we found an additional attractor that displays LFV over the first ocean mode ϕ_1, which has not been identified in the linear model. This attractor has a longer time scale ($\sim 80 - 100$ years) compared with the first attractor (which displays a timescale of approximately 70 years). In addition the two attractors display marked differences in the ocean and atmosphere flows. With one attractor producing the double gyre behaviour, similar to what is observed over the North Atlantic, and the other attractor displaying a more complex flow, where the main relationships are with the first ocean mode ϕ_1 and the fifth ocean mode ϕ_5. This attractor displayed the greatest degree of coupling between the ocean and

atmosphere, comparing with the other attractors, where all four variables are coupled. This leads to significantly lower positive Lyapunov exponents, which implies that this attractor would have a longer forecasting window. Further studies will need to be done to find if this attractor describes a real-world ocean-atmosphere flow.

The Dynamic Equilibria version of the model was run at higher model resolutions and it was found that these novel attractors were no longer attracting for different model resolutions. However a multistability persisted for some parameter values, and others showed a tendency to a stable positive double gyre system. Further studies are required to investigate what type of solutions could emerge by changing the bifurcation parameters in a systematic way, and explore whether other parameter ranges are needed to see the development of multistability.

A key reason for undertaking this study, and not linearising the longwave radiation terms, was to investigate the potential of tipping between multistabilities. While we found cases of distinct attractors for the same parameter values, we could not produce trajectories that switched intermittently between the attracting branches, though it is not possible to rule out the possibility of such trajectories existing. However, in the current model setup all external forcings are constant with respect to time. To test the robustness of the stability of each attractor model runs could be undertaken, where stochastic forcing or perturbations are included, to see if there is the potential for noise induced tipping between the attracting branches. Another potential source of tipping could come from periodic cycles, such as the annual solar cycle as implemented in a similar linearised model [Vannitsem, 2017].

With rising global temperatures, investigating the possibility and impact of tipping points in the climate is of great importance. Understanding how rising temperatures could impact existing multi-decadal patterns in the climate could lead to a better understanding of how established climate patterns may look in the future. Or if there is the possibility of abrupt transitions from one regime to another. This chapter has introduced a modified model that produces both multistabilities, as well as attractors that present LFV, that become stable for rising emissivity. These properties are of interest as it facilitates the study of attractors that allow forecasting well beyond the atmospheric Lyapunov time, as well as the potential of tipping from one attractor to the other. These aspects will be investigated in the future.

6

A Shell Model of Geostrophic Turbulence

This chapter is based on the following paper in preparation:

Oisín Hamilton, Henk Dijkstra, Stéphane Vannitsem: A Shell Model of Quasigeostrophic Turbulence

---

6.1 Introduction

As we have seen in this thesis, while reduced order models can display realistic atmospheric or coupled Low Frequency Variability (LFV), increasing model resolution can destroy this behaviour. This was first highlighted by Cehelsky and Tung [1987], where they found that reduced order models can exhibit "spurious chaos", or resonances in particular wave modes. This causes oscillations to appear in the solutions of reduced order models, which are not present in higher resolution models. This behaviour originates as a result of reduced order models not having proper channels, or nonlinear wave interactions, through which energy and enstrophy can cascade. The energy contained within each wavenumber was later calculated by [O'Brien and Branscome, 1989], which showed an energy buildup at small wavenumbers in low order models. In the case of the the MAOOAM model, De Cruz et al. [2016a] showed that the atmospheric model behaviour converged above resolutions of

6×6. These studies demonstrate that it is important to understand if reduced order models are displaying realistic behaviour, by accurately accounting for energy flows between scales of the atmosphere. To aid with our understanding of how energy and enstrophy are expected to flow in a two layer atmospheric model we have developed a minimal model that tracks these flows.

Turbulence extends across a huge number of scales, and with many nonlinear interactions between scales, making it challenging to efficiently model [Vallis, 2017; Lorenz, 1969]. Geostrophic turbulence refers to the turbulent flow in the atmosphere, flow with high Reynolds number, which is dominated by eddies of different sizes, which are in near geostrophic and hydrostatic balance [Rhines, 1979]. In other words, geostrophic turbulence refers to flows that are mainly governed by rotation and stratification in the atmosphere, which have time scales greater than one day, and spatial scales much larger than 100km [Charney, 1971].

Geostrophic turbulence is important for accurately forecasting eddies in the midlatitudes, and could play a role in driving low frequency variability [Arbic et al., 2014]. Theory and observations show that there is an inverse energy cascade in the atmosphere, meaning that large scale eddies absorb energy from the surrounding flow. Due to the difference in vertical verses horizontal length scales in the atmosphere [Leith, 1971], turbulence on these scales can be approximated using the theory of two dimensional turbulence [Bohr et al., 1998; Kraichnant and Montgomery, 1980]. This cascade of energy can explain the formation of jets (the planet Jupiter being a pretty example) and other large scale structures in the atmosphere [Vallis and Maltrud, 1993]. However on Earth, due to the unsymmetrical distribution of oceans and orography, not all these structures can be observed. The fact that the atmosphere behaves similarly to two dimensional turbulence helps explain the success of numerical weather prediction to forecast up to two weeks in advance. This is because in two dimensional turbulence decreasing the initial error increases, without bounds, the predictability time of the flow, where the same is not true for three dimensional turbulence [Vallis, 2017].

Modelling the turbulent transfer of energy across multiple scales, using machinery such as the Navier-Stokes equations, quickly becomes unfeasible due to the number of degrees of freedom required [Bohr et al., 1998]. The number of degrees of freedom scale with the power of the Reynolds number ($N \sim \mathrm{Re}^{9/4}$), meaning that, for Reynolds numbers typically found in the atmosphere, this can require up to $N \sim 10^{27}$ degrees of freedom [Vallis, 2017; Ditlevsen, 2010]. To overcome this issue, geostrophic turbulence has been studied using a mixture of theoretical and reduced order methods. Charney [1971] used a scaling argument to show that there is a k^{-3} power dependence on the kinetic energy at large scales, as in 2D turbulence. Rhines [1977] described the nonlinear turbulent cascades in terms of barotropic and baroclinic energies in the ocean. Salmon [1978] used a spectrally decomposed two layer quasigeostrophic model to show that the key features of the energy cascade of the atmosphere can be reproduced using this simplified set up (this work was expanded on in Salmon [1980]). A dual cascade has also been observed in data, which appears to be separated by the Rossby radius of deformation [Gage and Nastrom, 1986]. Since this numerous other studies have used the quasigeostrophic equations to investigate

the energy cascade [Chen, 2023; Arbic et al., 2014; Tung, 2003; Smith and Waleffe, 2002; Maltrud and Vallis, 1991; Herring, 1988]. The aim of this study is to simplify these cascade models to the extreme. We want to produce a minimal model, that reduces the number of degrees of freedom, while preserving the scales required for a proper distribution of energy.

A class of models that aims to do this are called shell models (reviews can be found in Ditlevsen [2010]; Biferale [2003]). These remove spatial components by decomposing the dynamics onto a set of wave modes (called shells), providing only a low number of degrees of freedom - usually two - for each mode. The variables for each mode, or shell, often refer to the velocity for the flow within a given shell, and the model provides a description for how the energy flows between these shells. Shell models were first introduced for providing a simple framework for studying the cascades in turbulence described by the Navier-Stokes equation. While shell models are a simplification of the Navier-Stokes equations, from a rigorous mathematical perspective they are almost as difficult as the original NSE to analyse [Alexakis and Biferale, 2018].

The original shell models were designed to create closed systems that could reproduce the Kolmogorov spectrum using attractive fixed points of differential equations [Obukhov, 1971; Gledzer, 1973; Desnianskii and Novikov, 1974]. Since this, such models have been used to study the difference in cascades between two and three dimensional turbulence [Boffetta et al., 2011; Chakraborty et al., 2010; Gilbert et al., 2002; Ditlevsen and Mogensen, 1996; Kadanoff et al., 1995; Aurell et al., 1994], the cascade properties of passive scalar turbulence [Cohen et al., 2002; Andersen and Muratore-Ginanneschi, 1999; Benzi et al., 1997; Wirth and Biferale, 1996], magnetohydrodynamic turbulence [Plunian et al., 2013; Lessinnes et al., 2009; Plunian and Stepanov, 2007; Frick and Sokoloff, 1998], and properties such as intermittency and chaos in turbulent systems [Olesen and Jensen, 2007; Kato and Yamada, 2003; Yagi et al., 1999; Kockelkoren et al., 1998; Ditlevsen, 1996; Eggers and Grossmann, 1991]. While shell models have been used to simulate the turbulence cascades in barotropic models [Kwasniok, 2004], we could not find models which present a dual cascade and incorporate both barotropic and baroclinic modes.

However, these models only satisfy certain global conservation properties and they exhibit substantial arbitrariness concerning both the structure of the nonlinear terms and the values of the coupling parameters. For this reason, their use is primarily to reproduce qualitatively the main scaling properties for the fluid system and to investigate their dependence on the particular model chosen [Biskamp, 1994].

In Section 6.2, we begin by introducing some key theoretical results from two dimensional, and geostrophic turbulence, to allow us to compare our numerical results. In Section 6.3 we present the derivation of the two layer quasigeostrophic shell model. The results obtained from this model are then shown in Section 6.4.

6.2 Two Dimensional Turbulence

6.2.1 Basic Properties

Two dimensional (2D) turbulence acts differently compared to 3D turbulence. We have some intuition of three dimensional turbulence from seeing hot air rising, or waves breaking in the ocean. However, in 2D turbulence, due to the lack of a third dimension, vortices cannot be stretched. In 3D this stretching leads to an increase in the vorticity in regions of the fluid, this in turn forms smaller eddies, and this cascading of energy continues to smaller and smaller scales. In 2D turbulence, due to the lack of vortex stretching, there is another conserved quantity called the enstrophy, which is a measure of the vorticity. This leads significantly different behaviour between 3D and 2D turbulence. In this section we will outline some foundational results about the behaviour of 2D turbulence. The results that follow were originally described in Batchelor [1969]; Leith [1968]; Kraichnan [1967].

We start with the 2D vorticity equations

$$\frac{\mathrm{D}\zeta}{\mathrm{D}t} = \frac{\partial \zeta}{\partial t} + \mathbf{u} \cdot \nabla \zeta = F + \nu \nabla^2 \zeta$$

where ζ is the relative vorticity $\zeta = \nabla^2 \psi$, F is the forcing or stirring, and ν are viscous forces that act on small scales. As we are working in two dimensions the advection term can be written using a Jacobian, and substituting the streamfunctions for the vorticity

$$\frac{\partial}{\partial t} \nabla^2 \psi + J(\psi, \nabla^2 \psi) = F + \nu \nabla^4 \psi \tag{6.1}$$

Multiplying by $-\psi$, setting the forcing and viscosity to zero (to obtain the unforced case), and integrating over the domain, we find an expression for the conservation of energy (using integration by parts and the fact that the Jacobian only acts to advect the vorticity)

$$E = \frac{1}{2} \int_D (\nabla \psi)^2 \qquad \frac{dE}{dt} = 0$$

Multiplying by ζ and integrating provides an expression for the conservation of enstrophy

$$Z = \frac{1}{2} \int_D (\nabla^2 \psi)^2 \qquad \frac{dZ}{dt} = 0$$

Due to the lack of vortex stretching in 2D turbulence, kinetic energy is transferred to larger scales, the opposite of 3D turbulence, while enstrophy cascades to smaller scales. This can be seen by imagining a ring of fluid being elongated by the flow. The vorticity in this elongated band is conserved but because the band is elongated the vorticity gradients increase and so enstrophy is moved to smaller scales [Vallis, 2017]. On average this stretching will occur in all directions and the overall scale of the streamfunction will also increase in all directions, thus meaning energy is transferred to larger scales. If energy is constantly being injected into the system, energy must be removed from large scales and enstrophy removed from small scales to obtain a statistically steady state.

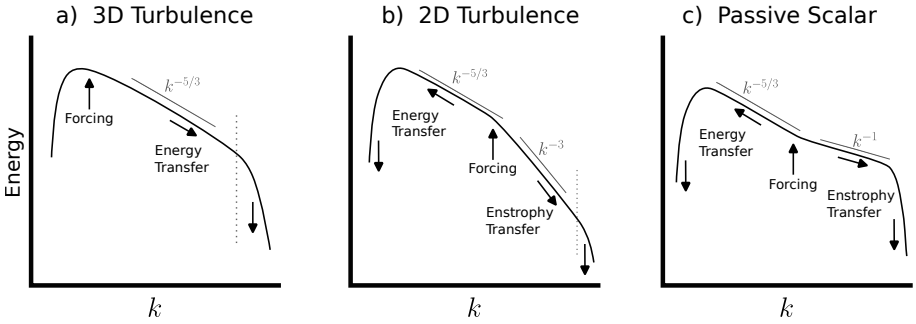


Figure 6.1: A sketch of the key scalings and energy transfers in different turbulent systems. Here the arrows present the flow of energy or enstrophy depending on the circumstance. The passive scalar regime shown here is that of 2D passive scalar turbulence [Vallis, 2017].

A power law for the energy and enstrophy spectra can be found using a dimensional analysis of Equation 6.1. To begin with, we introduce scales for the length (L), and time (T). Given this, velocity scales as $U \sim LT^{-1}$, the wavenumber as L^{-1}, and energy has a scale $E \sim U^2 \sim L^2T^{-2}$, and therefore the energy spectrum scales as $L^2T^{-2}(L^{-1})^{-1}$. The energy flux ε, or the rate of energy change, therefore has a scale L^2T^{-3}. The energy spectrum is defined to take the form $E(k) = C_E\varepsilon^x k^y$, where C_E is a constant. Taking the scaling that we introduced before, we see that

$$E(k) \sim L^3T^{-2} \sim L^{2x-y}T^{-3x} \sim C_E\varepsilon^x k^y$$

this gives the scaling of energy in the inertial range to scale as $E(k) = C_E\varepsilon^{\frac{2}{3}}k^{-\frac{5}{3}}$. Similarly, the scale of the enstrophy cascade can be found by letting η be the rate of enstrophy injection, and noting that $\Psi \sim L^2T^{-1}$ and therefore the vorticity has scale T^{-1}.

$$E(k) \sim L^3T^{-2} \sim L^{-y}T^{-3x} \sim C_Z\eta^x k^y$$

resulting in a scaling of $E(k) = C_Z\eta^{\frac{2}{3}}k^{-3}$. These scalings are sketched in Figure 6.1b.

6.2.2 Impact of Rotation

Basic theory can show us that uniform rotation itself will have no impact on the flow of a 2D layer. This can be seen by taking the conservation of potential vorticity in 2D ($\mathrm{D}q/\mathrm{D}t = 0$), and setting $f = f_0$, and we end with the two dimensional conservation of vorticity as seen above.

However, things change when we include non-constant rotation, such as the β plane approximation

$$\frac{D}{Dt}(\zeta + \beta y) = \frac{\mathrm{D}\zeta}{\mathrm{D}t} + \beta\frac{\mathrm{d}y}{\mathrm{d}t} = \frac{\partial\zeta}{\partial t} + \mathbf{u}\cdot\nabla\zeta + \beta v = 0$$

There are some key scales that we will come across here. The Rhines scale is the scale where the advection term and the rotation approximately balance

$$L_\beta \sim \sqrt{\frac{U}{\beta}} \tag{6.2}$$

Above this length scale rotation begins to dominate and we see Rossby waves [Vallis, 2017]. To bound the β term, we see that $v \to 0$, meaning that the north-south flow will decrease as scales get larger, and the flow is dominated by zonal flow, leading to jets. At smaller scales the advective flow will dominate and we see turbulence dominates.

6.2.3 Passive Tracer Spectrum

As we will see, at large scales the baroclinic streamfunctions act as a passive tracer being pushed by the mean flow of the barotropic flow. Here we introduce some key properties of passive tracer turbulence.

Given a passive tracer in a fluid, think a coloured dye in water, the turbulent flow will stretch out the dye. This will cause the variance in the tracer, or how patchy the tracer is, to be moved to smaller scales. Using the same scaling argument as shown in Section 6.2.1 we can derive an inertial rate of transfer of variance as

$$\mathcal{P}(k) = \mathcal{K}_\chi A^{-1/2} \chi k^{(n-5)/2} \tag{6.3}$$

where we take $\tau_k = (k^3 \mathcal{E}(k))^{-1/2}$ and we assume that the turbulent energy spectrum is given by $\mathcal{E}(k) = Ak^{-n}$. Note that no matter if we are dealing with 2D or 3D turbulence, the tracer is cascaded to smaller scales. If we are working with 2D turbulence, and we assume that the energy injection is at smaller scales than the tracer injection, we have a range of scales where energy is moving to larger scales and the tracer variance is moving the opposite direction. In this case we have $A = \mathcal{K}\varepsilon^{2/3}$, where ε is the rate of energy to small scales and $n = 5/3$, giving a passive scalar energy spectrum of

$$\mathcal{P}(k) = \mathcal{K}_\chi^{2D} \varepsilon^{-1/3} \chi k^{-5/3} \tag{6.4}$$

and the enstrophy inertial range is given by

$$\mathcal{P}(k) = \mathcal{K}_\chi^{2D} \eta^{-1/3} \chi k^{-1} \tag{6.5}$$

This is sketched in Figure 6.1c.

6.2.4 Turbulence in the Atmosphere

In the atmosphere, turbulence is present at small scales, seen as air rising on hot days and the formation of cumulus clouds. At these scales rotation will have negligible impact on the flow. At the same time we can see turbulent like structures in synoptic systems, where the length scales of the systems (> 1000km) is much greater than the height of the atmosphere [Holton, 2004]. Already this means we could include eddies ranging from the synoptic scale (10^6m) to the minimum length scale of the smallest eddies before molecular

friction dominates (10^{-3}m), which covers over nine orders of magnitude. However, as mentioned before, because of the large horizontal scales compared with the vertical scale of the atmosphere, it has been hypothesised that the large scale turbulence in the atmosphere has a similar behaviour to 2D turbulence [Charney, 1971].

Geostrophic turbulence is turbulence that occurs in flows that are stably stratified and in near geostrophic balance [Vallis, 2017]. This stratification can, in some instances, allow for further information to be gleamed on the flow, compared with solving the turbulence problem in other situations.

As discussed in Section 1.2, the most simplistic model describing large scale quasi-geostrophic flows are the two layer quasigeostrophic equations

$$\frac{\partial q_i}{\partial t}+J(\psi_i,q_i)+\beta\frac{\partial \psi_i}{\partial x}=0,\quad q_1=\nabla^2\psi_1+\frac{1}{2}k_R^2(\psi_2-\psi_1),\quad q_2=\nabla^2\psi_2+\frac{1}{2}k_R^2(\psi_1-\psi_2) \tag{6.6}$$

where J is the Jacobian, and $k_R^{-1}=NH/(2\sqrt{2}f_0)$ is the Rossby radius of deformation. Here N is the Brunt–Väisälä frequency, H is the width of the fluid layer, and f_0 is the first order approximation of the Coriolis parameter. This system can be looked at in terms of barotropic ($\psi=\frac{1}{2}(\psi_1+\psi_2)$) and baroclinic ($\theta=\frac{1}{2}(\psi_1-\psi_2)$) streamfunctions, which results in the equations (setting $\beta=0$ for the time being)

$$\begin{aligned}\frac{\partial}{\partial t}\nabla^2\psi+J\left(\psi,\nabla^2\psi\right)+J\left(\theta,\left(\nabla^2-k_R^2\right)\theta\right)&=0\\ \frac{\partial}{\partial t}\left(\nabla^2-k_R^2\right)\theta+J\left(\theta,\nabla^2\psi\right)+J\left(\psi,\left(\nabla^2-k_R^2\right)\theta\right)&=0\end{aligned} \tag{6.7}$$

At scales larger than the deformation radius the equations will simplify to a system of two dimensional flow in terms of the barotropic variables, that are forced by the baroclinic variables. The baroclinic variables are described by the same equation as a passive scalar. This can be seen by assuming $\nabla^2\sim k_n^2\ll k_R^2$, meaning that in terms including both ∇^2 and k_R^2, in Equation 6.7, the k_R^2 terms dominate [Vallis, 2017]. In addition, we note that $J(\theta,k_R^2\theta)=0$. This results in

$$\begin{aligned}\frac{\partial}{\partial t}\nabla^2\psi+J\left(\psi,\nabla^2\psi\right)+J\left(\theta,\nabla^2\theta\right)&=0\\ \frac{\partial\theta}{\partial t}+J\left(\psi,\theta\right)&=0\end{aligned} \tag{6.8}$$

The barotropic streamfunction equation is now the barotropic equation forced by the interaction of the baroclinic modes. The baroclinic streamfunction equation is the equation of a passive scalar, advected by the barotropic flow.

If we ignore the baroclinic streamfunctions for the moment, by setting $\theta=0$, we see that the barotropic equation acts as the 2D vorticity equation, Equation 6.1. This means that we expect turbulence at these scales to behave as 2D turbulence which results in an inverse cascade in energy $E(k)=C_E\varepsilon^{\frac{2}{3}}k^{-\frac{5}{3}}$, as shown in Figure 6.1b, for scales larger than the forcing. At the same time, we expect the baroclinic modes to act as a passive tracer, with enstrophy and energy cascading to smaller scales. It can be shown (see [Vallis,

2017]) that the energies in each of these two spectra are approximately the same, and as the energy density of the first is $(\nabla\psi)^2$ and the latter is $(\nabla\theta)^2 + k_R^2\theta^2 \sim k_R^2\theta^2$, this means that $(\nabla\theta)^2 \sim k_R^2\theta^2$, which results in $|\psi| \gg |\theta|$.

At scales smaller than the deformation radius we see that the k_R^2 terms in Equation 6.7 can be ignored. By using the original expression in Equation 6.6, we see that $q_i \approx \nabla^2\psi_i$, meaning the two layers become decoupled, and enstrophy from baroclinic instability cascades to smaller scales.

6.2.5 Shell models for 2D turbulence

Shell models present the flow equations as a spectral model, with a severe truncation on how nonlinear interactions can occur [Bohr et al., 1998]. The shell model for two or three dimension turbulence is given by the Sabra model [L'vov et al., 1998], shown in Equation 6.9, which is a modified version of the GOY model [Obukhov, 1971; Gledzer, 1973; Desnianskii and Novikov, 1974]. The advantage of the Sabra model over the GOY model is that the strong statistical locality induced by the phase invariance means that the energy spectra do not suffer from the unrealistic period-three oscillations [Biferale, 2003]. The model can be set up for either two or three dimensional turbulence by altering the coefficients (a, b, c) to either conserve energy, and enstrophy (2D) or helicity (3D)

$$\frac{\mathrm{d}u_n}{\mathrm{d}t} = ik_n(au^*_{n+1}u_{n+2} + bu^*_{n-1}u_{n+1} - cu_{n-2}u_{n-1}) - \nu k_n^2 u_n + f_n \tag{6.9}$$

However, it has been demonstrated that these shell model have a poor connection with 2D turbulence [Aurell et al., 1994]. This is due to the severe reduction in the number of degrees of freedom in each shell. This results in the inverse energy flux is overwhelmed by equilibrium fluctuations all known models for 2D turbulent flows that conserve energy and enstrophy [De Pietro et al., 2015]. This means that the energy dynamics in the model resemble a kind of thermal or randomized steady state, rather than an organized energy cascade like in real turbulence [Ditlevsen, 2012]. As a result of there only being one complex variable per shell, the inverse energy cascade cannot properly form due to the different role played by the equipartition solutions [Alexakis and Biferale, 2018].

Methods to overcome this include adding additional variables [Aurell et al., 1994, 1997], altering the scaling between the nonlinear terms [Gilbert et al., 2002], and introducing stochastic variables [Ditlevsen, 2012]. Each of these approaches have their own trade offs, however. In our study we are only expecting one inverse cascade. This is because we are not including small scale injection of energy, which would be expected to cascade to larger scales in 2D turbulence theory. For this reason, we have used a more traditional shell model approach, accepting the limitations.

6.3 Model Development

As discussed before, in this study we use the two layer quasi-geostrophic model. This model provides the minimal basis for modelling large scale atmospheric behaviour in the

midlatitudes [O'Brien and Branscome, 1989; Charney and DeVore, 1979]. The model is suitable for use in studying the large scale motion of the midlatitudes, where the β-plane approximation holds. This includes scales above a few hundred kilometres, below this the assumption of small vertical movement does not hold.

6.3.1 Spectral Model

We begin by expanding the two-layer QG equations using a Fourier series, in a similar manner that was shown in Section 2.2, by setting the fluid in a square with periodic domain of size L. For the time being we have set $\beta = 0$. We denote the barotropic and baroclinic streamfunctions as

$$\psi(x,y,t) = \sum_k \tilde{\psi}(\mathbf{k},t)e^{i\mathbf{k}\cdot\mathbf{x}} \qquad \theta(x,y,t) = \sum_k \tilde{\theta}(\mathbf{k},t)e^{i\mathbf{k}\cdot\mathbf{x}} \tag{6.10}$$

where $\mathbf{k} = \hat{\imath}k_x + \hat{\jmath}k_y$, $k^2 = k_x^2 + k_y^2$. We substitute these into Equation 6.7

$$\begin{aligned}
\frac{\partial}{\partial t}\left(\sum_{\mathbf{k}} -\mathbf{k}^2\tilde{\psi}(\mathbf{k},t)e^{i\mathbf{k}\cdot\mathbf{x}}\right) = &\sum_{\mathbf{p}} \mathrm{p}_x\tilde{\psi}(\mathbf{p},t)e^{i\mathbf{p}\cdot\mathbf{x}} \cdot \sum_{\mathbf{q}} -\mathrm{q}_y\mathbf{q}^2\tilde{\psi}(\mathbf{q},t)e^{i\mathbf{q}\cdot\mathbf{x}} \\
&- \sum_{\mathbf{p}} \mathrm{p}_y\tilde{\psi}(\mathbf{p},t)e^{i\mathbf{p}\cdot\mathbf{x}} \cdot \sum_{\mathbf{q}} -\mathrm{q}_x\mathbf{q}^2\tilde{\psi}(\mathbf{q},t)e^{i\mathbf{q}\cdot\mathbf{x}} \\
&+ \sum_{\mathbf{p}} \mathrm{p}_x\tilde{\theta}(\mathbf{p},t)e^{i\mathbf{p}\cdot\mathbf{x}} \cdot \sum_{\mathbf{q}} \mathrm{q}_y(-\mathbf{q}^2 - k_R^2)\tilde{\theta}(\mathbf{q},t)e^{i\mathbf{q}\cdot\mathbf{x}} \\
&- \sum_{\mathbf{p}} \mathrm{p}_y\tilde{\theta}(\mathbf{p},t)e^{i\mathbf{p}\cdot\mathbf{x}} \cdot \sum_{\mathbf{q}} \mathrm{q}_x(-\mathbf{q}^2 - k_R^2)\tilde{\theta}(\mathbf{q},t)e^{i\mathbf{q}\cdot\mathbf{x}}
\end{aligned} \tag{6.11}$$

$$\begin{aligned}
\frac{\partial}{\partial t}\left(\sum_{\mathbf{k}} -\mathbf{k}^2\tilde{\theta}(\mathbf{k},t)e^{i\mathbf{k}\cdot\mathbf{x}}\right) = &\sum_{\mathrm{p}} \mathrm{p}_x\tilde{\theta}(\mathbf{p},t)e^{i\mathbf{p}\cdot\mathbf{x}} \cdot \sum_{\mathbf{q}} -\mathrm{q}_y\mathbf{q}^2\tilde{\psi}(\mathbf{q},t)e^{i\mathbf{q}\cdot\mathbf{x}} \\
&- \sum_{\mathbf{p}} \mathrm{p}_y\tilde{\theta}(\mathbf{p},t)e^{i\mathbf{p}\cdot\mathbf{x}} \cdot \sum_{\mathbf{q}} -\mathrm{q}_x\mathbf{q}^2\tilde{\psi}(\mathbf{q},t)e^{i\mathbf{q}\cdot\mathbf{x}} \\
&+ \sum_{\mathbf{p}} \mathrm{p}_x\tilde{\psi}(\mathbf{p},t)e^{i\mathbf{p}\cdot\mathbf{x}} \cdot \sum_{\mathbf{q}} \mathrm{q}_y(-\mathbf{q}^2 - k_R^2)\tilde{\theta}(\mathbf{q},t)e^{i\mathbf{q}\cdot\mathbf{x}} \\
&- \sum_{\mathbf{p}} \mathrm{p}_y\tilde{\psi}(\mathbf{p},t)e^{i\mathbf{p}\cdot\mathbf{x}} \cdot \sum_{\mathbf{q}} \mathrm{q}_x(-\mathbf{q}^2 - k_R^2)\tilde{\theta}(\mathbf{q},t)e^{i\mathbf{q}\cdot\mathbf{x}}
\end{aligned}$$

we multiply both sides by $e^{-i\mathbf{k}\cdot\mathbf{x}}$, to remove the exponential on the left hand sides, and we integrate over the domain. This provides us with an equation that describes the evolution for the wavenumber $\mathbf{k}$. As the Fourier modes are orthogonal, the only non-zero integrals

are when for two wave numbers $\mathbf{p}$ and $\mathbf{q}$ such that $\mathbf{p}+\mathbf{q}=0$. This results in

$$\begin{aligned}\frac{\partial}{\partial t}\tilde{\psi}(\mathbf{k},t) &= \sum_{\mathbf{p},\mathbf{q}} A(\mathbf{k},\mathbf{p},\mathbf{q})\tilde{\psi}(\mathbf{p},t)\tilde{\psi}(\mathbf{q},t) \\ &\quad + \sum_{\mathbf{p},\mathbf{q}} B(\mathbf{k},\mathbf{p},\mathbf{q})\tilde{\theta}(\mathbf{p},t)\tilde{\theta}(\mathbf{q},t) \\ \frac{\partial}{\partial t}\tilde{\theta}(\mathbf{k},t) &= \sum_{\mathbf{p},\mathbf{q}} C(\mathbf{k},\mathbf{p},\mathbf{q})\tilde{\theta}(\mathbf{p},t)\tilde{\psi}(\mathbf{q},t) \\ &\quad + \sum_{\mathbf{p},\mathbf{q}} D(\mathbf{k},\mathbf{p},\mathbf{q})\tilde{\psi}(\mathbf{p},t)\tilde{\theta}(\mathbf{q},t)\end{aligned} \tag{6.12}$$

where the triad coefficients are defined

$$\begin{aligned}A(\mathbf{k},\mathbf{p},\mathbf{q}) &= \frac{\mathbf{q}^2}{\mathbf{k}^2}(\mathrm{p}_x\mathrm{q}_y - \mathrm{p}_y\mathrm{q}_x)\delta(\mathbf{p}+\mathbf{q}-\mathbf{k}) \\ B(\mathbf{k},\mathbf{p},\mathbf{q}) &= \frac{\mathbf{q}^2}{\mathbf{k}^2}(\mathrm{p}_x\mathrm{q}_y - \mathrm{p}_y\mathrm{q}_x)\delta(\mathbf{p}+\mathbf{q}-\mathbf{k}) \\ C(\mathbf{k},\mathbf{p},\mathbf{q}) &= \frac{\mathbf{q}^2}{\mathbf{k}^2+k_R^2}(\mathrm{p}_x\mathrm{q}_y - \mathrm{p}_y\mathrm{q}_x)\delta(\mathbf{p}+\mathbf{q}-\mathbf{k}) \\ D(\mathbf{k},\mathbf{p},\mathbf{q}) &= \frac{\mathbf{q}^2+k_R^2}{\mathbf{k}^2+k_R^2}(\mathrm{p}_x\mathrm{q}_y - \mathrm{p}_y\mathrm{q}_x)\delta(\mathbf{p}+\mathbf{q}-\mathbf{k})\end{aligned} \tag{6.13}$$

where the B coefficient is simplified by noticing that $J(\theta,k_R^2\theta)=0$, and $\delta(x)$ is the Kronecker delta, where $\delta(x)=1$ when $x=0$, and is 0 otherwise. Therefore, the only non-zero terms are where $\mathbf{p}+\mathbf{q}-\mathbf{k}=0$. These are called triads (collection of wavenumbers that add to zero) and they present the modes where the the energy transfers take place [Vallis, 2017; Ditlevsen, 2010].

We now non-dimensionalise the model by taking the scaling transformations

$$(\tilde{t},\ \tilde{\mathbf{k}},\ \tilde{\psi},\ \tilde{\theta}) \to (f_0 t,\ L\mathbf{k},\ L^{-2}f_0^{-1}\psi,\ L^{-2}f_0^{-1}\theta)$$

Using this scaling we see that each of the interaction coefficients scale as L^{-2}, and we introduce the lower case letter as the non-dimensonalised coefficient ($A(\mathbf{k},\mathbf{p},\mathbf{q}) \to L^{-2}a(\mathbf{k},\mathbf{p},\mathbf{q})$). In other words, we see that the interaction coefficients have the same

dimension as the square of the wavenumber, as $k = 1/L$

$$\begin{aligned}\frac{\partial}{\partial t}\psi(\mathbf{k},t) &= \sum_{\mathbf{p},\mathbf{q}} k^2 a(\mathbf{k},\mathbf{p},\mathbf{q})\psi(\mathbf{p},t)\psi(\mathbf{q},t) \\ &+ \sum_{\mathbf{p},\mathbf{q}} k^2 b(\mathbf{k},\mathbf{p},\mathbf{q})\theta(\mathbf{p},t)\theta(\mathbf{q},t) \\ \frac{\partial}{\partial t}\theta(\mathbf{k},t) &= \sum_{\mathbf{p},\mathbf{q}} k^2 c(\mathbf{k},\mathbf{p},\mathbf{q})\theta(\mathbf{p},t)\psi(\mathbf{q},t) \\ &+ \sum_{\mathbf{p},\mathbf{q}} k^2 d(\mathbf{k},\mathbf{p},\mathbf{q})\psi(\mathbf{p},t)\theta(\mathbf{q},t)\end{aligned} \tag{6.14}$$

6.3.2 Shell Model

To create a shell model from the spectral model derived above, we specify a set number of wave modes that we investigate. To cover a large number of scales in a small number of degrees of freedom usually the wavenumbers of the shells are defined to increase exponentially: $k_n = k_0\lambda^n$, where $1 < n \in \mathbb{R}$, but commonly set to $\lambda = 2$ or $\lambda = \varphi$, where φ is the golden ratio. Next, we severely restrict the possible non-linear interactions between shells, in this case given a wave number of k_n, we only include the two nearest neighbours above and below in wave number space ($k_{n\pm1}$, $k_{n\pm2}$). There has been debate over the accuracy of limiting interactions to the nearest neighbours in different forms of turbulence [Plunian and Stepanov, 2007; Verma et al., 2005]. However, for our case we are aiming to begin by building the most simple model representing geostrophic turbulence, so we have used only the two nearest neighbours.

Together, following the approach first used in Gledzer [1973] and later modified in L'vov et al. [1998], this results in the interaction coefficients being expressed as

$$a(k_n) = a_{1,n}\phi^*_{n+1}\phi_{n+2} + a_{2,n}\phi^*_{n-1}\phi_{n+1} + a_{3,n}\phi_{n-2}\phi_{n-1} \tag{6.15}$$

We now let the streamfunctions take complex values, done by letting $\psi^*_i(\mathbf{k}) = \psi_i(-\mathbf{k})$. The reason for introducing complex variables is to provide a second degree of freedom. It was found that single degree of freedom systems were overly constrained and convergence was slow [Ditlevsen, 2010]. The energy is now defined using complex conjugates: $E = \sum_n k_n^2\psi\psi^*/2$.

Altogether, this produces the coupled (unforced) shell model given in Equation 6.16, which we call the QG (quasigeostrophic) shell model

$$\begin{aligned}\dot{\psi}_n &= k_n^2 Q_n(\psi,\psi,a) + k_n^2 Q_n(\theta,\theta,b) \\ \dot{\theta}_n &= \frac{k_n^4}{k_n^2 + k_R^2} Q_n(\theta,\psi,c) + k_n^2 Q_n(\psi,\theta,d)\end{aligned} \tag{6.16}$$

where $Q_n(\phi,\gamma,\alpha) = i\left[\alpha_1\phi^*_{n+1}\gamma_{n+2} + \alpha_2\phi^*_{n-1}\gamma_{n+1} - \alpha_3\phi_{n-2}\gamma_{n-1}\right]$, and α contains the three interaction coefficients. This model has uses the same nonlinear interaction as shell models introduced by L'vov et al. [1998]; Yamada and Ohkitani [1987, 1988]; Gledzer [1973]. The main difference in this model, is that we have two clear scales, $k_R^2 \gg k_n^2$ and $k_R^2 \ll k_n^2$.

6.3.3 Energy Balance

To calculate the value of the coefficients, we use conditions where the model must conserve specific quantities [Vallis, 2017]. Namely, conservation of energy

$$\frac{\mathrm{d}E}{\mathrm{d}t} = \frac{\mathrm{d}}{\mathrm{d}t}\left(\int_A (\nabla\psi)^2\,\mathrm{d}A + \int_A \left[(\nabla\theta)^2 + k_R^2\theta^2\right]\mathrm{d}A\right) = 0$$

where energy is the sum of the barotropic and baroclinic energies. The model must also conserve enstrophy

$$\frac{\mathrm{d}Z}{\mathrm{d}t} = \frac{\mathrm{d}}{\mathrm{d}t}\left(\int_A \left(\nabla^2\psi\right)^2\,\mathrm{d}A + \left[\left(\nabla^2 - k_R^2\right)\theta\right]^2\,\mathrm{d}A\right) = 0$$

These conservation properties can be described for the spectral shell model

$$\begin{aligned}
T &= \frac{1}{2}\sum_n k_n^2\psi_n^2 & \frac{\mathrm{d}T}{\mathrm{d}t} &= \sum_n k_n^2\psi_n^*\dot{\psi}_n \\
C &= \frac{1}{2}\sum_n \left[k_n^2 + k_R^2\right]\theta_n^2 & \frac{\mathrm{d}C}{\mathrm{d}t} &= \sum_n \left[k_n^2 + k_R^2\right]\theta_n^*\dot{\theta}_n \\
Z &= \sum_n k_n^4\psi_n^2 + [k_n^2 + {k_R}^2]^2\theta_n^2 & \frac{\mathrm{d}Z}{\mathrm{d}t} &= \sum_n k_n^4\psi_n^*\dot{\psi}_n + [k_n^2 + {k_R}^2]^2\theta_n^*\dot{\theta}_n
\end{aligned} \tag{6.17}$$

In the case where there is no forcing on the shell model, we expect energy and enstrophy to be conserved. In the purely barotropic case we have $\theta = 0$, which reduces the QG shell model to the Sabra shell model

$$\dot{\psi}_i = a_1\psi^*_{n+1}\psi_{n+2} + a_2\psi^*_{n-1}\psi_{n+1} - a_3\psi_{n-2}\psi_{n-1}$$

For this system to conserve energy and enstrophy, we can use the definitions in Equations 6.17 and find that and the energy balance is given by

$$a_1 = \alpha, \qquad a_2 = -\frac{1+\lambda^2}{\lambda^6}\alpha, \qquad a_3 = \frac{1}{\lambda^{10}}\alpha \tag{6.18}$$

.

When $\theta \neq 0$ the purely barotropic energy balance is satisfied in the same manner (providing the coefficients for a and b), however we now also have the triads that involve two baroclinic modes and one barotropic. This leads to slightly convoluted coefficients,

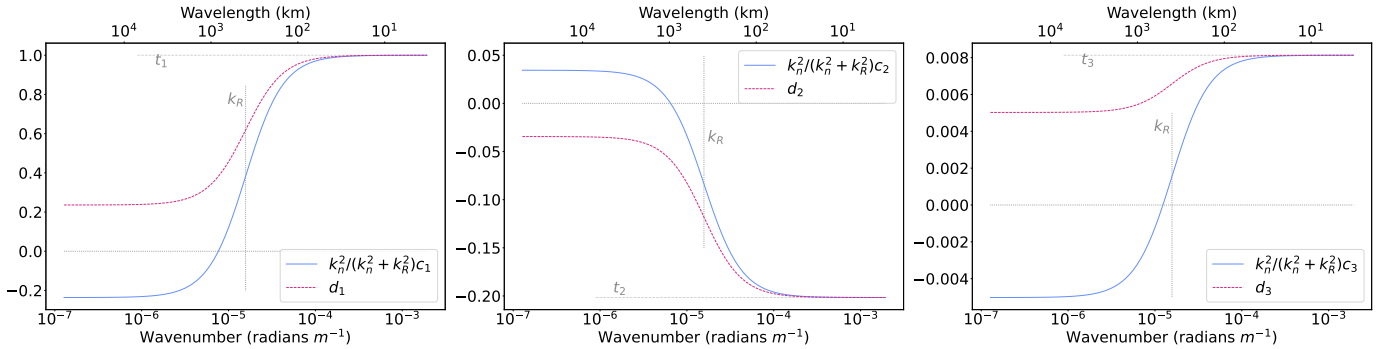


Figure 6.2: The value of the coefficients of the baroclinic equation c_i and d_i. We see that at small scales they are both equal, and match the barotropic coefficients (shown as grey lines). The transition between the two regimes occurs at the Rossby radius of deformation (k_R)

.

but they are calculated using the same process of requiring the energy and enstrophy to balance

$$\begin{aligned} c_1(n) &= \alpha\frac{\lambda^2(\lambda^2-1)k_n^2-k_R^2}{\lambda^2(\lambda^2-1)k_n^2} & d_1(n) &= \alpha\frac{\lambda^2(\lambda^2-1)k_n^2+k_R^2}{\lambda^2(\lambda^2-1)(k_n^2+k_R^2)} \\ c_2(n) &= -\alpha\frac{(\lambda^4-1)k_n^2-k_R^2}{\lambda^6(\lambda^2-1)k_n^2} & d_2(n) &= -\alpha\frac{(\lambda^4-1)k_n^2+k_R^2}{\lambda^6(\lambda^2-1)(k_n^2+k_R^2)} \\ c_3(n) &= \alpha\frac{(\lambda^2-1)k_n^2-k_R^2}{\lambda^{10}(\lambda^2-1)k_n^2} & d_3(n) &= \alpha\frac{(\lambda^2-1)k_n^2+k_R^2}{\lambda^{10}(\lambda^2-1)(k_n^2+k_R^2)} \end{aligned} \tag{6.19}$$

The derivation of the coefficients given in Equations 6.18 and 6.19 are provided in Appendix E.1.

6.3.4 Energy Transfers

Looking now at the energy transfers between triads for this model, we define the correlator function [Ditlevsen, 2010]

$$\Delta_n = k_{n-1}^4 \mathrm{Im}(\psi_{n-1}^*\psi_n^*\psi_{n+1}) \tag{6.20}$$

and using the definitions for energy and enstrophy for the purely barotropic atmosphere, and considering only the terms with shell numbers $(n-1, n, n+1)$ as this is the only triad centred on n, this gives

$$\begin{aligned} \dot{T}_{n-1} &= \Delta_n & \dot{Z}_{n-1} &= k_{n-1}^2\Delta_n \\ \dot{T}_n &= -\frac{\lambda^2+1}{\lambda^2}\Delta_n & \dot{Z}_n &= -(\lambda^2+1)k_{n-1}^2\Delta_n \\ \dot{T}_{n+1} &= \frac{1}{\lambda^2}\Delta_n & \dot{Z}_{n+1} &= \lambda^2 k_{n-1}^2\Delta_n \end{aligned}$$

here we see that $\dot{T}_{n-1}+\dot{T}_n+\dot{T}_{n+1}=0$ and $\dot{Z}_{n-1}+\dot{Z}_n+\dot{Z}_{n+1}=0$. We can now calculate the non-linear flux of energy (${}^E\Pi_n$) and enstrophy (${}^Z\Pi_n$) through a given shell n, which is calculated by taking the energy flow through the triads $(n-1,n,n+1)$ and $(n,n+1,n+2)$, which are the only triads that involve transfers through the shell n. We define the nonlinear flux of energy and enstrophy through shell n as

$${}^E\Pi_n = \frac{\mathrm{d}}{\mathrm{d}t}\sum_{m\le n} E_m \qquad {}^Z\Pi_n = \frac{\mathrm{d}}{\mathrm{d}t}\sum_{m\le n} Z_m \tag{6.21}$$

For the purely barotropic case, this results in the following transfers

$$\begin{aligned} {}^E\Pi_n &= \Delta_{n+1} - \lambda^{-2}\Delta_n \\ {}^Z\Pi_n &= \lambda^2 k_{n-1}^2(\Delta_{n+1}-\Delta_n) \end{aligned} \tag{6.22}$$

For the full shell model the energy transfers are calculated by expanding the definition of the correlator function $\Delta_n^{A,B,C} = k_{n-1}^4\mathrm{Im}(A_{n-1}^* B_n^* C_{n+1})$, and doing the same sum over

the modes of shell number $m \leq n$

$$
\begin{aligned}
{}^{E}\Pi_n^{\psi} &= (\Delta_{n+1}^{\psi\psi\psi} - \lambda^{-2}\Delta_n^{\psi\psi\psi}) + (\Delta_{n+1}^{\psi\theta\theta} - (1+\lambda^{-2})\Delta_n^{\theta\psi\theta} + \Delta_n^{\psi\theta\theta}) \\
{}^{E}\Pi_n^{\theta} &= c_1(n)\Delta_{n+1}^{\theta\theta\psi} + [\lambda^4 c_2(n) + c_1(n-1)]\Delta_n^{\theta\theta\psi} \\
&\quad + \frac{k_n^2 + k_R^2}{k_n^2} d_1(n)\Delta_{n+1}^{\theta\psi\theta} + \lambda^4 \frac{k_n^2 + k_R^2}{k_n^2} d_2(n)\Delta_n^{\psi\theta\theta} + \frac{k_{n-1}^2 + k_R^2}{k_{n-1}^2} d_1(n-1)\Delta_n^{\theta\psi\theta}
\end{aligned}
\tag{6.23}
$$

and the same for enstrophy

$$
\begin{aligned}
{}^{E}\Pi_n^{\psi} &= \lambda^2 k_{n-1}^2(\Delta_{n+1}^{\psi\psi\psi} - \Delta_n^{\psi\psi\psi}) + k_{n-1}^2(\lambda^2\Delta_{n+1}^{\psi\theta\theta} - (1+\lambda^2)\Delta_n^{\theta\psi\theta} + \Delta_n^{\psi\theta\theta}) \\
{}^{E}\Pi_n^{\theta} &= (k_n^2 + k_R^2)c_1(n)\Delta_{n+1}^{\theta\theta\psi} + [\lambda^4(k_n^2 + k_R^2)c_2(n) + (k_{n-1}^2 + k_R^2)c_1(n-1)]\Delta_n^{\theta\theta\psi} \\
&\quad + \frac{(k_n^2 + k_R^2)^2}{k_n^2} d_1(n)\Delta_{n+1}^{\theta\psi\theta} + \lambda^4 \frac{(k_n^2 + k_R^2)^2}{k_n^2} d_2(n)\Delta_n^{\psi\theta\theta} \\
&\quad + \frac{(k_{n-1}^2 + k_R^2)^2}{k_{n-1}^2} d_1(n-1)\Delta_n^{\theta\psi\theta}
\end{aligned}
\tag{6.24}
$$

where the coefficients shown above refer to those in Equation 6.19. The coefficients given in Equation 6.18 have already been substituted. A summary of the derivation to find the energy fluxes is provided in Appendix E.2

Structure functions $S_p(R)$ are another tool we can use to investigate how properties of the fluid, such as the velocity, change with the spatial scale R [Biferale, 2003]. In the spectral, shell model world they are given by: $S_p(k_n) = \langle |u_n|^p \rangle$. Scaling arguments can be used to find relationships between the structure functions and the energy dissipation.

6.3.5 Scale Analysis

Large Scales

For scales larger than the Rossby deformation radius ($k_n^2 \ll k_R^2$) the coefficients in the baroclinic equation, given in Equation 6.19, become

$$
c_1 = -d_1 = -\frac{\alpha}{\lambda^2(\lambda^2 - 1)}, \;\; c_2 = -d_2 = \frac{\alpha}{\lambda^6(\lambda^2 - 1)}, \;\; c_3 = -d_3 = -\frac{\alpha}{\lambda^{10}(\lambda^2 - 1)}
$$

here the barotropic equation is the same as the purely barotropic equation (Equation 6.18) but with an additional forcing term coming from the baroclinic terms. This results in a model similar to those that have been introduced to model passive scalar turbulence [Jensen et al., 1992; Wirth and Biferale, 1996; Benzi et al., 1997; Andersen and Muratore-Ginanneschi, 1999; Cohen et al., 2002; Mitra and Pandit, 2005]. As we have seen in Section 6.2.4, the baroclinic models are expected act as a passive scalar in the turbulent flow at large scales in the atmosphere.

While the coefficients are slightly different, it should be noted that the coupling in the model is similar to shell models that are used for modelling magnetohydrodynamic turbu-

lence [Plunian et al., 2013; Lessinnes et al., 2009; Plunian and Stepanov, 2007; Frick and Sokoloff, 1998; Biskamp, 1994]. Many studies have been done on this class of model in this field, and could provide useful insights into the large scale QG shell model.

Small Scales

For scales where $k_n^2 \gg k_R^2$ the coefficients are

$$a_1 = \alpha, \qquad a_2 = -\frac{\alpha(\lambda^2+1)}{\lambda^6}, \qquad a_3 = \frac{\alpha}{\lambda^{10}}$$

where $a_i = b_i = c_i = d_i$. Here we see that all the coefficients become identical and we have a coupled set of equations that closely resembles the purely barotropic equation. At these scales we expect the two atmospheric layers to be decoupled, meaning that each shell model should produce the same behaviour, which is satisfied by the coefficients.

6.3.6 Forcings

We have so far only dealt with the non-linear turbulent transfers in the model, we now turn our focus to look at energy forcings and energy sinks. We will model the input as a forcing into each equation f_n^ψ and f_n^θ for the barotropic and baroclinic equations respectively. In this study we forced the model only using the baroclinic forcing, at large scales to mimic the forcing of baroclinic instability on the atmosphere [Salmon, 1978]. We defined $f_n^\theta = F(1+i)\delta_{nj}/\lambda^{n-4}$ where $j = \{4,5,6\}$. For the model with 30 shells, this corresponds to the forcing taking place at approximately above the order of 10^4km. The forcings used in this chapter are injected at scales larger than the real atmosphere (where the values are between the orders of $10^3 - 10^4$km), but this was done to provide a larger spacing between the injection scale and the Rossby radius of deformation for a clear cascade to form.

At small scales, the energy lost to dissipation through viscosity is modelled using $-\nabla^n\psi$ and projecting onto a set of Fourier modes, we get $-\nu k^n \psi_n$. The conventional choice is $n = 4$, which is what we used, however studies have been done looking at the impact of super-viscosity for $n \geq 6$, which can have some qualitative differences [Maltrud and Vallis, 1991].

We have simplified the removal of energy at large scales. In the QG equations this is done through linear friction between the atmosphere layers and also with the ground [Smith et al., 2002]. Here we have introduced terms to the barotropic and baroclinic equations that act as drag, or friction over large scales, given by $-\eta k_n^{-2}\psi$ and $-\eta k_n^{-2}\theta$ [Ditlevsen and Mogensen, 1996; Aurell et al., 1994].

Lastly, we can approximate the impact of differential rotation using

$$ik_n^{-1}\beta\psi_n \qquad\qquad ik_n^{-1}\beta\theta_n$$

which is the Fourier decomposition of the rotation terms in the QG equations ($\partial_x\psi$), then multiplied by the k_n^{-2} term originating from the time derivatives [Hattori et al., 2004].

The final set of equations are

$$\dot{\psi}_n = k_n^2 Q_n(\psi,\psi,a) + k_n^2 Q_n(\theta,\theta,b) + f_n^{\psi} - \nu k_n^4 \psi_n - \eta k_n^{-2}\psi_n + i k_n^{-1}\beta\psi_n$$

$$\dot{\theta}_n = \frac{k_n^4}{k_n^2 + k_R^2} Q_n(\theta,\psi,c) + k_n^2 Q_n(\psi,\theta,d) + f_n^{\theta} - \nu k_n^4 \theta_n - \eta k_n^{-2}\theta_n + i k_n^{-1}\beta\theta_n \tag{6.25}$$

where $Q_n(\phi,\gamma,\alpha) = \alpha_1\phi^*_{n+1}\gamma_{n+2} + \alpha_2\phi^*_{n-1}\gamma_{n+1} + \alpha_3\phi_{n-2}\gamma_{n-1}$.

6.3.7 Lyapunov Exponents

Lyapunov exponents provide a measure of the growth rates of perturbations, of a given trajectory, in different directions in the state space [Kuptsov and Parlitz, 2012]. We provide an overview of the properties and calculation methods in Section 1.5.2. In this case we have two Lyapunov exponents for each variable, as they are complex valued Yagi et al. [1999]; Kockelkoren et al. [1998]. We introduce real and imaginary components of the streamfunctions to inspect the stability properties for each of the real and imaginary variables, using ($\psi_n = \psi_n^{\mathcal{R}} + i\psi_n^{\mathcal{I}}$), and create a vector

$$\Psi_n = [\psi_1^{\mathcal{R}}, \ldots, \psi_N^{\mathcal{R}}, \psi_1^{\mathcal{I}}, \ldots, \psi_N^{\mathcal{I}}, \theta_1^{\mathcal{R}}, \ldots, \theta_N^{\mathcal{R}}, \theta_1^{\mathcal{I}}, \ldots, \psi_N^{\mathcal{I}}]$$

where N is the number of shells in the model. We will end up with $4N$ Lyapunov exponents and vectors, four for every shell, two barotropic and two baroclinic.

6.4 Results

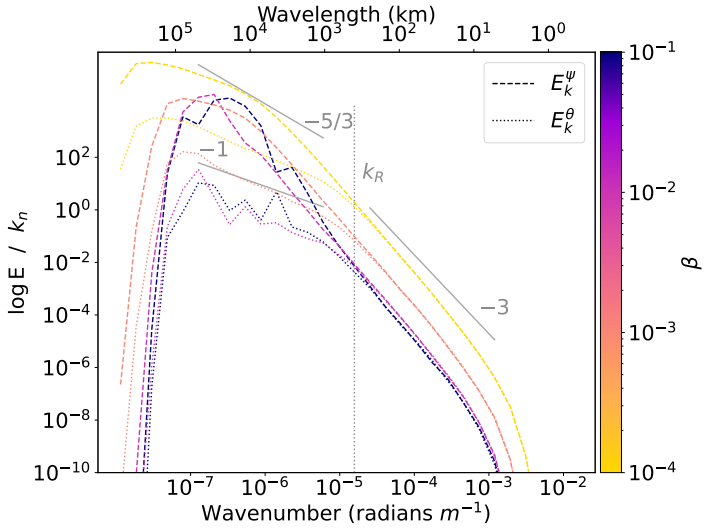
In this section we present some initial findings of the behaviour of the shell model that we introduced in Section 6.3. We begin by presenting the cascading behaviour, and test this for a range of parameter values.

The equations have coefficients that spans $2N\log_{10}\lambda$ orders of magnitude. This is clearly a stiff problem. We used the Backward Differentiation Formula [Curtiss and Hirschfelder, 1952] in the python library scipy [Virtanen et al., 2020] to numerically solve the equations, using a random set of initial conditions.

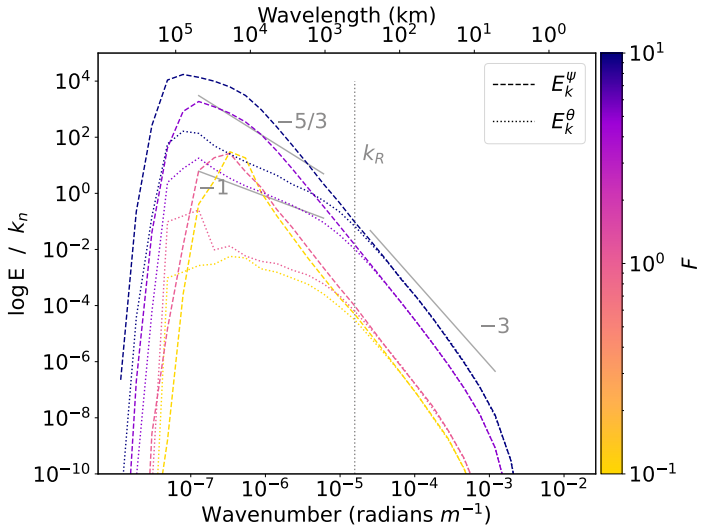
The results were obtained by running the model for different values of: the number of shells, the strength of the forcing, the strength of the sinks (viscosity and large scale friction), and the halting effect of rotation. The results consist of a comparison of the numerical results, and investigation of how well these fit with the theoretical results described in Section. We then investigate the properties of the model itself, looking at the measure of chaos using Lyapunov exponents.

6.4.1 Parameter Sensitivity Analysis

To understand the impact of the parameters on the cascading phenomenon, we analysed the impact of the following parameters on the cascade behaviour: β, F, ν, η, which are

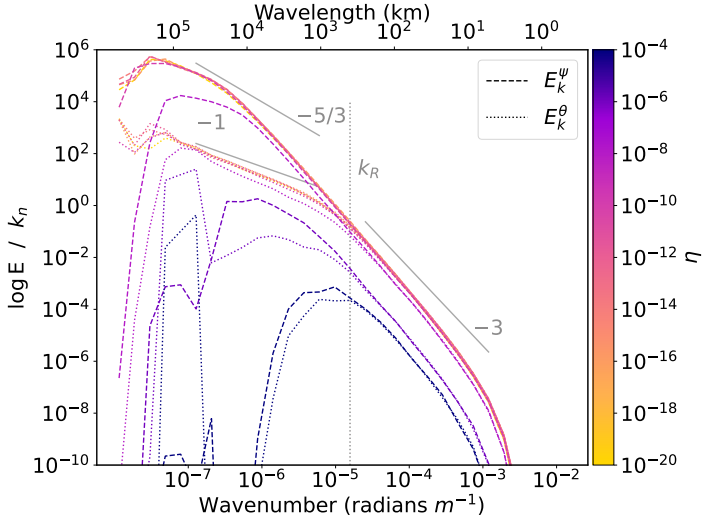


(a) Coriolis forcing β, which primarily impacts large scale shells

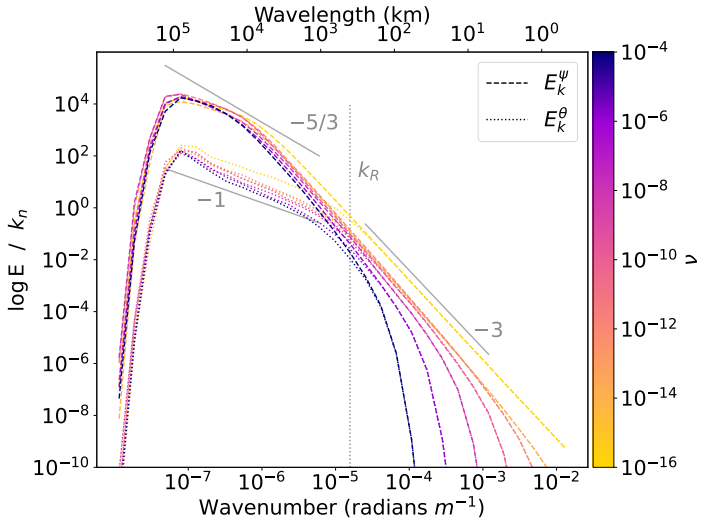


(b) Forcing of large scale baroclinic modes F

Figure 6.3: Sensitivity study for the key parameters in the QG shell model. The kinetic energies for barotropic (dashed) and baroclinic (dotted) energies. Each panel shows the results of varying a different parameter, where the colour bar shows the magnitudes of the parameter value. In these images we fix all parameters, except the stated one, to the values given in Section 6.3.6. The grey lines show the expected cascade slopes.



(a) Large scale removal of energy, or diffusion η



(b) Small scale removal of energy, or dissipation ν

Figure 6.4: Same as Figure 6.3, for parameters η and ν.

Parameter	Default value	Description
Shell Number	30	Number of shells in the model.
k_0	λ^{-15}	Largest scale in the model, approx 10^5km.
λ	$(1+\sqrt{5})/2$	Spacing between each shell, where $k_n = k_0\lambda^n$
β	-	Differential rotation.
F	-	Forcing of the model, modelling baroclinic instability
ν	-	Dissipation, small scales viscosity.
η	-	Diffusion, removal of energy at large scales, i.e. friction

Table 6.1: Parameters in the qg shell model

described in Section 6.3.6, and shown in Table 6.1. The kinetic energies of the barotropic and baroclinic stream functions are shown in Figures 6.3 and 6.4.

Here we see a clear inertial -3 scaling at small scales, pointing towards an enstrophy cascade. This is most clearly seen when the dissipation (ν) is set to low values. At smaller scales, we see that both the magnitudes of the energies of the barotropic and baroclinic kinetic energy are approximately equal. These results are as expected from theory and previous numerical simulations [Salmon, 1978]. At small scales we see a separation in energies between the baroclinic and barotropic stream functions, meaning that $|\theta| \ll |\psi|$, which is expected from theory [Vallis, 2017]. At smaller scales, the baroclinic kinetic energy appears to cascade with approximately $-6/5$ scaling. This is slightly larger than the the scaling of -1 expected from a forward cascade in enstrophy in passive scalar. However, we also expect energy to flow towards smaller scales in the baroclinic streamfunctions, which could impact the scaling.

Generally we see that the shell model successfully captures a dual cascade, and different behaviours either side of the Rossby radius, as desired. The impact of rotation, β, on the model is to impact the scales larger than Rossby radius of deformation. Increasing β appears to reduce the total energy, and increases the variability of the spectrum. This is shown in Figure 6.3a.

Increasing the magnitude of the sink terms (ν, η) clearly removes energy at small or large scales, depending on the parameter. For example, Figure 6.4b shows the spectra for different values of dissipation ν. Here we see that as ν increases the inertial range, where

the energy spectrum shows a -3 scaling, decreases as the dissipation removes more and more energy from larger and larger scales.

For reductions in η, however, there are clearly large jumps in the spectrum, shown in Figure 6.4a. This is due to the input of energy F remaining constant, while the amount of energy removed from large scales increases. As the diffusion becomes dominant the equations can be simplified to $\dot{\theta}_n \approx -\nu k_n^{-2} + \delta_{i,F} F$, resulting in an approximate fixed point for these shells, causing the discontinuous energy spectrum. The only source of energy into the system F shown in Figure 6.3b, impacts the total energy in the system.

To study the flow of both energy and enstrophy in the system, we use the expressions introduced in Section 6.3.4. The resulting energy transfers between the non linear terms are shown in Figures 6.5 and enstrophy transfers in Figure 6.6. The parameters used in these figures were $\{\beta, F, \eta, \nu\} = \{0.001, 10, 1\times10^{-6}, 1\times10^{-8}\}$. In this figure, forward cascades are positive, and negative cascades are shown as negative numbers The resulting flows are similar to those seen in Salmon [1978], and they broadly match the theoretical energy flows [Rhines, 1977]. We see that at small scales the energy transfers go to zero. This is because we have set the dissipation to be relatively large. However, we found for reduced values of ν, there was unrealistic oscillations at smaller scales, which we assume was due to an insufficient removal of enstrophy from small scales.

6.4.2 Lyapunov Analysis

Shell models have been used to study the transitions to chaos and bifurcation structure in turbulent systems and properties of intermittency as relatively low order dynamical systems [Kockelkoren et al., 1998; Kadanoff et al., 1997; Ditlevsen, 1996; Biferale et al., 1995].

We used the approach outlined in Section 6.3.7 to calculate the backwards Lyapunov exponents, called the Lyapunov spectrum, of the QG shell model, as well as the backwards Lyapunov vectors. We calculated the Lyapunov spectrum for the model with different number of shells, to study the impact of model 'resolution', or the number of scales included in the model, on the chaotic nature of the model. The spectrum is shown in Figure 6.7a. Here we can see that there are a large number of small magnitude exponents, likely from the inertial range. At large Lyapunov indices ($j \geq 60$) we see that there are some additional small plateaus for negative Lyapunov exponents. These plateaus originate from large removals of energy at small scales, from the dissipation, and the fact that the model tendencies at these scales are dominated by the removal of energy. These plateaus only originate when the dissipation dominates over the nonlinear transfer of energies.

We also show the normalised Lyapunov spectra, where the Lyapunov exponents are normalised by the Kolmogorov–Sinai entropy H [Yamada and Ohkitani, 1988]. The Kolmogorov–Sinai entropy is the sum of all the positive Lyapunov exponents $H = \sum_{i,\lambda_i>0} \lambda_i$. This is plotted against the Lyapunov index divided by the Kaplan–Yorke dimension, which is defined as

$$D = p + \frac{\sum_{j=1}^{p} \lambda_j}{|\lambda_{p+1}|}$$

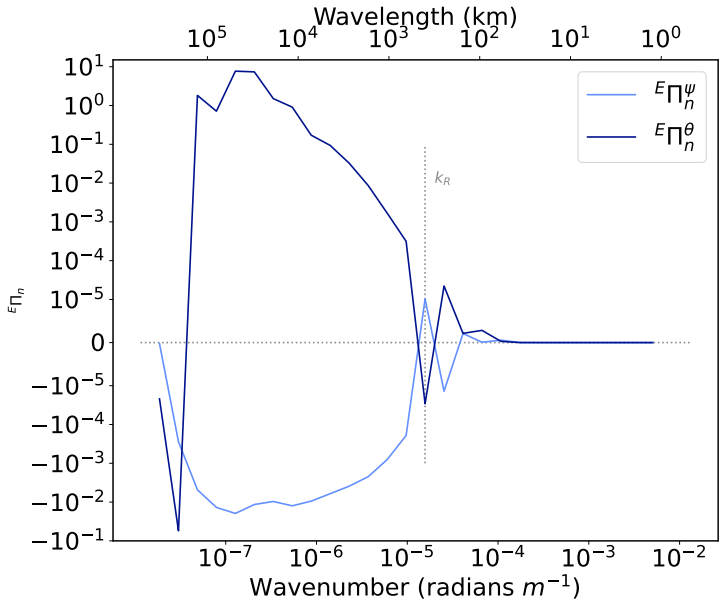


Figure 6.5: Energy transfers for the barotropic and baroclinic modes. We see that there is a forward cascade of energy for the baroclinic modes at large scales. this is injected into the barotropic modes close to k_R, where this creates an inverse cascade to large scales. At small scales we expect the energy transfer to go to zero as there should be an inverse cascade towards the Rossby radius of deformation. Close to k_R we see large variance in the energy flows, which we believe to be due to the transfer of energy at these scales.

where p is the largest index such that $\sum_{i=1}^{p} \lambda_j > 0$. In other words, the fractional part of the definition is the sum of the largest Lyapunov exponents, such that the resulting sum is still positive. This provides a fractional dimension of the strange attractor [Bohr et al., 1998]. The reason for doing this normalisation is to compare the ratio of the dimension of the state space compared with the dimension of the attractor [Ditlevsen, 2010]. This is shown in Figure 6.7b. Here the Lyapunov exponents for $j \leq D$ are dominated by the damping, which characterises the dissipative region of the attractor.The resulting spectra shows similarities compared with the Sabra shell model for two dimensional turbulence, where there is a long plateau for intermediate values of j indicates a large number of low magnitude Lyapunov exponents [Ohkitani and Yamada, 1989].

In this section we have shown that the QG shell model can produce a dual cascade in baroclinic and barotropic kinetic energy spectra. In addition, the energy flows due to the nonlinear interactions with the two nearest neighbours appears to satisfy the expected energy transfers that theory predicts. The model behaves predictably for altering the param-

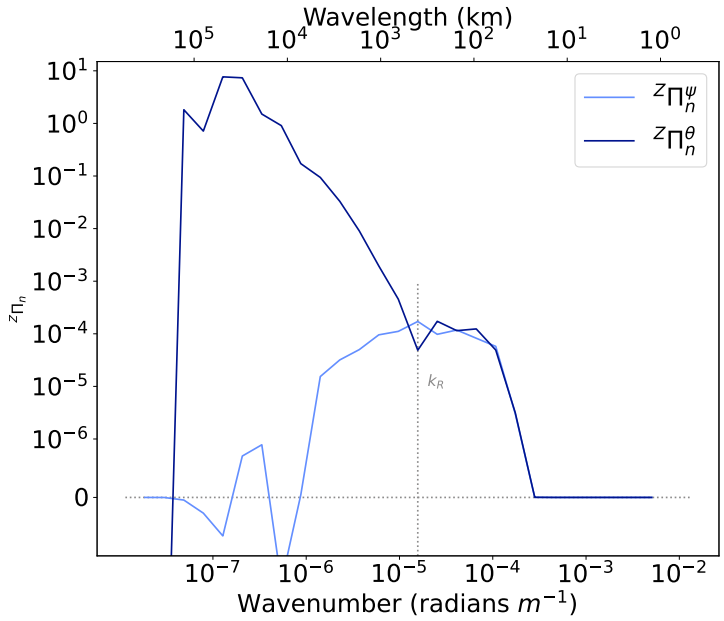
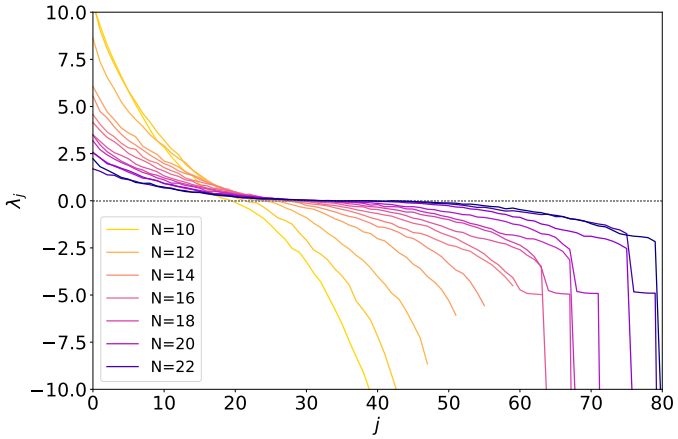


Figure 6.6: Same as Figure 6.5, but for enstrophy. We see that enstrophy is injected into the baroclinic modes at large scales, this then cascades to smaller scales. Around k_R some enstrophy is transferred to the barotropic modes. In this model the enstrophy appears to be injected at wave numbers significantly larger than k_R. The enstrophy in the system continues to cascade to smaller wavenumbers, where it is removed by dissipation, and it goes to 0.

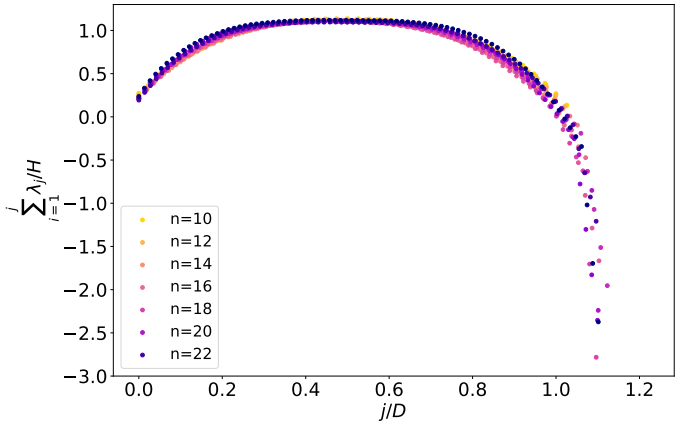
eters of sinks and sources, with the overall inertial energy and enstrophy spectra remaining. Lastly we have analysed the Lyapunov exponents and found that the model displays sensitivity to initial conditions, but also dominated by large negative lyapunov exponents corresponding to the model sinks.

6.5 Discussion and Conclusions

This chapter covered the basics of geostrophic turbulence, and demonstrated how a simple model can be derived to model large scale atmospheric turbulence. This was done by using a shell model to model the cascade properties and energy flows in a two layer baroclinic quasigeostrophic atmosphere. Here, we demonstrated that these energy flows can be modelled using a simple shell model, and that these models can produce similar results to higher dimensional models (such as the eddy-damped Markovian model presented by Salmon [1978]) with a relatively low number of degrees of freedom. In addition we found that the Lyapunov exponents point towards a chaotic system. We found that the dimension



(a) The Lyapunov spectra of the QG shell model, for a range of total shell numbers N. As the number of shells increase (the curves shown in darker purples) the energy sinks become more and more prominent, resulting in very large negative Lyapunov exponents. This also is the cause of the plateaus seen in the spectra for large Lyapunov indices. Here the model parameters are $\{\beta,\ F,\ \nu,\ \eta\} = \{-0.001,\ 10,\ 1\times10^{-6},\ 1\times10^{-10}\}$.



(b) The same Lyapunov spectra λ_j as shown in Figure 6.7a, but for $\sum_{i=1}^{j}\lambda_j/H$ plotted against j/D, where H is the Kolmogorov–Sinai entropy, and D is the Kaplan-Yorke dimension.

Figure 6.7: The Lyapunov spectra of the QG shell model.

of the chaotic attractor (in terms of Kaplan-Yorke) is relatively large, and the system has large negative exponents that correspond to the shells with high dissipation.

More recently, shell models have been used with success in the field of magnetohydrodynamic (MHD) turbulence to investigate the cascade processes of energy and magnetic helicity across scales in a computationally efficient framework [Plunian et al., 2013]. For this reason they have remained a useful modelling tool to this day. As in MHD turbulence, geostrophic turbulence extends across a large magnitude of scales, making it either computationally expensive, or unfeasible, to model directly using the governing equations. Here, shell models can aid with building an understanding of the cascade properties and energy transfers. Currently there is no clear consensus of the energy cascade that is observed in the real atmosphere [Ditlevsen, 2010].

A motivation for this study was to investigate whether simple energy transfer models could tell us something about turbulence in the real atmosphere. We found this model could reproduce the energy transfers as predicted by two layer quasigeostrophic theory [Vallis, 2017; Salmon, 1978; Rhines, 1977], which is reassuring, but not surprising as the QG shell model was derived directly from these equations. However, the next question is how accurate is the theory with observation? The answer is mixed.

Observational data from aircraft measurements show that there is a dual cascade in the atmosphere [Gage and Nastrom, 1986], where the two cascade spectra occurs at approximately 500km, which is close to the Rossby radius of deformation. However, at scales smaller than the deformation radius (on the order of 100km) the atmosphere displays a $-5/3$ spectra, which would point to either an inverse cascade of energy in the 2D turbulent paradigm, or a forward cascade in 3D turbulence. There are at least two possible reasons for this, the first is that energy is injected into the system at small scales, possibly from latent heat release [Ditlevsen, 2010]. The other possibility is that our assumption that the atmosphere displays 2D turbulent properties, or the quasigeostrophic assumptions, breaks down at these scales. Some evidence has been found, for example, that the spectra found at smaller scales is due to interacting gravity waves [Stephan et al., 2022], which cannot be modelled in our two layer QG setup.

However, at scales close to and slightly smaller than the deformation radius a -3 spectra cascade is observed, which would point to a cascade of enstrophy. Another explanation could be that in the QG shell model we have left a large spacing between the Rossby deformation radius and the Rhines scale, where the Coriolis force becomes dominant, whereas in the real atmosphere this separation can be smaller, depending on latitude, which could result in a limited distance in wavenumber space for the inverse cascade to form in the real atmosphere [Vallis, 2017].

To complicate matters further different observational and reanalysis data sets do not agree on the presence of a dual cascade in the atmosphere. Reanalysis data from ECMWF found an approximate spectra of -3 for smaller scales, and an accompanying forward transfer of enstrophy. In addition there was an inverse cascade of energy at larger scales, but this was not clear from the energy spectra [Straus and Ditlevsen, 1999]. More recently,

the spectral energy in a number of atmospheric models, and reanalysis data, was analysed [Stephan et al., 2022]. It was found that while the models agreed on the synoptic and sub-synoptic canonical shape of the spectra, there were significant differences in total energy levels, spectral slopes and spectral crossing scales of the energy spectra. This shows that there are still uncertainties in the key processes contributing to turbulence in the atmosphere, especially at sub-grid scales. This would suggest the shell model introduced in this paper may not be accurate for sub-synoptic scales.

Another motivation for this study was to investigate the hypotheses that severe truncations in the number of wave modes, included in spectral models, could incorrectly model the energy flows in such models, and thus lead to inaccurate solutions due to over energised modes [Cehelsky and Tung, 1987]. We believe shell models, such as the one introduced in this study, could provide a cheap means for testing energy flows in a two layer set up, and for estimating the spectra that should be expected.

As mentioned in this study, shell models struggle with accurately modelling the dual cascade in two dimensional turbulence [Aurell et al., 1994], due to the formation of a steady state solution. In this study we found three cascading behaviours, one for each of the baroclinic and barotropic streamfunctions at large scales, and a single behaviour at scales smaller than the deformation radius. This behaviour is caused by the transition of the interaction coefficients in the baroclinic equation. In the barotropic equation, however, the coefficients remain fixed either side of the deformation radius, and therefore this component of the model should be studied further to investigate whether the behaviour witnessed at large scales is due to a real inverse cascade.

Another potential weakness of this shell model is the harsh reduction in possible nonlinear interactions between scales. A hallmark of turbulence is the highly nonlinear nature of the system, as well as the many interacting scales. Here we have reduced these interactions, and therefore potentially removed key properties of the system. Studies have investigated the impact of the number of nearest neighbours included in the interactions [Plunian and Stepanov, 2007], and a similar approach could be taken with this model to investigate if additional nonlinear interactions are important features in the dynamics.

This reduced order system could also be useful for investigating the structure of the instability properties of the baroclinic and barotropic modes. Work along these lines have been done using the average components of the backwards Lyapunov vectors [Ohkitani and Yamada, 1989], showing three different regions in the stability landscape. This work could be expanded by studying the covariant Lyapunov vectors [Kuptsov and Parlitz, 2012] which can provide information about the degree of coupling between variables through the direction of stable and unstable manifolds.

Reducing the number of degrees of freedom of a model of geostrophic turbulence to approximately 100 will doubtless introduce limitations to what such a model can accurately model. In this chapter we have shown that such a system can however produce realistic energy flows at low computation cost and results that can qualitatively match the theory.

7

Conclusions

The weather in the midlatitudes shows significant variability over the spans of weeks, months, and years. It is the hope that identifying certain repeating behaviours in these cycles could allow us to forecast the weather beyond the current limit of approximately two weeks [Zhang et al., 2019].

The midlatitudes are home to about 40% of the Earth's population [Kummu and Varis, 2011]. It is of great importance to be able to accurately forecast the weather in these regions to protect people from extreme events. As a society we require a good understanding of the weather and climate to plan our infrastructure to withstand extreme events. This will become more difficult with climate change, which is expected to cause a wide range of changes in the Earth's climate. Even small changes to the circulation in the midlatitudes could lead to vast changes in regional climates [Vallis et al., 2015]. For these reasons understanding variability in the midlatitudes is crucial for policy makers and forecasters.

This thesis focused on methods for studying and understanding variability in simplified, low order climate models. The thesis was structured around four questions, that were posed in the introduction.

7.1 Specific Conclusions

7.1.1 Can periodic orbit theory be used to categorise transitions?

To answer this question we focused on the identification of unstable periodic orbits (UPOs) in a coupled land-atmosphere model. This was approached with the aim of understanding transitions in the low frequency variability in the model, that had been found to produce atmospheric blocking like behaviour [Xavier et al., 2024]. In this study we successfully identified the UPOs that clearly cluster the chaotic attractor into different blocking regimes, as well as zonal transition periods. Once the UPOs had been identified, continuation software was used to investigate the potential origin of the clusters in the attractor, by investigat-

ing the routes to chaos from stable periodic orbits. We also investigated the behaviour of blocking onsets and decays by analysing the shadowing properties of specific UPOs.

This work was facilitated by a significant modification of the qgs framework [Demaeyer et al., 2020, 2025], through the use of symbolic Python. In addition we developed an automated workflow for using the AUTO continuation software [Demaeyer and Hamilton, 2025].

We found that the low frequency variability observed in the model is driven by the ground temperature anomaly, which transitions between the western and eastern parts of the domain. The clusters that we identified correspond to these two phases. The anomalies reinforce variability in the atmosphere, thus causing increased atmospheric blocking over the positive temperature anomaly.

We demonstrated how collections of unstable periodic orbits can be used to provide an indication of transitions between regimes. We did this by introducing the concept of cumulative shadowing of collections of UPOs. The orbits contained in these collections were identified using the cumulative shadowing, or the proportion of time a trajectory spends in a neighbourhood of the orbit. Orbits were included in the collection if it was found that this ratio was above a given threshold. Comparing the cumulative shadowing between different collections of UPOs was found to provide an early warning indicator for transitions.

7.1.2 What does quasigeostrophic theory tell us about transitions in the model climate?

We studied the impact of simplified climate change forcings on a reduced order coupled land-atmosphere model. This was done for a selected set of parameters, and by expanding these parameters as a Fourier decomposition to allow for gradients in the parameter values. We conducted this research across several model resolutions to investigate the impact on the results.

It was found that increasing the gradient of the atmospheric insolation increases the north-south gradient in geopotential height, and causes a change in the distribution of blocking in the model climate. This collapse in blocking was linked with the destabilising of a region of the chaotic attractor, highlighted by the disappearance of unstable periodic orbits through fold bifurcations. In general, this response was opposed by altering the direct heat exchange, and the static stability. This reinforces the findings of previous studies that have shown that climate change will cause conflicting changes in the atmosphere, thus making it difficult to determine the final impact of the changes.

Introducing a gradient in the parameter values was found to have large impacts on the low resolution version of the model. The main impact on the model climate was to cause a difference in coupling between the north and south of the model, resulting in shears in the anomaly. Introducing these gradients required modifying the qgs framework, and the resulting model tendencies.

We investigated the impact of model resolution on these results, and found that stepping from the 2×2 model to either the 4×4 or 6×6 model produced differing results

when incorporating climate change forcings. This chapter did not conclude with a clear understanding of the causes for this. However, to try to investigate the discrepancies between resolutions we introduced an intermediate resolution version of the model. This was achieved by identifying the terms in the model tendencies that exist in the higher resolution version, while not in the lower. We then introduced a new parameter which can be changed to transition between model resolutions in a continuous manner. We hope that this version can be useful in the future for identifying the causes for large dynamical differences between the resolutions.

7.1.3 Is it possible to create multiple stable climatologies in a coupled atmosphere model by altering the radiation scheme?

In this chapter we demonstrated how there can exist multiple stable climates in a low order coupled atmosphere model. To do this we modified the radiation scheme in the model, to no longer take a fixed zero order linearisation of the Stefan-Boltzmann law. This resulted in two new models, the dynamic equilibria version, taking the same linearisation but allowing the zero order term to be dynamic, and the T4 version, which completely removed the linearisation. The resulting behaviour and multistability was similar between the dynamic temperature and T4 versions of the model. This implies that fixing the zero order term in the linearisation, or the mean global model temperature, is what removes the possibility of multistability.

Finding multistability in a model, or for the resulting climatology to be impacted, when introducing a different radiation scheme is not surprising. What this study found, however, is that these alterations created the possibility for multiple stable strange attractors to exist for the same parameter values. These strange attractors result in vastly different circulation patterns as well as different average temperatures and the attractors display different levels of predictability, as measured using Lyapunov spectra. It was found using the covariant Lyapunov vectors that the different attractors have a different degree of coupling between the ocean and the atmosphere, which helps explain the resulting Lyapunov spectra.

Sensitivity tests were undertaken, using a similar approach to Vannitsem [2015], for a generalised coupling parameter, and for the atmospheric emissivity. It was found that altering these parameters resulted in windows of parameter values which resulted in between one, two, or three of the strange attractors being stable. Further work could be done here to systematically test the parameters of the model. In addition, the method used to find whether the attractors were stable for given parameter values could be made more robust.

As model resolution was increased, the three distinct attractors found did not extend to the 6×6 version of the model. A possible reason for this could be inaccuracies in low order models to properly model energy flows and sinks in the model [Cehelsky and Tung, 1987]. Further work is required to understand if it is the energy pooling at certain wavenumbers and causing resonances in modes is the cause of markedly different behaviours between model resolutions.

Lastly, in this study we could not find cases where trajectories transitioned from one attractor to the other. Further work is required to test the stability of these attractors to noise, or other periodic forcings, such as the seasonal cycle, and whether such additions could retain the three distinct attractors, while introducing transitions between them.

7.1.4 Are simplified turbulence models able to describe the turbulent energy transfers in a quasigeostrophic atmosphere?

A novel shell model describing geostrophic turbulent energy transfers was introduced in this chapter. We derived this model from the two layer quasigeostrophic equations, and by projecting these equations using a spectral decomposition. The spectral equations were converted into a shell model by reducing the number of degrees of freedom of each wavenumber and harshly restricting the nonlinear energy transfers between shells.

This model was derived to test whether shell models, the simplest family of models that capture the turbulent energy cascade, can be applied to geostrophic turbulence. Geostrophic turbulence introduces additional features that the shell model must capture, namely the change in behaviour and energy flows either side of the Rossby radius of deformation. This was achieved by using variable interaction coefficients, which transition between two limits.

Using the QG shell model, we found that we could reproduce similar results to those found in previous numerical studies using Eddy Damped Markovian models [Salmon, 1978], but using a simpler modelling approach. We found that the energy and enstrophy flows match the expected behaviour from two layer QG theory, and we could reproduce the key scaling expected for forward enstrophy cascades and backwards energy cascades. In addition we did some preliminary investigations into the chaotic properties of the model and found that the chaotic attractor had a large Kaplan-Yorke dimension.

We identified a number of potential weaknesses in the model. These include the limitation in the number of nonlinear transfers included, the potential missing small scale energy sources, and the potential inaccuracy of the barotropic equation to model a dual cascade. The first of these issues, the limitation of nonlinear interactions, was a conscious decision. We aimed to derive the most simple model for geostrophic turbulence, thus requiring the harsh truncation in possible triad interactions. This is a limitation that should be tested, however, to ensure key energy transfers are not missing. This could be done by incorporating additional transfers and investigating how the behaviour changes, potentially as we did in Chapter 4 by incorporating higher order nonlinear terms continuously. The latter potential issue, the inaccuracy of certain shell models when modelling dual cascades, should be tested in the model that we derived. However, the QG shell model can produce both an inverse cascade of energy and a forward cascade in enstrophy across the model, which is due to the variable coefficients that we introduced, which is a significant difference in pre-existing fixed coefficient shell models of 2D turbulence.

7.2 General Conclusions

This thesis investigated the behaviour of simple reduced order quasigeostrophic models of the atmosphere. We did this by primarily focusing on low frequency variability that is produced in the simplified atmosphere, when coupled with another model displaying longer time scales through heat and inertia exchanges. The work here contributes to extending our understanding of the sources of the LFV and how such LFV can be studied using dynamical systems theory by analysing the properties of the chaotic attractor.

We have focused on understanding low frequency variability in such models by investigating the properties of different regions of the attractor. Our approach involved using unstable solutions of the system to understand the basic structure of the chaotic attractor. This structure then allowed us to show that the orbits could provide early warning indicators for transitions between regimes of the attractor. This study was framed in the context of atmospheric blocking and the LFV in the atmosphere that is created by the ground heat. In addition, this study introduced two useful tools for studying the dynamical properties of two layer atmospheres; the symbolic representation of the qgs framework, and the automated running of the AUTO continuation software. These tools were then applied for investigating the impact of climate change in such models. We found that changes in particular parameters led to opposing changes in the model atmosphere. This makes it difficult to predict the magnitude of possible changes in the midlatitude circulation. In addition, we highlighted how the spectral decomposition of models, or the model resolution, can play a large role in the resulting dynamics. We discussed possible methods for investigating the impact of model resolution, and introduced the intermediate resolution version of the model, which we hope could be used to describe the differences between the behaviour in different model resolutions.

We have demonstrated that reduced order coupled models are capable of displaying multiple stable climatologies, which produce multiple different variability patterns. This is an interesting result in the context of circulation patterns and long term repeating patterns in the atmosphere. In addition, transitions between different states are of considerable interest in the context of climate tipping points. Again, these results were dependant on model resolution, again highlighting the importance of future studies into the dynamical reasons for these differences.

We presented a possible approach for studying the energy transfers in the model, using a simplified shell turbulence model. We derived this model from the two layer quasigeostrophic equations, and found that the overall energy transfers match those expected from theory. While this thesis did not apply this model back into the context of coupled spectral atmosphere models, we hope that it can provide an approach to understanding the energy transfers in such models. This is an important line of research to investigate the impact of the collection of energy at particular scales of truncated spectral models.

7.3 Perspectives

The thesis explored how two layer atmosphere models can be used to investigate features of the real atmosphere, in a reduced complexity setup. As a result we gained the following perspectives, and identified the following areas for future studies on the topic.

The two layer quasigeostrophic model can simulate the large scale behaviour of the real world atmosphere. Through couplings, and the introduction of different timescales this behaviour can be modified, and new low frequency variability can emerge. The structure and different regions of the chaotic attractor can aid with understanding and analysing the transitions and behaviours. This thesis showed how structures in the attractor, specifically the unstable periodic orbits, can be used to classify regimes of the attractor.

Between these regimes the UPOs were found to provide early warning signals for transitions. This was done by extending the concept of UPO shadowing to collections of UPOs, whereas in previous studies shadowing was measured either for single UPOs, or a ranked list of UPOs. Here we identified collections of UPOs, where these collections appeared to provide some level of predictability for where a trajectory may pass to next. For example, in Chapter 3 we found that the persistent blocking behaviour, seen through the location of the ground temperature anomaly, resulted from the trajectory remaining in the neighbourhood of a particular set of UPOs. The upcoming decay of the blocking event could be observed in the distance of the trajectory from the collection of UPOs, thus providing an indicator.

There are some limitations with this approach, however. First, finding the UPOs remains computationally expensive, and only becomes more difficult as the number of dimensions increase. The hope of extending this approach to very high dimensional systems, such as more accurate weather models, and finding a useful number of UPOs seems unlikely. However, there are signs that perhaps explicitly finding the UPOs may not be necessary. We believe there is a potential for data analysis, be it machine learning or more traditional methods, to identify near recurrent regions of state space to identify areas where trajectories could remain for longer than expected time periods.

We found that the linearisation in the radiation scheme was removing the possibility of multiple chaotic attractors in the ocean-atmosphere coupled model. This work showed that, for fixed parameter values, there were up to three stable attractors, each displaying different mean temperatures, originating from markedly different low frequency variability patterns. The modifications made to the model, to include other radiation schemes that produce multistability, provide a testbed for a range of further studies. Firstly, we could not produce transitions between these attractors. The stability and resilience of these attractors to perturbations could be investigated for this reason. Secondly, the multistability found in this coupled model could not be reproduced in the land-atmosphere coupled model. This is assumed to be due to either the larger separation in timescales between the heat storage in the ocean and atmosphere, or due to the ocean flow interacting with the atmosphere to produce different LFV. Lastly, the identification of the attractors, in this thesis, for different parameter values was done in a brute force way, and improvements could be made on how to identify changes in attractor structure, or the LFV in the model, in a more systematic

manner. This could be done through the use of continuation software, as we have shown numerous times in this thesis, or by using statistical analysis to identify differences in the behaviour of particular variables across the different attractors.

Truncated spectral models of the two layer quasigeostrophic equations, particularly low resolution models, have been shown to display susceptibility to certain parameter values which causes the model to display particular sets of behaviour. The clear regimes, designating LFV, in low order models can disappear when increasing model resolution. This study has highlighted this issue, where increasing model resolution did not always produce a clear hierarchy in the model behaviour. This is an important outstanding issue with using very low order models, as results from these models would have much more utility if it could be identified whether the behaviour extends to higher resolution versions. This is important for creating the model hierarchy to allow us to distil complex atmospheric behaviour to its key components.

On a more practical side, this thesis introduced a number of modifications to the qgs framework, an open source platform for building and running two layer quasigeostrophic models. First, we introduced two new radiation schemes, the dynamical temperature version, and the T^4 nonlinearised version, as discussed above. Through the use of symbolic python the qgs framework can now output the model tendencies in any programming language, allowing for the model to be used in a number of different pipelines. An example of this is the ability to directly output the tendencies for use in the AUTO continuation software. In addition, we introduced Fourier decompositions of key parameters, to test the impact of parameter gradients on the climatology. Lastly, we created a version of the model which allows for intermediate resolutions, through continuously turning on or off high order terms in the model tendencies. This version of the model could be useful in understanding how model resolution can impact structures in the chaotic attractor. There is the potential to use this alongside an energy transfer model, such as the shell model discussed above, to identify the nonlinear terms which impact the energy flow in the system. This could then be used to test the hypothesis that it is trapped energy at certain wavenumbers that causes the unrealistic responses.

To conclude, we have used a collection of simplified atmospheric coupled models to study variability in the atmosphere. This topic is of great importance for three key reasons. First, through using simplified models of the coupled atmosphere system we can gain a better physical understanding of the behaviour in the real world. Second, variability in the atmosphere, specifically low frequency variability, could provide a method to provide forecasts beyond the typical limit of numerical weather prediction. Finally, the changing climate will impact the circulation of the midlatitudes. To what extent it will impact the behaviour is still uncertain. To understand the potential impacts, models across the complexity hierarchy will need to be employed to ensure the physical behaviour is understood. This is vital for preparing our response to adapt to climate change, and warn of potential catastrophic impacts.

Appendix A

Appendix to the Introduction

A.1 Conservation Form of the PV QG equation

Starting with Equation 1.16 we write this in terms of the geopotential

$$\frac{1}{f_0}\nabla^2\frac{\partial\Phi}{\partial t} = -\mathbf{u}_\mathrm{g}\cdot\nabla\left(\frac{1}{f_0}\nabla^2\Phi + f\right) + f_0\frac{\partial\omega}{\partial p} \tag{A.1}$$

where the geostrophic vorticity can be written in terms of the geopotential using $\zeta_\mathrm{g} = 1/f_0\nabla^2\Phi$.

The thermodynamic equation (Equation 1.18) can also be written in terms of the geopotential, using the hydrostatic equation

$$\left(\frac{\partial}{\partial t} + \mathbf{u}_\mathrm{g}\cdot\nabla\right)\left(-\frac{\partial\Phi}{\partial p}\right) - \sigma\omega = \frac{RJ}{c_p\, p}$$

Multiplying this by f_0/σ, and taking the derivative with respect to p gives us

$$\frac{\partial}{\partial p}\left(\frac{f_0}{\sigma}\frac{\partial}{\partial p}\frac{\partial\Phi}{\partial t}\right) = -\frac{\partial}{\partial p}\left[\frac{f_0}{\sigma}\mathbf{u}_\mathrm{g}\cdot\nabla\left(\frac{\partial\Phi}{\partial p}\right)\right] - f_0\frac{\partial\omega}{\partial p} - f_0\frac{\partial}{\partial p}\left(\frac{RJ}{\sigma c_p\, p}\right) \tag{A.2}$$

We now let $J = 0$, in Equation A.2, to simplify the analysis. This has the impact of assuming that no heat is gained or lost. We now eliminate vertical velocities by adding Equations A.1 and A.2 to remove ω. This results in

$$\left[\nabla^2 + \frac{\partial}{\partial p}\left(\frac{f_0^2}{\sigma}\frac{\partial}{\partial p}\right)\right]\frac{\partial\Phi}{\partial t} = -f_0\mathbf{u}_\mathrm{g}\cdot\nabla\left(\frac{1}{f_0}\nabla^2\Phi + f\right) - \frac{\partial}{\partial p}\left[-\frac{f_0^2}{\sigma}\mathbf{u}_\mathrm{g}\cdot\nabla\left(-\frac{\partial\Phi}{\partial p}\right)\right] \tag{A.3}$$

this equation is called the geopotential tendency equation and it provides a relationship between the local geopotential terms and the distributions of vorticity advection and thickness advection.

This equation can be expressed in a conservation form by using the chain rule of the last term of the equation

$$\frac{\partial}{\partial p}\left[-\frac{f_0^2}{\sigma}\mathbf{u}_\mathrm{g}\cdot\nabla\left(-\frac{\partial\Phi}{\partial p}\right)\right]=-\mathbf{u}_\mathrm{g}\cdot\nabla\frac{\partial}{\partial p}\left(\frac{f_0^2}{\sigma}\frac{\partial\Phi}{\partial p}\right)+\frac{f_0^2}{\sigma}\frac{\partial\mathbf{u}_\mathrm{g}}{\partial p}\cdot\nabla\frac{\partial\Phi}{\partial p}$$

in the last term of this expansion, the terms $\partial_p\mathbf{u}_\mathrm{g}$ and $\nabla\partial_p\Phi$ are perpendicular, as $\partial_p\mathbf{u}_\mathrm{g}=\hat{k}\times\nabla\partial_p\Phi$. This means that the last term can be removed. This simplifies Equation A.3

$$\left[\nabla^2+\frac{\partial}{\partial p}\left(\frac{f_0^2}{\sigma}\frac{\partial}{\partial p}\right)\right]\frac{\partial\Phi}{\partial t}=-f_0\mathbf{u}_\mathrm{g}\cdot\nabla\left[\frac{1}{f_0}\nabla^2\Phi+f+\frac{\partial}{\partial p}\left(\frac{f_0}{\sigma}\frac{\partial\Phi}{\partial p}\right)\right]$$

Finally, we end with the quasi-geostrophic potential vorticity equation in conservation form

$$\left(\frac{\partial}{\partial t}+\mathbf{u}_\mathrm{g}\cdot\nabla\right)q=\frac{\mathrm{D}q}{\mathrm{D}t}=0$$

where

$$q=\left[\frac{1}{f_0}\nabla^2\Phi+f+\frac{\partial}{\partial p}\left(\frac{f_0}{\sigma}\frac{\partial\Phi}{\partial p}\right)\right]$$

A.2 Rossby Waves in the Barotropic Model

Here we show how Rossby waves can be obtained from the barotropic model, that we described in Section 1.3.3. To understand some key behaviour of Rossby waves we can analyse Equation 1.19, by first introducing a β-plane assumption ($f=f_0+\beta y$)

$$\frac{\partial\zeta}{\partial t}+J(\psi,\zeta)+\beta\frac{\partial\psi}{\partial x}=0$$

where we have introduced a streamfunction $\psi(x,y)$, which is defined such that the flow can be written in terms of the streamfunction $u=-\partial_y\psi$ and $v=\partial_x\psi$. This means that the vorticity can be written as $\zeta=\nabla^2\psi$. We now linearise this equation assuming we have a fixed zonal mean flow $-Uy$ with a small perturbation $\psi'(x,y,t)$, or $\psi=-Uy+\psi'$. We neglect nonlinear terms to obtain

$$\frac{\partial}{\partial t}\nabla^2\psi'+U\frac{\partial}{\partial x}\nabla^2\psi'+\beta\frac{\partial\psi'}{\partial x}=0$$

Looking for wave solutions, of the form $\psi'=\tilde{\psi}\exp(i(kx+ly-\omega t))$, to this equation gives us

$$\left[(-\omega+Uk)\left(k^2+l^2\right)-\beta k\right]\tilde{\psi}=0$$

which implies the the dispersion relation for Rossby waves is

$$\omega=Uk-\frac{\beta k}{k^2+l^2}$$

and the phase speed of the wave is

$$c_p=\frac{\omega}{k}=U-\frac{\beta}{k^2+l^2} \tag{A.4}$$

this is less than the mean flow speed U, and thus these waves move westward compared with the flow. Note here we are looking at the non-divergent barotropic equation, or one with infinite deformation radius or equal height, so it is a fairly gross simplification of the real atmosphere. Realism can be incorporated by using a variable thickness version of the barotropic vorticity equation, which models changes in vorticity due to expansion or shrinking of the air column due to orography, leading to topographic Rossby waves.

A.3 Baroclinic Instability in Two Layer Model

Taking the two layer QG equations, given in Equation 1.20, we will assume that the streamfunctions can be expressed as linearly dependant on the y coordinate, and small perturbations that are dependant on x and t. In addition, the vertical velocities are only dependant on x and t

$$\begin{aligned}\psi_1 &= -U_1 y + \psi_1'(x,t)\\ \psi_3 &= -U_3 y + \psi_3'(x,t)\\ \omega &= \omega'(x,t)\end{aligned}$$

where U_1 and U_3 are the zonal flow velocities for the given level. This means that the perturbation fields have only meridional and vertical velocity components. In addition, we take the hydrostatic thermodynamic equation, in terms of streamfunction ψ_i and vertical velocity ω, a simplification of Equation 1.18, which has been taken for a virtual mid-layer using a finite difference approximation

$$\frac{\partial}{\partial t}(\psi_1 - \psi_3) = -\mathbf{u}_2 \cdot \nabla(\psi_1 - \psi_3) + \frac{\sigma \Delta p}{f_0}\omega \tag{A.5}$$

Substituting these linearisations into Equations 1.20 and A.5 gives us

$$\begin{aligned}\left(\frac{\partial}{\partial t} + U_1\frac{\partial}{\partial x}\right)\frac{\partial^2 \psi_1'}{\partial x^2} + \beta\frac{\partial \psi_1'}{\partial x} &= f_0\frac{\omega}{\Delta p}\\ \left(\frac{\partial}{\partial t} + U_3\frac{\partial}{\partial x}\right)\frac{\partial^2 \psi_3'}{\partial x^2} + \beta\frac{\partial \psi_3'}{\partial x} &= -f_0\frac{\omega}{\Delta p}\\ \left(\frac{\partial}{\partial t} + \frac{1}{2}(U_1+U_3)\frac{\partial}{\partial x}\right)(\psi_1' - \psi_3') + \frac{1}{2}(U_3 - U_1)\frac{\partial}{\partial x}(\psi_1' + \psi_3') &= \frac{\sigma \Delta p}{f_0}\omega\end{aligned}$$

To track barotropic and baroclinic perturbations, we define the barotropic as the mean, and the baroclinic as the shear of the perturbations, where we drop the primes to simplify the expressions

$$\psi = \frac{\psi_1' + \psi_3'}{2} \qquad\qquad \theta = \frac{\psi_1' - \psi_3'}{2}$$

similarly, we linearly interpolate the zonal flow velocities to give us the vertically averaged zonal and thermal winds

$$U_Z = \frac{U_1 + U_3}{2} \qquad\qquad U_T = \frac{U_1 - U_3}{2}$$

where incorporating these terms in the above two layer model gives us

$$\left(\frac{\partial}{\partial t}+(U_Z+U_T)\frac{\partial}{\partial x}\right)\frac{\partial^2}{\partial x^2}(\psi+\theta)+\beta\frac{\partial}{\partial x}(\psi+\theta)=f_0\frac{\omega}{\Delta p} \tag{A.6}$$

$$\left(\frac{\partial}{\partial t}+(U_Z-U_T)\frac{\partial}{\partial x}\right)\frac{\partial^2}{\partial x^2}(\psi-\theta)+\beta\frac{\partial}{\partial x}(\psi-\theta)=-f_0\frac{\omega}{\Delta p} \tag{A.7}$$

$$\left(\frac{\partial}{\partial t}+U_Z\frac{\partial}{\partial x}\right)\theta-U_T\frac{\partial}{\partial x}\psi=2\frac{\sigma\Delta p}{f_0}\omega \tag{A.8}$$

By adding Equations A.6 and A.7 we get

$$\left(\frac{\partial}{\partial t}+U_Z\frac{\partial}{\partial x}\right)\frac{\partial^2\psi}{\partial x^2}+U_T\frac{\partial}{\partial x}\left(\frac{\partial^2\theta}{\partial x^2}\right)+\beta\frac{\partial\psi}{\partial x}=0 \tag{A.9}$$

and by subtracting A.7 from A.6

$$\left(\frac{\partial}{\partial t}+U_Z\frac{\partial}{\partial x}\right)\frac{\partial^2\theta}{\partial x^2}+U_T\frac{\partial}{\partial x}\left(\frac{\partial^2\psi}{\partial x^2}\right)+\beta\frac{\partial\theta}{\partial x}=\frac{f_0}{\Delta p}\omega \tag{A.10}$$

Finally we use Equation A.8 to remove the vertical velocity term from Equation A.10 to give us

$$\left(\frac{\partial}{\partial t}+U_Z\frac{\partial}{\partial x}\right)\left(\frac{\partial^2\theta}{\partial x^2}-2\lambda^2\theta\right)+U_T\frac{\partial}{\partial x}\left(\frac{\partial^2\psi}{\partial x^2}+2\lambda^2\psi\right)+\beta\frac{\partial\theta}{\partial x}=0 \tag{A.11}$$

where $\lambda^2 = f_0^2/(\sigma\Delta p^2)$, which determines the wavenumber of the deformation radius. This governs the scale at which buoyancy forces become as important as rotational effects.

Together, Equations A.9 and A.11 provide the barotropic and baroclinic perturbations of the vorticity. As in the case of the barotropic vorticity equation, we now look for wave-like solutions to these perturbation equations, in the form of

$$\psi=\tilde{\psi}e^{i(kx-\omega t)} \qquad \theta=\tilde{\theta}e^{i(kx-\omega t)}$$

where k is the horizontal wavenumber, and ω is the wave phase. These solutions only depend on x as the solution is linear in y. We then substitute these into the two perturbation vorticity equations, and dividing by the exponential, gives us the coupled equations

$$\begin{aligned}\left[k(\omega-kU_Z)+\beta\right]\tilde{\psi}-k^2U_T\tilde{\theta}&=0\\ \left[(\omega-kU_Z)(k^2+2\lambda^2)+k\beta\right]\tilde{\theta}-U_Tk\left[k^2-2\lambda^2\right]\tilde{\psi}&=0\end{aligned} \tag{A.12}$$

$$\begin{vmatrix} k(\omega-kU_Z)+\beta & -k^2U_T \\ -kU_T(k^2-2\lambda^2) & (\omega-kU_Z)(k^2+2\lambda^2)+k\beta \end{vmatrix}=0$$

$$k(k^2+2\lambda^2)(\omega-kU_Z)^2+2\beta(k^2+\lambda^2)(\omega-kU_Z)+k\beta^2-k^3U_T^2(k^2-2\lambda^2)=0$$

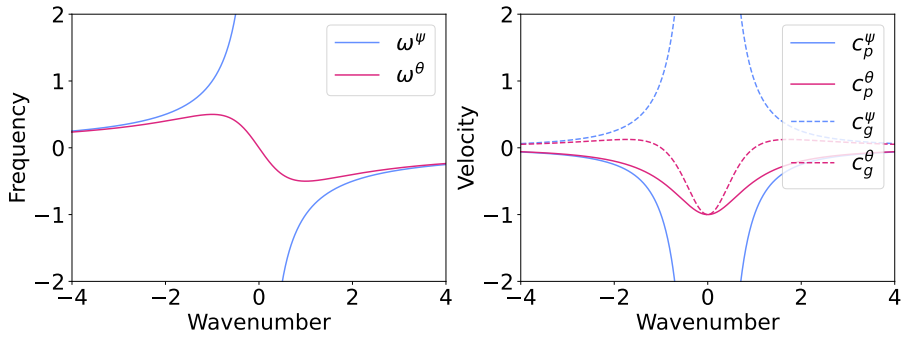


Figure A.1: Left: The dispersion relations of the barotropic and baroclinic waves, In the barotropic case, we see that for longer zonal scales, the frequency increases and the dispersion increases. For the baroclinic case, large scale waves scale almost linearly. Right: The corresponding zonal and phase velocities $c_p = \omega/k_x$ and $c_g = \partial\omega/\partial k$. The phase velocities (solid curves) are always negative, and so are always to the west. The group velocities of the barotropic waves (dashed blue) are always to the east, but long baroclinic waves have a westward group velocity. Short baroclinic and barotropic waves have the same velocities, where their group and phase velocities are equal and opposite. This has the effect of wave crests moving to the east, while the wave packet moves westward [Vallis, 2017].

using the quadratic formula, to search for roots of $x = \omega - kU_Z$, we can find the phase speed of the solution to be of the form

$$c_p = \frac{\omega}{k} = U_Z - \frac{\beta(k^2+\lambda^2)}{k^2(k^2+2\lambda^2)} \pm \frac{\sqrt{\delta}}{k} \tag{A.13}$$

where

$$\delta = \frac{\beta^2\lambda^4}{k^2(k^2+2\lambda^2)^2} + \frac{k^2U_T^2(k^2-2\lambda^2)}{k^2+2\lambda^2}$$

To recap, the system, shown in Equations A.9 and A.11, has the wave solutions assumed, only if the phase speed satisfies the relation in Equation A.13.

We now will investigate the relation shown in Equation A.13 to understand the properties of such waves. Below we break the analysis down into the key cases.

Barotropic Rossby Waves

If we assume that $U_T = 0$, or that there is no shear in the flow, or that the flow is barotropic, then the $-\delta$ term of the phase speed is given by

$$c_p = U_Z - \frac{\beta}{k^2}$$

This is exactly the same phase speed as barotropic Rossby waves, given in Equation A.4, but with no y dependence. We present the frequency, and phase and group velocities in

Figure A.1. In addition, substituting this value for the phase speed into the coupled perturbation system, Equation A.12, shows that the $\tilde{\theta}$ terms are zero, showing that these waves are indeed barotropic in nature. This system, therefore, retains the barotropic Rossby waves, which we discussed before.

Baroclinic Rossby Waves

Again assuming that $U_T = 0$ and taking the $+\delta$ term, the phase speed is thus

$$c_p = U_Z - \frac{\beta}{k^2 + 2\lambda^2}$$

This phase speed is similar to the barotropic case, but now includes the $2\lambda^2$ term in the denominator, which has the impact of modifying the wave speed, based on the vertical stretching. If we substitute this into Equation A.12, we get the following relation

$$\frac{2\lambda^2\beta}{k^2 + 2\lambda^2}\tilde{\psi} = 0 \iff \tilde{\psi} = 0$$

as all terms in the coefficient are positive. This means that $\psi = \psi_1' + \psi_3' = 0$, resulting in $\psi_1' = -\psi_3'$, or that the flow in the two levels is 180° out of phase, and the perturbation is completely baroclinic, though the background flow is barotropic. The frequencies and wave velocities can be visualised in Figure A.1.

Baroclinic Instability

We begin by introducing baroclinic instability informally, to focus primarily on the mechanisms that form the instability. We do this by looking at waves in each of the two layers, and how they can interact constructively to produce an instability [Vallis, 2017].

We take $\beta = 0$, to ignore the differential in rotation, and set the mean zonal wind to zero $U_Z = 0$. This reduces Equation A.13 to

$$c_p = \frac{\omega}{k} = \pm\frac{\sqrt{\delta}}{k} = U_T\sqrt{\frac{k^2 - 2\lambda^2}{k^2 + 2\lambda^2}}$$

this term is purely imaginary when $k^2 < 2\lambda^2$, and we can express it as $c = ic_\mathrm{I}$. Substituting this into Equation A.12 we get

$$\tilde{\theta} = \frac{\omega}{kU_T}\tilde{\psi} = e^{i\pi/2}\frac{c_\mathrm{I}}{U_T}\tilde{\psi}$$

this means that the wave in the θ streamfunction lags/leads that in ψ by 90°, for $c_\mathrm{I} > 0$ and $c_\mathrm{I} < 0$ respectively. These correspond to growing and shrinking waves. Now we look at the impact of the meridional flow, which has the impact of transporting heat to the north. If we let $V = \partial\psi/\partial x$ be the vertically averaged meridional flow, we can find

$$\tilde{V} = \frac{\partial\tilde{\psi}}{\partial x} = ik\tilde{\psi} = k\frac{U_T}{c_\mathrm{I}}\tilde{\theta}$$

As we will discuss in Section 1.4.2, the baroclinic streamfunction is proportional to the temperature. The above expression shows that the meridional velocity is exactly in phase

with the temperature for growing waves, and exactly out of phase with the temperature for shrinking waves. As a result, for unstable or growing waves, poleward flow transports heat towards the poles. For shrinking waves the poleward flow has low temperatures, or heat is transported towards the equator.

For neutral waves, or $c = c_{\mathrm{R}}$ is a real number and $\tilde{\tau} = c_{\mathrm{R}}\tilde{\psi}/U_T$, then $\tilde{V} = ik\tilde{\theta}U_T/c_{\mathrm{R}}$. Here, the barotropic and baroclinic streamfunctions are in phase, and the meridional velocity and temperature are 90° out of phase. In other words, heat is not transported.

Now taking the general case, and taking all the expressions in Equation A.13, we see that if $\delta < 0$ then the phase speed has an imaginary component resulting in an exponential term in the solution. This means the wave solutions would either grow to infinity or shrink to zero with time. If we look at the case where $\delta = 0$ this implies

$$U_T^2 \frac{k^8}{\lambda^8} - 4U_T^2 \frac{k^4}{\lambda^4} + \frac{\beta^2}{\lambda^4} = 0 \tag{A.14}$$

and now we use the quadratic equation to solve for k^2/λ^2

$$\frac{1}{2}\left(\frac{k^2}{\lambda^2}\right)^2 = 2\left(\frac{k^2}{2\lambda^2}\right)^2 = 1 \pm \left[1 - \left(\frac{\beta}{2\lambda^2 U_T}\right)^2\right]^{1/2}$$

where we have expressed this solution in terms of $k^2/(2\lambda^2)$ and $2\lambda^2 U_T/\beta$ as these are the non-dimensionalised quantities of the zonal wave number and the thermal wind. Figure A.2 shows this curve, as well as the regions of stability and instability, given the values of k and U_T.

Looking at the relationship between k and U_T, we see that the solution can only be unstable (imaginary) if $|2\lambda^2 U_T/\beta| > 1 \Rightarrow |U_T| > \beta/(2\lambda^2)$. Thus the minimum value of the thermal wind, or the wind shear required for instability, is largely dependant on the value of β. In other words, the β effect strongly stabilises the system, particularly for long waves ($k \to 0$).

We can find conditions on the wavenumber, for baroclinic instability to exist. These can be found by searching for wavelengths such that, from Equation A.14

$$U_T^2 \frac{k^4}{\lambda^4}\left(4 - \frac{k^4}{\lambda^4}\right) > \frac{\beta^2}{\lambda^4}$$

meaning that a necessary condition for instability is $\sqrt{2}\lambda > k$, or that the wavelength must be longer than the deformation radius ($\sqrt{2}\lambda$) for unstable waves to exist, and all waves shorter than this are stable. This is due to the uncoupling of the layers, as seen in the previous section.

Similarly, we can find an approximate lower bound, by assuming that the wavenumber is small, or that the wavelength is large. In other words, $k \ll \lambda$, which allows us to write Equation A.14 as

$$-4U_T^2 k^4 + \beta^2 \lesssim 0 \tag{A.15}$$

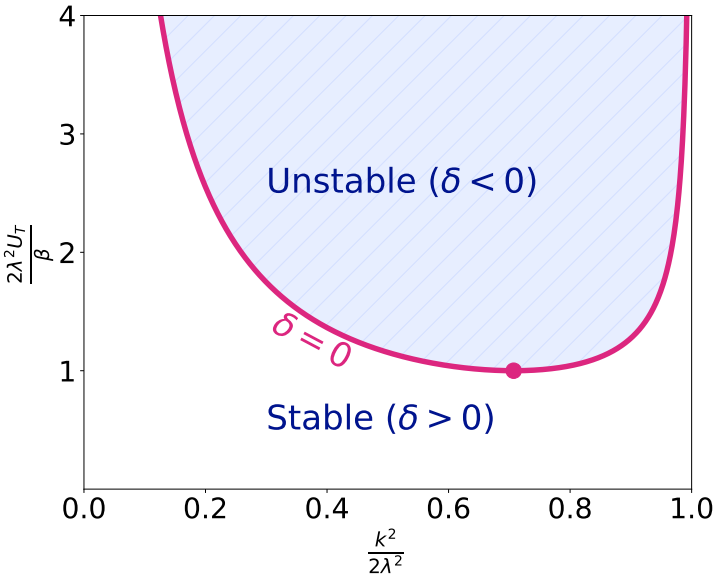


Figure A.2: Stability plot for the two layer QG model. The pink curve shows neutral stability. The pink dot at $(1/\sqrt{2}, 1)$ is the point of maximum instability. The axes are the normalised and scaled wavenumber, and the scaled thermal wind [Holton, 2004].

where we use the relational operator $\lesssim$ to mean that this inequality is approximately true. This results in $\beta/(2U_T) < k^2$. Together, unstable waves lie in the approximate interval

$$\sqrt{\beta/(2U_T)} \lesssim k < \sqrt{2}\lambda \tag{A.16}$$

Lastly, we can find wavenumber for waves with maximum instability. In other words, the local minimum of the curve $\delta = 0$ in Figure A.2. This is because as we go up the y axis (by raising the shear wind U_T), this is the first wavenumber that becomes unstable. It is found by taking the derivative of Equation A.14 with respect to k, and setting $\mathrm{d}U_t/\mathrm{d}k = 0$, and find that $k^2 = \sqrt{2}\lambda^2$, shown with a dot in Figure A.2. In the model, as well as in the real world, we expect the eddies formed from baroclinic instability to approximately have this wavenumber. This is because as the shear flow increases, the waves with wavelength $k_c = \sqrt[4]{2}\lambda$ become unstable first. These waves would grow in amplitude, thus removing energy from the mean thermal wind. This has the impact of reducing U_T and this has the effect of stabilising the flow.

To compare these key wavenumbers with the real atmosphere we approximate $\lambda \approx 1.41 \times 10^{-6}\mathrm{m}^{-1}$, found using values from Table 1.1. This gives us the maximum instability wavelength as $L_c \approx 3700\mathrm{km}$, which is similar to the common eddy size found in synoptic

system. At this wavelength, the minimum thermal wind required for instability is $U_T \approx 2.5\text{m}\,\text{s}^{-1}$, which is equivalent to a shear of $5\text{m}\,\text{s}^{-1}$, and shears of such magnitude are possible, and have been observed, in synoptic systems. According to the bounds calculated above, we find the following approximate bounds on the wavelengths of synoptic systems

$$3000\text{km} < L < 4400\text{km} \leq 3000\sqrt{U_T}\ \text{km}$$

These wavelengths, while approximated and rounded, are close to the average wavelength for midlatitude synoptic systems.

A.4 Lyapunov Vectors

A.4.1 Oseledec subspaces

To further our understanding of the expansion and contraction of state space, and what happens to any arbitrary vector when propagated forwards or backwards in time, we introduce the concept of Oseledec subspaces. To deal with the case where there are multiple of the same Lyapunov exponents, or they are not distinct, we introduce new notation to keep track of the distinct Lyapunov exponents. The reason for doing this is that if there are two or more Lyapunov exponents with the same size, say λ_i and λ_{i+1}, then the expansion rate of any vector in span$\{\boldsymbol{\varphi}_i(t), \boldsymbol{\varphi}_{i+1}(t)\}$ will be identical. As we want to track the distinct stretching or contracting rates, in this example we can bundle the identical stretching rates of λ_i and λ_{i+1} together. We will say that there are s distinct Lyapunov exponents ($1 \leq s \leq m$), and we will say that $\lambda^{(i)}$ for $i = 1, \ldots, s$ is the ith distinct Lyapunov exponent, where there are $\nu^{(i)}$ Lyapunov exponents of size $\lambda^{(i)}$. Together, we have $\lambda^{(1)} > \cdots > \lambda^{(s)}$ and $\sum_{i=1}^{s} \nu^{(i)} = m$. The forwards/backwards Lyapunov vectors that correspond to the ith distinct Lyapunov vector $\lambda^{(i)}$ is given by $\boldsymbol{\varphi}^{\pm}_{\lambda^{(i)},j}$, where $j = 1, \ldots, \nu^{(i)}$.

Now we can define the Oseledec subspaces, spanned by the forward Lyapunov vectors

$$S^+_j(t) = \text{span}\{\boldsymbol{\varphi}^+_{\lambda^{(i)}}(t) \mid i = j, j+1, \ldots, s\}, \quad S^+_{s+1} = \emptyset$$

where $\emptyset = S^+_{s+1}(t) \subset S^+_s(t) \subset S^+_{s-1}(t) \subset \cdots \subset S^+_1(t) = \mathbb{R}^m$. These subspaces are spanned by the forward Lyapunov vectors $\boldsymbol{\varphi}^+_{\lambda^{(i)}}(t)$, which have a corresponding Lyapunov exponent of magnitude $\lambda^{(i)}$ or less. The dimension of these subspaces are $\dim(S^+_j(t)) = \sum_{i=j}^{s} \nu^{(i)}$. Thus, the subspace $S^+_j(t)$ consists of vectors that asymptotically expand or shrink with rate $\lambda \leq \lambda^{(j)}$.

Similarly, we can define subspaces spanned by the backwards Lyapunov vectors

$$S^-_j(t) = \text{span}\{\boldsymbol{\varphi}^-_{\lambda^{(i)}}(t) \mid i = 1, 2, \ldots, j\}, \quad S^-_0 = \emptyset$$

where $\emptyset = S^-_0(t) \subset S^-_1(t) \subset S^-_2(t) \subset \cdots \subset S^-_s(t) = \mathbb{R}^m$. Vectors in the subspace $S^-_j(t)$ expand or shrink exponentially with a rate $\lambda \geq \lambda^{(j)}$, backwards in time.

For example, given a vector $\boldsymbol{v}^{(j)}(t) \in S^+_j(t) \backslash S^+_{j+1}(t)$. It is orthogonal to all forward Lyapunov vectors $\boldsymbol{\varphi}^+_{\lambda^{(i)}}(t)$ for $i < j$, and has non zero projection onto at least one of

the vectors $\boldsymbol{\varphi}^{+}_{\lambda^{(j)}}(t)$, related to the jth distinct Lyapunov exponent $\lambda^{(j)}$. As this vector is propagated forwards in time the vector exponentially grows with average rate $\lambda^{(j)}$. In the same manner the vector $\boldsymbol{v}^{(j)}(t_1) \in S^{-}_{j}(t) \backslash S^{-}_{j-1}(t)$ will grow with an average rate of $-\lambda^{(j)}$ when propagated backwards in time. In other words

$$\begin{aligned} \boldsymbol{v}^{(j)}(t) \in S^{+}_{j}(t) \backslash S^{+}_{j+1}(t) &\Rightarrow ||\mathcal{F}(t_1, t_1 + t)\boldsymbol{v}^{(j)}(t_1)|| \sim \exp(\lambda^{(j)} t) \\ \boldsymbol{v}^{(j)}(t) \in S^{-}_{j}(t) \backslash S^{-}_{j-1}(t) &\Rightarrow ||\mathcal{F}(t_1 - t, t_1)^{-1}\boldsymbol{v}^{(j)}(t_1)|| \sim \exp(-\lambda^{(j)} t) \end{aligned} \tag{A.17}$$

These subspaces now allow us to peel the tangent space apart, and categorise how quickly different sets of vectors will expand or contract. For example, take the Lorenz system from the previous section. We can numerically find that the Lyapunov exponents (numerical methods for finding Lyapunov exponents and vectors are given in Appendix A.4.4) are $(\lambda^{(1)}, \lambda^{(2)}, \lambda^{(3)}) \approx (0.8845, 0, -14.5533)$. We see that the subset $S^{+}_{1}(t) \backslash S^{+}_{2}(t)$ fills almost the entire tangent space, as the subset $S^{+}_{2}(t)$ is a two dimensional surface, and has a measure 0 in $\mathbb{R}^3$. It means that (almost) any vector that we pick will grow exponentially with an average rate of $\lambda^{(1)} \approx 0.8845$. In addition, we know that under the action of the propagator, almost any vector will tend towards the subspace $\text{span}\{\boldsymbol{\varphi}^{-}_{\lambda^{(1)}}(t)\} = S^{-}_{1}(t)$.

If we take a square area in tangent space, we see that there is almost always a vector that has zero projection on the forward Lyapunov vector $\boldsymbol{\varphi}^{+}_{\lambda^{(1)}}$, meaning that it lives in the subspace $S^{+}_{2}(t) \backslash S^{+}_{3}(t)$, and that these vectors expand or shrink with factor $\lambda^{(2)}$. Overall, the area of the square grows with exponent $\lambda^{(1)} + \lambda^{(2)}$. All vectors, apart from a single one, within this square will converge to $\text{span}\{\boldsymbol{\varphi}^{-}_{\lambda^{(1)}}(t)\} = S^{-}_{1}(t)$. The single vector that does not converge to this subspace is the one that goes to $S^{-}_{2}(t) \backslash S^{-}_{1}(t)$.

Lastly, if we take the entire space, there is a single vector that is in the subspace $S^{+}_{3}(t)$, which tends towards the subset $S^{-}_{3}(t) \backslash S^{-}_{2}(t)$. A three dimensional volume will grow with rate $\lambda^{(1)} + \lambda^{(2)} + \lambda^{(3)}$. In the case of the Lorenz system we see that this sum is less than zero, again pointing to the fact that the system is dissipative. In addition, we see that $\lambda^{(2)} = 0$. This corresponds to the flow rate, or the rate of growth along the direction of travel of the trajectory, which is by definition $\exp(0 \cdot t) = 1$.

Generalising this, under the action of the propagator, almost any k dimensional volume asymptotically grows or shrinks with average exponential rate $\sum_{i=1}^{k} \lambda_i$, and tends towards the subspace S^{-}_{i}, where $\dim(S^{-}_{i-1}(t)) < k \leq \dim(S^{-}_{i}(t))$. Likewise, in backwards time, almost any k dimensional volume being iterated backwards in time grows or shrinks with exponential rate $\sum_{i=1}^{k} \lambda_i^{-1}$ and tends towards $S^{+}_{i}(t)$, where $\dim(S^{+}_{i+1}(t)) < k \leq \dim(S^{+}_{i}(t))$. This can be expressed as

$$\begin{aligned} \mathcal{F}(t_1, t) V_k(t_1) &\underset{t_1 \to -\infty}{\subset} S^{-}_{i}(t) \\ \mathcal{F}(t_1, t)^{-1} V_k(t_2) &\underset{t_2 \to +\infty}{\subset} S^{+}_{i}(t) \end{aligned} \tag{A.18}$$

A.4.2 Finite Time Lyapunov Vectors

Above, we discussed how vectors in the tangent space of the model behave as time goes to positive or negative infinity. If we only look at finite steps in time, we find that the image of orthogonal Lyapunov vectors, when propagated, are not necessarily still Lyapunov vectors. Take a Lyapunov vector, $\boldsymbol{\varphi}^+_{\lambda^{(i)},j}(t_1) \in S^+_i(t_1) \backslash S^+_{i+1}(t_1)$. We propagate it forwards in time from t_1 to time t_2, where $j = 1, \ldots, \nu^{(i)}$, which gives us the vector $\mathcal{F}(t_1, t_2)\boldsymbol{\varphi}^+_{\lambda^{(i)},j}(t_1) \in S^+_i(t_2) \backslash S^+_{i+1}(t_2) = \boldsymbol{\psi}^+_{\lambda^{(i)},j}(t_2)$. Which is a result of the subspaces being invariant under the tangent flow

$$\begin{aligned} \mathcal{F}(t_1, t_2) S^+_i(t_1) &= S^+_i(t_2) \\ \mathcal{F}(t_1, t_2) S^-_i(t_1) &= S^-_i(t_2) \end{aligned} \tag{A.19}$$

However, the Lyapunov vectors are likely not invariant with the flow. This is because the propagator $\mathcal{F}(t_1, t_2)$ does not generally preserve orthogonality. This can be see by looking at the vector $\boldsymbol{\psi}^+_{\lambda^{(i)},j}(t_2)$. We see that it is orthogonal to vectors $\boldsymbol{\varphi}^+_{\lambda^{(n)},j}(t_2)$ for $n < i$. This is because the vector is in the subspace $S^+_i(t_2) \backslash S^+_{i+1}(t_2)$, and this subspace does not include any projection on the vectors $\boldsymbol{\varphi}^+_{\lambda^{(n)}}(t_2)$, for $n < i$. However, the vector $\boldsymbol{\psi}^+_{\lambda^{(i)},j}(t_2)$ is in the subspace $S^+_i(t_2) \backslash S^+_{i+1}(t_2)$, which is not identical with the vectors spanned by the forward Lyapunov vector $\boldsymbol{\varphi}^+_{\lambda^{(i)}}(t_2)$. Most of the time, given a vector $\boldsymbol{v} \in S^+_i(t_2) \backslash S^+_{i+1}(t_2)$, this vector is orthogonal to all vectors $\boldsymbol{\varphi}^+_{\lambda^{(n)}}(t_2)$ for $n < i$, and it has non zero projection in span$\{\boldsymbol{\varphi}^+_{\lambda^{(i)}}(t_2)\}$, but the key point is that $\boldsymbol{v}$ likely has a non zero projection on all vectors $\boldsymbol{\varphi}^+_{\lambda^{(n)}}(t_2)$ for $n > i$. This continues all the way to the last local Lyapunov vector $\boldsymbol{\varphi}^+_{\lambda^{(s)}}(t_2)$, which is orthogonal to all other vectors. This means that it is colinear with its preimage $\boldsymbol{\varphi}^+_{\lambda^{(s)}}(t_1)$, or $\boldsymbol{\varphi}^+_{\lambda^{(s)}}(t_2) = c\, \boldsymbol{\varphi}^+_{\lambda^{(s)}}(t_1)$. Working our way back through the vectors, we see that $\boldsymbol{\psi}^+_{\lambda^{(s-1)}}(t_2)$ is orthogonal to all vectors $n < s - 1$, but could have some projection on $\boldsymbol{\varphi}^+_{\lambda^{(s-1)}}(t_2)$ and $\boldsymbol{\varphi}^+_{\lambda^{(s)}}(t_2)$, and so on.

For example, if we are in $\mathbb{R}^3$, and we assume all Lyapunov exponents are unique, the subspace $S^+_2(t) \backslash S^+_3(t)$ is a plane, excluding the one dimensional subspace span$\{\boldsymbol{\varphi}^+_{\lambda^{(3)}}(t)\}$. A vector in the subspace $S^+_2(t) \backslash S^+_3(t)$, apart from one that is colinear with span$\{\boldsymbol{\varphi}^+_{\lambda^{(2)}}(t)\}$, will be orthogonal with $\boldsymbol{\varphi}^+_{\lambda^{(1)}}(t)$ and it will have some projection on $\boldsymbol{\varphi}^+_{\lambda^{(2)}}(t)$. However, it will also have some projection on the vector span$\{\boldsymbol{\varphi}^+_{\lambda^{(3)}}(t)\}$, assuming it is not colinear. This is sketched in Figure A.3.

To simplify the notation we write the matrix expression $\mathcal{F}(t_1, t_2)\boldsymbol{\Phi}^+(t_1) = \boldsymbol{\Psi}^+(t_2)$, where $\boldsymbol{\Phi}^+(t) = [\boldsymbol{\varphi}^+_1(t), \ldots, \boldsymbol{\varphi}^+_m(t)]$ is the matrix of the forward Lyapunov vectors, and $\boldsymbol{\Psi}^+(t) = [\boldsymbol{\psi}^+_1(t), \ldots, \boldsymbol{\psi}^+_m(t)]$ is the image of the forward vectors. From the above analysis we can find a transformation between the two matrices as

$$\begin{aligned} \boldsymbol{\Psi}^+(t_2) &= \boldsymbol{\Phi}^+(t_2)\mathbf{L}(t_1, t_2) \\ \iff \mathcal{F}(t_1, t_2)\boldsymbol{\Phi}^+(t_1) &= \boldsymbol{\Phi}^+(t_2)\mathbf{L}(t_1, t_2) \\ \iff \mathcal{F}(t_1, t_2)^{-1}\boldsymbol{\Phi}^+(t_2) &= \boldsymbol{\Phi}^+(t_1)\mathbf{L}(t_1, t_2)^{-1} \end{aligned}$$

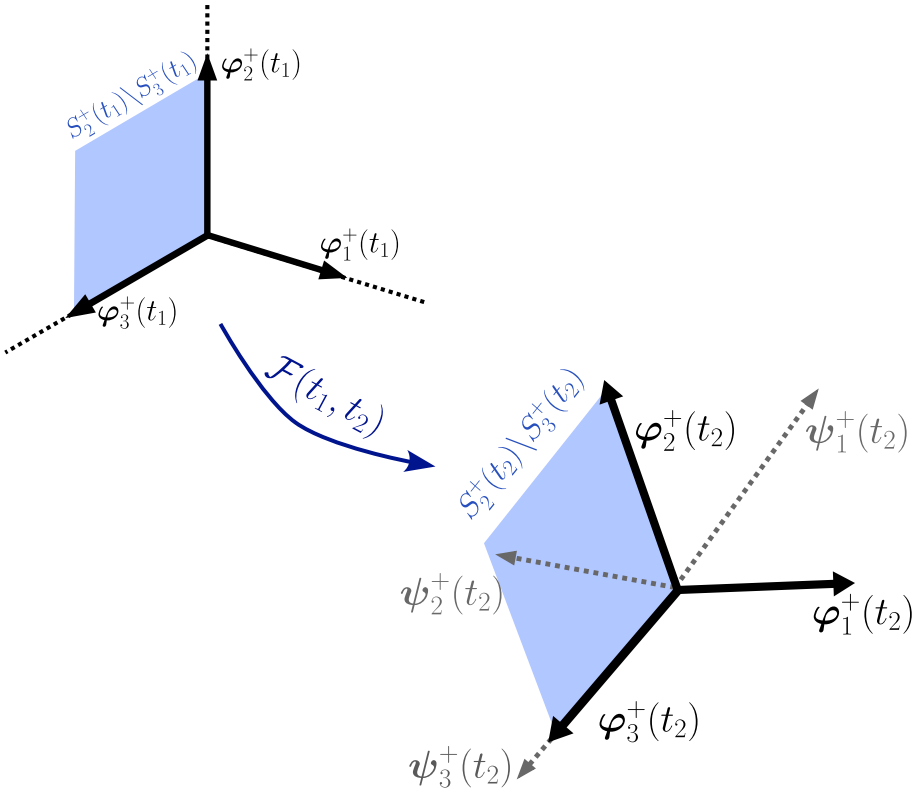


Figure A.3: A sketch of the impact of the propagator on the forward Lyapunov vectors $\boldsymbol{\varphi}_i^+$. The propagator has the following action on the FLVs: $\mathcal{F}(t_1, t_2)\boldsymbol{\varphi}_i^+(t_1) = \boldsymbol{\psi}_i^+(t_2)$. The vector $\boldsymbol{\psi}_3^+(t_2)$ is colinear with the FLV $\boldsymbol{\varphi}_3^+(t_2)$. The vector $\boldsymbol{\psi}_2^+(t_2) \in S_2^+(t_2)\backslash S_3^+(t_2)$, is orthogonal with $\boldsymbol{\varphi}_1^+(t_2)$, but has a nonzero projection on the other two FLVs. Lastly, $\boldsymbol{\psi}_1^+(t_2)$ has a nonzero projection on all FLVs. Image created by Oisín Hamilton, influenced by Kuptsov and Parlitz [2012].

where $\mathbf{L}(t_1, t_2)$ is a lower triangular matrix, and it is invertible as the propagator is non singular and the $\boldsymbol{qL}$ factorisation is unique. If the Lyapunov exponents are distinct ($\nu^{(j)} = 1,\ \forall j$) then the matrix $\mathbf{L}$ is unique. If they are not distinct, there are multiple possible matrices $\mathbf{L}$ that satisfy the above expression, but a solution still exists.

To summarise, the propagator maps forward Lyapunov vectors, which are orthogonal at t_1, onto a set of vectors which need not be orthogonal to one another at time t_2. Using the Oseledec subspaces we showed that a given image $\boldsymbol{\psi}^+_{\lambda^{(i)}}(t_2)$ will be orthogonal with the forward Lyapunov vector $\boldsymbol{\varphi}^+_{\lambda^{(n)}}(t_2)$, for $n < i$, but need not be for $i \leq n$. To transform these new vectors back into an orthogonal basis of Lyapunov vectors it is necessary to perform a $\boldsymbol{qL}$ factorisation.

A similar analysis can be done with backward Lyapunov vectors, but the resulting matrix after $\boldsymbol{qL}$ factorisation is a upper triangular matrix

$$\begin{aligned} &\mathcal{F}(t_1, t_2)^{-1}\boldsymbol{\Phi}^-(t_2) = \boldsymbol{\Phi}^-(t_1)\mathbf{R}(t_1, t_2) \\ \iff\ &\mathcal{F}(t_1, t_2)\boldsymbol{\Phi}^-(t_1) = \boldsymbol{\Phi}^-(t_2)\mathbf{R}(t_1, t_2)^{-1} \end{aligned} \tag{A.20}$$

A.4.3 Covariant Lyapunov Vectors

Forward and backward Lyapunov vectors suffer from some undesirable properties. As they are orthogonal by construction they cannot indicate the true directions of the stable and unstable manifolds, which need not be orthogonal. We have also seen how they do not remain invariant when propagated forwards or backwards in time. Here, we introduce Covariant Lyapunov Vectors (CLVs) which are invariant with the flow [Ginelli et al., 2013]. CLVs can also indicate whether there are tangencies in the invariant manifold of the attractor. Such tangencies points towards non-hyperbolic behaviour in a chaotic attractor, which means that the number of shrinking or expanding dimensions changes at different points of the attractor [Ginelli et al., 2007].

As stated in Equation A.19, the Oseledec subspaces are invariant under the tangent flow, and therefore are invariant and are covariant with the dynamics. As we have seen, this is not the case for the forwards and backwards Lyapunov vectors. We now want to look for a set of vectors contained in these invariant subspaces which are also invariant. Such vectors are called Covariant Lyapunov Vectors (CLVs) and we will denote these as $\boldsymbol{\gamma}_j(t)$. By definition, these vectors are stretch or shrink with the flow, while remaining invariant

$$||\mathcal{F}(t_1, t_1 \pm t)\boldsymbol{\gamma}_j(t_1)|| \sim \exp(\pm\lambda_j t) \tag{A.21}$$

This means that these set of vectors satisfy the properties required in Equation A.17, and therefore

$$\begin{aligned} &\boldsymbol{\gamma}_j(t) \in S^+_j(t)\backslash S^+_{j+1}(t) \quad \text{and} \quad \boldsymbol{\gamma}_j(t_1) \in S^-_j(t)\backslash S^-_{j-1}(t) \\ &\Rightarrow \boldsymbol{\gamma}_j(t) \in S^+_j(t)\backslash S^+_{j+1}(t)\ \cap\ S^-_j(t)\backslash S^-_{j-1}(t) \\ &\Rightarrow \boldsymbol{\gamma}_j(t) \in S^+_j(t)\ \cap\ S^-_j(t) \end{aligned} \tag{A.22}$$

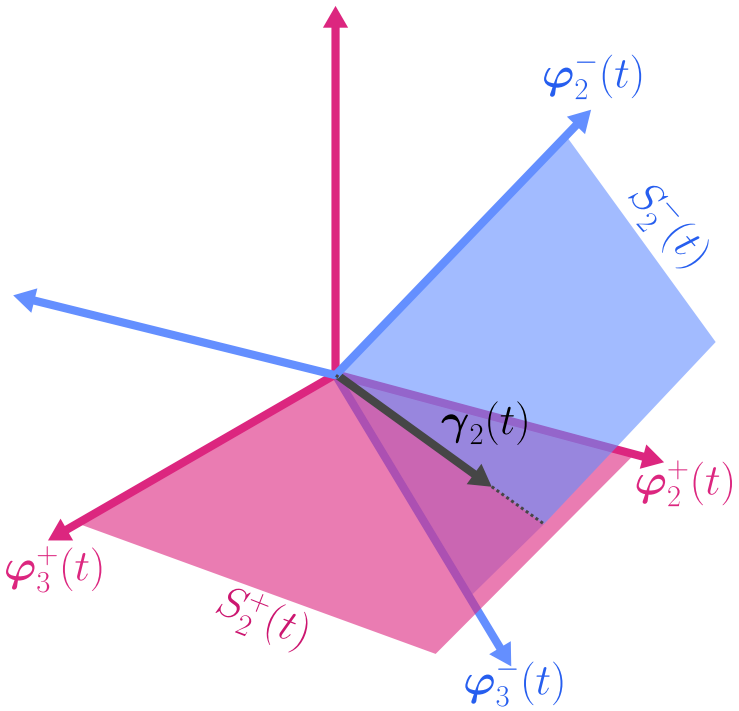


Figure A.4: A sketch of how covariant Lyapunov vectors are found by taking the intersection of the Oseledec subspaces. In this three dimensional sketch, the intersection is a line, where the covariant Lyapunov vector spans this line. Image created by Oisín Hamilton, influenced by Kuptsov and Parlitz [2012].

In other words, the intersection of the Oseledec subspaces. Here, the last line simplifies the intersection, showing that the jth CLV can be found in the intersection of the jth Oseledec subspaces. The intersections of these subspaces are non-empty because the sum of the dimension of the Oseledec subspaces is always higher than the dimension of the whole tangent space. Figure A.4 provides a sketch of a CLV originating from the intersection of two subspaces.

The CLVs are related to the BLV and FLVs. We can find this relation by taking arbitrary vectors $\boldsymbol{v}^{(j)}(t) \in S_j^+(t) \backslash S_{j+1}^+(t)$, where j is the index of distinct Lyapunov exponents. The entire set of such vectors can be written using matrices

$$\mathbf{V}(t) = \mathbf{\Phi}^+(t)\mathbf{A}^+(t)$$

where $\mathbf{A}^+(t)$ is a lower triangular matrix and $\mathbf{\Phi}^+(t)$ is a matrix comprising of the FLVs. When the propagator $\mathcal{F}$ is applied to these vector(s) $\boldsymbol{v}^{(1)}(t) \in S_1^+(t) \backslash S_2^+(t)$ grow or shrink

with exponent $\lambda^{(1)}$, vector(s) $\boldsymbol{v}^{(2)}(t) \in S_2^+(t) \backslash S_3^+(t)$ grow or shrink with exponent $\lambda^{(2)}$, and so on.

We can construct a similar matrix, using BLVs, $\boldsymbol{v}^{(j)}(t) \in S_j^-(t) \backslash S_{j-1}^-(t)$, where

$$\mathbf{V}(t) = \mathbf{\Phi}^-(t)\mathbf{A}^-(t)$$

where $\mathbf{A}^-(t)$ is an upper triangular matrix. Now, when acted on by the inverse propagator $\mathcal{F}^{-1}$ the vector(s) $\boldsymbol{v}^{(1)}(t) \in S_1^-(t) \backslash S_0^-(t)$ grow or shrink with exponent $-\lambda^{(1)}$, and so on.

We now introduce a new matrix $\mathbf{\Gamma}(t) = [\boldsymbol{\gamma}_1(t), \ldots, \boldsymbol{\gamma}_m(t)]$, which is a matrix consisting of all the CLVs. From the definition of CLVs, given in Equation A.21, they must satisfy both forwards and backwards asymptotic behaviour. This implies that there exists upper ($\mathbf{A}^-(t)$) and lower ($\mathbf{A}^+(t)$) triangular matrices such that

$$\mathbf{\Gamma}(t) = \mathbf{\Phi}^-(t)\mathbf{A}^-(t) = \mathbf{\Phi}^+(t)\mathbf{A}^+(t) \tag{A.23}$$

In fact, the above property is equivalent to that given in Equation A.22.

A.4.4 Numerical Calculation of Lyapunov Vectors

Backward Lyapunov Vectors

It is not possible to directly calculate the propagator $\mathcal{F}(t_1, t_2)$, due to the length of integration required of the tangent linear system. This is because if we integrate a set of vectors forwards from time t_1 almost any vector we pick will approach the first backwards Lyapunov vector $\boldsymbol{\varphi}_1^-(t)$. In other words, almost any vector we pick will fall into the subspace $S_1^-(t)$, as $t \to \infty$.

An alternative numerical approach is given by Equation A.20, which shows how backward Lyapunov vectors at time t_1 are mapped onto backward Lyapunov vectors at time t_2. The idea is to use an arbitrary orthogonal basis, which when iterated forwards using the propagator will become embedded in the subspace spanned by the backwards Lyapunov vectors, as shown in Equation A.18. This idea was proposed by Benettin et al. [1980] and Shimada and Nagashima [1979].

Given an arbitrary orthogonal basis $\boldsymbol{q}(t_n) \in \mathbb{R}^{m \times m}$, when propagated forwards in time $\mathcal{F}(t_n, t_{n+1})\boldsymbol{q}(t_n) = \boldsymbol{q}(t_{n+1})\mathbf{R}(t_n, t_{n+1})^{-1}$, using Equation A.20, this basis will converge towards the backward Lyapunov vectors. The algorithm is applied as follows:

The propagator $\mathcal{F}(t_n, t_{n+1})$ is calculated for some interval $t_{n+1} - t_n$, which tends to be small. It is small because, as we have seen, the error growth can saturate after a given time. Initially, an arbitrary orthogonal basis is propagated forwards

$$\boldsymbol{v}(t_{n+1}) = \mathcal{F}(t_1, t_2)\boldsymbol{q}(t_n)$$

The first vector column $\boldsymbol{v}_1$ of $\boldsymbol{v}(t_{n+1})$ approaches the subspace $\boldsymbol{v}_1 \in S_1^-$, as required. Therefore it will approach the largest backwards Lyapunov vector, but it will be stretched,

or contracted, as propagated. To prevent the magnitude of this vector becoming too large, or too small, we normalise it at each propagation step. We call this normalised vector $\boldsymbol{q}_1 = \boldsymbol{v}_1/||\boldsymbol{v}_1||$. The finite time Lyapunov exponents can be obtained by storing the magnitude of the stretched or contracted vectors, or $\lambda_1(t_n) = \ln(||\boldsymbol{v}_1||)/(t_n - t_{n-1})$.

Assuming $\lambda_2 < \lambda_1$, the plane span$\{\boldsymbol{v}_1, \boldsymbol{v}_2\}$ approaches the subspace S_2^-. However, as we have seen, the vector $\boldsymbol{v}_2$ is not invariant with the flow, and will most likely have some projection onto the largest backward Lyapunov vector $\boldsymbol{\varphi}_1^-$. This means that the vector $\boldsymbol{v}_2$ will also converge towards φ_1^- if not modified at each propagation step. At the same time, we need to ensure that the orientation of the plane span$\{\boldsymbol{v}_1, \boldsymbol{v}_2\}$ remains the same, to ensure it converges to S_2^-. Both of these requirements can be achieved if the new vector $\boldsymbol{q}_2$ is defined such that it is orthogonal to $\boldsymbol{q}_1$ ($\boldsymbol{q}_1 \cdot \boldsymbol{q}_2 = 0$), and $\boldsymbol{q}_2 \in$ span$\{\boldsymbol{v}_1, \boldsymbol{v}_2\}$. Again, to prevent the magnitude of the vector overflowing or underflowing, it is normalised. If $\lambda_2 = \lambda_1$ then the same method is used as above, even though the degeneracy means there are other possible options.

This process is continued for the remaining dimensions. For example, $\boldsymbol{q}_3$ is defined as $\boldsymbol{q}_1 \cdot \boldsymbol{q}_3 = \boldsymbol{q}_2 \cdot \boldsymbol{q}_3 = 0$, and $\boldsymbol{q}_3 \in$ span$\{\boldsymbol{v}_1, \boldsymbol{v}_2, \boldsymbol{v}_3\}$, and so on until all columns of $\boldsymbol{q}(t_{n+1})$ are calculated. This matrix is then used for the initial conditions of the next propagation step $\mathcal{F}(t_{n+1}, t_{n+2})$, and the process is started again. After many iterations, the columns of $\boldsymbol{q}(t_n)$ converge to the backward Lyapunov vectors. Note, that this orthogonalisation process, due to the projection of vectors $\boldsymbol{q}_i$ only onto vectors $\boldsymbol{q}_j$ for $j \leq i$, can be written as $\boldsymbol{v} = \boldsymbol{q}\mathbf{R}$, where $\boldsymbol{q}$ is the matrix made up of the orthonormal vector basis $\boldsymbol{q}_i$, and $\mathbf{R}$ is an upper right triangular matrix. This is known as QR factorisation, which is usually done using the Gram-Schmidt algorithm, or Householder transformations for higher precision cases.

Forward Lyapunov Vectors

The computation of FLVs is similar to the one presented for BLVs, but uses the inverse propagator $\mathcal{F}^{-1}$. However, calculating the FLVs as such comes with the drawback that the vectors are computed in reverse order, meaning that this method requires all vectors to be calculated, rather than just the nth largest ones required. Computationally, it is preferable to instead use the inverse adjoint propagator, which can be found by integrating the system

$$\delta\dot{\boldsymbol{x}}(t) = -\mathbf{J}(\boldsymbol{x}, t)^{\mathrm{T}}\delta\boldsymbol{x}(t)$$

along with the system $\dot{\boldsymbol{x}} = f(\boldsymbol{x}(t))$, backwards in time. The same QR factorisation is used, as described for the BLVs, is then used to find the FLVs. For further explanation on why it is preferable to use the adjoint propagator, Kuptsov and Parlitz [2012] provides more detail.

Covariant Lyapunov Vectors

To calculate the CLVs one can find the intersection of the Oseledec subspaces, which are in turn calculated from the forward and backwards Lyapunov vectors. This method thus requires calculating the forward and backwards vectors, as outlined above, constructing the subspaces, and then obtaining the intersections. The intersections can be calculated using principle angles between subspaces.

There are other possible methods for determining the CLVs that do not require calculating and storing the entire spectrum of FLVs and BLVs if only the first few CLVs are required. Examples of such methods are the LU factorisation method, or similarly, the orthogonal complement method [Wolfe and Samelson, 2007], which use the relation between CLVs, $\mathbf{\Gamma}(t) = [\boldsymbol{\gamma}_1(t), \ldots, \boldsymbol{\gamma}_m(t)]$, BLVs, $\mathbf{\Phi}^-(t) = [\boldsymbol{\varphi}_1^-(t), \ldots, \boldsymbol{\varphi}_m^-(t)]$, and FLVs, $\mathbf{\Phi}^+(t) = [\boldsymbol{\varphi}_1^+(t), \ldots, \boldsymbol{\varphi}_m^+(t)]$, given in Equation A.23. Another approach is called the iterative method [Ginelli et al., 2007], which uses the asymptotic properties of CLVs as shown in Equation A.21.

A.5 Tensor Correction Method for Finding UPOs

We first construct and then solve the linear system, as discussed in the Newton Raphson method outlined above

$$A \cdot \begin{bmatrix} \Delta \mathbf{x}_i \\ \Delta T_i \end{bmatrix} = \begin{bmatrix} \mathbf{x}_i - S^{T_i}(\mathbf{x}_i) \\ 0 \end{bmatrix} \tag{A.24}$$

where A is the matrix shown in Equation 1.27. Issues arise when the matrix A is close to a singular matrix. Such cases are a symptom of the linearisation assumption breaking down for certain directions in state space. To overcome this, the resulting step size of the algorithm in these directions may need to be very small. Thus leading to an increase in the time taken to reach an optimum solution.

To overcome these issues Gritsun [2008] proposed using a tensor correction method [Schnabel and Frank, 1984; Bader, 2005], where the second order non-linear terms are included in the Taylor series. To do this we expand the original equation as in Equation 1.26. To simplify how this is written we will first introduce some new notion, note we have slightly modified the notation found in Gritsun [2008]. We construct a $N+1$ dimensional vector $w_i = [\mathbf{x}_i, T_i]$ and a $N+1$ dimensional vector $\Delta w_i = [\Delta \mathbf{x}_i, \Delta T_i]$, the latter designating the correction step.

We also define a function $F : \mathbb{R}^{N+1} \mapsto \mathbb{R}$ as the difference between the initial condition, and the integrated initial condition. In other words F measures the gap between the starting and finishing position of the estimated UPO: $F(\mathbf{x}_i, T_i) = F(w_i) = S^{T_i}(\mathbf{x}_i) - \mathbf{x}_i$. Also, as we are now primarily working with the vector w_i, the dimension of the following system will be $N+1$, where N is the dimension of the state space. Finally taking the Taylor series to the second order we obtain

$$\begin{aligned} F(w_{i+1}) &= F(w_i + \Delta w_i) \\ &\approx F(w_i) + \frac{\partial F(w_i)}{\partial [w_i]_j}[\Delta w_i]_j + \frac{1}{2}\frac{\partial}{\partial [w_i]_j}\frac{\partial F(w_i)}{\partial [w_i]_k}[\Delta w_i]_k[\Delta w_i]_j \end{aligned} \tag{A.25}$$

Where $[w_i]_j$ denotes the j-th element of the vector of the i-th iteration of the algorithm.

As in Equation A.24 we can express the equation in matrix form

$$A\Delta w_i + \frac{1}{2}\frac{\partial}{\partial [w_i]_j}[A\Delta w_i][\Delta w_i]_j = -F(w_i) \tag{A.26}$$

Again, the reason we are including the tensor correction is that the matrix A could be close to singular. So we focus on the columns of the singular value decomposition $A = U\Sigma V^{\mathrm{T}}$ that are close to zero, and which are causing the issue. The decomposition sorts the diagonal, or 'singular', values of Σ so that they are decreasing in magnitude. Now we are interested in the singular values which are sufficiently small, which will occur in the last columns of the matrix. Let's assume that the first K singular values are 'large enough', meaning that the last $N + 1 - K$ values are too close to zero. We start by multiplying Equation A.26 by U^{T}, and making the substitutions $V^{\mathrm{T}}\Delta w_i = l$ and $-U^{\mathrm{T}}F(w_i) = g$

$$\Sigma l + U^{\mathrm{T}}\frac{1}{2}\frac{\partial}{\partial[w_i]_j}(AVl)[Vl]_j = g \tag{A.27}$$

We can separate the solution into an orthogonal sum of vectors $l = l_1 + l_2$ which correspond to the basis of the matrix V. Gritsun [2008] found that for numerically finding UPOs, it was sufficient to take $K = N - 1$, in other words only, focus on the final two singular values of the system. This reduces the problem into a linear system of dimension $N - 1$, and a non-linear problem of dimension 2. This means that the two orthogonal vectors will look like: $l_1 = (v_1, \ldots, v_{N-1}, 0, 0)$ and $l_2 = (0, \ldots, 0, v_N, v_{N+1})$. Therefore we can solve the first $N - 1$ linear equations to obtain l_1 by taking $[l_1]_k = [\Sigma^{-1}]_k\, g_k$ for $k = 1, \ldots, N - 1$. We then substitute l_1 into the following two non-linear equations

$$\begin{aligned}
\sigma_N[l_2]_N + \Bigg(u_N, \frac{1}{2}\frac{\partial}{\partial[w_i]_j}(A(Vl_1 + v_n[l_2]_N + v_{N+1}[l_2]_{N+1})) \\
[Vl_1 + v_n[l_2]_N + v_{N+1}[l_2]_{N+1}]_j\Bigg) = [g]_N \\
\sigma_{N+1}[l_2]_N + \Bigg(u_{N+1}, \frac{1}{2}\frac{\partial}{\partial[w_i]_j}(A(Vl_1 + v_n[l_2]_N + v_{N+1}[l_2]_{N+1})) \\
[Vl_1 + v_n[l_2]_N + v_{N+1}[l_2]_{N+1}]_j\Bigg) = [g]_{N+1}
\end{aligned} \tag{A.28}$$

where $\sigma_i,\ v_i,\ u_i$ are the i-th column of the matrices $\Sigma,\ V$, and U respectively. The non-linear terms in both equations are the same, but they are projected onto the direction of u_N or u_{N+1}.

To calculate the non-linear terms we have to calculate the directional derivatives

$$\frac{\partial}{\partial[w_i]_j}(A\alpha)[\beta]_j = \frac{\partial}{\partial\beta}(A\alpha)$$

Where $\alpha, \beta \in [Ql_1,\ v_n,\ v_{N+1}]$ there are therefore nine permutations possible. For example if we take $\alpha = v_N,\ \beta = v_{N+1}$ we can approximate the derivative by taking a finite difference approximation

$$\frac{\partial}{\partial v_{N+1}}(Av_N) \approx \frac{1}{\delta}\Bigg(A(u_i + \delta v_N)v_{N+1} - A(u_i)v_{N+1}\Bigg)$$

The calculation of $A(w_i+\delta v_N)v_{N+1}$ is equivalent to integrating the tangent linear model, as in Equation 1.26. It consists in integrating the tangent linear model from an initial condition $[\mathbf{x}_i]_j + \delta[v_N]_j$ (for $j \in [1, N]$) for a time of $T_i + \delta[v_N]_{N+1}$.

We already have the value of $A(w_i)$ from the construction of the linear system. As we have nine different permutations for α and β this boils down to doing nine additional integrations of the tangent linear model.

We then solve the two non-linear simultaneous equations numerically. There could be up to four possible solutions for $([l_2]_N, [l_2]_{N+1})$ as the solutions are the intersection of two parabolas, and we pick between these solutions by picking the one that results in the lowest numerical error of the non-linear system. This gives us the full vector $l = l_1 + l_2$, and in turn the next correction step: $\Delta w_i = Vl$. The line search step is used to ensure we take the magnitude of the correction $(\Delta \mathbf{x}_i, \Delta T_i)$ which minimises $F(w_{i+1})$.

This method clearly increases the run time for each step (by approximately an order of 10), so we limit the use of the tensor correction to only steps where the matrix A has close to 0 singular values.

Appendix B

Appendix to Chapter 3

B.1 Model Climatology

In Figure B.1 we present the climatology of the model at the three centroids, shown in Figure 2 in the main paper. We plot the atmospheric geopotential height anomaly and the temperature anomaly in the ground.

B.2 Origin of Blocking Clusters - Continued

This section continues the bifurcation analysis, presented in Section 3.3.3. Figure B.3 shows the bifurcation diagram for $C_{\mathrm{g},1}$. For parameter values around $k_d = 0.085$ and $C_{\mathrm{g},1} = 380\mathrm{W\,m}^{-2}$, there exists a stable periodic orbit, centred in the right hand cluster. We tracked this orbit for $C_{\mathrm{g},1}$ (Figure B.3). For decreasing $C_{\mathrm{g},1}$ a fold bifurcation occurs and the orbit looses stability, and for increasing the parameter the orbit looses stability at a torus bifurcation. We see that this branch has a number of period doubling bifurcations, and following these bifurcations we see that a large number of periodic branches stem from this original branch.

In Figure B.2 we decrease the value of $C_{\mathrm{g},1}$, and present UPOs coloured as in the inset in Figure B.3. Here we see that they again form a central structure within the cluster of UPOs, and for this parameter values we can follow the branches to the values of $C_{\mathrm{g},1}$ that we use in the analysis.

B.3 UPO shadowing - RHS figures

Here we display the three set of UPOs for the RHS cluster, as shown for the LHS in the main paper in Section 3.3.6.

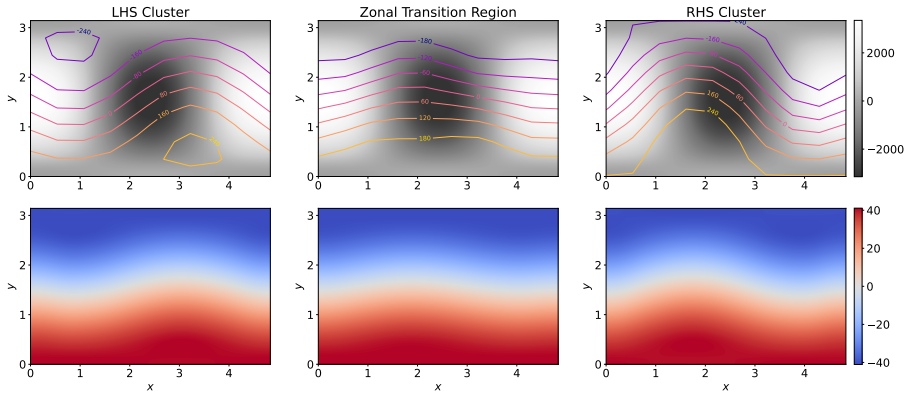


Figure B.1: The climates of the three centroids, that are displayed in Figure 2 of the main paper. Each column of this figure shows a cluster, with the top row showing the atmospheric geopotential height anomaly, and the bottom row showing the ground temperature anomaly. The geopotential height anomaly is shown in meters, as contours, with the orography profile shown in greyscale, and is also in meters. The ground temperature anomaly is plotted in Kelvin. We see that the Left Hand Side (LHS) cluster corresponds to atmospheric blocking to windward of the orography, and the RHS cluster shows leeward blocking. The Transition Region, presents zonal behaviour in the atmosphere. We see that there is a close link between the location of increased ground temperature with areas of high geopotential height.

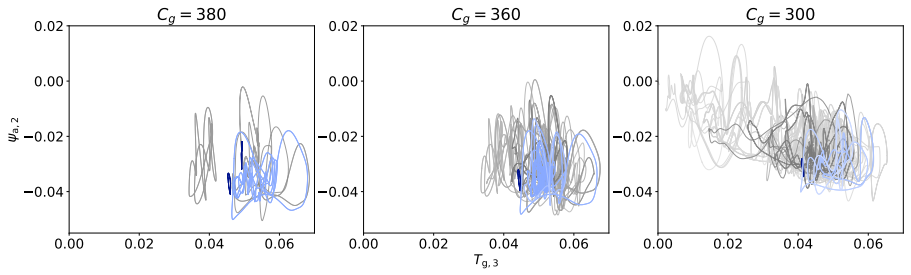


Figure B.2: State space for variables ($\delta T_{\mathrm{g},3}$, $\psi_{\mathrm{a},2}$), for decreasing values of $C_{\mathrm{g},1}$. The orbits shown in blues correspond to the branches shown in the inset plots in Figure B.3. Grey orbits are show the other branches found, that do not directly branch from the key orbits. On the left we show the parameter values where a stable orbit was found, we then decrease the parameter values to end up with the clusters, as shown in the main paper in Figure 2, where the extents, relative to the entire attractor, are also shown in this figure.

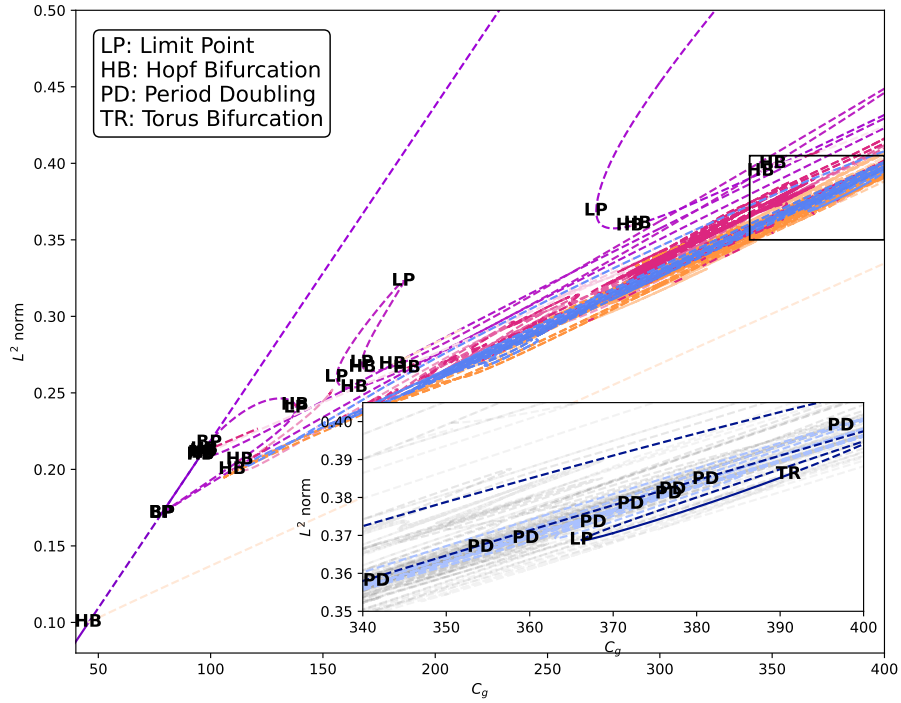


Figure B.3: Bifurcation diagram for all fixed points (shown in purple) and the bifurcation and branching points that lead to the periodic orbits (shown in orange and pink depending on the cluster the orbit belongs to) of the model for varying $C_{\mathrm{a},1}$ and fixed $k_d = 0.085$. The dotted lines represent unstable regions and the solid lines represent stable regions. The black rectangle is zoomed in on and shown in the inset, and focuses on four key branches of periodic orbits, shown in blue. A stable periodic orbit is found for large values of $C_{\mathrm{a},1} \approx 380\mathrm{W\,m^{-2}}$ (shown in dark blue), stability is lost through a fold and a torus bifurcation. This branch is tracked along with any branching points or period doubling branches (these are shown in light blue).

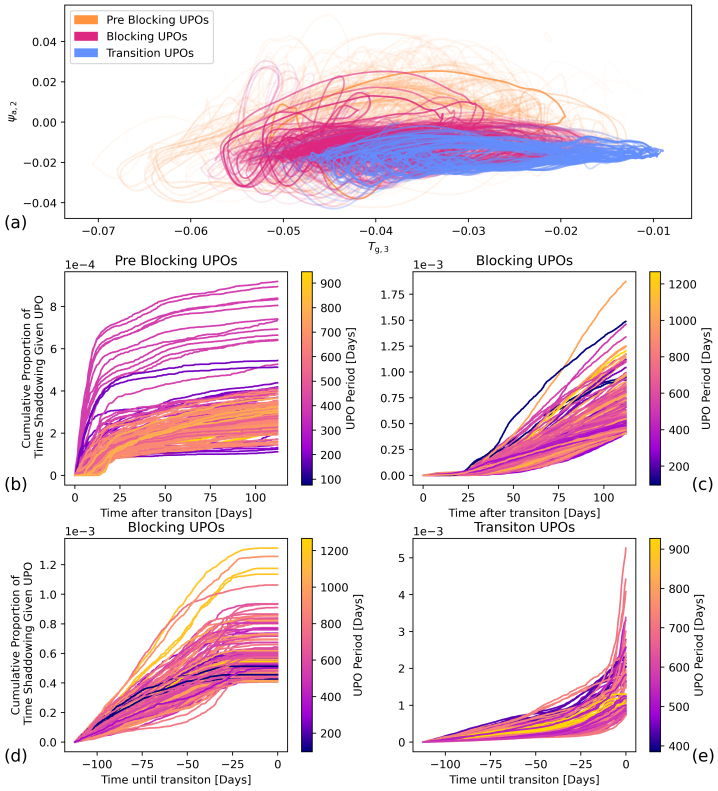


Figure B.4: Same as shown in Figure 3.10 but for the RHS cluster. Figure (a) shows the three sets of UPOs, colour coded by which set they are in, the shade of the colour displays the magnitude of cumulative shadowing (CS) overall, with darker shades representing UPOs that are shadowed more frequently. (b) each line represents a UPO, and the y-axis shows the proportion of time that the UPO shadows the trajectory. The shading is the UPO period. This subplot shows the CS of the UPOs in the Pre-Blocking set (those in orange in (a)), for the first 100 days of the time in the cluster. (c) same as (b), but showing the CS of the Blocking set of UPOs, shown in pink in (a). (d) shows the CS of the set of Blocking UPOs for the final 100 days before transitioning. (e) shows the same as (d), but for the Transition set of UPOs, shown in blue in (a).

Appendix C

Appendix to Chapter 4

C.1 Projection of Parameters on Basis Modes

The model equations are transformed to ODEs using a Galerkin method, by taking the inner product of the equations with each of the basis modes. Projecting λ onto the set of basis modes requires introducing a new tensor $K_{i,j,k} = \langle F_i, F_j F_k \rangle$.

In this chapter, we use the basis functions introduced in Equation 2.1, and let $i, k \in \{1, \ldots, 3n_y(1 + 2n_x)\}$, where $n_x \times n_y$ is the model resolution. However, we limit the parameter basis to introduce the gradient defined by F_1, and the constant basis mode $F_0 = 1$, so $j \in \{0, 1\}$. This reduces the above inner product to the tensor $K_{i,j,k}$, where $K_{i,0,k} = \delta_{i,k}$, and $K_{i,1,k} = \langle F_i, \sqrt{2}\cos y \; F_k \rangle$.

The resulting matrix is non-zero at only the indices (i, k), where i is the mode $F^{\alpha}_{M,P}$, then k is the index of the mode(s) $F^{\alpha}_{M,P\pm1}$, where α is one of the three types of modes $\{A, K, L\}$. Also, $P \in \{1, \ldots, n_y\}$ given the model resolution $n_x \times n_y$, corresponding to Equation 2.1. At these indices the matrix value is $1/\sqrt{2}$. This is seen by substituting each of the three basis mode types shown in Equation 2.1 into the inner product $K_{i,1,k}$ and the fact that $\langle F_i, F_k \rangle = \delta_{i,k}$.

This modification introduces a symmetry around the parameter λ_1. This produces a set of even and odd variables in the model with respect to the symmetry, where if $\mathbf{x} = [\psi_{\mathrm{a},\,1}, \ldots, \theta_{\mathrm{a},\,1}, \ldots, \delta T_{\mathrm{g},\,1}, \ldots]$ is a solution of the system $\dot{\mathbf{x}} = f(\mathbf{x}, \lambda_1)$, there exists another solution $\tilde{\mathbf{x}}$ at the parameter value $-\lambda_1$ with odd variables with respect to the symmetry having their sign flipped. For example, for the 2×2 model this results in the even variables being those corresponding to the modes $F_1, F_2, F_3, F_9, F_{10}$, and the odd being F_4, F_5, F_6, F_7, F_8, therefore $\tilde{\mathbf{x}} = [\psi_{\mathrm{a},\,1}, \psi_{\mathrm{a},\,2}, \psi_{\mathrm{a},\,3}, -\psi_{\mathrm{a},\,4}, \ldots]$. The even and odd variables are determined by the tensor that governs the non-linear interactions described by $g_{i,j,k} = \langle F_i,\ J(F_j, F_k) \rangle$. This fact allows us to reduce the number of parameter choices for λ_1 that we need to analyse, as any solution for λ_1 map to a solution for $-\lambda_1$.

C.2 Jet Stream

Jet streams are narrow band of high velocity wind. There are two main jets on the planet, the sub-tropical jet, found at the poleward extent of the Hadley circulation, and the mid-latitude jets (also known as polar or eddy driven), located in the midlatitudes or the Polar front [Holton, 2004; Barry and Chorley, 2003]. The sub-tropical jet arises due to the westerly acceleration associated with poleward moving air, the midlatitude jet is a result of the momentum and heat forcing arising from the effects of transient midlatitude eddies through convergence [Woollings et al., 2010]. Due to asymmetries on the planet in orography, continental distributions, and heating from the ocean, these jets are not always distinct and can merge or separate. In the simplified atmosphere of this study, we model the jet as the band of wind in the upper atmosphere layer that has the largest velocity. This arises due to the gradient between eddies in the model, and shares this similarity with the midlatitude jet in the real atmosphere.

To identify jets, we take three related approaches. The first is a simple plot of mean zonal wind (mean of the u wind velocity over time and longitude). This provides a simple distribution of zonal wind speeds, which we can use to identify the latitude of greatest wind speed. Next, we can take the mean of the wind intensity over time, to obtain a map of the wind intensity across space. This allows us to see the dominant wave patterns. As we are working with a severely truncated Fourier decomposition, there are only limited wave shapes that the resulting jet can take, and if there are dominant patterns this will show up in these plots. Lastly, to measure the speed of the jet, as well as measure the 'waviness', we divide the domain into a grid, and then use Dijkstra's shortest path finding algorithm to find the 'fastest' path from west to east. The use of Dijkstra's algorithm for finding jets was introduced in Molnos et al. [2017], and here we use the same approach, but simplify the weights between each node so that we only consider the wind speed strength and how closely aligned the wind direction is with the edge direction.

The path weights are calculated taking the weighted sum of the wind intensity at a given grid point ($w(x, y) = \sqrt{u(x, y)^2 + v(x, y)^2}$), and the angle between the wind direction and the direction of the edge between two grid points, calculated by using the dot product of the two vectors:

$$1 - \frac{1}{\pi} \arccos\left(\frac{v1 \cdot v2}{|v1| \cdot |v2|}\right)$$

This represents the alignment of the wind with the direction of travel, where two vectors that overlap in direction get a weighting of 1, and vectors that are in opposite directions of one another get a weighting of 0.

The jet stream in this model arises from areas of high gradient in the geopotential between high and low eddies in the upper layer streamfunctions. Here we investigate how the jet stream in the 2×2 resolution version of the model maps onto the dynamical system representation. As introduced above, we use a shortest path finding method to identify the position of the jet for a given time step of the integration.

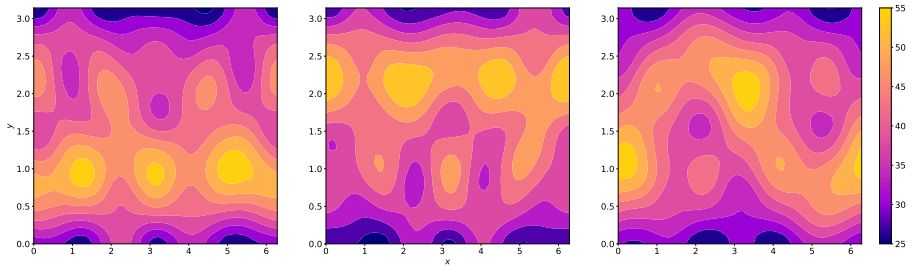


Figure C.1: The average wind intensity, or speed, in the upper layer of the atmosphere in the 2×2 model. The wind speeds were averaged based on whether the corresponding trajectory point was in the low latitude (left panel), high latitude (middle panel), or the wavy jet (right panel) cluster.

Once the jet path was found, we used the DBSCAN algorithm [Ester et al., 1996] to identify clusters using the variables (max latitude, min latitude, mean wind speed, weighted path cost). We used this clustering method as this method does not require us to input the number of clusters we are looking for. We found three clusters in the data, which are most clearly seen when projecting onto the max and min latitudinal extent of the jet. These clusters identify a 'wavy' jet, and two straight jets, one at high latitudes and one at low latitudes. These three jet types are shown in Figure C.1. This was produced by taking the average of the the wind intensity of the upper layer in the model, for each of the three groups of trajectory points described above.

Projecting these three clusters onto the attractor we found that the two straight jets are separated by their magnitude in $\psi_{\mathrm{a},\,4}$ which is the barotropic component of the wave mode $F_4 = \sqrt{2}\cos 2y$. The high latitude jet is associated primarily with negative $\psi_{\mathrm{a},\,4}$ values, and the low latitude jet a positive value, due to the resulting direction of the barotropic flow. The wavy jet corresponds to small magnitudes of $\psi_{\mathrm{a},\,4}$. The value of $\psi_{\mathrm{a},\,4}$ fluctuates relatively quickly (on the order of a rotation every 3-4 days), meaning that the behaviour of the jet also changes quickly, relative to the LFV found in Hamilton et al. [2025].

To understand how the rate of oscillation of $\psi_{\mathrm{a},\,4}$ is impacted depending on the approximate location in the state space, we investigated rate of oscillations, over this mode, of a set of unstable periodic orbits (shown in Figure 4.1a). The UPOs were chosen for this as they provide a basic structure of the attractor and can provide information on the future path of nearby trajectories [Cvitanović et al., 2020]. We took the fast Fourier transform [Cooley and Tukey, 1965] of the value of $\psi_{\mathrm{a},\,4}$ to identify the key frequencies. In Figure C.2 we show a heatmap of the frequencies across a projection of the attractor. It is understood that different parts of the attractor lead to different atmospheric blocking regimes in the model [Hamilton et al., 2025; Xavier et al., 2024], however the regimes discussed in these studies focus on the LFV associated with the ground temperature in the model, which in turn alters the likelihood of blocking occurring over the heated ground, as discussed in Chapter 4.

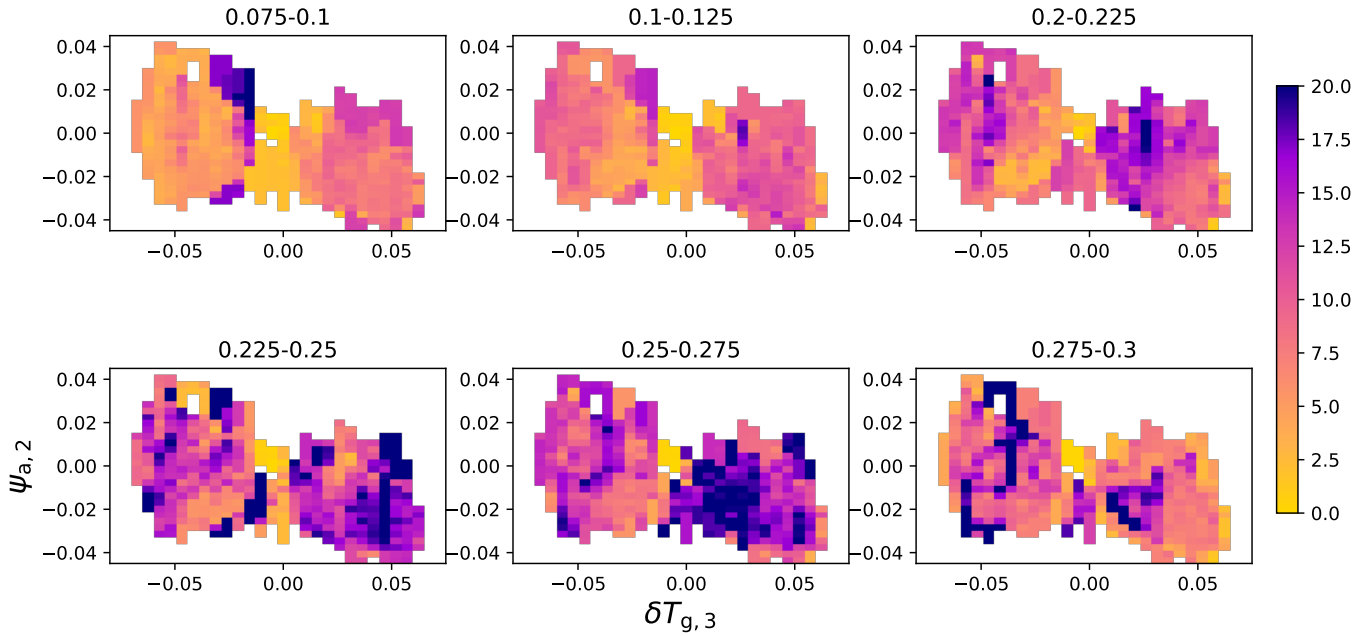


Figure C.2: Heat map of the magnitude of the frequencies of the oscillations in $\psi_{a,4}$. Each plot shows the averaged magnitude of the frequencies in the range shown in each of the titles. The frequencies are given in cycles per day. We see that there are specific regions on the attractor which display different frequencies of the jet oscillations.

Appendix D

Appendix to Chapter 5

D.1 Video Links

The videos discussed in Section 5.3.1.2 and 5.3.2.1 can be accessed from the links in the below table.

Link	C value [kgm^{-2}s^{-1}]	ε value	Colour
doi.org/10.5446/60104	$C = 0.009$	$\varepsilon = 0.7$	Orange
doi.org/10.5446/60105	$C = 0.0125$	$\varepsilon = 0.7$	Blue
doi.org/10.5446/60106	$C = 0.0125$	$\varepsilon = 0.7$	Pink
doi.org/10.5446/60107	$C = 0.01175$	$\varepsilon = 0.9$	Blue
doi.org/10.5446/60108	$C = 0.01175$	$\varepsilon = 0.9$	Orange
doi.org/10.5446/60109	$C = 0.01175$	$\varepsilon = 0.9$	Pink

D.2 High Resolution Model Attractors

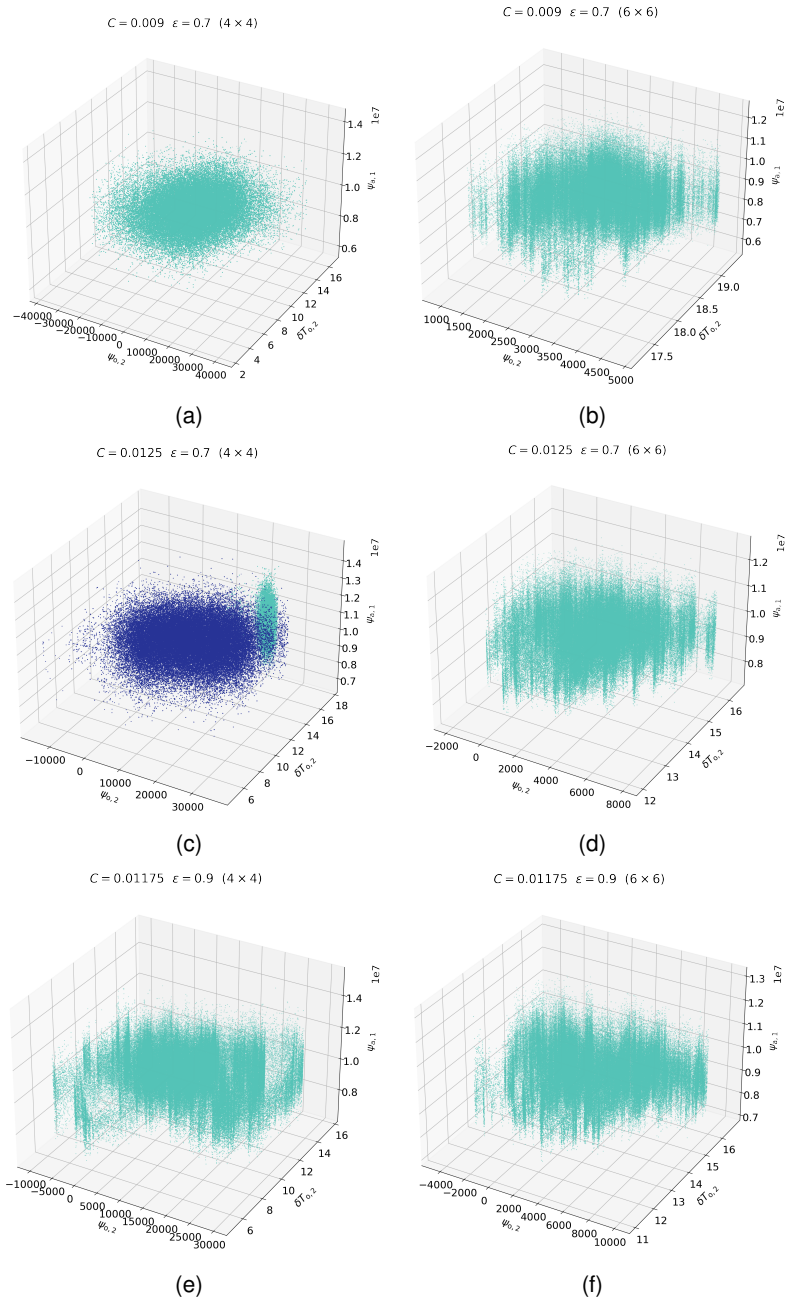


Figure D.1: The resulting attractors of each high resolution model run.

Appendix E

Appendix to Chapter 6

E.1 Deriving Nonlinear Interaction Coefficients

Barotropic Coefficients

Given the conservation properties in Equation 6.17, and the unforced barotropic shell model given in Equation 6.16, with $\theta = 0$, we can write the conservation of energy as

$$\begin{aligned}
\frac{\mathrm{d}T}{\mathrm{d}t} &= \frac{1}{2}\sum_n ik_n^2\psi_n^* \left[k_n^2(a_1\psi_{n+1}^*\psi_{n+2} + a_2\psi_{n-1}^*\psi_{n+1} - a_3\psi_{n-2}\psi_{n-1})\right] + c.c. &= 0 \\
&= \frac{1}{2}\sum_n i\left[k_n^4(a_1\psi_n^*\psi_{n+1}^*\psi_{n+2} + a_2\psi_{n-1}^*\psi_n^*\psi_{n+1} - a_3\psi_{n-2}\psi_{n-1}\psi_n^*)\right] + c.c. &= 0 \\
&= \frac{1}{2}\sum_n i\left[(k_n^4a_1 + k_{n+1}^4a_2 + k_{n+2}^4a_3)\psi_n^*\psi_{n+1}^*\psi_{n+2}\right] + c.c. &= 0 \\
&\iff a_1 + \lambda^4 a_2 + \lambda^8 a_3 = 0
\end{aligned}$$

where we have made changes to the subscripts to obtain the same triplets for each nonlinear term. The coefficient a_3 becomes positive in the last steps as we swap the terms in the complex conjugate part ($c.c.$). Similarly, the conservation of enstrophy gives

$$a_1 + \lambda^6 a_2 + \lambda^{12} a_3 = 0$$

We set the coefficient to be equal to a parameter $alpha$, and we then can calculate the values of a_2 and a_3 with respect to this parameter, as shown in Equation 6.18.

Baroclinic Coefficients

Similar to the barotropic case, for the coupled shell model, given in Equation 6.16, we can use the conservation of energy and enstrophy to find a set of simultaneous equations that

restrict the values of the coefficients

$$\begin{aligned}\frac{\mathrm{d}T}{\mathrm{d}t} = \frac{1}{2}\sum_n & ik_n^4[a_1 + \lambda^4 a_2 + \lambda^8 a_3]\psi_n^*\psi_{n+1}^*\psi_{n+2} \\ & + ik_n^4[a_1\psi_n^*\theta_{n+1}^*\theta_{n+2} + \lambda^4 a_2\theta_n^*\psi_{n+1}^*\theta_{n+2} \\ & + \lambda^8 a_3\theta_n^*\theta_{n+1}^*\psi_{n+2}] + c.c. = 0\end{aligned}$$

$$\begin{aligned}\frac{\mathrm{d}C}{\mathrm{d}t} = \frac{1}{2}\sum_n & ik_n^4[c_1\theta_n^*\theta_{n+1}^*\psi_{n+2} + \lambda^4 c_2\theta_n^*\theta_{n+1}^*\psi_{n+2} + \lambda^8 c_3\theta_n^*\psi_{n+1}^*\theta_{n+2}] \\ & + ik_n^2[K_n d_1\theta_n^*\psi_{n+1}^*\theta_{n+2} + \lambda^2 K_{n+1} d_2\psi_n^*\theta_{n+1}^*\theta_{n+2} \\ & + \lambda^4 K_{n+2} d_3\psi_n^*\theta_{n+1}^*\theta_{n+2}] + c.c. = 0\end{aligned}$$

where $K_n = k_n^2 + k_R^2$ and the triads are colour coded to show which terms are required to cancel. This results in the equations

$$\begin{aligned} a_1 + \lambda^4 a_2 + \lambda^8 a_3 &= 0 \\ k_n^4 a_1 + \lambda^2 k_n^2 K_{n+1} d_2 + \lambda^4 K_{n+2} k_n^2 d_3 &= 0 \\ K_n k_n^2 d_1 + \lambda^4 k_n^4 a_2 + \lambda^8 k_n^4 c_3 &= 0 \\ k_n^4 c_1 + \lambda^4 k_n^4 c_2 + \lambda^8 k_n^4 a_3 &= 0 \end{aligned}$$

Similarly, the triads are collected from the conservation of enstrophy. This results in eight equations for nine unknowns. We again let $a_1 = \alpha$ be a free parameter, and calculate the other coefficients in terms of α, resulting in eight unknowns and eight equations.

E.2 Deriving Barotropic Energy Transfer Expressions

Assuming that energy is conserved, this means that $\dot{T} = 0$, as in Equation 6.17. As in Appendix E.1 we substitute the definition of the nonlinear terms in this expression to give

$$\frac{\mathrm{d}T_n}{\mathrm{d}t} = \frac{1}{2}\left(k_n^2\psi_n^*\left[k_n^2(a_1\psi_{n+1}^*\psi_{n+2} + a_2\psi_{n-1}^*\psi_{n+1} - a_3\psi_{n-2}\psi_{n-1})\right] + c.c.\right) = 0$$

We now take only the terms which involve shell numbers $n-1$, n, $n+1$. In the case of the above equation this gives

$$\begin{aligned}\dot{T}_{n-1} &= a_1\Delta_n = \Delta_n \\ \dot{T}_{n-1} &= \lambda^4 a_2\Delta_n = -\frac{1+\lambda^2}{\lambda^2}\Delta_n \\ \dot{T}_{n-1} &= \lambda^8 a_2\Delta_n = \frac{1}{\lambda^2}\Delta_n\end{aligned}$$

Given the correlator $\Delta_n = k_{n-1}^4 \mathrm{Im}(\psi_{n-1}^*\psi_n^*\psi_{n+1})$. In these terms, the additional λ terms come from the k_{n-1}^4 term in the correlator, and shifting the subscript. The same can be done for the enstrophy.

Once we have these terms we can define the energy flow through a given shell as given in Equation 6.21. In the barotropic case this can be found by

$$\begin{aligned} {}^{E}\Pi_n &= (\dot{T}_{n-1})_n + (\dot{T}_n)_n + (\dot{T}_{n-1})_{n+1} \\ &= \Delta_n - \frac{\lambda^2+1}{\lambda^2}\Delta_n + \Delta_{n+1} \\ &= \Delta_{n+1} - \lambda^{-2}\Delta_n \end{aligned}$$

Here the the subscripts on the triad energy $(\dot{T}_i)_j$ give the i-th shell where the triad is centred on the j-th shell. As the triads only consist of three neighbouring shells, this means that $i = \{j-1, j, j+1\}$. A more in depth discussion on triad interactions and nonlinear fluxes can be found in Chapter 3.9 of Ditlevsen [2010]. The same process is taken for the enstrophy, and then for the baroclinic case.

Appendix F

List of Publications Related to the Thesis

First author

Hamilton, O., Demaeyer, J., Crucifix, M. & Vannitsem, S. (2025) Using Unstable Periodic Orbits to Understand Blocking Behaviour in a Low Order Land-Atmosphere Model. *Chaos*; 35 (8): 083126. 10.1063/5.0268852 (Chapter 3)

Hamilton, O., Demaeyer, J., Vannitsem, S. & Crucifix, M. (2023) Multistability in a Coupled Ocean–Atmosphere Reduced-Order Model: Nonlinear Temperature Equations. *Quarterly Journal of the Royal Meteorological Society*, 1–17. 10.1002/qj.4564 (Chapter 5)

Co-author

Demaeyer, Jonathan, and **Oisín Hamilton**. (2025) auto-AUTO: A Python Layer for Automatically Running the AUTO-07p Continuation Software [under review]. Submitted to JOSS 10.5281/zenodo.14901321

Xavier, A. K., **Hamilton, O.**, Faranda, D., Vannitsem, S. (2024) Predictability of North Pacific Blocking Events: Analogue Based Analysis of Historical MIROC6 Simulations. [Under Review] Submitted to Quarterly Journal of the Royal Meteorological Society 10.48550/arXiv.2504.17691

References

Alberti, T., Donner, R. V., and Vannitsem, S. (2021). Multiscale fractal dimension analysis of a reduced order model of coupled ocean–atmosphere dynamics. *Earth System Dynamics*, 12(3):837–855. 10.5194/esd-12-837-2021.

Alexakis, A. and Biferale, L. (2018). Cascades and transitions in turbulent flows. *Physics Reports*, 767–769:1–101. 10.1016/j.physrep.2018.08.001.

Altmann, E. G., Portela, J. S. E., and Tél, T. (2013). Leaking chaotic systems. *Reviews of Modern Physics*, 85(2):869–918. 10.1103/RevModPhys.85.869.

Andersen, K. H. and Muratore-Ginanneschi, P. (1999). Shell Model for Time-correlated Random Advection of Passive Scalars. *Physical Review E*, 60(6):6663–6681. 10.1103/PhysRevE.60.6663.

Ansmann, G., Karnatak, R., Lehnertz, K., and Feudel, U. (2013). Extreme events in excitable systems and mechanisms of their generation. *Physical Review E*, 88(5):052911. 10.1103/PhysRevE.88.052911.

Ansmann, G., Lehnertz, K., and Feudel, U. (2016). Self-Induced Switchings between Multiple Space-Time Patterns on Complex Networks of Excitable Units. *Physical Review X*, 6(1):011030. 10.1103/PhysRevX.6.011030.

Arbic, B. K., Müller, M., Richman, J. G., Shriver, J. F., Morten, A. J., Scott, R. B., Sérazin, G., and Penduff, T. (2014). Geostrophic Turbulence in the Frequency–Wavenumber Domain: Eddy-Driven Low-Frequency Variability*. *Journal of Physical Oceanography*, 44(8):2050–2069. 10.1175/JPO-D-13-054.1.

Armstrong McKay, D. I., Staal, A., Abrams, J. F., Winkelmann, R., Sakschewski, B., Loriani, S., Fetzer, I., Cornell, S. E., Rockström, J., and Lenton, T. M. (2022). Exceeding 1.5°C global warming could trigger multiple climate tipping points. *Science*, 377(6611):eabn7950. 10.1126/science.abn7950.

Årthun, M., Wills, R. C. J., Johnson, H. L., Chafik, L., and Langehaug, H. R. (2021). Mechanisms of Decadal North Atlantic Climate Variability and Implications for the Recent Cold Anomaly. *Journal of Climate*, 34:19.

Ashwin, P., Wieczorek, S., Vitolo, R., and Cox, P. (2012). Tipping points in open systems: Bifurcation, noise-induced and rate-dependent examples in the climate system. *Philosophical Transactions of the Royal Society A: Mathematical, Physical and Engineering Sciences*, 370(1962):1166–1184. 10.1098/rsta.2011.0306.

Aurell, E., Boffetta, G., Crisanti, A., Frick, P., Paladin, G., and Vulpiani, A. (1994). Statistical mechanics of shell models for two-dimensional turbulence. *Physical Review E*, 50(6):4705–4715. 10.1103/PhysRevE.50.4705.

Aurell, E., Dormy, E., and Frick, P. (1997). Binary tree models of high-Reynolds-number turbulence. *Physical Review E*, 56(2):1692–1698. 10.1103/PhysRevE.56.1692.

Bader, B. W. (2005). Tensor-Krylov Methods for Solving Large-Scale Systems of Nonlinear Equations. *SIAM Journal on Numerical Analysis*, 43(3):1321–1347. 10.1137/040607095.

Badza, A. and Froyland, G. (2024). Identifying the onset and decay of quasi-stationary families of almost-invariant sets with an application to atmospheric blocking events. *Chaos: An Interdisciplinary Journal of Nonlinear Science*, 34(12):123153. 10.1063/5.0225848.

Ballester, J., Quijal-Zamorano, M., Méndez Turrubiates, R. F., Pegenaute, F., Herrmann, F. R., Robine, J. M., Basagaña, X., Tonne, C., Antó, J. M., and Achebak, H. (2023). Heat-related mortality in Europe during the summer of 2022. *Nature Medicine*, 29(7):1857–1866. 10.1038/s41591-023-02419-z.

Barreto, E., Hunt, B. R., Grebogi, C., and Yorke, J. A. (1997). From High Dimensional Chaos to Stable Periodic Orbits: The Structure of Parameter Space. *Physical Review Letters*, 78(24):4561–4564. 10.1103/PhysRevLett.78.4561.

Barry, R. G. and Chorley, R. J. (2003). *Atmosphere, Weather and Climate*. Routledge. 10.4324/9780203871027.

Barsugli, J. J. and Battisti, D. S. (1998). The Basic Effects of Atmosphere–Ocean Thermal Coupling on Midlatitude Variability. *JOURNAL OF THE ATMOSPHERIC SCIENCES*, 55:17.

Batchelor, G. K. (1969). Computation of the Energy Spectrum in Homogeneous Two-Dimensional Turbulence. *The Physics of Fluids*, 12(12):II–233–II–239. 10.1063/1.1692443.

Bauer, P., Thorpe, A., and Brunet, G. (2015). The quiet revolution of numerical weather prediction. *Nature*, 525:47–55. 10.1038/nature14956.

Bembenek, E., Straub, D. N., and Merlis, T. M. (2020). Effects of Moisture in a Two-Layer Model of the Midlatitude Jet Stream. *Journal of the Atmospheric Sciences*, 77(1):131–147. 10.1175/JAS-D-19-0021.1.

Benettin, G., Galgani, L., Giorgilli, A., and Strelcyn, J.-M. (1980). Lyapunov Characteristic Exponents for smooth dynamical systems and for hamiltonian systems; a method for computing all of them. Part 1: Theory. *Meccanica*, 15(1):9–20. 10.1007/BF02128236.

Benzi, R., Biferale, L., and Wirth, A. (1997). Analytic Calculation of Anomalous Scaling in Random Shell Models for a Passive Scalar. *Physical Review Letters*, 78(26):4926–4929. 10.1103/PhysRevLett.78.4926.

Berloff, P., Dewar, W., Kravtsov, S., and McWilliams, J. (2007). Ocean Eddy Dynamics in a Coupled Ocean–Atmosphere Model*. *Journal of Physical Oceanography*, 37(5):1103–1121. 10.1175/JPO3041.1.

Bhatnagar, B. (2024). Statement – Heat claims more than 175 000 lives annually in the WHO European Region, with numbers set to soar. URL: `https://www.who.int/europe/news/item/01-08-2024-statement--heat-claims-more-than-175-000-lives-annually-in-the-who-european-region--with-numbers-set-to-soar`. Accessed on 2025-04-03.

Biferale, L. (2003). Shell Models of Energy Cascade in Turbulence. *Annual Review of Fluid Mechanics*, 35(1):441–468. 10.1146/annurev.fluid.35.101101.161122.

Biferale, L., Lambert, A., Lima, R., and Paladin, G. (1995). Transition to chaos in a shell model of turbulence. *Physica D: Nonlinear Phenomena*, 80(1-2):105–119. 10.1016/0167-2789(95)90065-9.

Birkhoff, G. D. (1927). On the periodic motions of dynamical systems. *Acta Mathematica*, pages 359–379. 10.1007/BF02421325.

Biskamp, D. (1994). Cascade models for magnetohydrodynamic turbulence. *Physical Review E*, 50(4):2702–2711. 10.1103/PhysRevE.50.2702.

Bjerknes, V. (2009). The problem of weather prediction, considered from the viewpoints of mechanics and physics. *Meteorologische Zeitschrift*, 18(6):663–667. 10.1127/0941-2948/2009/416.

Blackport, R. and Fyfe, J. C. (2022). Climate models fail to capture strengthening wintertime North Atlantic jet and impacts on Europe. *Science Advances*, 8(45):eabn3112. 10.1126/sciadv.abn3112.

Blackport, R. and Screen, J. A. (2020). Insignificant effect of Arctic amplification on the amplitude of midlatitude atmospheric waves. *Science Advances*, 6(8):eaay2880. 10.1126/sciadv.aay2880.

Boffetta, G., De Lillo, F., and Musacchio, S. (2011). Shell model for quasi-two-dimensional turbulence. *Physical Review E*, 83(6):066302. 10.1103/PhysRevE.83.066302.

Bohr, T., Jensen, M. H., Paladin, G., and Vulpiani, A. (1998). *Dynamical Systems Approach to Turbulence*. Cambridge University Press. 10.1017/CBO9780511599972.

Booth, J. F., Wang, S., and Polvani, L. (2013). Midlatitude storms in a moister world: Lessons from idealized baroclinic life cycle experiments. *Climate Dynamics*, 41(3-4):787–802. 10.1007/s00382-012-1472-3.

Bourke, W. (1988). Spectral Methods in Global Climate and Weather Prediction Models. In Schlesinger, M. E., editor, *Physically-Based Modelling and Simulation of Climate and Climatic Change*, volume 243, pages 169–220. Springer Netherlands, Dordrecht. 10.1007/978-94-009-3041-4_4.

Boyd, J. (2015). Dynamical Meteorology | Solitary Waves. In *Encyclopedia of Atmospheric Sciences*, pages 417–422. Elsevier. 10.1016/B978-0-12-382225-3.00374-1.

Brunetti, M., Kasparian, J., and Vérard, C. (2019). Co-existing climate attractors in a coupled aquaplanet. *Climate Dynamics*, 53(9-10):6293–6308. 10.1007/s00382-019-04926-7.

Butler, A. H., Thompson, D. W. J., and Heikes, R. (2010). The Steady-State Atmospheric Circulation Response to Climate Change–like Thermal Forcings in a Simple General Circulation Model. *Journal of Climate*, 23(13):3474–3496. 10.1175/2010JCLI3228.1.

Callendar, G. S. (1938). The artificial production of carbon dioxide and its influence on temperature. *Quarterly Journal of the Royal Meteorological Society*, 64(275):223–240. 10.1002/qj.49706427503.

Canuto, C., Hussaini, M. Y., and Quarteroni, A. (2007). *Spectral Methods: Evolution to Complex Geometries and Applications to Fluid Dynamics*. Springer e-books, Berlin Heidelberg.

Catto, J. L., Ackerley, D., Booth, J. F., Champion, A. J., Colle, B. A., Pfahl, S., Pinto, J. G., Quinting, J. F., and Seiler, C. (2019). The Future of Midlatitude Cyclones. *Current Climate Change Reports*, 5(4):407–420. 10.1007/s40641-019-00149-4.

Cavallini, F. and Crisciani, F. (2013). *Quasi-Geostrophic Theory of Oceans and Atmosphere: Topics in the Dynamics and Thermodynamics of the Fluid Earth*, volume 45. Springer Netherlands, Dordrecht. 10.1007/978-94-007-4691-6.

Cehelsky, P. and Tung, K. K. (1987). Theories of Multiple Equilibria and Weather Regimes—A Critical Reexamination. Part II: Baroclinic Two-Layer Models. *Journal of the atmospheric sciences*, 44(21):3282–3303. 10.1175/1520-0469(1987)044<3282:TOMEAW>2.0.CO;2.

Cessi, P. (2000). Thermal Feedback on Wind Stress as a Contributing Cause of Climate Variability. *Journal of Climate*, 13(1):232–244. 10.1175/1520-0442(2000)013<0232:TFOWSA>2.0.CO;2.

Chakraborty, S., Jensen, M. H., and Sarkar, A. (2010). On two-dimensionalization of three-dimensional turbulence in shell models. *The European Physical Journal B*, 73(3):447–453. 10.1140/epjb/e2010-00003-0.

Chandler, G. J. and Kerswell, R. R. (2013). Invariant recurrent solutions embedded in a turbulent two-dimensional Kolmogorov flow. *Journal of Fluid Mechanics*, 722:554–595. 10.1017/jfm.2013.122.

Chang, E. K. M. (2006). An Idealized Nonlinear Model of the Northern Hemisphere Winter Storm Tracks. *Journal of the Atmospheric Sciences*, 63(7):1818–1839. 10.1175/JAS3726.1.

Charney, J. G. (1947). The Dynamics of Long Waves in a Baroclinic Westerly Current. *Journal of Meteorology*, 4(5):136–162. 10.1175/1520-0469(1947)004<0136:TDOLWI>2.0.CO;2.

Charney, J. G. (1948). On the Scales of Atmospheric Motions. *Geofys. Publikasjoner*, 17(2):1–17.

Charney, J. G. (1971). Geostrophic Turbulence. *Journal of the Atmospheric Sciences*, 28(6):1087–1095. 10.1175/1520-0469(1971)028<1087:GT>2.0.CO;2.

Charney, J. G. and DeVore, J. G. (1979). Multiple Flow Equilibria in the Atmosphere and Blocking. *Journal of Atmospheric Sciences*, 36(7):1205–1216. 10.1175/1520-0469(1979)036<1205:MFEITA>2.0.CO;2.

Charney, J. G., Fjortoft, R., and von Neumann, J. (1950). Numerical Integration of the Barotropic Vorticity Equation. *Tellus*, 2(4):237–254. 10.1111/j.2153-3490.1950.tb00336.x.

Charney, J. G. and Phillips, N. A. (1953). NUMERICAL INTEGRATION OF THE QUASI-GEOSTROPHIC EQUATIONS FOR BAROTROPIC AND SIMPLE BAROCLINIC FLOWS. *Journal of Meteorology*, 10(2):71–99. 10.1175/1520-0469(1953)010<0071:NIOTQG>2.0.CO;2.

Charney, J. G. and Straus, D. M. (1980). Form-drag instability, multiple equilibria and propagating planetary waves in baroclinic, orographically forced, planetary wave systems. *Journal of Atmospheric Sciences*, 37(6):1157–1176. http://dx.doi.org/10.1175/1520-0469(1980)037

Chen, L. G. and Dewar, W. K. (1993). Intergyre Communication in a Three-Layer Model. *Journal of Physical Oceanography*, 23(5):855–878. 10.1175/1520-0485(1993)023<0855:ICIATL>2.0.CO;2.

Chen, S.-N. (2023). Revisiting the Baroclinic Eddy Scalings in Two-Layer, Quasigeostrophic Turbulence: Effects of Partial Barotropization. *Journal of Physical Oceanography*, 53(3):891–913. 10.1175/JPO-D-22-0102.1.

Clewley, P., Sherwood, W., LaMar, M., and Guckenheimer, J. (2007). PyDSTool, a software environment for dynamical systems modeling. URL: `https://sourceforge.net/projects/pydstool/`.

Cohen, J., Zhang, X., Francis, J., Jung, T., Kwok, R., Overland, J., Ballinger, T. J., Bhatt, U. S., Chen, H. W., Coumou, D., Feldstein, S., Gu, H., Handorf, D., Henderson, G., Ionita, M., Kretschmer, M., Laliberte, F., Lee, S., Linderholm, H. W., Maslowski, W., Peings, Y., Pfeiffer, K., Rigor, I., Semmler, T., Stroeve, J., Taylor, P. C., Vavrus, S., Vihma, T., Wang, S., Wendisch, M., Wu, Y., and Yoon, J. (2020). Divergent consensuses on Arctic amplification influence on midlatitude severe winter weather. *Nature Climate Change*, 10(1):20–29. 10.1038/s41558-019-0662-y.

Cohen, Y., Gilbert, T., and Procaccia, I. (2002). Statistically preserved structures in shell models of passive scalar advection. *Physical Review E*, 65(2):026314. 10.1103/PhysRevE.65.026314.

Cooley, J. W. and Tukey, J. W. (1965). An algorithm for the machine calculation of complex Fourier series. *Mathematics of Computation*, 19(90):297–301. 10.1090/S0025-5718-1965-0178586-1.

Crane, D. L., Davidchack, R. L., and Gorban, A. N. (2025). Minimal cover of high-dimensional chaotic attractors by embedded recurrent patterns. *Communications in Nonlinear Science and Numerical Simulation*, 140:108345. 10.1016/j.cnsns.2024.108345.

Crofts, J. J. and Davidchack, R. L. (2009). On the use of stabilizing transformations for detecting unstable periodic orbits in high-dimensional flows. *Chaos: An Interdisciplinary Journal of Nonlinear Science*, 19(3):033138. 10.1063/1.3222860.

Curtiss, C. F. and Hirschfelder, J. O. (1952). Integration of Stiff Equations. *Proceedings of the National Academy of Sciences*, 38(3):235–243. 10.1073/pnas.38.3.235.

Cvitanović, P. (1988). Invariant Measurement of Strange Sets in Terms of Cycles. *Physical Review Letters*, 61(24):2729–2732. 10.1103/PhysRevLett.61.2729.

Cvitanović, P., Artuso, R., Mainieri, M., Tanner, G., and Vattay, G. (2020). *Chaos: Classical and Quantum*. ChaosBook.org, Niels Bohr Institute, Copenhagen.

Czaja, A. and Marshall, J. (2001). Observations of atmosphere-ocean coupling in the North Atlantic. *Quarterly Journal of the Royal Meteorological Society*, 127(576):1893–1916. 10.1002/qj.49712757603.

Dai, P. and Nie, J. (2022). Robust Expansion of Extreme Midlatitude Storms Under Global Warming. *Geophysical Research Letters*, 49(10):e2022GL099007. 10.1029/2022GL099007.

Davini, P., Cagnazzo, C., Gualdi, S., and Navarra, A. (2012). Bidimensional Diagnostics, Variability, and Trends of Northern Hemisphere Blocking. *Journal of Climate*, 25(19):6496–6509. 10.1175/JCLI-D-12-00032.1.

Davini, P. and D'Andrea, F. (2020). From CMIP3 to CMIP6: Northern Hemisphere Atmospheric Blocking Simulation in Present and Future Climate. *Journal of Climate*, 33(23):10021–10038. 10.1175/JCLI-D-19-0862.1.

De Cruz, L., Demaeyer, J., and Vannitsem, S. (2016a). The Modular Arbitrary-Order Ocean-Atmosphere Model: MAOOAM v1.0. *Geoscientific Model Development*, 9(8):2793–2808. 10.5194/gmd-9-2793-2016.

De Cruz, L., Demaeyer, J., and Vannitsem, S. (2016b). The Modular Arbitrary-Order Ocean-Atmosphere Model: MAOOAM v1.0. *Geoscientific Model Development*, 9(8):2793–2808. 10.5194/gmd-9-2793-2016.

De Cruz, L., Schubert, S., Demaeyer, J., Lucarini, V., and Vannitsem, S. (2018). Exploring the Lyapunov instability properties of high-dimensional atmospheric and climate models. *Nonlinear Processes in Geophysics*, 25:387–412. 10.5194/npg-25-387-2018.

De Pietro, M., Biferale, L., and Mailybaev, A. A. (2015). Inverse energy cascade in nonlocal helical shell models of turbulence. *Physical Review E*, 92(4):043021. 10.1103/PhysRevE.92.043021.

Delforge, D., Wathelet, V., Below, R., Sofia, C. L., Tonnelier, M., Loenhout, J. A., and Speybroeck, N. (2025). EM-DAT: The Emergency Events Database. 10.21203/rs.3.rs-3807553/v2, URL: `https://www.researchsquare.com/article/rs-3807553/v2`. Accessed on 2025-03-09.

Demaeyer, J., De Cruz, L., and Hamilton, O. (2022). Qgs version 0.2.6 release. URL: `https://doi.org/10.5281/zenodo.7404671`.

Demaeyer, J., De Cruz, L., and Hamilton, O. (2025). Qgs. 10.5281/ZENODO.15102613, URL: `https://zenodo.org/doi/10.5281/zenodo.15102613`. Accessed on 2025-05-27.

Demaeyer, J., De Cruz, L., and Vannitsem, S. (2020). Qgs: A flexible Python framework of reduced-order multiscale climate models. *Journal of Open Source Software*, 5(56):2597. 10.21105/joss.02597.

Demaeyer, J. and Hamilton, O. (2025). Climdyn/auto-AUTO: V0.5.1. *Zenodo*. doi.org/10.5281/zenodo.14901321.

Demaeyer, J., Penny, S. G., and Vannitsem, S. (2021). Identifying efficient ensemble perturbations for initializing subseasonal-to-seasonal prediction. *arXiv:2109.07979 [nlin, physics:physics]*.

Demaeyer, J. and Vannitsem, S. (2018). Comparison of stochastic parameterizations in the framework of a coupled ocean–atmosphere model. *Nonlinear Processes in Geophysics*, 25(3):605–631. 10.5194/npg-25-605-2018.

Demaeyer, J. and Vannitsem, S. (2020). Correcting for model changes in statistical postprocessing – an approach based on response theory. *Nonlinear Processes in Geophysics*, 27(2):307–327. 10.5194/npg-27-307-2020.

Desnianskii, V. and Novikov, E. (1974). Simulation of cascade processes in turbulent flows. *Journal of Applied Mathematics and Mechanics*, 38(3):468–475. 10.1016/0021-8928(74)90041-0.

Dewar, W. K. (2001). On Ocean Dynamics in Midlatitude Climate. *Journal of Climate*, 14(23):4380–4397. 10.1175/1520-0442(2001)014<4380:OODIMC>2.0.CO;2.

Dijkstra, H. A. (2013). *Nonlinear Climate Dynamics*. Cambridge University Press. 10.1017/CBO9781139034135.

Ditlevsen, P. D. (1996). Temporal intermittency and cascades in shell models of turbulence. *Physical Review E*, 54(1):985–988. 10.1103/PhysRevE.54.985.

Ditlevsen, P. D. (2010). *Turbulence and Shell Models*. Cambridge University Press. 10.1017/CBO9780511919251.

Ditlevsen, P. D. (2012). A stochastic model of cascades in two-dimensional turbulence. *Physics of Fluids*, 24(10):105109. 10.1063/1.4761834.

Ditlevsen, P. D. and Mogensen, I. A. (1996). Cascades and statistical equilibrium in shell models of turbulence. *Physical Review E*, 53(5):4785–4793. 10.1103/PhysRevE.53.4785.

Doedel, E. J. and Oldeman, B. E. (2012). *Auto-07p: Continuation and Bifurcation Software.* Concordia University Canada, Montreal, Canada.

Eckmann, J. P. and Ruelle, D. (1985). Ergodic theory of chaos and strange attractors. *Reviews of Modern Physics*, 57(3):617–656. 10.1103/RevModPhys.57.617.

Edwards, P. N. (2011). History of climate modeling. *WIREs Climate Change*, 2(1):128–139. 10.1002/wcc.95.

Egger, J. (1978). Dynamics of Blocking Highs. *Journal of the Atmospheric Sciences*, 35(10):1788–1801. 10.1175/1520-0469(1978)035<1788:DOBH>2.0.CO;2.

Eggers, J. and Grossmann, S. (1991). Does deterministic chaos imply intermittency in fully developed turbulence? *Physics of Fluids A: Fluid Dynamics*, 3(8):1958–1968. 10.1063/1.857926.

Ehrendorfer, M. (2011). *Spectral Numerical Weather Prediction Models*. Society for Industrial and Applied Mathematics.

Ellsaesser, H. W. (1966). Evaluation of Spectral Versus Grid Methods of Hemispheric Numerical Weather Prediction. *Journal of Applied Meteorology*, 5(3):246–262. 10.1175/1520-0450(1966)005<0246:eosvgm>2.0.co;2.

Elson, P., Elliott Sales de Andrade, Lucas, G., May, R., Hattersley, R., Campbell, E., Comer, R., Dawson, A., Little, B., Raynaud, S., scmc72, Snow, A. D., Igolston, Blay, B., Killick, P., Ibdreyer, Peglar, P., Wilson, N., Andrew, Szymaniak, J., Berchet, A., Bosley, C., Davis, L., Filipe, Krasting, J., Bradbury, M., stephenworsley, and Kirkham, D. (2024). SciTools/cartopy: REL: V0.24.1. 10.5281/ZENODO.1182735, URL: `https://zenodo.org/doi/10.5281/zenodo.1182735`. Accessed on 2025-08-31.

Ester, M., Kriegel, H.-P., and Xu, X. (1996). A Density-Based Algorithm for Discovering Clusters in Large Spatial Databases with Noise. *AAAI Press*, 96(34):226–231.

Ferreira, D., Frankignoul, C., and Marshall, J. (2001). Coupled Ocean–Atmosphere Dynamics in a Simple Midlatitude Climate Model. *Journal of Climate*, 14(17):3704–3723. 10.1175/1520-0442(2001)014<3704:COADIA>2.0.CO;2.

Flynn, C. M., Moemken, J., Pinto, J. G., and Messori, G. (2024). A New Database of Extreme European Winter Windstorms. 10.5194/essd-2024-298, URL: `https://essd.copernicus.org/preprints/essd-2024-298/`. Accessed on 2025-03-09.

Francis, J. A. (2017). Why Are Arctic Linkages to Extreme Weather Still up in the Air? *Bulletin of the American Meteorological Society*, 98(12):2551–2557. 10.1175/BAMS-D-17-0006.1.

Francis, J. A. and Vavrus, S. J. (2012). Evidence linking Arctic amplification to extreme weather in mid-latitudes. *Geophysical Research Letters*, 39(6). 10.1029/2012GL051000.

Frick, P. and Sokoloff, D. (1998). Cascade and dynamo action in a shell model of magnetohydrodynamic turbulence. *Physical Review E*, 57(4):4155–4164. 10.1103/PhysRevE.57.4155.

Frierson, D. M. W. (2006). Robust increases in midlatitude static stability in simulations of global warming. *Geophysical Research Letters*, 33(24):2006GL027504. 10.1029/2006GL027504.

Frierson, D. M. W. (2008). Midlatitude Static Stability in Simple and Comprehensive General Circulation Models. *Journal of the Atmospheric Sciences*, 65(3):1049–1062. 10.1175/2007JAS2373.1.

Gage, K. S. and Nastrom, G. D. (1986). Theoretical Interpretation of Atmospheric Wavenumber Spectra of Wind and Temperature Observed by Commercial Aircraft During GASP. *Journal of the Atmospheric Sciences*, 43(7):729–740. 10.1175/1520-0469(1986)043<0729:TIOAWS>2.0.CO;2.

Ghil, M., Groth, A., Kondrashov, D., and Robertson, A. W. (2019). Extratropical Sub-seasonal to Seasonal Oscillations and Multiple Regimes: The Dynamical Systems View. In *Sub-Seasonal to Seasonal Prediction*, pages 119–142. Elsevier. 10.1016/B978-0-12-811714-9.00006-1.

Ghil, M. and Lucarini, V. (2020). The physics of climate variability and climate change. *Reviews of Modern Physics*, 92(3):035002. 10.1103/RevModPhys.92.035002.

Ghil, M. and Robertson, A. W. (2002). "Waves" vs. "particles" in the atmosphere's phase space: A pathway to long-range forecasting? *Proceedings of the National Academy of Sciences*, 99(Supplement 1):2493–2500. 10.1073/pnas.012580899.

Gilbert, T., L'vov, V. S., Pomyalov, A., and Procaccia, I. (2002). Inverse Cascade Regime in Shell Models of Two-Dimensional Turbulence. *Physical Review Letters*, 89(7):074501. 10.1103/PhysRevLett.89.074501.

Ginelli, F., Chate', H., Livi, R., and Politi, A. (2013). Covariant Lyapunov vectors. *Journal of Physics A: Mathematical and Theoretical*, 46(25):254005. 10.1088/1751-8113/46/25/254005.

Ginelli, F., Poggi, P., Turchi, A., Chaté, H., Livi, R., and Politi, A. (2007). Characterizing Dynamics with Covariant Lyapunov Vectors. *Physical Review Letters*, 99(13):130601. 10.1103/PhysRevLett.99.130601.

Gledzer, E. (1973). System of hydrodynamic type admitting two quadratic integrals of motion. *Doklady Akademii Nauk SSSR*, 209(5):1046–1048.

Golding, B., Mylne, K., and Clark, P. (2004). The history and future of numerical weather prediction in the Met Office. *Weather*, 59(11):299–306. 10.1256/wea.113.04.

Goodman, J. and Marshall, J. (1999). A Model of Decadal Middle-Latitude Atmosphere–Ocean Coupled Modes. *Journal of Climate*, 12(2):621–641. 10.1175/1520-0442(1999)012<0621:AMODML>2.0.CO;2.

Goosse, H. (2015). *Climate System Dynamics and Modeling*. Cambridge University Press, Cambridge. 10.1017/CBO9781316018682.

Grafke, T. and Vanden-Eijnden, E. (2019). Numerical computation of rare events via large deviation theory. *Chaos: An Interdisciplinary Journal of Nonlinear Science*, 29(6):063118. 10.1063/1.5084025.

Grebogi, C., Ott, E., and Yorke, J. A. (1988). Unstable periodic orbits and the dimensions of multifractal chaotic attractors. *Physical Review A*, 37(5):1711–1724. 10.1103/PhysRevA.37.1711.

Grenci, L. M. and Nese, J. M. (2018). *A World of Weather : Fundamentals of Meteorology*. Kendall Hunt, Penn State University.

Gritsun, A. (2013). Statistical characteristics, circulation regimes and unstable periodic orbits of a barotropic atmospheric model. *Philosophical Transactions of the Royal Society A: Mathematical, Physical and Engineering Sciences*, 371(1991):20120336. 10.1098/rsta.2012.0336.

Gritsun, A. S. (2008). Unstable periodic trajectories of a barotropic model of the atmosphere. *Russian Journal of Numerical Analysis and Mathematical Modelling*, 23(4). 10.1515/RJNAMM.2008.021.

Gritsun, A. S. (2010). Unstable periodic orbits and sensitivity of the barotropic model of the atmosphere. *Russian Journal of Numerical Analysis and Mathematical Modelling*, 25(4). 10.1515/rjnamm.2010.020.

Gu, Q., Gervais, M., Danabasoglu, G., Kim, W. M., Castruccio, F., Maroon, E., and Xie, S.-P. (2024). Wide range of possible trajectories of North Atlantic climate in a warming world. *Nature Communications*, 15(1):4221. 10.1038/s41467-024-48401-2.

Haarsma, R. J., Roberts, M. J., Vidale, P. L., Senior, C. A., Bellucci, A., Bao, Q., Chang, P., Corti, S., Fučkar, N. S., Guemas, V., Von Hardenberg, J., Hazeleger, W., Kodama, C., Koenigk, T., Leung, L. R., Lu, J., Luo, J.-J., Mao, J., Mizielinski, M. S., Mizuta, R., Nobre, P., Satoh, M., Scoccimarro, E., Semmler, T., Small, J., and Von Storch, J.-S. (2016). High Resolution Model Intercomparison Project (HighResMIP v1.0) for CMIP6. *Geoscientific Model Development*, 9(11):4185–4208. 10.5194/gmd-9-4185-2016.

Hamilton, O., Demaeyer, J., Crucifix, M., and Vannitsem, S. (2025). Using unstable periodic orbits to understand blocking behavior in a low order land–atmosphere model. *Chaos: An Interdisciplinary Journal of Nonlinear Science*, 35(8):083126. 10.1063/5.0268852.

Hamilton, O., Demaeyer, J., Vannitsem, S., and Crucifix, M. (2023). Multistability in a coupled ocean–atmosphere reduced-order model: Nonlinear temperature equations. *Quarterly Journal of the Royal Meteorological Society*, 149(757):3423–3439. 10.1002/qj.4564.

Hannachi, Abdel., Straus, D. M., Franzke, C. L. E., Corti, S., and Woollings, T. (2017). Low-frequency nonlinearity and regime behavior in the Northern Hemisphere extratropical atmosphere. *Reviews of Geophysics*, 55(1):199–234. 10.1002/2015RG000509.

Harvey, B. J., Cook, P., Shaffrey, L. C., and Schiemann, R. (2020). The Response of the Northern Hemisphere Storm Tracks and Jet Streams to Climate Change in the CMIP3, CMIP5, and CMIP6 Climate Models. *Journal of Geophysical Research: Atmospheres*, 125(23):e2020JD032701. 10.1029/2020JD032701.

Harvey, B. J., Shaffrey, L. C., and Woollings, T. J. (2015). Deconstructing the climate change response of the Northern Hemisphere wintertime storm tracks. *Climate Dynamics*, 45(9-10):2847–2860. 10.1007/s00382-015-2510-8.

Hattori, Y., Rubinstein, R., and Ishizawa, A. (2004). Shell model for rotating turbulence. *Physical Review E*, 70(4):046311. 10.1103/PhysRevE.70.046311.

Held, I. M. and Soden, B. J. (2006). Robust Responses of the Hydrological Cycle to Global Warming. *Journal of Climate*, 19(21):5686–5699. 10.1175/JCLI3990.1.

Herring, J. R. (1988). The inverse cascade range of quasi-geostrophic turbulence. *Meteorology and Atmospheric Physics*, 38(1-2):106–115. 10.1007/BF01029952.

Hogg, A. M. C., Dewar, W. K., Killworth, P. D., and Blundell, J. R. (2003). A Quasi-Geostrophic Coupled Model (Q-GCM). *Monthly Weather Review*, 131(10):2261–2278. 10.1175/1520-0493(2003)131<2261:AQCMQ>2.0.CO;2.

Hogg, A. M. C., Dewar, W. K., Killworth, P. D., and Blundell, J. R. (2006). Decadal Variability of the Midlatitude Climate System Driven by the Ocean Circulation. *Journal of Climate*, 19(7):1149–1166. 10.1175/JCLI3651.1.

Holton, J. R. (2004). *An Introduction to Dynamic Meteorology*, volume 88. Elsevier Academic Press, Burlington, MA.

Hoskins, B. J., McIntyre, M. E., and Robertson, A. W. (1985). On the use and significance of isentropic potential vorticity maps. *Quarterly Journal of the Royal Meteorological Society*, 111(470):877–946. 10.1002/qj.49711147002.

Houghton, J. (1986). *The Physics of the Atmospheres (2nd Ed)*. Cambridge University Press.

Hunt, B. R. and Ott, E. (1996a). Optimal Periodic Orbits of Chaotic Systems. *Physical Review Letters*, 76(13):2254–2257. 10.1103/PhysRevLett.76.2254.

Hunt, B. R. and Ott, E. (1996b). Optimal periodic orbits of chaotic systems occur at low period. *Physical Review E*, 54(1):328–337. 10.1103/PhysRevE.54.328.

Hurrell, J. W., Kushnir, Y., Ottersen, G., and Visbeck, M. (2003). An overview of the North Atlantic Oscillation. In Hurrell, J. W., Kushnir, Y., Ottersen, G., and Visbeck, M., editors, *Geophysical Monograph Series*, volume 134, pages 1–35. American Geophysical Union, Washington, D. C. 10.1029/134GM01.

Intergovernmental Panel On Climate Change (IPCC) (2023). *Climate Change 2021 – The Physical Science Basis: Working Group I Contribution to the Sixth Assessment Report of the Intergovernmental Panel on Climate Change*. Cambridge University Press. 10.1017/9781009157896.

Itoh, H. and Kimoto, M. (1996). Multiple Attractors and Chaotic Itinerancy in a Quasi-geostrophic Model with Realistic Topography: Implications for Weather Regimes and Low-Frequency Variability. *Journal of the Atmospheric Sciences*, 53(15):2217–2231. 10.1175/1520-0469(1996)053<2217:MAACII>2.0.CO;2.

Jeevanjee, N., Hassanzadeh, P., Hill, S., and Sheshadri, A. (2017). A perspective on climate model hierarchies. *Journal of Advances in Modeling Earth Systems*, 9(4):1760–1771. 10.1002/2017MS001038.

Jensen, M. H., Paladin, G., and Vulpiani, A. (1992). Shell model for turbulent advection of passive-scalar fields. *Physical Review A*, 45(10):7214–7221. 10.1103/PhysRevA.45.7214.

Kadanoff, L., Lohse, D., and Schörghofer, N. (1997). Scaling and linear response in the GOY turbulence model. *Physica D: Nonlinear Phenomena*, 100(1-2):165–186. 10.1016/S0167-2789(96)00174-1.

Kadanoff, L., Lohse, D., Wang, J., and Benzi, R. (1995). Scaling and dissipation in the GOY shell model. *Physics of Fluids*, 7(3):617–629. 10.1063/1.868775.

Kaplan, J. L. and Yorke, J. A. (1979). Chaotic behavior of multidimensional difference equations. In Peitgen, H.-O. and Walther, H.-O., editors, *Functional Differential Equations and Approximation of Fixed Points*, volume 730, pages 204–227. Springer Berlin Heidelberg, Berlin, Heidelberg. 10.1007/BFb0064319.

Karnatak, R., Ansmann, G., Feudel, U., and Lehnertz, K. (2014). Route to extreme events in excitable systems. *Physical Review E*, 90(2):022917. 10.1103/PhysRevE.90.022917.

Kato, S. and Yamada, M. (2003). Unstable periodic solutions embedded in a shell model turbulence. *Physical Review E*, 68(2):025302. 10.1103/PhysRevE.68.025302.

Katsafados, P., Mavromatidis, E., and Spyrou, C. (2022). *Numerical Weather Prediction and Data Assimilation*. Wiley. 10.1002/9781119560463.

Kautz, L.-A., Martius, O., Pfahl, S., Pinto, J. G., Ramos, A. M., Sousa, P. M., and Woollings, T. (2022). Atmospheric blocking and weather extremes over the Euro-Atlantic sector – a review. *Weather and Climate Dynamics*, 3(1):305–336. 10.5194/wcd-3-305-2022.

Kawahara, G. and Kida, S. (2001). Periodic motion embedded in plane Couette turbulence: Regeneration cycle and burst. *Journal of Fluid Mechanics*, 449:291–300. 10.1017/S0022112001006243.

Kawahara, G., Kida, S., and Van Veen, L. (2006). Unstable periodic motion in turbulent flows. *Nonlinear Processes in Geophysics*, 13(5):499–507. 10.5194/npg-13-499-2006.

Kazantsev, E. (1998). Unstable periodic orbits and attractor of the barotropic ocean model. *Nonlinear Processes in Geophysics*, 5(4):193–208. 10.5194/npg-5-193-1998.

Kazantsev, E. (2001). Sensitivity of the attractor of the barotropic ocean model to external influences: Approach by unstable periodic orbits. *Nonlinear Processes in Geophysics*, 8(4/5):281–300. 10.5194/npg-8-281-2001.

Keel, T., Brierley, C., Edwards, T., and Frame, T. H. A. (2024). Exploring Uncertainty of Trends in the North Pacific Jet Position. *Geophysical Research Letters*, 51(16):e2024GL109500. 10.1029/2024GL109500.

Kidston, J. and Vallis, G. K. (2012). The Relationship between the Speed and the Latitude of an Eddy-Driven Jet in a Stirred Barotropic Model. *Journal of the Atmospheric Sciences*, 69(11):3251–3263. 10.1175/JAS-D-11-0300.1.

Kobras, M., Lucarini, V., and Ambaum, M. H. (2024). Latitudinal storm track shift in a reduced two-level model of the atmosphere. *Physica D: Nonlinear Phenomena*, 458:133926. 10.1016/j.physd.2023.133926.

Kockelkoren, J., Okkels, F., and Jensen, M. H. (1998). Chaotic Behavior in Shell Models and Shell Maps. *Journal of Statistical Physics*, 93(3/4):833–842. 10.1023/B:JOSS.0000033165.51531.8c.

Kostelich, E. J., Kan, I., Grebogi, C., Ott, E., and Yorke, J. A. (1997). Unstable dimension variability: A source of nonhyperbolicity in chaotic systems. *Physica D: Nonlinear Phenomena*, 109(1-2):81–90. 10.1016/S0167-2789(97)00161-9.

Kraichnan, R. H. (1967). Inertial Ranges in Two-Dimensional Turbulence. *The Physics of Fluids*, 10(7):1417–1423. 10.1063/1.1762301.

Kraichnant, R. H. and Montgomery, D. (1980). Two-dimensional turbulence. *Reports on Progress in Physics,*, 43(5). 10.1088/0034-4885/43/5/001.

Kravtsov, S., Berloff, P., Dewar, W. K., Ghil, M., and McWilliams, J. C. (2006). Dynamical Origin of Low-Frequency Variability in a Highly Nonlinear Midlatitude Coupled Model. *Journal of Climate*, 19(24):6391–6408. 10.1175/JCLI3976.1.

Kravtsov, S. and Robertson, A. (2002). Midlatitude ocean-atmosphere interaction in an idealized coupled model. *Climate Dynamics*, 19(8):693–711. 10.1007/s00382-002-0256-6.

Kreilos, T. and Eckhardt, B. (2012). Periodic orbits near onset of chaos in plane Couette flow. *Chaos: An Interdisciplinary Journal of Nonlinear Science*, 22(4):047505. 10.1063/1.4757227.

Krishnamurti, T. N., Hardiker, V. M., Bedi, H. S., and Ramaswamy, L. (2006). *An Introduction to Global Spectral Modeling*. Springer, New York, N.Y.

Kummu, M. and Varis, O. (2011). The world by latitudes: A global analysis of human population, development level and environment across the north–south axis over the past half century. *Applied Geography*, 31(2):495–507. 10.1016/j.apgeog.2010.10.009.

Kuptsov, P. V. and Parlitz, U. (2012). Theory and computation of covariant Lyapunov vectors. *Journal of Nonlinear Science*, 22(5):727–762. 10.1007/s00332-012-9126-5.

Kuznetsov, S. P. (2012). *Hyperbolic Chaos*. Springer Berlin Heidelberg, Berlin, Heidelberg. 10.1007/978-3-642-23666-2.

Kwasniok, F. (2004). Empirical Low-Order Models of Barotropic Flow. *Journal of the Atmospheric Sciences*, 61(2):235–245. 10.1175/1520-0469(2004)061<0235:ELMOBF>2.0.CO;2.

Lai, Y.-C., Nagai, Y., and Grebogi, C. (1997). Characterization of the Natural Measure by Unstable Periodic Orbits in Chaotic Attractors. *Physical Review Letters*, 79(4):649–652. 10.1103/PhysRevLett.79.649.

Laîné, A., Lapeyre, G., and Rivière, G. (2011). A Quasigeostrophic Model for Moist Storm Tracks. *Journal of the Atmospheric Sciences*, 68(6):1306–1322. 10.1175/2011JAS3618.1.

Legras, B. and Ghil, M. (1985). Persistent Anomalies, Blocking and Variations in Atmospheric Predictability. *Journal of the Atmospheric Sciences*, 42(5):433–471. 10.1175/1520-0469(1985)042<0433:PABAVI>2.0.CO;2.

Legras, B. and Vautard, R. (1996). A Guide to Liapunov Vectors. In Palmer, T., editor, *Predictability*, volume I, pages 135–146. ECMWF, Reading, UK.

Leith, C. E. (1968). Diffusion Approximation for Two-Dimensional Turbulence. *The Physics of Fluids*, 11(3):671–672. 10.1063/1.1691968.

Leith, C. E. (1971). Atmospheric Predictability and Two-Dimensional Turbulence. *Journal of the Atmospheric Sciences*, 28(2):145–161. 10.1175/1520-0469(1971)028<0145:APATDT>2.0.CO;2.

Lenton, T. M., Held, H., Kriegler, E., Hall, J. W., Lucht, W., Rahmstorf, S., and Schellnhuber, H. J. (2008). Tipping elements in the Earth's climate system. *Proceedings of the National Academy of Sciences*, 105(6):1786–1793. 10.1073/pnas.0705414105.

Lessinnes, T., Carati, D., and Verma, M. K. (2009). Energy transfers in shell models for magnetohydrodynamics turbulence. *Physical Review E*, 79(6):066307. 10.1103/PhysRevE.79.066307.

Li, D., He, Y., Huang, J., Bi, L., and Ding, L. (2018). Multiple Equilibria in a Land–Atmosphere Coupled System. *Journal of Meteorological Research*, 32(6):950–973. 10.1007/s13351-018-8012-y.

Lorenz, D. J. (2022). The Role of Temperature Gradients versus Static Stability on the Zonal Wind and Eddy Kinetic Energy Response to Thermal Perturbations. *Journal of Climate*, 35(21):7041–7056. 10.1175/JCLI-D-22-0139.1.

Lorenz, E. N. (1960). Maximum Simplification of the Dynamic Equations. *Tellus A: Dynamic Meteorology and Oceanography*, 12(3):243–254. 10.3402/tellusa.v12i3.9406.

Lorenz, E. N. (1963a). Deterministic Nonperiodic Flow. *Journal of the Atmospheric Sciences*, 20(2):130–141. 10.1175/1520-0469(1963)020<0130:DNF>2.0.CO;2.

Lorenz, E. N. (1963b). The Mechanics of Vacillation. *Journal of the Atmospheric Sciences*, 20(5):448–465. 10.1175/1520-0469(1963)020<0448:TMOV>2.0.CO;2.

Lorenz, E. N. (1969). The predictability of a flow which possesses many scales of motion. *Tellus*, 21(3):289–307. 10.1111/j.2153-3490.1969.tb00444.x.

Lorenz, E. N. (1982). Atmospheric predictability experiments with a large numerical model. *Tellus*, 34(6):505–513. 10.1111/j.2153-3490.1982.tb01839.x.

Lorenz, E. N. (1984). Irregularity: A fundamental property of the atmosphere. *Tellus A*, 36A(2):98–110. 10.1111/j.1600-0870.1984.tb00230.x.

Lu, J., Vecchi, G. A., and Reichler, T. (2007). Expansion of the Hadley cell under global warming. *Geophysical Research Letters*, 34(6):2006GL028443. 10.1029/2006GL028443.

Lucarini, V. and Gritsun, A. (2019). A new mathematical framework for atmospheric blocking events. *Climate Dynamics*, 54(1-2):575–598. 10.1007/s00382-019-05018-2.

L'vov, V. S., Podivilov, E., Pomyalov, A., Procaccia, I., and Vandembroucq, D. (1998). Improved shell model of turbulence. *Physical Review E*, 58(2):1811–1822. 10.1103/PhysRevE.58.1811.

Lynch, P. (2008). The origins of computer weather prediction and climate modeling. *Journal of Computational Physics*, 227(7):3431–3444. 10.1016/j.jcp.2007.02.034.

Lynch, P. (2014). *The Emergence of Numerical Weather Prediction: Richardson's Dream*. Cambridge Univ. Press, New York.

Maher, P., Gerber, E. P., Medeiros, B., Merlis, T. M., Sherwood, S., Sheshadri, A., Sobel, A. H., Vallis, G. K., Voigt, A., and Zurita-Gotor, P. (2019). Model Hierarchies for Understanding Atmospheric Circulation. *Reviews of Geophysics*, 57(2):250–280. 10.1029/2018RG000607.

Maiocchi, C. C., Lucarini, V., and Gritsun, A. (2022). Decomposing the dynamics of the Lorenz 1963 model using unstable periodic orbits: Averages, transitions, and quasi-invariant sets. *Chaos: An Interdisciplinary Journal of Nonlinear Science*, 32(3):033129. 10.1063/5.0067673.

Maiocchi, C. C., Lucarini, V., Gritsun, A., and Sato, Y. (2024). Heterogeneity of the attractor of the Lorenz '96 model: Lyapunov analysis, unstable periodic orbits, and shadowing properties. *Physica D: Nonlinear Phenomena*, 457:133970. 10.1016/j.physd.2023.133970.

Mak, M. (1989). A study of topographically induced multiple equilibria and low-frequency variability. I. Idealized topography. *Quarterly Journal of the Royal Meteorological Society*, 115(485):45–77. 10.1002/qj.49711548504.

Maltrud, M. E. and Vallis, G. K. (1991). Energy spectra and coherent structures in forced two-dimensional and beta-plane turbulence. *Journal of Fluid Mechanics Digital Archive*, 228:321. 10.1017/S0022112091002720.

Mestel, B. and Percival, I. (1987). Newton method for highly unstable orbits. *Physica D: Nonlinear Phenomena*, 24(1-3):172–178. 10.1016/0167-2789(87)90072-8.

Met-Office (2025). A look back on Storm Éowyn. URL: `https://www.metoffice.gov.uk/blog/2025/a-look-back-on-storm-eowyn`. Accessed on 2025-03-31.

Meurer, A., Smith, C. P., Paprocki, M., Čertík, O., Kirpichev, S. B., Rocklin, M., Kumar, Am., Ivanov, S., Moore, J. K., Singh, S., Rathnayake, T., Vig, S., Granger, B. E., Muller, R. P., Bonazzi, F., Gupta, H., Vats, S., Johansson, F., Pedregosa, F., Curry, M. J., Terrel, A. R., Roučka, Š., Saboo, A., Fernando, I., Kulal, S., Cimrman, R., and Scopatz, A. (2017a). SymPy: Symbolic computing in Python. *PeerJ Computer Science*, 3:e103. 10.7717/peerj-cs.103.

Meurer, A., Smith, C. P., Paprocki, M., Čertík, O., Kirpichev, S. B., Rocklin, M., Kumar, Am., Ivanov, S., Moore, J. K., Singh, S., Rathnayake, T., Vig, S., Granger, B. E., Muller, R. P., Bonazzi, F., Gupta, H., Vats, S., Johansson, F., Pedregosa, F., Curry, M. J., Terrel, A. R., Roučka, Š., Saboo, A., Fernando, I., Kulal, S., Cimrman, R., and Scopatz, A. (2017b). SymPy: Symbolic computing in Python. *PeerJ Computer Science*, 3:e103. 10.7717/peerj-cs.103.

Mitra, D. and Pandit, R. (2005). Dynamics of Passive-Scalar Turbulence. *Physical Review Letters*, 95(14):144501. 10.1103/PhysRevLett.95.144501.

Molnos, S., Mamdouh, T., Petri, S., Nocke, T., Weinkauf, T., and Coumou, D. (2017). A network-based detection scheme for the jet stream core. *Earth System Dynamics*, 8(1):75–89. 10.5194/esd-8-75-2017.

Molteni, F., Buizza, R., Palmer, T., and Petroliagis, T. (1994). The ECMWF Ensemble Prediction System - methodology and validation. *ECMWF*. 10.21957/JL1B71OQJ.

Moon, W., Kim, B.-M., Yang, G.-H., and Wettlaufer, J. S. (2022a). Wavier jet streams driven by zonally asymmetric surface thermal forcing. *Proceedings of the National Academy of Sciences*, 119(38):e2200890119. 10.1073/pnas.2200890119.

Moon, W., Manucharyan, G. E., and Dijkstra, H. A. (2022b). Baroclinic instability and large-scale wave propagation in a planetary-scale atmosphere. *Quarterly Journal of the Royal Meteorological Society*, 148(743):809–825. 10.1002/qj.4232.

Moore, P., Coleman, L., Hally, A., Murphy, A., Turcu, A., Walsh, S., Watters, V., and Laura, Z. (2018). Storm Emma. Technical report.

Muis, S., Aerts, J. C. J. H., Á. Antolínez, J. A., Dullaart, J. C., Duong, T. M., Erikson, L., Haarsma, R. J., Apecechea, M. I., Mengel, M., Le Bars, D., O'Neill, A., Ranasinghe, R., Roberts, M. J., Verlaan, M., Ward, P. J., and Yan, K. (2023). Global Projections of Storm Surges Using High-Resolution CMIP6 Climate Models. *Earth's Future*, 11(9):e2023EF003479. 10.1029/2023EF003479.

Nabizadeh, E., Hassanzadeh, P., Yang, D., and Barnes, E. A. (2019). Size of the Atmospheric Blocking Events: Scaling Law and Response to Climate Change. *Geophysical Research Letters*, 46(22):13488–13499. 10.1029/2019GL084863.

Nauw, J. J. and Dijkstra, H. A. (2001). The origin of low-frequency variability of double-gyre wind-driven flows. *Journal of Marine Research*, 59(4):567–597. 10.1357/002224001762842190.

Nese, J. M. (1989). Quantifying local predictability in phase space. *Physica D: Nonlinear Phenomena*, 35(1-2):237–250. 10.1016/0167-2789(89)90105-X.

Nese, J. M. and Dutton, J. A. (1993). Quantifying Predictability Variations in a Low-Order Occan-Atmosphere Model: A Dynamical Systems Approach. *Journal of Climate*, 6(2):185–204. 10.1175/1520-0442(1993)006<0185:QPVIAL>2.0.CO;2.

O'Brien, E. and Branscome, L. E. (1989). Minimal modeling of the extratropical general circulation. *Tellus A*, 41A(4):292–307. 10.1111/j.1600-0870.1989.tb00384.x.

Obukhov, A. M. (1971). Turbulence in an atmosphere with a non-uniform temperature. *Boundary-Layer Meteorology*, 2(1):7–29. 10.1007/BF00718085.

O'Gorman, P. A. (2010). Understanding the varied response of the extratropical storm tracks to climate change. *Proceedings of the National Academy of Sciences*, 107(45):19176–19180. 10.1073/pnas.1011547107.

Ohkitani, K. and Yamada, M. (1989). Temporal Intermittency in the Energy Cascade Process and Local Lyapunov Analysis in Fully-Developed Model Turbulence. *Progress of Theoretical Physics*, 81(2):329–341. 10.1143/PTP.81.329.

Olesen, P. and Jensen, M. H. (2007). Exact Periodic Solutions of Shells Models of Turbulence. *Nonlinearity*, 20(10):2333–2352. 10.1088/0951-7715/20/10/004.

Oseledec, V. I. (1968). A multiplicative ergodic theorem, Lyapunov characteristic numbers for dynamical systems. *Transactions of the Moscow Mathematical Society*, 19:197–231.

Ossó, A., Bladé, I., Karpechko, A., Li, C., Maraun, D., Romppainen-Martius, O., Shaffrey, L., Voigt, A., Woollings, T., and Zappa, G. (2024). Advancing Our Understanding of Eddy-driven Jet Stream Responses to Climate Change – A Roadmap. *Current Climate Change Reports*, 11(1):2. 10.1007/s40641-024-00199-3.

Palmer, T. N. (1993). A nonlinear dynamical perspective on climate change. *Weather*, 48(10):314–326. 10.1002/j.1477-8696.1993.tb05802.x.

Palmer, T. N. (1999). A Nonlinear Dynamical Perspective on Climate Prediction. *Journal of Climate*, 12(2):575–591. 10.1175/1520-0442(1999)012<0575:ANDPOC>2.0.CO;2.

Paltridge, G. W. (1979). Climate and thermodynamic systems of maximum dissipation. *Nature*, 279(5714):630–631. 10.1038/279630a0.

Parker, T. S. and Chua, L. O. (1989). *Practical Numerical Algorithms for Chaotic Systems*. Springer New York, New York, NY. 10.1007/978-1-4612-3486-9.

Pedlosky, J. (1987). *Geophysical Fluid Dynamics*. Springer New York, New York, NY. 10.1007/978-1-4612-4650-3.

Pelly, J. L. and Hoskins, B. J. (2003). A New Perspective on Blocking. *Journal of the Atmospheric Sciences*, 60(5):743–755. 10.1175/1520-0469(2003)060<0743:ANPOB>2.0.CO;2.

Pereira, R. F., De S. Pinto, S. E., Viana, R. L., Lopes, S. R., and Grebogi, C. (2007). Periodic orbit analysis at the onset of the unstable dimension variability and at the blowout bifurcation. *Chaos: An Interdisciplinary Journal of Nonlinear Science*, 17(2):023131. 10.1063/1.2748619.

Pierini, S. (2011). Low-Frequency Variability, Coherence Resonance, and Phase Selection in a Low-Order Model of the Wind-Driven Ocean Circulation. *Journal of Physical Oceanography*, 41(9):1585–1604. 10.1175/JPO-D-10-05018.1.

Pinheiro, M. C., Ullrich, P. A., and Grotjahn, R. (2019). Atmospheric blocking and intercomparison of objective detection methods: Flow field characteristics. *Climate Dynamics*, 53(7-8):4189–4216. 10.1007/s00382-019-04782-5.

Plaut, G. and Vautard, R. (1994). Spells of Low-Frequency Oscillations and Weather Regimes in the Northern Hemisphere. *Journal of the Atmospheric Sciences*, 51(2):210–236. 10.1175/1520-0469(1994)051<0210:SOLFOA>2.0.CO;2.

Plunian, F. and Stepanov, R. (2007). A non-local shell model of hydrodynamic and magnetohydrodynamic turbulence. *New Journal of Physics*, 9(8):294–294. 10.1088/1367-2630/9/8/294.

Plunian, F., Stepanov, R., and Frick, P. (2013). Shell models of magnetohydrodynamic turbulence. *Physics Reports*, 523(1):1–60. 10.1016/j.physrep.2012.09.001.

Pughe-Sanford, J. L., Quinn, S., Balabanski, T., and Grigoriev, R. O. (2023). Computing Chaotic Time-Averages from a Small Number of Periodic Orbits. URL: `http://arxiv.org/abs/2307.09626`. Accessed on 2023-08-21.

Randall, D. A., Wood, R. A., Bony, S., Colman, R., Fichefet, T., Fyfe, J., Kattsov, V., Pitman, A., Shukla, J., Srinivasan, J., Stouffer, R. J., Sumi, A., Taylor, K. E., AchutaRao, K., Allan, R., Berger, A., Blatter, H., Bonfils, C., Boone, A., Bretherton, C., Broccoli, A., Brovkin, V., Dirmeyer, P., Doutriaux, C., Drange, H., Frei, A., Ganopolski, A., Gent, P., Gleckler, P., Goosse, H., Graham, R., Gregory, J. M., Gudgel, R., Hall, A., Hallegatte, S., Hasumi, H., Henderson-Sellers, A., Hendon, H., Hodges, K., Holland, M., Holtslag, A. A. M., Hunke, E., Huybrechts, P., Ingram, W., Joos, F., Kirtman, B., Klein,

S., Koster, R., Kushner, P., Lanzante, J., Latif, M., Pavlova, T., Federationi, R., Petoukhov, V., Phillips, T., Power, S., Rahmstorf, S., Raper, S. C. B., Renssen, H., Rind, D., Roberts, M., Rosati, A., Schär, C., Schmittner, A., Scinocca, J., Seidov, D., Slater, A. G., Slingo, J., Smith, D., Soden, B., Stern, W., Stone, D. A., Sudo, K., Takemura, T., Tselioudis, G., Webb, M., Wild, M., Manzini, E., Matsuno, T., and McAvaney, B. (2007). Climate Models and Their Evaluation. In *Climate Change 2007: The Physical Science Basis. Contribution of Working Group I to the Fourth Assessment Report of the Intergovernmental Panel on Climate Change*. Cambridge University Press.

Rantanen, M., Karpechko, A. Y., Lipponen, A., Nordling, K., Hyvärinen, O., Ruosteenoja, K., Vihma, T., and Laaksonen, A. (2022). The Arctic has warmed nearly four times faster than the globe since 1979. *Communications Earth & Environment*, 3(1):168. 10.1038/s43247-022-00498-3.

Rantanen, M., Räisänen, J., Sinclair, V. A., and Järvinen, H. (2019). Sensitivity of idealised baroclinic waves to mean atmospheric temperature and meridional temperature gradient changes. *Climate Dynamics*, 52(5-6):2703–2719. 10.1007/s00382-018-4283-3.

Ray, A., Rakshit, S., Basak, G. K., Dana, S. K., and Ghosh, D. (2020). Understanding the origin of extreme events in El Niño southern oscillation. *Physical Review E*, 101(6):062210. 10.1103/PhysRevE.101.062210.

Reinhold, B. B. and Pierrehumbert, R. T. (1982). Dynamics of Weather Regimes: Quasi-Stationary Waves and Blocking. *Monthly Weather Review*, 110(9):1105–1145. 10.1175/1520-0493(1982)110<1105:DOWRQS>2.0.CO;2.

Reynolds, C. A. and Errico, R. M. (1999). Convergence of Singular Vectors toward Lyapunov Vectors. *Monthly Weather Review*, 127(10):2309–2323. 10.1175/1520-0493(1999)127<2309:cosvtl>2.0.co;2.

Rhines, P. B. (1975). Waves and turbulence on a beta-plane. *Journal of Fluid Mechanics*, 69(3):417–443. 10.1017/S0022112075001504.

Rhines, P. B. (1977). The dynamics of unsteady currents. *The Sea*, 6:189–318.

Rhines, P. B. (1979). Geostrophic Turbulence. *Annual Review of Fluid Mechanics*, 11(1):401–441. 10.1146/annurev.fl.11.010179.002153.

Riboldi, J., Lott, F., D'Andrea, F., and Rivière, G. (2020). On the Linkage Between Rossby Wave Phase Speed, Atmospheric Blocking, and Arctic Amplification. *Geophysical Research Letters*, 47(19):e2020GL087796. 10.1029/2020GL087796.

Richardson, L. F. (1922). *Weather Prediction by Numerical Process*. Cambridge University Press, London.

Salmon, R. (1978). Two-layer quasi-geostrophic turbulence in a simple special case. *Geophysical & Astrophysical Fluid Dynamics*, 10(1):25–52. 10.1080/03091927808242628.

Salmon, R. (1980). Baroclinic instability and geostrophic turbulence. *Geophysical & Astrophysical Fluid Dynamics*, 15(1):167–211. 10.1080/03091928008241178.

Saltzman, B. (1962). Finite Amplitude Free Convection as an Initial Value Problem—I. *Journal of the Atmospheric Sciences*, 19(4):329–341. 10.1175/1520-0469(1962)019<0329:FAFCAA>2.0.CO;2.

Saravanan, R. and Mc Williams, J. C. (1995). Multiple Equilibria, Natural Variability, and Climate Transitions in an Idealized Ocean–Atmosphere Model. *Journal of Climate*, 8(10):2296–2323. 10.1175/1520-0442(1995)008<2296:MENVAC>2.0.CO;2.

Sasaki, E., Kawahara, G., and Jiménez, J. (2021). Bifurcation structure of unstable periodic orbits in plane Couette flow with the Smagorinsky model. *Physical Review Fluids*, 6(8):084608. 10.1103/PhysRevFluids.6.084608.

Scherrer, S. C., Croci-Maspoli, M., Schwierz, C., and Appenzeller, C. (2006). Two-dimensional indices of atmospheric blocking and their statistical relationship with winter climate patterns in the Euro-Atlantic region. *International Journal of Climatology*, 26(2):233–249. 10.1002/joc.1250.

Schnabel, R. and Frank, P. (1984). Tensor Methods for Nonlinear Equations. *SIAM Journal on Numerical Analysis*, 21(5).

Schneider, T., O'Gorman, P. A., and Levine, X. J. (2010). Water Vapor and the Dynamics of Climate Changes. *Reviews of Geophysics*, 48(3):RG3001. 10.1029/2009RG000302.

Schubert, W., Ruprecht, E., Hertenstein, R., Ferreira, R. N., Taft, R., Rozoff, C., Ciesielski, P., and Kuo, H.-C. (2004). English translations of twenty-one of Ertel's papers on geophysical fluid dynamics. *Meteorologische Zeitschrift*, 13(6):527–576. 10.1127/0941-2948/2004/0013-0527.

Screen, J. A. and Simmonds, I. (2013). Exploring links between Arctic amplification and mid-latitude weather. *Geophysical Research Letters*, 40(5):959–964. 10.1002/grl.50174.

Selten, F. M. and Branstator, G. (2004). Preferred Regime Transition Routes and Evidence for an Unstable Periodic Orbit in a Baroclinic Model. *Journal of the Atmospheric Sciences*, 61(18):2267–2282. 10.1175/1520-0469(2004)061<2267:PRTRAE>2.0.CO;2.

Shaw, T. A. (2019). Mechanisms of Future Predicted Changes in the Zonal Mean Mid-Latitude Circulation. *Current Climate Change Reports*, 5(4):345–357. 10.1007/s40641-019-00145-8.

Shaw, T. A., Arblaster, J. M., Birner, T., Butler, A. H., Domeisen, D. I. V., Garfinkel, C. I., Garny, H., Grise, K. M., and Karpechko, A. Yu. (2024). Emerging Climate Change Signals in Atmospheric Circulation. *AGU Advances*, 5(6):e2024AV001297. 10.1029/2024AV001297.

Shaw, T. A., Baldwin, M., Barnes, E. A., Caballero, R., Garfinkel, C. I., Hwang, Y.-T., Li, C., O'Gorman, P. A., Rivière, G., Simpson, I. R., and Voigt, A. (2016). Storm track processes and the opposing influences of climate change. *Nature Geoscience*, 9(9):656–664. 10.1038/ngeo2783.

Shaw, T. A., Barpanda, P., and Donohoe, A. (2018). A Moist Static Energy Framework for Zonal-Mean Storm-Track Intensity. *Journal of the Atmospheric Sciences*, 75(6):1979–1994. 10.1175/JAS-D-17-0183.1.

Shaw, T. A. and Miyawaki, O. (2024). Fast upper-level jet stream winds get faster under climate change. *Nature Climate Change*, 14(1):61–67. 10.1038/s41558-023-01884-1.

Shaw, T. A. and Voigt, A. (2015). Tug of war on summertime circulation between radiative forcing and sea surface warming. *Nature Geoscience*, 8(7):560–566. 10.1038/ngeo2449.

Shimada, I. and Nagashima, T. (1979). A Numerical Approach to Ergodic Problem of Dissipative Dynamical Systems. *Progress of Theoretical Physics*, 61(6):1605–1616. 10.1143/PTP.61.1605.

Silberman, I. (1954). Planetary Waves in the Atmosphere. *Journal of Meteorology*, 11(1):27–34. 10.1175/1520-0469(1954)011<0027:pwita>2.0.co;2.

Smith, K. S., Boccaletti, G., Henning, C. C., Marinov, I., Tam, C. Y., Held, I. M., and Vallis, G. K. (2002). Turbulent diffusion in the geostrophic inverse cascade. *Journal of Fluid Mechanics*, 469:13–48. 10.1017/S0022112002001763.

Smith, L. M. and Waleffe, F. (2002). Generation of slow large scales in forced rotating stratified turbulence. *Journal of Fluid Mechanics*, 451:145–168. 10.1017/S0022112001006309.

Spydell, M. and Cessi, P. (2003). Baroclinic Modes in a Two-Layer Basin. *Journal of Physical Oceanography*, 33(3):610–622. 10.1175/1520-0485(2003)033<0610:BMIATL>2.0.CO;2.

Staten, P. W., Lu, J., Grise, K. M., Davis, S. M., and Birner, T. (2018). Re-examining tropical expansion. *Nature Climate Change*, 8(9):768–775. 10.1038/s41558-018-0246-2.

Steffen, W., Rockström, J., Richardson, K., Lenton, T. M., Folke, C., Liverman, D., Summerhayes, C. P., Barnosky, A. D., Cornell, S. E., Crucifix, M., Donges, J. F., Fetzer, I., Lade, S. J., Scheffer, M., Winkelmann, R., and Schellnhuber, H. J. (2018). Trajectories of the Earth System in the Anthropocene. *Proceedings of the National Academy of Sciences*, 115(33):8252–8259. 10.1073/pnas.1810141115.

Stendel, M., Francis, J., White, R., Williams, P. D., and Woollings, T. (2021). The jet stream and climate change. In *Climate Change*, pages 327–357. Elsevier. 10.1016/B978-0-12-821575-3.00015-3.

Stephan, C. C., Duras, J., Harris, L., Klocke, D., Putman, W. M., Taylor, M., Wedi, N. P., Žagar, N., and Ziemen, F. (2022). Atmospheric Energy Spectra in Global Kilometre-Scale Models. *Tellus A: Dynamic Meteorology and Oceanography*, 74(2022):280–299. 10.16993/tellusa.26.

Straus, D. M. and Ditlevsen, P. (1999). Two-dimensional turbulence properties of the ECMWF reanalyses. *Tellus A: Dynamic Meteorology and Oceanography*, 51(5):749. 10.3402/tellusa.v51i5.14473.

Tibaldi, S. and Molteni, F. (1990). On the operational predictability of blocking. *Tellus A*, 42(3):343–365. 10.1034/j.1600-0870.1990.t01-2-00003.x.

Tibaldi, S. and Molteni, F. (2018). *Atmospheric Blocking in Observation and Models*, volume 1. Oxford University Press. 10.1093/acrefore/9780190228620.013.611.

Tierney, G., Posselt, D. J., and Booth, J. F. (2018). An examination of extratropical cyclone response to changes in baroclinicity and temperature in an idealized environment. *Climate Dynamics*, 51(9-10):3829–3846. 10.1007/s00382-018-4115-5.

Tung, K. K. (2003). The k{-3} and k{-5/3} Energy Spectrum of Atmospheric Turbulence: Quasi-geostrophic Two-Level Model Simulation. *Journal of the Atmospheric Sciences*, 60.

Vallis, G. (2017). *Atmospheric and Oceanic Fluid Dynamics*. Cambridge University Press.

Vallis, G. K. and Maltrud, M. E. (1993). Generation of Mean Flows and Jets on a Beta Plane and over Topography. *Journal of Physical Oceanography*, 23(7):1346–1362. 10.1175/1520-0485(1993)023<1346:GOMFAJ>2.0.CO;2.

Vallis, G. K., Zurita-Gotor, P., Cairns, C., and Kidston, J. (2015). Response of the large-scale structure of the atmosphere to global warming. *Quarterly Journal of the Royal Meteorological Society*, 141(690):1479–1501. 10.1002/qj.2456.

van der Avoird, E., H., D., J., N., and C., S. (2002). Nonlinearly induced low-frequency variability in a midlatitude coupled ocean-atmosphere model of intermediate complexity. *Climate Dynamics*, 19(3-4):303–320. 10.1007/s00382-001-0220-x.

Van Westen, R. M., Kliphuis, M., and Dijkstra, H. A. (2024). Physics-based early warning signal shows that AMOC is on tipping course. *Science Advances*, 10(6):eadk1189. 10.1126/sciadv.adk1189.

Vanderborght, E., Demaeyer, J., Manucharyan, G., Moon, W., and Dijkstra, H. A. (2024). Physics of the Eddy Memory Kernel of a Baroclinic Midlatitude Atmosphere. *Journal of the Atmospheric Sciences*, 81(3):691–711. 10.1175/JAS-D-23-0146.1.

Vannitsem, S. (2015). The role of the ocean mixed layer on the development of the North Atlantic Oscillation: A dynamical system's perspective. *Geophysical Research Letters*, 42(20):8615–8623. 10.1002/2015GL065974.

Vannitsem, S. (2017). Predictability of large-scale atmospheric motions: Lyapunov exponents and error dynamics. *Chaos: An Interdisciplinary Journal of Nonlinear Science*, 27(3):032101. 10.1063/1.4979042.

Vannitsem, S. and De Cruz, L. (2014). A 24-variable low-order coupled ocean–atmosphere model: OA-QG-WS v2. *Geoscientific Model Development*, 7(2):649–662. 10.5194/gmd-7-649-2014.

Vannitsem, S., Demaeyer, J., De Cruz, L., and Ghil, M. (2015). Low-frequency variability and heat transport in a low-order nonlinear coupled ocean–atmosphere model. *Physica D: Nonlinear Phenomena*, 309:71–85. 10.1016/j.physd.2015.07.006.

Vannitsem, S., Demaeyer, J., and Ghil, M. (2021). Extratropical Low-Frequency Variability With ENSO Forcing: A Reduced-Order Coupled Model Study. *Journal of Advances in Modeling Earth Systems*, 13(6). 10.1029/2021MS002530.

Vannitsem, S. and Ghil, M. (2017). Evidence of coupling in ocean-atmosphere dynamics over the North Atlantic. *Geophysical Research Letters*, 44(4):2016–2026. 10.1002/2016GL072229.

Vannitsem, S. and Lucarini, V. (2016). Statistical and Dynamical Properties of Covariant Lyapunov Vectors in a Coupled Atmosphere-Ocean Model - Multiscale Effects, Geometric Degeneracy, and Error Dynamics. *Journal of Physics A: Mathematical and Theoretical*, 49(22):224001. 10.1088/1751-8113/49/22/224001.

Vautard, R., Cattiaux, J., Happé, T., Singh, J., Bonnet, R., Cassou, C., Coumou, D., D'Andrea, F., Faranda, D., Fischer, E., Ribes, A., Sippel, S., and Yiou, P. (2023). Heat extremes in Western Europe increasing faster than simulated due to atmospheric circulation trends. *Nature Communications*, 14(1):6803. 10.1038/s41467-023-42143-3.

Vautard, R. and Legras, B. (1988). On the Source of Midlatitude Low-Frequency Variability. Part II: Nonlinear Equilibration of Weather Regimes. *Journal of the Atmospheric Sciences*, 45(20):2845–2867. 10.1175/1520-0469(1988)045<2845:OTSOML>2.0.CO;2.

Veltz, R. (2020). BifurcationKit.jl. URL: `https://hal.science/hal-02902346`.

Verma, M. K., Ayyer, A., Debliquy, O., Kumar, S., and Chandra, A. V. (2005). Local shell-to-shell energy transfer via nonlocal interactions in fluid turbulence. *Pramana*, 65(2):297. 10.1007/BF02898618.

Veronis, G. (1963). An Analysis of Wind-Driven Ocean Circulation with a Limited Number of Fourier Components. *Journal of the Atmospheric Sciences*, 20(6):577–593. 10.1175/1520-0469(1963)020<0577:AAOWDO>2.0.CO;2.

Virtanen, P., Gommers, R., Oliphant, T. E., Haberland, M., Reddy, T., Cournapeau, D., Burovski, E., Peterson, P., Weckesser, W., Bright, J., Van Der Walt, S. J., Brett, M., Wilson, J., Millman, K. J., Mayorov, N., Nelson, A. R. J., Jones, E., Kern, R., Larson, E., Carey, C. J., Polat, İ., Feng, Y., Moore, E. W., VanderPlas, J., Laxalde, D., Perktold, J., Cimrman, R., Henriksen, I., Quintero, E. A., Harris, C. R., Archibald, A. M., Ribeiro, A. H., Pedregosa, F., Van Mulbregt, P., SciPy 1.0 Contributors, Vijaykumar, A., Bardelli, A. P., Rothberg, A., Hilboll, A., Kloeckner, A., Scopatz, A., Lee, A., Rokem, A., Woods, C. N., Fulton, C., Masson, C., Häggström, C., Fitzgerald, C., Nicholson, D. A., Hagen, D. R., Pasechnik, D. V., Olivetti, E., Martin, E., Wieser, E., Silva, F., Lenders, F., Wilhelm, F., Young, G., Price, G. A., Ingold, G.-L., Allen, G. E., Lee, G. R., Audren, H., Probst, I., Dietrich, J. P., Silterra, J., Webber, J. T., Slavič, J., Nothman, J., Buchner, J., Kulick, J., Schönberger, J. L., De Miranda Cardoso, J. V., Reimer, J., Harrington, J., Rodríguez, J. L. C., Nunez-Iglesias, J., Kuczynski, J., Tritz, K., Thoma, M., Newville, M., Kümmerer, M., Bolingbroke, M., Tartre, M., Pak, M., Smith, N. J., Nowaczyk, N., Shebanov, N., Pavlyk, O., Brodtkorb, P. A., Lee, P., McGibbon, R. T., Feldbauer, R., Lewis, S., Tygier, S., Sievert, S., Vigna, S., Peterson, S., More, S., Pudlik, T., Oshima, T., Pingel, T. J., Robitaille, T. P., Spura, T., Jones, T. R., Cera, T., Leslie, T., Zito, T., Krauss, T., Upadhyay, U., Halchenko, Y. O., and Vázquez-Baeza, Y. (2020). SciPy 1.0: Fundamental algorithms for scientific computing in Python. *Nature Methods*, 17(3):261–272. 10.1038/s41592-019-0686-2.

Voigt, A., Albern, N., Ceppi, P., Grise, K., Li, Y., and Medeiros, B. (2021). Clouds, radiation, and atmospheric circulation in the present-day climate and under climate change. *WIREs Climate Change*, 12(2):e694. 10.1002/wcc.694.

Voigt, A. and Shaw, T. A. (2015). Circulation response to warming shaped by radiative changes of clouds and water vapour. *Nature Geoscience*, 8(2):102–106. 10.1038/ngeo2345.

Watt-Meyer, O. and Frierson, D. M. W. (2017). Local and Remote Impacts of Atmospheric Cloud Radiative Effects Onto the Eddy-Driven Jet. *Geophysical Research Letters*, 44(19). 10.1002/2017GL074901.

Weng, W. and Neelin, J. D. (1998). On the role of ocean-atmosphere interaction in midlatitude interdecadal variability. *Geophysical Research Letters*, 25(2):167–170. 10.1029/97GL03507.

Wirth, A. and Biferale, L. (1996). Anomalous scaling in random shell models for passive scalars. *Physical Review E*, 54(5):4982–4989. 10.1103/PhysRevE.54.4982.

Wolfe, C. L. and Samelson, R. M. (2007). An efficient method for recovering Lyapunov vectors from singular vectors. *Tellus A: Dynamic Meteorology and Oceanography*, 59(3):355. 10.1111/j.1600-0870.2007.00234.x.

Woollings, T., Barriopedro, D., Methven, J., Son, S.-W., Martius, O., Harvey, B., Sillmann, J., Lupo, A. R., and Seneviratne, S. (2018). Blocking and its Response to Climate Change. *Current Climate Change Reports*, 4(3):287–300. 10.1007/s40641-018-0108-z.

Woollings, T., Drouard, M., O'Reilly, C. H., Sexton, D. M. H., and McSweeney, C. (2023a). Trends in the atmospheric jet streams are emerging in observations and could be linked to tropical warming. *Communications Earth & Environment*, 4(1):125. 10.1038/s43247-023-00792-8.

Woollings, T., Hannachi, A., and Hoskins, B. (2010). Variability of the North Atlantic eddy-driven jet stream: Variability of the North Atlantic Jet Stream. *Quarterly Journal of the Royal Meteorological Society*, 136(649):856–868. 10.1002/qj.625.

Woollings, T., Hoskins, B., Blackburn, M., and Berrisford, P. (2008). A New Rossby Wave–Breaking Interpretation of the North Atlantic Oscillation. *Journal of the Atmospheric Sciences*, 65(2):609–626. 10.1175/2007JAS2347.1.

Woollings, T., Li, C., Drouard, M., Dunn-Sigouin, E., Elmestekawy, K. A., Hell, M., Hoskins, B., Mbengue, C., Patterson, M., and Spengler, T. (2023b). The role of Rossby waves in polar weather and climate. *Weather and Climate Dynamics*, 4(1):61–80. 10.5194/wcd-4-61-2023.

Wu, L. and Liu, Z. (2005). North Atlantic Decadal Variability: Air–Sea Coupling, Oceanic Memory, and Potential Northern Hemisphere Resonance*. *Journal of Climate*, 18(2):331–349. 10.1175/JCLI-3264.1.

Xavier, A. K., Demaeyer, J., and Vannitsem, S. (2024). Variability and predictability of a reduced-order land–atmosphere coupled model. *Earth System Dynamics*, 15(4):893–912. 10.5194/esd-15-893-2024.

Xavier, A. K., Hamilton, O., Faranda, D., and Vannitsem, S. (2025). Predictability of north Pacific blocking events : Analogue based analysis of historical MIROC6 simulations. 10.48550/ARXIV.2504.17691, URL: `https://arxiv.org/abs/2504.17691`. Accessed on 2025-08-31.

Yagi, M., Itoh, S.-I., Itoh, K., and Fukuyama, A. (1999). Numerical study of chaos based on a shell model. *Chaos: An Interdisciplinary Journal of Nonlinear Science*, 9(2):393–402. 10.1063/1.166416.

Yamada, M. and Ohkitani, K. (1987). Lyapunov Spectrum of a Chaotic Model of Three-Dimensional Turbulence. *Journal of the Physical Society of Japan*, 56(12):4210–4213. 10.1143/JPSJ.56.4210.

Yamada, M. and Ohkitani, K. (1988). Lyapunov spectrum of a model of two-dimensional turbulence. *Physical Review Letters*, 60(11):983–986. 10.1103/PhysRevLett.60.983.

Zhang, F., Sun, Y. Q., Magnusson, L., Buizza, R., Lin, S.-J., Chen, J.-H., and Emanuel, K. (2019). What Is the Predictability Limit of Midlatitude Weather? *Journal of the Atmospheric Sciences*, 76(4):1077–1091. 10.1175/JAS-D-18-0269.1.